Swansea University
Prifysgol Abertawe

A high-performance boundary element method and its applications in engineering

Biao Liu

Faculty of Science and Engineering
Swansea University

SUBMITTED TO SWANSEA UNIVERSITY IN FULFILLMENT OF THE REQUIREMENTS FOR THE DEGREE OF DOCTOR OF PHILOSOPHY

December 2022

Declaration and Statements

DECLARATION

This work has not previously been accepted in substance for any degree and is not being concurrently submitted in candidature for any degree.

Signed ..... [redacted] ..... (candidate)

Date ..... 12/07/2023 .....

STATEMENT 1

This thesis is the result of my own investigations, except where otherwise stated. Other sources are acknowledged by footnotes giving explicit references. A bibliography is appended.

Signed ..... [redacted] ..... (candidate)

Date ..... 12/07/2023 .....

STATEMENT 2

I hereby give consent for my thesis, if accepted, to be available for photocopying and for inter-library loans after expiry of a bar on access approved by the Swansea University.

Signed ..... [redacted] ..... (candidate)

Date ..... 12/07/2023 .....

Abstract

As a semi-numerical and semi-analytical method, owing to the inherent advantage, of boundary-only discretisation, the boundary element method (BEM) has been widely applied to problems with complicated geometries, stress concentration problems, infinite domain problems, and many others. However, domain integrals and non-symmetrical and dense matrix systems are two obstacles for BEM which have hindered the its further development and application. This thesis is aimed at proposing a high-performance BEM to tackle the above two drawbacks and broaden the application scope of BEM.

In this thesis, a detailed introduction to the traditional BEM is given and several popular algorithms are introduced or proposed to enhance the performance of BEM. Numerical examples in heat conduction analysis, thermoelastic analysis and thermoelastic fracture problems are performed to assess the efficiency and correction of the algorithms. In addition, necessary theoretical derivations are embraced for establishing novel boundary integral equations (BIEs) for specific engineering problems. The following three parts are the main content of this thesis.

(1) The first part (Part II consisting of two chapters) is aimed at heat conduction analysis by BEM.

The coefficient matrix of equations formed by BEM in solving problems is fully-populated which occupy large computer memory. To deal with that, the fast multipole method (FMM) is introduced to energize the line integration boundary element method (LIBEM) to performs better in efficiency.

In addition, to compute domain integrals with known or unknown

integrand functions which are caused by heat sources or heterogeneity, a novel BEM, the adaptive orthogonal interpolation moving least squares (AOIMLS) method enhanced LIBEM, which also inherits the advantage of boundary-only discretisation, is proposed. Unlike LIBEM, which is an accurate and stable method for computing domain integrals, but only works when the mathematical expression of integral function in domain integrals is known, the AOIMLS enhanced LIBEM can compute domain integrals with known or unknown integral functions, which ensures all the nonlinear and nonhomogeneous problems can be solved without domain discretisation. In addition, the AOIMLS can adaptively avoid singular or ill-conditioned moment matrices, thus ensuring the stability of the calculation results.

(2) In the second part (Part III consisting of four chapters), the thermoelastic problems and fracture problems are the main objectives.

Due to considering thermal loads, domain integrals appear in the BIEs of the thermoelastic problems, and the expression of integrand functions is known or not depending on the temperature distribution given or not, the AOIMLS enhanced LIBEM is introduced to conduct thermoelasticity analysis thereby.

Besides, a series of novel unified boundary integral equations based on BEM and DDM are derived for solving fracture problems and thermoelastic fracture problems in finite and infinite domains. Two sets of unified BIEs are derived for fracture problems in finite and infinite domains based on the direct BEM and DDM respectively, which can provide accurate and stable results. Another two sets of BIEs are addressed by employing indirect BEM and DDM, which cannot ensure a stable result, thereby a modified indirect BEM is proposed which performs much more stable. Moreover, a set of novel BIEs based on the direct BEM and DDM for cracked domains under thermal stress is proposed.

(2) In the third part (Part IV consisting of one chapter), a high-efficiency combined BEM and discrete element method (DEM) is proposed to compute the inner stress distribution and particle breakage of particle assemblies based

on the solution mapping scheme.

For the stress field computation of particles with similar geometry, a template particle is used as the representative particle, so that only the related coefficient matrices of one template particle in the local coordinate system are needed to be calculated, while the coefficient matrices of the other particles, can be obtained by mapping between the local and global coordinate systems. Thus, the combined BEM and DEM is much more effective when modelling a large-scale particle system with a small number of distinct possible particle shapes. Furthermore, with the help of the Hoek-Brown criterion, the possible cracks or breakage paths of a particle can be obtained.

Keywords: Domain integrals; Non-symmetrical and dense matrix system; AOIMLS enhanced LIBEM; Heat conduction; Thermoelastic problems; Fracture problems; Thermoelastic fracture mechanics.

Publications

The following publications are based on the research presented in this thesis:

[1] W Zhou, **B Liu**, Q Wang, X Chang, X Chen. Formulations of displacement discontinuity method for crack problems based on boundary element method. Engineering Analysis with Boundary Elements, 2020, 115: 86-95.

[2] **B Liu**, W Zhou, Q Wang. The novel boundary integral equation with adaptive orthogonal IMLS based line integration method for cracked domains under thermal stress. Engineering Fracture Mechanics, 2020, 239: 107325.

[3] **B Liu**, W Zhou, Q Wang, X Chang. An AOIMLS enhanced LIBEM and for solving 3D thermo-elastic problems and nonhomogeneous heat conduction problems with heat generation. International Journal of Thermal Sciences, 2021, 163: 106864.

[4] **B Liu**, Q Wang, W Zhou, X Chang. NURBS-enhanced line integration BEM for thermo-elastic problems considering the gravity load. Engineering Analysis with Boundary Elements, 2021, 126: 118-127.

[5] **B Liu**, W Zhou, Q Wang, X Chang. The fast multipole method accelerated line integration boundary element method for 3D heat conduction analysis with heat source. Engineering Computations, 2022. (In revision).

[6] **B Liu**, Q Wang, Y.T. Feng, W Zhou, T Qu, G Ma, M Wang. A combined boundary element method and discrete element method for particle stress field and breakage evaluation of granular systems with similar particle shapes. Engineering with Computers, 2022. (Under Review).

[7] **B Liu**, Q Wang, W Zhou, Y.T. Feng, Z Peng, G Ma, Y Li, J Xu, K Guo. of

stress field and particle breakage paths for granular system based on the combined boundary-discrete element method [J]. Rock and Soil Mechanics, 2022. (Accepted; In Chinese)

[8] **B Liu**, Y Gao, T Li, Y Chen, Q Wang, W Zhou. Thermal stress analysis based on line integration boundary element method and its application in engineering. Yangtze River, 2022, 53 (3): 1-7. (In Chinese)

[9] Y Gao, **B Liu**, T Li, X Yang, Q He, Q Wang, W Zhou, Y Cao. Research on heat conduction problem with heat source based on line integration boundary element method. Journal of Civil Engineering and Management, 2021, 38(6): 95-99. (In Chinese)

[10] Y Gao, Y Cao, **B Liu**, T Li, Q Wang, W Zhou. Development and application of CAE software based on boundary element method [J]. Engineering Journal of Wuhan University, 2022. (Accepted; In Chinese)

[11] Q Wang, **B Liu**. High-performance boundary integral equation method [M]. (In publication)

The publications separate to this PhD thesis:

[12] W Zhou, **B Liu**, Q Wang, Y Cheng, G Ma, X Chang, X Chen. NURBS-enhanced boundary element method based on independent geometry and field approximation for 2D potential problems. Engineering Analysis with Boundary Elements, 2017, 83: 158-166.

[13] Q Wang, W Zhou, Y Cheng, G Ma, X Chang, **B Liu**. A NURBS-enhanced improved interpolating boundary element-free method for 2D potential problems and accelerated by fast multipole method. Engineering Analysis with Boundary Elements, 2019, 98: 126-136.

[14] M Wang, T Qu, S Guan, T Zhao, **B Liu**, Y.T. Feng. Data-driven strain-stress modelling of granular materials via temporal convolution neural network. Computers and Geotechnics, 2022, 105049.

[15] Q Wang, X Yang, C Wang, **B Liu**. Comparison of three intelligent models in dam safety monitoring. Dam & Safety, 2014, 6: 44-47+56. (In Chinese)

[16] X Yang, Y Liu, C Wang, **B Liu**, Q Wang. Study of dam safety monitoring

model based on improved PSO algorithm and SVM theory. Yangtze River, 2015, 46: 97-100+104. (In Chinese)

[17] H Liu, X Feng, X Yang, C Wang, **B Liu**. Dam reliability analysis method based on FEM-SVM. Water Resources and Power, 2015, 33: 43-45+21. (In Chinese)

[18] E Zhao, P Kuai, Y Cheng, D Chu, **B Liu**. Exploration of the construction of characteristic research-oriented and applied comprehensive disciplines—Taking the undergraduate major of civil engineering as an example. Economic research guide, 2017, 34: 152-153+183. (In Chinese)

Patents

The following patents are based on the research presented in this thesis:

[1] **B Liu**, Q Wang, W Zhou, G Ma. Method and device for solving the crack problem of engineering structures. State Intellectual Property Office of China, Application date: 2019.09.24, Public date: 2020.02.14, Authorization date: 2021.07.16, Publish number: CN110795820.B, Application (Patent) number: ZL201910905694.6.

[2] Q Wang, **B Liu**, W Zhou, G Ma. Method and device for solving static thermoelastic problems of isotropic solid materials. State Intellectual Property Office of China, Application date: 2019.09.19, Public date: 2020.01.17, Authorization date: 2021.05.18, Publish number: CN110705057.B, Application (Patent) number: ZL201910886169.4.

[3] Q Wang, **B Liu**, W Zhou, Q Yue, C Huang, G Ma, X Ji, W Tian, K Huang, Y Liu, S Zhang. An analysis method and device for internal stress and breakage of large-scale granular materials. State Intellectual Property Office of China, Application date: 2020.09.03, Public date: 2020.12.15, Authorization date: 2022.02.28, Publish number: CN112084647.A, Application (Patent) number: ZL202010917113.3.

[4] Q Wang, **B Liu**, W Zhou, Q Yue, C Huang. Simulation method and device for solving heat conduction problems of engineering structures with heat sources. State Intellectual Property Office of China, Application (Patent) number: ZL202010720362.3.

The patents separate to this PhD thesis:

[5] Y Gao, **B Liu**, T Li, Q Wang, W Zhou, Q Yue, C Huang, X Chang. Optimization method of the concrete dam body. State Intellectual Property Office of China, Application (Patent) number: ZL202011591747.0.

[6] Q Wang, Q Yue, W Zhou, **B Liu**, W Tian, X Ji, C Huang. A universal phase field method for simulating different failure modes of brittle materials. State Intellectual Property Office of China, Application date: 2020.08.03, Public date: 2020.12.08, Authorization date: 2021.05.18, Publish number: CN112051142.B, Application (Patent) number: ZL202010768671.8.

Software copyrights

The following software copyrights are based on the research presented in this thesis:

[1] **B Liu**, Q Wang, W Zhou, C Huang. Software for model optimization and static elastic computation based on BEM and NURBS v1.0, No.2020SR0199519, Registration date: 2020.03.02.

[2] **B Liu**, Q Wang, W Zhou. Software for simulation of crack problems considering thermal stress based on BEM and AOIMLS-LIM v1.0, No.2020SR0718450, Registration date: 2020.07.03.

[3] **B Liu**, Q Wang, W Zhou. Software for heat conduction analysis of inhomogeneous material with heat sources based on BEM and AOIMLS-LIM v1.0, No.2020SR0824404, Registration date: 2020.07.24.

[4] **B Liu**, Y Chen, Q Wang, W Zhou. Fast solver software for at conduction analysis with heat sources based on FMM and LIBEM v1.0, No.2021SR1143275, Registration date: 2021.08.03.

[5] Q Wang, **B Liu**, W Zhou, G Ma. Crack problem-solving software based on modified indirect BEM and DDM v1.0, No.2020SR0092358, Registration date: 2020.01.17.

[6] Q Wang, **B Liu**, W Zhou, G Ma. Thermoelasticity problem-solving software based on BEM and LIM, No.2020SR0092350, Registration date: 2020.01.17.

[7] Q Wang, **B Liu**, W Zhou. Software for heat conduction analysis of self-heating materials based on BEM and LIM v1.0, No.2020SR0824411, Registration date: 2020.07.24.

[8] Q Wang, **B Liu**, Y Chen, W Zhou. Software for the simulation and analysis of internal stress of large-scale granular materials based on BEM v1.0, No.2021SR1143274, Registration date: 2021.08.03.

Contents

Acknowledgement

Foremost, I would like to express my deepest and sincerest gratitude to my supervisor, Prof. Y.T. Feng, for his constant guidance, full respect and strong support throughout my PhD career. He is the one who is always thinking about what he can devote to helping students to become outstanding researchers. Prof. Y.T. Feng does not only offer us constructive suggestions but also is willing to teach us everything he knows tirelessly as he owns profound knowledge in computational mechanics and mathematics. For me, he is not only a supervisor, but also a good friend, a life counsellor, and a sage. I can share my happiness and confusion in life with him. I am so honored to be his student and I hope we can keep a lifelong teacher-pupil relationship. Moreover, may the happiness and good health be with Prof. Y.T. Feng forever.

Next, I want to express my appreciation to Swansea University and Wuhan Unversity for providing me with a PhD scholarship, thereby becoming a student here. I am so lucky to be the first PhD student who was selected as a member of the "Double Doctoral Degree" jointly addressed by Swansea University and Wuhan University, that is a great honor for me and I appreciate all the relevant staff for their efforts to make the proposal of this program true. In addition, I am so grateful to all the officers and workers in the library, Unihub and Engineering central for their warm-hearted help. Swansea is a wonderful city with cosy weather, friendly inhabitants and haunting coastal scenery. I really love this city and hope I can come back here again in the future!

I am also grateful to Prof. EA De Souza Neto (the other supervisor at

Swansea university), Prof. Wei Zhou (Wuhan University), Dr. Qiao Wang (Wuhan University), Dr. Dunhui Xiao (Swansea University), Dr. Tongming Qu (Hong Kong University of Science and Technology) and Dr. Jinlong Fu (Swansea university) for their invaluable advice. Furthermore, I want to thank all the students and friends in A130 in engineering central for their generous help and company, including Zhanfeng Li, Guangshuai Sun, Yang Li, Shaoheng Guan, Mengqi Wang and Linzhi Peng.

Last but not least, I can hardly express my gratitude to my beloved parents and sister in words. Thank my parents for bringing me up and telling me to be down-to-earth and hard-working if I want to achieve success. Thank my parents for giving me a mature and correct worldview, outlook on life and values. Thank my sister for her meticulous care when I was in a bad mood or in a dilemma. May the happiness and good health be with my family forever!

Nomenclature

Abbreviations

BEM	Boundary element method
FEM	Finite element method
DEM	Discrete element method
LIM	Line integration method
FMM	Fast multipole method
LIBEM	Line integration boundary element method
DDM	Displacement discontinue method
FSM	Fictitious stress method
BIEs	Boundary integral equations
NURBS	Non-uniform rational B-Spline
FDM	Finite difference method
FVM	Finite volume method
SPH	Smooth particle hydrodynamics method
PUM	Partition of unity method
EFGM	Element-free Galerkin method
DRM	Dual reciprocity method
RBFs	Radial basis functions
PSM	Particular solution method
MRM	Multiple reciprocity method
TRM	Triple reciprocity method
RIM	Radial integration method

AOIMLS	Adaptive orthogonal interpolation moving least squares
DBEM	Direct boundary element method
IBEM	Inirect boundary element method
DBIE	Displacement boundary integral equation
CBEM	Conventional boundary element method
HBIE	Hypersingular boundary integral equation
FM-LIBEM	FMM enhanced LIBEM
M2M	Multipole to multipole
M2L	Multipole to local
L2L	Local to local
MLS	Moving least squares
GMLS	Generalized moving least squares
IMLS	Interpolating moving least squares
IIMLS	Improved interpolated moving least squares
MMLS	Improved moving least squares
LBFs	Lagrangian basis functions
BNM	Boundary node method
BFM	Boundary face method
BEFM	Boundary element-free method
IGA	Isogeometric analysis
ISO	International standards organization
DD-IBEM	Displacement discontinue indirect BEM
FS-IBEM	Fictitious stress indirect BEM
M-DD-IBEM	Modified DD-IBEM
M-FS-IBEM	Modified FS -IBEM
SIFs	Stress intensity factors
NSIFs	Normalized stress intensity factors
CODs	Crack opening displacements
RE-CODMC	Relative error of COD at the middle of the crack
B-DEM	Combined BEM and DEM
FRM	Fragment replacement model

BPM	Bonded particle model
SVD	Singular value decomposition

Some commonly used notations

σ_{ij}	Stress tensor
ε_{ij}	Strain tensor
E	Young's modulus
ν	Poisson's ratio
λ	Lame constant
μ	Shear modulus
δ_{ij}	Kronecker symbol
k	Thermal conductivity coefficient
θ	Temperature
$q(\mathbf{x})$	Heat flux
Ω	Target domain
Γ	Boundary of Ω
$\mathbf{n}$	Outer normal vector on boundary
$B(\mathbf{x})$	Heat source
$\hat{\theta}$	Normalized temperature
$T(\mathbf{x})$	Thermal conductivity function
$\theta_{,i}$	Partial derivatives of θ with respect to x_i
β	Thermal expansion coefficient
ρ	Density

g	Acceleration of gravity
$B_{i,n}$	Bernstein polynomial of order n
w_i	Weight factor
$R_{i,p}$	B-spline basis function in p order
$u_{i,jj}$ and $u_{i,jj}$	Derivatives of displacement u
S^+ and S^-	Two surfaces of a crack
Δu_i	Crack opening displacement
$\mathbf{f}^i$	i^{th} contact force vector
$\mathbf{a}$	Acceleration vector
$\mathbf{U}(\mathbf{x},\mathbf{y})$ and $\mathbf{T}(\mathbf{x},\mathbf{y})$	Kelvin kernels
$\mathbf{u}^K(\mathbf{x})$	Displacement of particle K in the global coordinate system
$\tilde{\mathbf{u}}^K(\mathbf{s})$	Displacement of the template particle in the local coordinate system
$\tilde{\boldsymbol{\varepsilon}}^K(\mathbf{s})$	Strain tensors of the template particle in the local coordinate system
$\tilde{\boldsymbol{\sigma}}^K(\mathbf{s})$	Scaled stress tensors of the template particle in the local coordinate system
σ_1	Major principal stresses
σ_3	Minor principal stresses,
σ_c	Uniaxial compressive strength of the material

List of tables

List of figures

Part I

Background

Chapter 1

Introduction

Summary

This chapter introduces the background and motivations of this thesis. In **Section 1.2**, a general review of the numerical methods based on continuum mechanics which are popular now and widely exerted in engineering are presented. In addition, the advantages, development and challenges of BEM are addressed. Next, the research scope of this thesis is shown in **Section 1.3** and a layout is presented in **Section 1.4**, which can tell readers the main aim and content of this thesis.

1.1 Background and motivation

The high-performance BEM proposed in this thesis is applied to heat conduction problems, thermoelastic problems and thermoelastic fracture mechanics. The following sub-sections present the background and motivation from an application point of view.

1.1.1 Heat

1.1.1.1 Heat conduction

In the 18th and 19th centuries, thermal science was increasingly developed as a part of physics, when some general principles are studied, such as molecular kinematics theory, ideal gas equation of state, laws of thermodynamics, heat transfer, etc. At the same time, some basic physical quantities related to heat, physical quantities related to thermodynamic properties, and physical quantities related to heat transfer were determined.

Heat conduction can be defined as a heat transfer without macroscopic medium motion. It can also be described as a process of heat energy transferred from the high-temperature zone to the low-temperature zone. As shown in **Fig.1.2**, the phenomenon of heat conduction [1-3] is prevalent in nature from daily life to engineering fields and from solid to liquid to gas [4, 5].

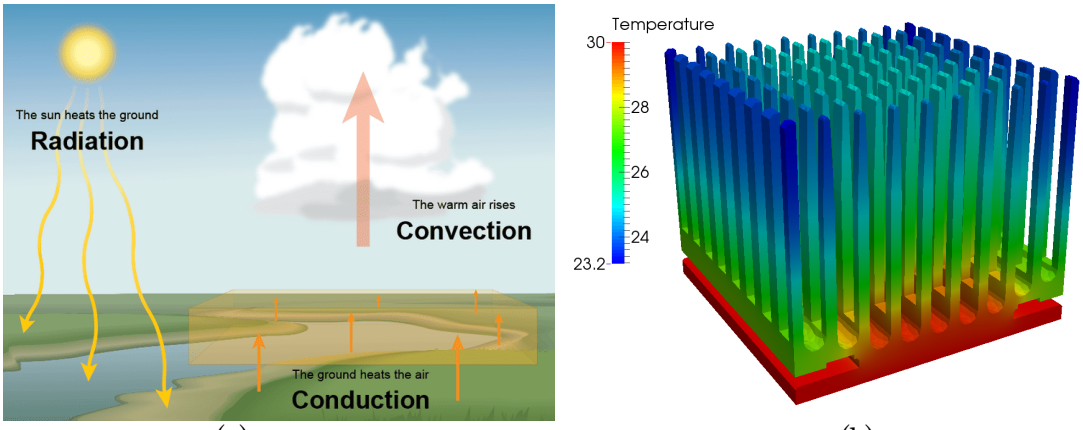

(a) (b)

Fig.1.1 Ubiquitous heat conduction phenomenon: (a) heat transfer phenomenon in nature; (b) heat conduction simulation[1]

In the engineering world, heat conduction plays a vital role during design and construction, such as machinery, architecture, hydraulic structure, aerospace, chemical industry and energy industry and so on. For example, in

[1]Fig.1.1 (a): https://scied.ucar.edu/learning-zone/earth-system/conduction
[1]Fig.1.1 (b): https://quickersim.com/cfdtoolbox/heat-transfer/

mechanical engineering, the temperature distribution in metal materials affects the thermoforming result directly; in civil engineering, the internal Heating, Ventilation and Air Conditioning (HVAC) and temperature control of buildings are the key points that need to be considered during design; in hydraulic engineering, the temperature control scheme during the construction of concrete dams is vital for crack prevention; in aerospace engineering, during the high-speed flight of aircraft, the high-speed airflow rubs against the surface of aircraft, the temperature of the aircraft structure must be controlled within a range that materials can withstand to ensure safety; in nuclear energy engineering, reactor cooling and heat recovery technology are the two key technologies of nuclear power plants.

1.1.1.2 Thermal stress

The modern linear thermal stress theory was founded in 1835. In February of that year, Duhamel[6, 7] gave a speech at the French Academy of Sciences and proposed for the first time that when the temperature changes, thermal stress is generated due to some constraints on a part of the object, which consists of two parts: (1) the pressure that is equal in all directions and proportional to the temperature change; (2) the stress that is caused by the strain without changing the temperature. That is the famous Duhamel formula. Later in 1841, the German Neumann advocated the derivation of the linear thermal stress theory for the first time. There is not much difference between the two theories, so the modern linear thermal stress theory is usually called the Duhamel-Neumann theory [8, 9].

Thermoelasticity is an important branch of solid mechanics as thermal stress [10, 11] appears frequently whenever the structures, like engines or concrete components, are enduring thermal shock or cooling while their expansion or volume reduction are restricted, which may further result in changes in mechanical behaviour, and even failure.

Therefore, research on heat conduction and thermal stress has always attracted much attention. Before the advent of computers, the combination of experiments and theoretical calculation was adopted for heat conduction and

thermal stress analysis. As industrial technology upgraded faster and faster, using experimental or theoretical analysis methods to analyze heat conduction on structures could no longer meet the needs, especially theoretical analysis is limited to simple structures, and cannot be applied to thermal analysis of complex structures. Since the advent of computers, numerical methods have developed rapidly and played an increasingly important role in the design and simulation of engineering structures [12, 13].

1.1.2 Fracture

Cracked structures are prevalent in the engineering world. As stated by Jiazheng Pan, a well-known hydropower engineering expert in China, said, "There is no crack-free dam in the world". It is impracticably to completely prevent cracks in massive concrete structures such as dams (See **Fig.1.2** (a)). As shown in **Fig.1.3** (b), in machinery manufacturing, crack is one of the key factors which induce frequent failure of mechanical components when enduring impact load, thermal load, periodic load, etc. Furthermore, particle breakage can be classified into fracture problems as well, although particle materials are discontinuous, while the propagation process of breakage paths of a single particle is a fracture problem of continuous mediums (See **Fig.1.2** (c)).

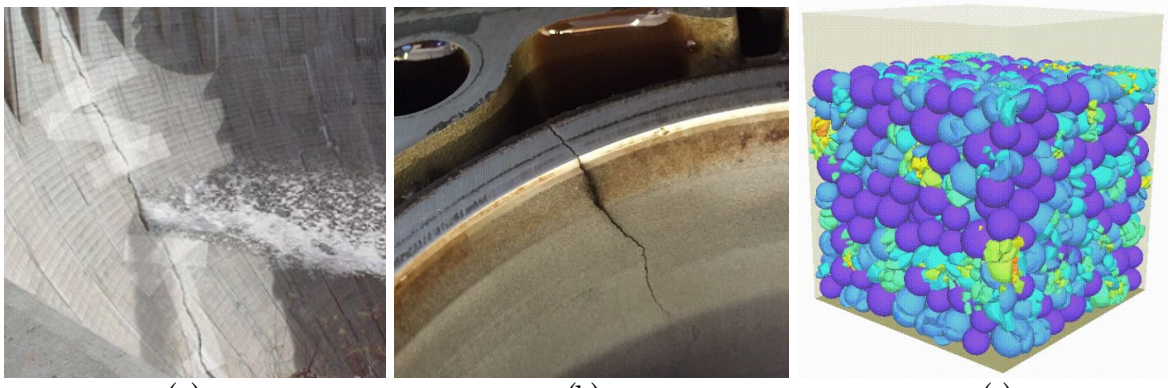

(a) (b) (c)

Fig 1.2 Cracked structures: (a) cracked concrete dams; (b) cracked engine; (c) particle breakage[2]

Before the establishment of fracture mechanics [14-16], both researchers and engineers believed that the reliability of structural design only needed to be checked through stress analysis, and regarded materials as ideal defect-free

[2]Fig.1.2 (a): http://noahpinionblog.blogspot.com/2017/01/cracks-in-anti-behavioral-dam.html
[2]Fig.1.2 (b): https://autochimps.com/cracked-engine-block-symptoms/
[2]Fig.1.2 (c): http://jzhao.people.ust.hk/research.html

structures. However, in massive engineering practices, many materials fail when the stress is far lower than the allowable stress which is more prevalent in high-strength materials and that phenomena is difficult to explain by traditional strength theories, and has gradually attracted the attention of researchers. For example: In World War II, dozens of American warships suddenly broke without being subjected to high-strength loads, which caused catastrophic accidents and economic losses. Later, engineers found that the key to those unanticipated accidents was that there are many defects and tiny cracks inside materials due to manufacturing techniques so the inner stress distribution of structures is different from that of a hypothetical homogeneous elastomer. Due to stress concentration at the tip of tiny cracks, although the average cross-section stress of structures is below the design standard, the stress near the crack tip has already exceeded the allowable stress, which leads to crack propagation and further structure failure. Therefore, fracture mechanics for mechanical properties and the deterioration mechanism of cracks have gradually developed.

Griffith [17], the founder of fracture mechanics, discovered that many glass-based structures often failed well below design strengths. After thorough research, he claimed that when the external load magnitude of glass materials is lower than the allowable strength, due to the stress near internal defects or tiny crack areas reaching the allowable strength first, and then these cracks gradually expand which results in structural failure eventually. He also proposed the relationship between the fracture stress of materials and the geometric size of cracks:

$$\sigma_c = \left(\frac{2E\mathrm{N}_s}{\pi L} \right)^{0.5} \tag{1.1}$$

where, σ_c denotes the critical stress of crack propagation，E denotes elastic modulus, N_s is the unit surface energy of materials, L represents half of the crack length。

Based on Griffith's theory, in the following decades, scientists represented by Irwin and Orowan [18] made great contributions to the research of brittle fracture, and finally established the discipline of fracture mechanics. Generally

speaking, fracture mechanics was formally formed in the 1950s. As the discipline was born from engineering based on massive experiments, it focuses on fractures based on solid mechanics and is a further expanding and deepening of material mechanics. The fracture mode and propagation mode of cracked engineering structures have been linked with the property of materials--fracture toughness. Since the 21st century, many new materials have emerged, the application scope of fracture mechanics is gradually expanding, and its basic theory is also constantly developing and improving.

In the subsequent chapters, in order to demonstrate the correctness of the proposed method, the stress intensity factors (SIFs) in fracture mechanics are applied for comparison and verification. SIFs were proposed by Irwin in the 1950s and used to characterise the stress and displacement fields at the crack tip, Irwin proposed three basic crack propagation modes according to different stress conditions:

(1) Open mode (I), the main force of crack propagation is uniform tension, and the crack boundary shows an opening trend;

(2) Slip-open type (II), the main force of crack propagation is shear stress, and the relative displacement of crack boundaries is mainly relative slip;

(3) Tearing mode (III), the main stress direction of crack propagation is perpendicular to the crack boundary and parallel to the crack tip.

Previous research has proved that stress intensity factors are positively correlated with loads. The concept of fracture toughness mentioned earlier is the critical stress intensity factor when cracks are about to begin to propagate. In this thesis, the first two modes are used for verification, namely, mode I and II stress intensity factors, and the normalized stress intensity factors (NSIFs).

1.2 Methodology

1.2.1 Overview of numerical methods

With the development of science and technology, the engineering problems that need to be tackled are becoming more and more complicated. Due to the complexity of geometry or the nonlinearity of the computational domain, it is

much harder for researchers to derive analytical results. Moreover, since computer performance has been largely improved, numerical methods for solving engineering problems are becoming more and more mature. Now almost all large-scale engineering problems need to be analyzed or evaluated with the help of numerical calculation, so as to provide a reference for engineering design.

Nowadays, there are five representative numerical methods based on continuum mechanics widely exerted in the field of engineering: finite difference method (FDM) [19-21], finite volume method (FVM) [22], finite element method (FEM) [23-26], meshless method [27, 28] and BEM [29-31].

1.2.1.1 Finite difference method

The core gist of FDM is that divides the target domain into grids, approximates differentiation with a difference, and turns differential equations into difference equations. In other words, with the help of mathematical approximation, computing differential equations are transferred to solving algebraic equations about unknowns of nodes. This method is simple and easy to understand and can compute complex differential equations easily, so it is widely used in fluid mechanics. However, when the shape of a target domain is complex, it becomes difficult to discretise by the spatial coordinates, and the orthogonality of meshes is not easy to be preserved, which results in the reduction of the calculation accuracy.

1.2.1.2 Finite volume method

FVM is a numerical method based on the integral form of the governing equation of physical problems. The fundamental thought is: discretizing the target domain into non-overlapping elements within a finite number and establishing a set of discretised algebraic equations by acting as the governing integral equation on each element. FVM owns the characteristics of both FDM and FEM, i.e., simple enough and excellent geometric adaptability. Now, It has played a dominant role in numerical methods for modern computational fluid dynamics. However, the spatial derivative correlation of physical quantities is

determined by the value at the centre of the surrounding elements, so the calculation accuracy of FVM is unsatisfactory, especially when it comes to the values close to the boundary.

1.2.1.3 Finite element method

FEM [32, 33] is on the fundamental of volume integral equations with weight function (shape and number) established via the variational theorem. The basic characteristic of FEM is that the target domain is discretised into non-overlapping regular nodes within a finite number, and then each element is integrated and formed into a set of overall algebraic equations, every element can be in different shapes and material properties and combined with each other by different connection modes. Therefore, FEM owns the advantages of strong geometric adaptability and flexible handling of different physical parameters. The disadvantage of FEM is that the spatial derivative of a physical quantity is obtained by deriving the shape function, so the accuracy is one order lower than the physical quantity itself. For moving boundary problems, such as metal forming, optimization calculation and free surface determination of seepage problem, finite element meshes may be distorted and overlapped, then the calculation accuracy can be reduced or the calculation will be suspended. In addition, for an infinite or semi-infinite domain, such as semi-infinite foundations in civil engineering, infinite and semi-infinite domain needs to be approximated into a finite domain, and there is no mature theoretical basis for this process, engineers need to set the size and shape of the approximated finite domain according to personal experience, and discrete the boundary manually. To get accurate enough results, a large number of discrete elements are needed and there are also high requirements for the size and shape of the approximate finite domain.

1.2.1.4 Meshless method

The meshless method is proposed in the 1980s, and until now, various forms of meshless methods have been developed, including smooth particle hydrodynamics method (SPH), partition of unity method (PUM) [34, 35], and element-free Galerkin method (EFGM) [36-39], etc. At the end of the 20th

century, Mukherjee [40] and others also proposed the boundary point method, which only needs to place points on the boundary, and is a very representative boundary-type meshless method.

The meshless method [41-44] is based on the construction of point interpolation functions, only a series of discrete points are needed to be preset in the target domain and no mesh is required, which results in strong flexibility. However, meshless method is not mature enough, and lacks solid theoretical foundation and strict mathematical basis. In addition, the number and scheme of preset sample points can affect the computation time and accuracy. Moreover, it is difficult to determine whether the redistributed points are internal, external, or boundary points when the boundary changes for moving boundary problems with complex geometric shapes.

Since there is no mesh requirement, meshless method can avoid remesh when the crack propagates. However, massive nodes need to be arranged at the crack tip to obtain satisfactory results. In addition, the background cells are required during integration, so it is not completely out of the grid constraints; secondly, the computational accuracy of the meshless method also depends on the distribution of nodes.

1.2.1.5 Boundary element method

BEM is developed based on transforming the governing differential equations into boundary integral equations via Green's formula and the fundamental solution [45-47]. Its main advantages are as follows: (1) Only the boundary of target domains needs to be discretised [48, 49], so it is simple and convenient for complex geometry modelling; (2) BEM is suitable for computing infinite and semi-infinite domains because it can automatically meet the boundary conditions of infinite domains; (3) The calculation formula of a spatial derivative of physical quantities can be analytically derived from the basic boundary integral equation. Therefore, the accuracy of derivatives (such as flux, stress, etc.) related to a physical quantity is at the same level as the physical quantity itself. When it comes to moving boundary problems, the information of new boundary elements can be naturally formed by adding the

displacement of the moving boundary node to the coordinates of the original boundary node instead of special element reconstruction, so there will be no mesh-overlapping. Furthermore, because of the existence of boundary elements, it is handy to determine whether a point is an internal, external or boundary point by element integration. Based on these advantages, BEM performs better than FEM in some fields (such as convenient motion boundary problems, fracture problems, contact problems, radiation problems, infinite and semi-infinite field problems and so on).

1.2.2 Developments and challenges of BEM

In this thesis, high-performance algorithms are proposed to enhance BEM and the main application scope is heat conduction, thermal stress and fracture problems, hence, this section is focused on the research progress of BEM in those application scopes.

1.2.2.1 Nonlinear and nonhomogeneous problem

Traditional BEM is powerful for linear problems, but for nonlinear and nonhomogeneous problems, it is difficult to obtain the fundamental solutions of governing equations, so fundamental solutions corresponding to the linear and homogeneous problems are used to derive integral equations for nonlinear and nonhomogeneous problems, which leads to domain integrals. The advantage of boundary-only discretisation will be neutralized by a domain integral which is the weakness that requires inner meshes and is an obstacle to the development of BEM.

BEM is developed on the fundamental of integral equations and absorbs the idea, discretisation, of FEM. By using fundamental solutions with singular functions as weight functions, which can satisfy infinite or semi-infinite field equations [50, 51], the domain integral equation derived from governing equations can be transformed into a boundary integral equation. Then with the help of boundary-only discretisation, the unknowns on the boundary can be obtained.

BEM has been under development for nearly 60 years. The indirect

boundary integral equation of potential problems and elastic problems was derived and solved numerically by Jaswon et al. [52, 53] in the 1960s. Later, Rizzo [54] exerted the direct boundary integral equation to compute 2D elastic problems, which was extended to 3D elastic problems by Cruse [55, 56] in 1969. To distinguish from FEM, the name of boundary element method, was gradually determined in the mid-1970s.

The main obstacle to heat conduction and thermal stress analysis by BEM is domain integration caused by thermal load, heat generation, heterogeneity of materials and so on, which can be classified into non-homogeneous problems. If domain integrals were not tackled, the advantage, boundary-only discretisation, of BEM will be neutralized. So far, many methods have been proposed to evaluate the domain integrals [10, 57-59] in BEM.

To compute domain integrals in the boundary integral equation, partitioning the domain with volume elements and computing the domain integrals in volume elements may be the most natural way. The direct volume integration method [60] was reported to be a significantly better choice for computing domain integrals compared to some other methods. However, BEM will lose the advantage of boundary-only discretisation by using volume elements.

Therefore, developing an algorithm that can retain the advantages of BEM has become the focus of researchers and several methods have been proposed so far, such as dual reciprocity method (DRM) [61-63], which is proposed by Partridge et al. nonhomogeneous terms can be approximated by a series of functions, such as radial basis functions (RBFs) [64], and then second reciprocity is applied to convert domain integrals to boundary integrals. Only the points in the domain or on the boundary are needed to provide the information described by the nonhomogeneous terms. However, the accuracy of DRM highly depends on the distribution and location of the domain points and the type of functions employed to approximate the nonhomogeneous terms. Similar to the basic idea of the DRM and proposed at the same time, another dimension reduction method is the particular solution method (PSM) [65],

which is an effective method to approximate domain integrals by constructing a special solution, but it requires knowing the particular solution of the control function and thus may not be suitable for general cases. At present, DRM is one of the most widely used domain integral reduction methods, and it is applied to heat conduction, static dynamics and many other problems. However, the accuracy of DRM depends on the distribution and density of sample points in the domain to a large extent. In addition, the types and properties of RBFs used to approximate nonhomogeneous terms also can affect the accuracy of DRM.

The other method is the multiple reciprocity method (MRM) [66-68], which was proposed by Nowak et al. and its core gist is to apply the reciprocity theorem to a sequence of higher order fundamental solutions based on the divergence theorem so that the domain integral can be transformed to a boundary integral [69, 70]. MRM has been exerted to solve static elastic problems, heat conduction and so on. MRM is best at the calculation of eigenvalues, but there are several shortcomings: (1) due to the need for high-order fundamental solutions, it is difficult to be applied to problems with complex fundamental solutions; (2) the convergence of MRM is not stable when it comes to domain integrals in complex form.

To solve the above problems, some improved MRMs came into being, for example, the triple reciprocity method (TRM) uses an approximate function to replace high-order fundamental solutions in order to meet the needs for being applied to domain integrals in complex form, and the function will degenerate into a Dirichlet function after twice Laplace operator calculation, thereby its highest order is only 3 orders, which overcomes the instability of MRM when computes complex domain integration, and that is the reason why it is called TRM. And based on that advantage, the application scope of TRM is further expanded beyond MRM, like nonhomogeneous problems. At the end of the 19th century, Ochiai [71, 72], a researcher at Kinki University, successfully applied TRM to the study of thermal stress analysis and achieved fruitful results.

Later, the radial integration method (RIM) [73-75] was proposed. Based on

the polar coordinate system, RIM can reduce the dimension of various domain integrals and convert them into boundary integrals and radial integrals [76]. Radial integrals can be calculated analytically in some cases which means there is no numerical error. When the analytical radial integral cannot be obtained, radial integrals can be interpolated by RBF. In addition, RIM can also avoid singular integrals. Once proposed, RIM has been widely used in various fields and becomes a new "shining star" among the current domain integral transformation methods. Inevitably, when using RBF for interpolating, it is necessary to set sample points in the target domain, which will increase the complexity of computation. In 2017, Qu et al. [10] successfully applied RIM and indirect BEM to analyze 3D thermal stress problems.

In this thesis, the line integration method (LIM) [77, 78] is applied to compute domain integrals. Based on the divergence theorem in the cartesian coordinate system, the domain integrals are transformed into boundary integrals and only line integrals on straight lines are needed to be computed.

1.2.2.2 Singular integral

The fundamental solutions used in BEM are singular. It is necessary to eliminate the integral singularity first to obtain accurate calculation results during numerical calculation. Over the years, researchers have proposed many methods [79-82] for calculating singular integrals considering computational efficiency and accuracy, such as analytical elimination method for linear elements, the element subdivision method for weak singular integrals, indirect calculation method for strong singular integrals, direct calculation method for high-order integrals, etc. These methods are very effective in computing weakly singular and strong singular integrals, but their stability when dealing with higher-order singular integrals requires further discussion.

1.2.2.3 Non-symmetrical and dense matrix system

The coefficient matrix of equations formed by BEM in solving problems is fully-populated, so it will occupy large computer memory and cannot be applied to compute large-scale engineering problems. To solve that problem,

two effective methods have been proposed:

(1) Couple fast multipole method (FMM) [83-86] with BEM to reduce the calculation and storage order of matrix-vector multiplication by using series expansion of singular kernel function, so as to save the computational storage and enhance computation speed.

(2) With the help of the domain decomposition method, the target domain is divided into several sub-domains, the matrix equation is established for each sub-domain, then integrated into the overall equation system by using the traction equilibrium condition and displacement compatibility condition on the common nodes between subdomains. The coefficient matrix formed in this way is a sparse block matrix, which can be effectively calculated by using mature sparse matrix solvers (such as the LU decomposition method and generalized minimum residual method). Moreover, the domain decomposition method can solve be applied to solve composite medium problems composed of different materials by dividing the target domain into sub-domains according to the material properties, and the fracture mechanics problem by dividing the target domain into sub-domains along the crack surface.

Both the fast multipole method and domain decomposition method are widely used in BEM. In this thesis, FMM is applied to enhance the performance of BEM.

1.2.2.4 Boundary integral equations for fracture mechanics

So far, researchers all over the world have proposed many derivative methods to solve fracture problems based on BEM, such as the dual boundary element method [87-89], sub-region method [90], Green's function method [91, 92] and displacement discontinuity method (DDM) [48, 93]. The basic gist and background of these methods are as follows:

(1) Dual boundary element method. The basic theory of the dual boundary element method is proposed by Hong and Chen [94], which can be used to compute 2D or 3D problems with preset cracks. Romlay et al. [95] recently applied the dual boundary element method to compute crack propagations. The main gist of the dual boundary element method is that the displacement

boundary integral equation is used on the outer boundary and one crack boundary, while the traction boundary integral equation is used on the other crack, which can avoid singular matrices when the two crack boundaries overlapped with each other.

(2) Green's function method. The Kelvin solutions are replaced by Green's function that considers cracks in boundary integral equations, therefore, cracks do not need to be considered during numerical modelling, and it also owns the advantage of high accuracy, but its main drawback is that it only can be used for numerical models with a single straight crack problem without tractions.

(3) Sub-region method. The main merit of the sub-region method lies in the introduction of artificial boundaries, then, the target domain can be divided into several sub-domains by artificial boundaries. The characteristics of these sub-domains are that there is no overlapping crack boundary, thereby the displacement boundary integral equation can be used on each sub-domain. The introduction of artificial boundaries is a double-edged sword for the sub-region method. Because the computation accuracy depends on the rationality of the introduction of artificial boundaries which also need to be discretised by boundary elements and cause the increase of unknowns, further, the size of coefficient matrices will expand and the computation time will inevitably increase.

(4) Displacement discontinuity method, DDM was developed by Crouch [96] and has become a popular way of computing elastic problems with cracks since its emergence. The main merit of DDM is that the crack surface is assumed to be a real boundary, while the outer boundary is regarded as a virtual boundary, and when the virtual displacement imposed on the crack surface makes the displacement or traction responses on the outer boundaries meets the boundary condition, then the virtual displacement on the crack surface is considered as the wanted result. In 2014, the equivalence of DDM and BEM for the crack problem was proved by Liu and Li [97]. While most research on fracture problems based on BEM focuses on cracks in infinite domains based

on BEM or DDM [98]. However, there is very little research for finite cracked domains based on direct BEM and DDM which is absolutely feasible. In this thesis, boundary integral equations (BIEs) for the cracked domains is proposed based on direct BEM and DDM, and BIEs can be degenerated to solve fracture problems in infinite domains.

Moreover, there are few studies on solving cracked finite domains considering thermal stress. Aliabadi [99] combined J integral and BEM to compute stress intensity factors at the crack tip for cracked domains under thermal stress. In addition, Ekhlakov et al. [100] carried out research on cracked functionally graded materials based on BEM and applied RIM to deal with domain integrals. In this thesis, based on the direct BEM and DDM, novel BIEs for computing cracked finite domains considering thermal stress are derived. To compute the BIEs, an enhanced BEM, the adaptive orthogonal interpolation moving least squares (AOIMLS) enhanced line integration boundary element method (LIBEM) is proposed.

1.3 Research scope

As discussed above, with the help of its unique merit, boundary-only discretisation, BEM has become one of the indispensable numerical methods developed based on continuum mechanics. However, there are two crucial obstacles in the way of the development and application of BEM, the domain integrals and the non-symmetrical and dense matrix systems.

This thesis explores the development of high-performance BEM to overcome the two obstacles mentioned above based on the theoretical derivation and algorithm development, and further expands its application scope in engineering. The research objective is achieved through three interrelated modules:

Domain integrals, an adaptive orthogonal interpolating moving least-square method (AOIMLS) enhanced line integration boundary element method enhanced (LIBEM) is proposed to compute BIEs containing domain integrals of nonlinear and nonhomogeneous problems without losing the unique “gift”,

boundary-only discretisation, of traditional BEM. The enhanced BEM will be proved in the analysis of non-homogeneous heat conduction with heat sources, thermoelasticity and thermos-elastic fracture problems.

Non-symmetrical and dense matrix systems, algorithms for improving computation efficiency are proposed and applied to enhance the performance of BEM. (1) The fast multipole method accelerated LIBEM is developed to improve computing efficiency, which is proved by the analysis of heat conduction with heat sources. It can reduce the calculation and storage order of matrix-vector multiplication by using the series expansion of the singular kernel function. (2) Mapping the solutions between the local and global coordinate systems is designed for stress field computation of granular materials to avoid computing the non-symmetrical and dense matrix system for each particle, thereby improving computation efficiency.

Fracture problems, a set of unified novel boundary integral equations for computing infinite and finite cracked domains under (or not under) thermal loads are derived, which can be computed numerically by the AOIMLS enhanced LIBEM. In addition, a novel roughly breakage path evaluation method in static stress calculations of particle breakage based on BEM and strength criterion in fracture mechanics is proposed.

1.4 Thesis layout

The research works corresponding to the three interrelated modules are distributed in nine chapters of this thesis, as illustrated in **Fig.1.3**.

Chapter 1: Introduction

This chapter gives the background and motivations of the thesis.

Chapter 2: The basic theory of BEM

In this chapter, the basic theory of BEM is introduced, including the derivation of boundary integral equations for elasticity and heat conduction and the numerical computation process of BEM.

Chapter 3: To avoid The fast multipole method accelerated line integration boundary element method for 3D heat conduction analysis with heat sources

In this chapter, the fast multipole method is exerted to couple with line integration method and BEM for computational acceleration which is applied to analyze 3D heat conduction with heat sources successfully. Besides, the domain integrals in BIEs are computed by LIM which only can compute domain integrals with known integrand functions, thereby avoiding domain meshing.

Chapter 4: An AOIMLS enhanced LIBEM for solving 3D non-homogeneous heat conduction with heat sources

In this chapter, an novel high-performance BEM, i.e., adaptive orthogonal interpolating moving least-square method enhanced line integration boundary element method is proposed to numerically compute the BIEs with domain integrals which contain known or unknown integrand functions. And the AOIMLS enhanced LIBEM is applied to solve 3D non-homogeneous heat conduction with heat sources successfully.

Chapter 5: NURBS enhanced line integration BEM for thermo-elastic problems considering the gravity load

In this chapter, the Non-uniform rational B-spline is applied to enhance the line integration BEM which ensures that the boundary shape of the numerical models will not change during the refinement and the error of model discretisation will be avoided. And NURBS-enhanced LIBEM is applied to compute 2D thermos-elastic problems.

Chapter 6: Solving 3D thermoelastic problem by the AOIMLS enhanced LIBEM

In this chapter, the AOIMLS enhanced LIBEM is applied to compute 3D thermoelastic problems. Because thermal loads can result in domain integrals in BIEs, and whether the integrand function in domain integrals is known or not is determined by whether temperature distribution is known or not. Dealing with domain integrals with unknown integrand functions beyond the capability of LIBEM. Thereby the AOIMLS enhanced LIBEM is exerted.

Chapter 7: Formulations of displacement discontinuity method for crack problems based on boundary element method

In this chapter, four sets of unified BIEs are derived based on direct BEM, indirect BEM and DDM respectively for the finite and infinite cracked domain. Besides, the numerical results of the two BIEs are unstable, thereby a novel modified indirect BEM is proposed for improvement. Numerical examples have proved that the two modified BIEs based on the modified indirect BEM and DDM perform much better.

Chapter 8: The novel boundary integral equation with adaptive orthogonal IMLS-based line integration method for cracked domains under thermal stress

In this chapter, on the fundamental of the BIEs based on direct BEM and DDM for cracked structures established in Chapter 7, a set of novel BIEs for computing cracked structures under thermal stress is derived which are numerically computed by the AOIMLS enhanced LIBEM.

Chapter 9: A combined boundary element method and discrete element method for particle stress field and breakage evaluation of granular systems with similar particle shapes

In this chapter, a combined BEM and discrete element method (DEM), named B-DEM, is developed to compute particle stress fields and breakage paths of granular brittle materials. The interaction between particles is simulated via DEM, while the stress field of a particle is computed, when needed, by BEM. By mapping coefficient matrices between the local and global coordinate systems for particles with similar geometry with the help of a selected templet particle, the proposed method is much more time-effective when modelling a large-scale particle system with a small number of distinct possible particle shapes. Furthermore, the Delaunay triangulation and Hoek-Brown criterion are employed to evaluate the possible cracks or breakage paths of a particle.

Chapter 10: Conclusions and Outlook

The main attributions and innovations of this thesis are summarised and directions for possible future research are pointed out.

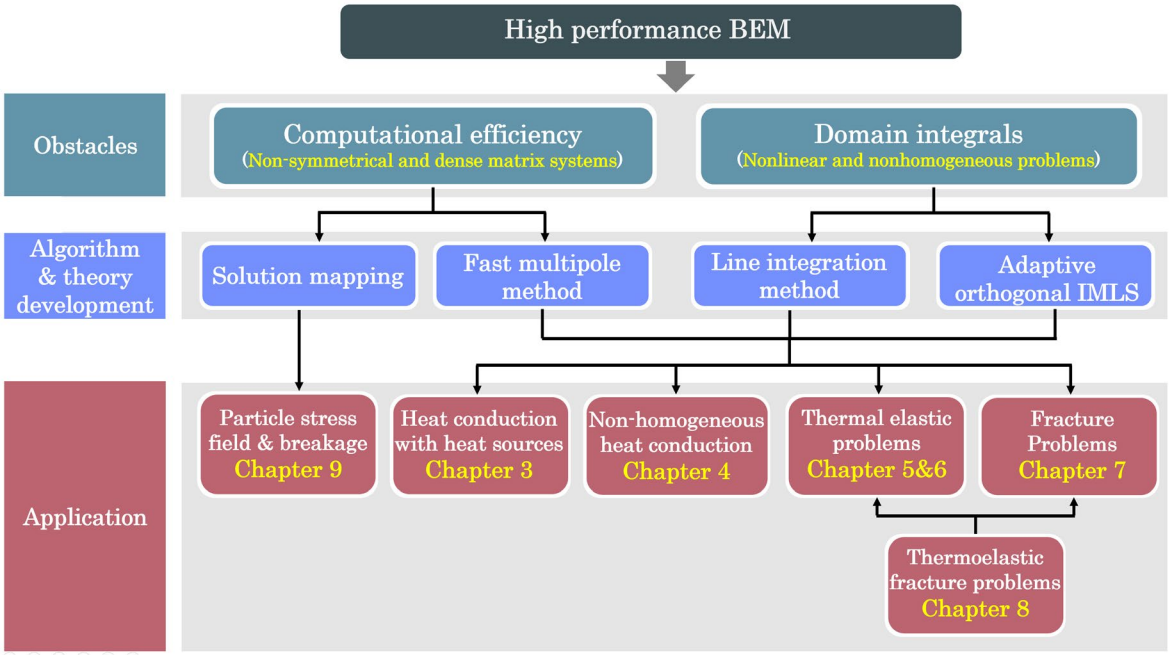

Fig.1.3 Layout of the thesis

Chapter 2

The basic theory of BEM

Summary

As a semi-analytical and semi-numerical method, owning to the well-known advantage, boundary-only discretisation, BEM has become a popular numerical method overwhelmingly. This chapter mainly introduces the derivation and numerical discretisation process of BIEs for elasticity and heat conduction problems in detail, which are the basis of the subsequent chapters. Besides, different singular integrals and their computation methods are shown in detail.

2.1 Introduction

As shown in **Fig.2.1**, mathematical models used to describe physical problems generally can be divided into three categories. The first one is the variational theorem that integrates the whole target domain. The second one is the differential equation that describes the infinitesimal element, and the third one is the boundary integral equation related to the boundary of the target domain. Generally speaking, any physical problem can be described with the help of the above three theorems. If there is an analytical solution, then results can be obtained. However, in complex engineering problems, deriving analytical solutions are rather hard, so various numerical methods have sprung up. The representative numerical method originated from the variational theorem is FEM. FDM is a representative method developed based on differential equations, which has become a very overwhelmingly popular numerical method. Among the numerical methods proposed based on boundary integral equations, the most representative is BEM.

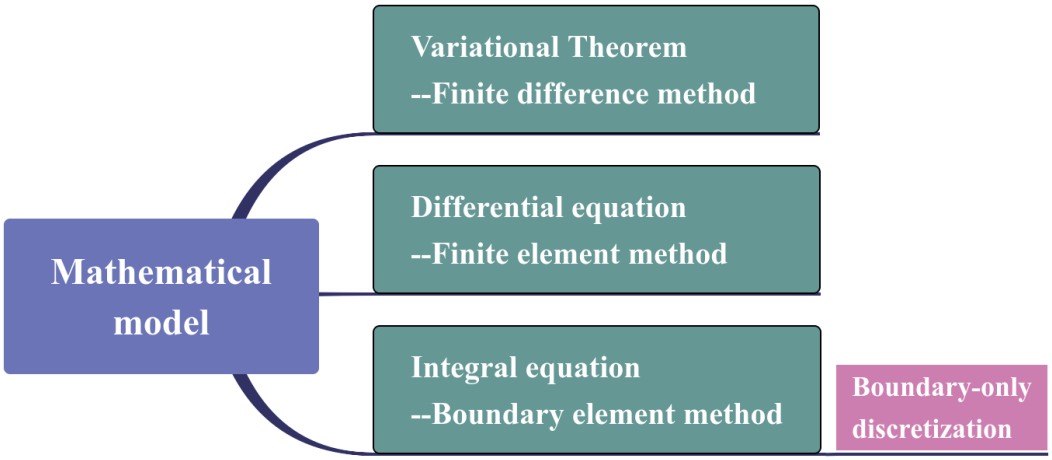

Fig.2.1 Mathematical models

BEM is one of the boundary numerical methods and is semi-analytical and semi-numerical. Based on Green's theorem [101, 102], the dimension of the target domain can be reduced one order lower in combination with the basic solution (as shown in **Fig.2.2**), specifically, for a three-dimensional problem, only a two-dimensional mesh is needed to discretise its surface, and for a two-dimensional problem, only a one-dimensional mesh is needed to discretise its boundary,

which is the most prominent advantage of BEM, and that is why it is called boundary element method.

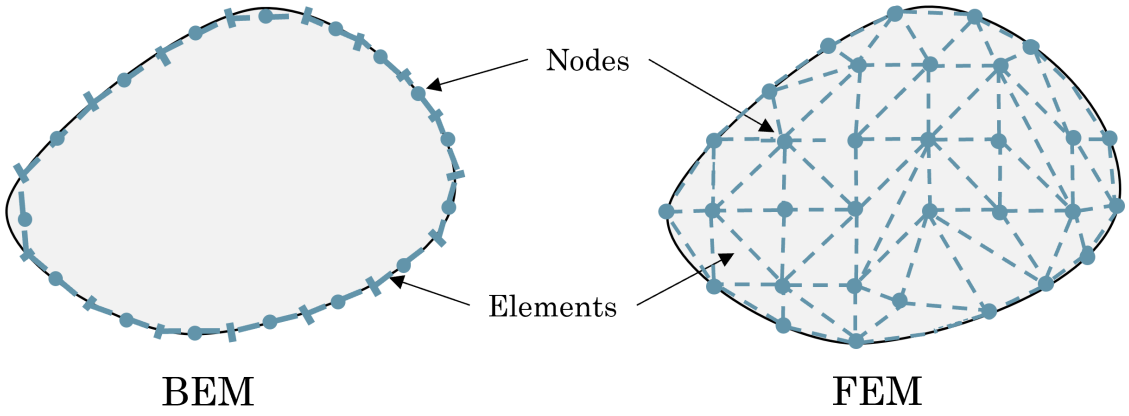

Fig.2.2 Comparison between BEM and FEM

The advantage, boundary-only discretisation, of BEM can significantly reduce the number of unknowns. Taking elasticity analysis as an example, to achieve satisfactory accuracy, thousands of equations need to be solved in FEM, while we only need to deal with hundreds of equations to obtain the same degree of accuracy if using BEM. In addition, when it comes to infinite or semi-finite domains, suitable finite domains are needed to approximate and substitute infinite or semi-finite domains if using FEM, which will inevitably lead to errors. Moreover, the size and shape of the finite domain used for substitution will also affect the accuracy of results, and the tests for suitable substitution can increase the workload as well. While BEM domain approximation is not necessary for BEM, because the singularity of the fundamental solutions in BIEs makes it directly applicable to the infinite or semi-infinite domains. Definitely, BEM and FEM also share similarities, such as both need element discretisation, nodes and shape functions.

2.2 Categories of BEM

BEM can be divided into two categories: Direct BEM [103, 104] and Indirect BEM [105, 106].

Suppose there is an N-dimensional domain Ω with boundary Γ. After boundary discretisation, there should be 2N physical quantities (N displacements and N forces) for each node. For a specific problem, the number

of known physical quantities on the boundary should be N, and the rest is the unknown physical quantities that need to be calculated. Then, the unknown quantities on the boundary can be obtained with the help of fundamental solutions and given known boundary conditions. When all the physical quantities on the boundary are known, the displacement and stress in the target domain can be obtained by using the BIE again. This process using variables with clear physical meaning to establish BIEs, and then directly computing the actual physical quantities (displacement or force) on the boundary is called the direct boundary element method (DBEM).

DBEM can be subdivided into many forms of BEM, one of which is the boundary element method based on the displacement boundary integral equation (DBIE), also known as the conventional boundary element method (CBEM). This method is derived from the generalized Hooke's law based on the reciprocity theorem. The other one is based on the hypersingular boundary integral equation (HBIE) which is also known as the traction boundary integral equation and is derived from the displacement derivative, strain with the help of the stress-strain relationship based on DBIE. The reason why it is called hypersingular boundary integral equation is the singularity of fundamental solutions in its integral equation.

For elastic mechanics, the indirect BEM can be further divided into the fictitious stress method (FSM) [107-109] and the displacement discontinuity method (DDM) [48, 110]. The virtual quantity in FSM is the traction; while the virtual quantity in DDM is the discontinuous displacement quantity on the real crack or the virtual crack (impose at the boundary position of the target domain).

The core gist of the indirect BEM is to classify the N-dimensional domain into an infinite domain, and then apply a virtual load (virtual displacement or virtual stress, as shown in **Fig.2.3**) on its boundary Γ. If the stress or displacement caused by the virtual load can meet the original preset boundary conditions according to a certain distribution approach, then the stress or displacement field of the domain is the required result. The reason that this

method is called indirect BEM is that virtual variables without clear physical meaning are taken as unknown variables and the relevant boundary integral equations are solved, then the real displacements and stresses at the boundary and in the domain are calculated.

It should be pointed out that except for **Chapter 7**, the derivation of BIEs involved in this thesis is based on the DBEM.

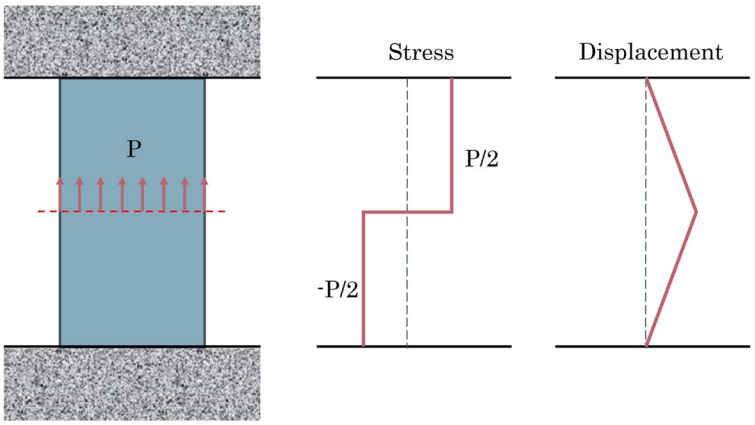

(a) Fictitious stress method

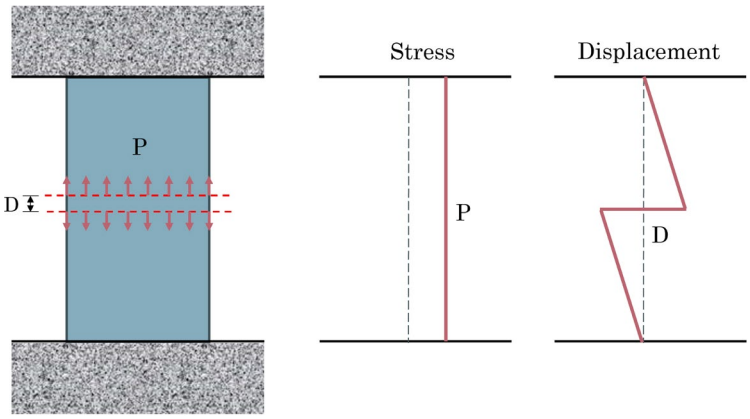

(b) Displacement discontinuity method

Fig.2.3 Classification of IBEM

2.3 Boundary integral equation of elasticity

For isotropic linear elastomer, assuming that its deformation under loads is sufficiently small, its strain tensor can be defined as:

$$\varepsilon_{ij} = \frac{u_{i,j} + u_{j,i}}{2} \tag{2.1}$$

Hooke's law is defined as:

$$\sigma_{ij} = \lambda \sigma_{ij} \varepsilon_{kk} + 2\mu \varepsilon_{ij} \tag{2.2}$$

where σ_{ij} is the stress tensor, λ and μ are Lame constant and shear modulus.

Considering an infinitesimal hexahedral element inside an isotropic linear elastomer, the Navier-Cauchy stress equation about the stress tensor can be derived from the equilibrium conditions of the forces in three directions:

$$\sigma_{ij,i} + b_j = 0 \tag{2.3}$$

where b_j is the body force in the *j*-direction。

The displacement and traction fundamental solution of the Navier-Cauchy equation, $U_{ij}(\mathbf{x},\mathbf{y})$ and $T_{ij}(\mathbf{x},\mathbf{y})$ can be presented as:

$$U_{ij}(\mathbf{x},\mathbf{y}) = \frac{1}{2A_1\mu r^h}\left\{A_2\delta_{ij}\left[(h-2)\ln\left(\frac{1}{r}\right)+h-1\right]+r_{,i}r_{,j}\right\} \tag{2.4}$$

$$T_{ij}(\mathbf{x},\mathbf{y}) = \frac{-1}{A_1 r^h}\left\{r_{,k}n_k\left[A_3\delta_{ij}+3r_{,i}r_{,j}\right]-A_3\left(r_{,i}n_j - r_{,j}n_i\right)\right\} \tag{2.5}$$

where

$$\begin{cases} A_1 = 4\pi(1-v) \\ A_2 = 3-4v \\ A_3 = 1-2v \end{cases} \tag{2.6}$$

and r is the distance between $\mathbf{x}$ and $\mathbf{y}$

$$r_{,i} = \frac{\partial r}{\partial x_i} \tag{2.7}$$

which represents the derivates of r with respect to x_i. And $\mathbf{x}$ and $\mathbf{y}$ are the source point and field point. For 2D problems, we have

$$\begin{cases} \mathbf{x} = \mathbf{x}(x_1, x_2) \\ \mathbf{y} = \mathbf{y}(y_1, y_2) \\ h = 1 \end{cases} \tag{2.8}$$

For 3D problems, we have

$$\begin{cases} \mathbf{x} = \mathbf{x}(x_1, x_2, x_3) \\ \mathbf{y} = \mathbf{y}(y_1, y_2, y_3) \\ h = 2 \end{cases} \tag{2.9}$$

The basic physical meaning of $U_{ij}(\mathbf{x},\mathbf{y})$ is that after imposing a concentrated force f_i^* at point $\mathbf{x}$ in the *i-direction*, the displacement $u_j(\mathbf{y})$ at point $\mathbf{y}$ in the *j-direction* can be obtained and expressed as

$$u_j(\mathbf{y}) = U_{ij}(\mathbf{x},\mathbf{y}) f_i(\mathbf{x}) \tag{2.10}$$

Similarly, the traction relationship can be obtained with the help of

fundamental solutions and expressed as

$$t_j(\mathbf{y}) = T_{ij}(\mathbf{x},\mathbf{y}) f_i(\mathbf{x}) \tag{2.11}$$

The next step is to deduce the boundary integral equation. Eq.(2.4) can be obtained by combining the displacement-strain relationship formula (2.1) and Hooke's law formula (2.2) and written as

$$\mu u_{i,jj} + (\lambda + \mu) u_{j,ji} + b_i = 0 \tag{2.12}$$

Assuming there is a domain Ω with its boundary Γ and there are two equilibrium states, $(\sigma_{ij}, \varepsilon_{ij})$ and $(\sigma_{ij}^*, \varepsilon_{ij}^*)$, Multiply both sides of Hooke's law, Eq.(2.2) by ε_{ij}^*, one can obtain

$$\begin{aligned} \sigma_{ij}\varepsilon_{ij}^* &= \lambda\delta_{ij}\varepsilon_{kk}\varepsilon_{ij}^* + 2\mu\varepsilon_{ij}\varepsilon_{ij}^* \\ &= \lambda\varepsilon_{kk}\varepsilon_{mm}^* + 2\mu\varepsilon_{ij}\varepsilon_{ij}^* \\ &= \varepsilon_{ij}\left(\lambda\delta_{ij}\varepsilon_{mm}^* + 2\mu\varepsilon_{ij}^*\right) \\ &= \sigma_{ij}^*\varepsilon_{ij} \end{aligned} \tag{2.13}$$

The following is obtained by integrating both sides of Eq.(2.11)

$$\int_\Omega \sigma_{ij}\varepsilon_{ij}^* \mathrm{d}\Omega = \int_\Omega \sigma_{ij}^*\varepsilon_{ij} \mathrm{d}\Omega \tag{2.14}$$

which proves Betti's reciprocal theorem. Then, Using Eq.(2.1) and the symmetry property of stress tensor, one obtains

$$\int_\Omega \sigma_{ij}\varepsilon_{ij}^* \mathrm{d}\Omega = \int_\Omega \sigma_{ij} u_{i,j}^* \mathrm{d}\Omega \tag{2.15}$$

Then, with the help of the traction-stress relationship, the following can be derived:

$$t_i = \sigma_{ij} n_j \tag{2.16}$$

where n_j denotes the unit outer normal vector of boundary, then using Eq.(2.4) and adopting partial integration on both sides of Eq.(2.12), one can get

$$\begin{cases} I_L = \int_\Gamma t_i u_i^* \mathrm{d}\Gamma + \int_\Omega b_i u_i^* \mathrm{d}\Omega \\ I_R = \int_\Gamma t_i^* u_i \mathrm{d}\Gamma + \int_\Omega b_i^* u_i \mathrm{d}\Omega \end{cases} \tag{2.17}$$

Further, Eq.(2.15) can be written as

$$\begin{aligned} &\int_\Gamma t_j^*(\mathbf{y}) u_j(\mathbf{y}) \mathrm{d}\Gamma(\mathbf{y}) + \int_\Omega b_j^*(\mathbf{x}) u_j(\mathbf{x}) \mathrm{d}\Omega \\ &= \int_\Gamma t_j(\mathbf{y}) u_j^*(\mathbf{y}) \mathrm{d}\Gamma(\mathbf{y}) + \int_\Omega b_j(\mathbf{x}) u_j^*(\mathbf{x}) \mathrm{d}\Omega \end{aligned} \tag{2.18}$$

where $t_j^*(\mathbf{y})$ and $u_j^*(\mathbf{x})$ are the displacement and traction response induced by the unit concentrated force f_i^*. Combining the definition of fundamental solutions, one can obtain

$$\begin{cases} u_j^*(\mathbf{y}) = U_{ij}(\mathbf{x},\mathbf{y}) f_i^*(\mathbf{x}) \\ t_j^*(\mathbf{y}) = T_{ij}(\mathbf{x},\mathbf{y}) f_i^*(\mathbf{x}) \end{cases} \tag{2.19}$$

Then, combining Eq.(2.19) with the Somigliana identity, one can get

$$\begin{aligned} \int_\Omega \delta_{ij}\delta(\mathbf{x},\mathbf{y}) u_j(\mathbf{y}) \mathrm{d}\Omega(\mathbf{y}) = & \int_\Gamma U_{ij}(\mathbf{x},\mathbf{y}) t_j(\mathbf{y}) \mathrm{d}\Gamma(\mathbf{y}) \\ & - \int_\Gamma T_{ij}(\mathbf{x},\mathbf{y}) u_j(\mathbf{y}) \mathrm{d}\Gamma(\mathbf{y}) \end{aligned} \tag{2.20}$$

where

$$b_j^*(\mathbf{y}) = \delta(\mathbf{x},\mathbf{y}) f_i^*(\mathbf{x}) \tag{2.21}$$

Then the following can be derived[73~75]

$$u_i(\mathbf{x}) = \int_\Gamma U_{ij}(\mathbf{x},\mathbf{y}) t_j(\mathbf{y}) \mathrm{d}\Gamma(\mathbf{y}) - \int_\Gamma T_{ij}(\mathbf{x},\mathbf{y}) u_j(\mathbf{y}) \mathrm{d}\Gamma(\mathbf{y}) \tag{2.22}$$

The above boundary integral equation is the displacement boundary integral equation and can be applied to compute the displacement and stress of the internal point of a target domain. When the source point is located on the boundary, as shown in **Fig.2.4**, the infinitely small part Γ_1 of boundary Γ near point $\mathbf{x}$ can be topologically formed into a semicircle of radius r_ε, so that the source point is inside the boundary. Then combined with Somigliana identity, the displacement boundary integral equation can finally be obtained and written as

$$c_{ij}(\mathbf{x}) u_i(\mathbf{x}) = \int_\Gamma U_{ij}(\mathbf{x},\mathbf{y}) t_j(\mathbf{y}) \mathrm{d}\Gamma(\mathbf{y}) - \int_\Gamma T_{ij}(\mathbf{x},\mathbf{y}) u_j(\mathbf{y}) \mathrm{d}\Gamma(\mathbf{y}) \tag{2.23}$$

where

$$c_{ij}(\mathbf{x}) = \begin{cases} \dfrac{1}{2}\delta_{ij}, & \mathbf{x} \textit{ on boundary } \Gamma \\ \delta_{ij}, & \mathbf{x} \textit{ inside domain} \end{cases} \tag{2.24}$$

Combining the strain-displacement relationship again, i.e., Eq.(2.1), the internal stress integral equation can be obtained as

$$\sigma_{ij}(\mathbf{x}) = \int_\Gamma U_{ijk}(\mathbf{x},\mathbf{y}) t_k(\mathbf{y}) \mathrm{d}\Gamma - \int_\Gamma \mathrm{T}_{ijk}(\mathbf{x},\mathbf{y}) u_k(\mathbf{y}) \mathrm{d}\Gamma \tag{2.25}$$

where

$$U_{ijk}(\mathbf{x},\mathbf{y}) = \frac{1}{A_1 r^h}\left[A_3\left(\delta_{ki} r_{,j} + \delta_{kj} r_{,i} - \delta_{ij} r_{,k}\right) + (h+1) r_{,i} r_{,j} r_{,k} \right] \tag{2.26}$$

$$\begin{aligned} T_{ijk}(\mathbf{x},\mathbf{y}) = \frac{2\mu}{A_1 r^h} \Big\{ & (h+1) r_{,m} n_m \left[A_3 \delta_{ij} r_{,k} + \nu\left(\delta_{ik} r_{,j} - \delta_{jk} r_{,i}\right) - (h+3) r_{,i} r_{,j} r_{,k} \right] \\ & + \nu(h+1)\left(n_i r_{,j} r_{,k} + n_j r_{,i} r_{,k}\right) + A_3\left[(h+1) n_k r_{,i} r_{,j} + n_j \delta_{ik} + n_i \delta_{jk} \right] \\ & - (A_2 - 2) n_k \delta_{ij} \Big\} \end{aligned} \tag{2.27}$$

When $\mathbf{x} \in \Gamma$, the traction can be obtained by

$$c_{ij}(\mathbf{x})\mathbf{t}_j(\mathbf{x}) = c_{ij}(\mathbf{x})\sigma_{ij}(\mathbf{x})n_j(\mathbf{x}),\ \mathbf{x}\in\Gamma \tag{2.28}$$

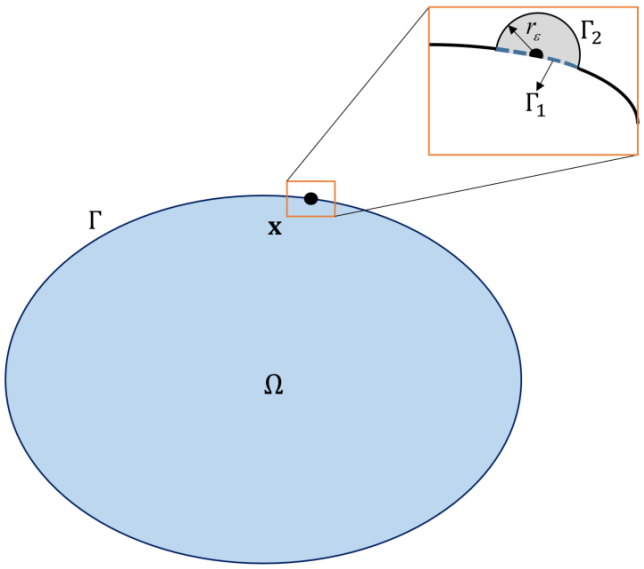

Fig.2.4 Topological boundary when the source point is on the boundary

2.4 Boundary integral equations for heat conduction problems

Heat conduction is a heat transfer phenomenon when there is no macroscopic motion in the medium. It is very common in both life and engineering. As long as there is a temperature difference in the medium or between mediums, heat transfer will always occur. In addition, in engineering structures, thermal stress, which is caused by the temperature change of structures that cannot be freely stretched or the temperature of each internal part is different, is the key factor affecting the safety of the structure.

The governing equation of heat conduction in an isotropic medium without an internal heat source is:

$$\frac{\partial}{\partial x_i}\left[k\frac{\partial\theta(\mathbf{x})}{\partial x_i}\right]=0 \tag{2.29}$$

where k denotes the thermal conductivity coefficient, θ represents temperature, $\mathbf{x}$ is a point inside domain Ω.

The boundary conditions can be set as

$$\begin{cases}\theta(\mathbf{x})=\tilde{\theta}(\mathbf{x})\\ q(\mathbf{x})=-k\dfrac{\partial\theta(\mathbf{x})}{\partial\mathbf{n}}=\tilde{q}(\mathbf{x})\end{cases} \tag{2.30}$$

where $q(\mathbf{x})$ denotes heat flux.

Multiply Eq.(2.29) by the weight function u^*, then integrate domain Ω, we

can get

$$\int_{\Omega} u^{*} \frac{\partial}{\partial x_i}\left(k \frac{\partial \theta}{\partial x_j} \right) \mathrm{d}\Omega = 0 \tag{2.31}$$

Then with the help of a series of transformations[119], such as partial integration, the following boundary integral equation can be obtained

$$\begin{aligned} c(\mathbf{x})\hat{\theta}(\mathbf{x}) = &-\int_{\Gamma} U(\mathbf{x},\mathbf{y}) q(\mathbf{y}) \mathrm{d}\Gamma(\mathbf{y}) \\ &-\int_{\Gamma} Q(\mathbf{x},\mathbf{y}) \hat{\theta}(\mathbf{y}) \mathrm{d}\Gamma(\mathbf{y}) \end{aligned} \tag{2.32}$$

where $\hat{\theta}=k\theta$ denotes the regularized temperature, for the points on the smooth boundary, $c=1/2$, for inner points, $c=0$, $P(\mathbf{x},\mathbf{y})$ and $Q(\mathbf{x},\mathbf{y})$ are the fundamental solutions [12] and can be written as

$$P(\mathbf{x},\mathbf{y}) = \begin{cases} \dfrac{1}{2\pi} \ln\left(\dfrac{1}{r}\right), & 2D\ problems \\ \dfrac{1}{4\pi r}, & 3D\ problems \end{cases} \tag{2.33}$$

$$Q(\mathbf{x},\mathbf{y}) = \begin{cases} -\dfrac{1}{2\pi r}\dfrac{\partial r}{\partial \mathbf{n}}, & 2D\ problems \\ -\dfrac{1}{4\pi r^2}\dfrac{\partial r}{\partial \mathbf{n}}, & 3D\ problems \end{cases} \tag{2.34}$$

where $\mathbf{n}$ denotes the outer normal vector on boundary Γ and constituted by n_i , r is the distance between $\mathbf{x}$ and $\mathbf{y}$, i.e.,

$$r = \|\mathbf{x} - \mathbf{y}\| \tag{2.35}$$

2.5 The singular integrals of boundary integral equations

2.5.1 Overview of singular integrals

As an inevitable "double-edged sword" in the development of BEM, singular integrals have been widely concerned by scholars at home and abroad. On the one hand, the singularity of the fundamental solution in boundary integral equations makes it more suitable for computing infinite problems and semi-infinite problems, such as fracture problems. On the other hand, the existence of singular integrals makes numerical computation more difficult.

Fundamental solutions are the basis for the numerical computation of BEM. It can be seen that the fundamental solutions in the boundary integral equations of both elasticity and heat conduction problems contain terms like

$\ln(1/r)$, $1/r$ or $1/r^2$. When r approaches zero, the value of $\ln(1/r)$, $1/r$ and $1/r^2$ will tend to infinity, which makes the fundamental solutions singular. Only by properly dealing with the integral singularity, the calculation results can be stable and accurate.

2.5.2 Classification of singular integrals

In BIEs, the general form of boundary integral can be written as follows

$$\int_\Gamma \xi(\mathbf{x},\mathbf{y})\mathrm{d}\Gamma(\mathbf{y}) = \int_\Gamma \frac{\tilde{\xi}(\mathbf{x},\mathbf{y})}{r^\chi(\mathbf{x},\mathbf{y})}\mathrm{d}\Gamma(\mathbf{y}) \tag{2.36}$$

where the integrand function $\xi(\mathbf{x},\mathbf{y})$ in the target domain is bounded and can be expressed in the following general form

$$\xi(\mathbf{x},\mathbf{y}) = \frac{\tilde{\xi}(\mathbf{x},\mathbf{y})}{r^\chi(\mathbf{x},\mathbf{y})} \tag{2.37}$$

where χ is an integer and can represent the order of function singularity, $\tilde{\xi}(\mathbf{x},\mathbf{y})$ denotes the rest part of $\xi(\mathbf{x},\mathbf{y})$ after the term $r^\chi(\mathbf{x},\mathbf{y})$ is decomposed.

Assuming that $\tilde{\xi}(\mathbf{x},\mathbf{y})$ is bounded in the definition domain and ϖ is the number of times of integrals, the following classification can be further made according to the order of singularity of the integrand function $\xi(\mathbf{x},\mathbf{y})$:

(1) Regularity integrals: $\chi \le 0$;

(2) Weak singularity integral: $0 < \chi \le \varpi$;

(3) Strong singularity integral: $\chi = \varpi$;

(4) Super singularity integral: $\chi = \varpi + 1$;

(5) Supersingularity integral: $\chi > \varpi + 1$。

In general, the values of regular integrals and weakly singular integrals are bounded. In this thesis, Eqs.(2.6) and (2.27) are integrals with weak singularities, and Eq.(2.28) is a integral with strong singularities.

However, the strong singular integral in BIEs can be solved in the definition of the Cauchy principal value integral, because in the derivation process of BIEs, the minimal domain near the source point is separated, and it exists in the BIE as a free term.

2.5.3 Computation methods for singular integral

Scholars have proposed various solutions to solve singular integrals,

including particular solution method, partial integral calculus, regularized power series expansion method; polynomial expansion method; regularization method under isoparametric coordinates, coordinate transformation method, etc.

(1) Particular solution method. Also known as the indirect method, this method is to put the integrals with strong singularity and the free items in boundary integral equations together and places them on the diagonal of the coefficient matrix formed after the discretisation computation. The elements on the diagonal, which are non-singular, are calculated first, and then the values of the diagonal elements are evaluated according to the values of the non-singular elements on the non-diagonal. An improved particular solution method that can compute the supersingular integrals is developed later.

(2) Partial integral calculus. The main idea of this method is to convert the integrand function into a relatively simpler form through differentiation. This method was later applied to solve the crack problem. Budiansky[111] transferred some derivative terms in the fundamental solution with super singularity to the boundary of the target domain, which can reduce the order of the singularity of the integrand function, and then make the traction boundary integral equation solvable.

(3) Regularized power series expansion method. The basic idea is to eliminate the overall singularity by expanding the nonsingular part of the integrand function of the singularity integral into the power series of the distance between the source point and the field point. In the beginning, this method is based on the global coordinate system, and can only be applied to compute two-dimensional singularity integrals. Later, this method is further improved by placing the expansion of power series in the isoparametric coordinate system, and the application can be extended to various high-order singular integrals.

(4) Polynomial expansion method. The basic idea of it is to expand the kernel function in singular integrals and calculate it in the form of truncated cardinality to approximate the analytical solution of the singular integral. This

method is mainly used to solve the hypersingular integral.

(5) Regularization method in isoparametric coordinates. It is proposed by Guiggianiti[112] in 1992 and its main principle is to expand the kernel function with singularity in isoparametric coordinates by using the Laurent series, and then the singularity can be eliminated. Later, it was further extended by Aliabadi to compute the hypersingular integral.

(6) Coordinate transformation method. Also known as the element subdivision method, was first proposed by Lachat et al. [113] in 2010. The basic idea of it is to make the Jacobi value of the kernel function at the singular point zero through coordinate transformation, so as to eliminate the singularity of integrals. It is mainly applied to weak singular integrals and is exerted in this thesis. Based on the coordinate transformation method, the $\{\alpha, \beta\}$ coordinate conversion is proposed.

2.6 Discretisation and computation of BIEs

In this section, the discretisation process will be introduced by taking the displacement integral equation for elasticity as an example, i.e., Eq.(2.21). Firstly, the boundary Γ of the target domain Ω needs to be discretised and the number of boundary elements is defined as N_e. For any point $\mathbf{x}$ on the boundary, its global coordinates can be expressed by the shape function $N_l = N_l(\xi)$ as

$$x_i = \sum_{l=1}^{M} N_l x_i^l \tag{2.38}$$

where M is the number of nodes in the element.

In addition, it is also necessary to use the shape function to denote the displacement and traction at any point in the element:

$$u_j(\mathbf{x}) = \sum_{l=1}^{M} N_l u_i^l \tag{2.39}$$

and

$$t_j(\mathbf{x}) = \sum_{l=1}^{M} N_l t_i^l \tag{2.40}$$

It should be noted that the above approach can be used to characterize the physical quantities of continuous elements, while discontinuous elements are

needed to represent nodes with discontinuous surface forces or displacements. Then the displacement boundary integral equation can be discretised as:

$$\begin{aligned} C_{ij}(\mathbf{x})u_j(\mathbf{x}) = &\sum_{e=1}^{Ne}\left[\sum_{l=1}^{M} t_j^l \int_{\Gamma_e} U_{ij}(\mathbf{x},\mathbf{y})\mathrm{N}_l(\mathbf{y})d\Gamma(\mathbf{y})\right] \\ &-\sum_{e=1}^{Ne}\left[\sum_{l=1}^{M} u_j^l \int_{\Gamma_e} T_{ij}(\mathbf{x},\mathbf{y})\mathrm{N}_l(\mathbf{y})d\Gamma(\mathbf{y})\right] \end{aligned} \tag{2.41}$$

where Γ_e denotes the eth boundary element。

The two integrand functions on the handside of Eq.(2.41) are known, which can be calculated directly by Gaussian integral. Let

$$\begin{cases} \overline{G_{ij}^{el}} = \int_{\Gamma_e} U_{ij}(\mathbf{x},\mathbf{y})\mathrm{N}_l(\mathbf{y})d\Gamma(\mathbf{y}) \\ \overline{H_{ij}^{el}} = \int_{\Gamma_e} T_{ij}(\mathbf{x},\mathbf{y})\mathrm{N}_l(\mathbf{y})d\Gamma(\mathbf{y}) \end{cases} \tag{2.42}$$

then, Eq.(2.41) can be transformed into

$$C_{ij}(\mathbf{x})u_j(\mathbf{x}) = \sum_{e=1}^{Ne}\sum_{l=1}^{M} t_j^l \overline{G_{ij}^{el}} - \sum_{e=1}^{Ne}\sum_{l=1}^{M} u_j^l \overline{H_{ij}^{el}} \tag{2.43}$$

Finally, the following equation can be obtained

$$\mathbf{Hu = Gt} \tag{2.44}$$

By shifting the unknown physical quantity, we can get

$$\mathbf{AX = Y} \tag{2.45}$$

In Eq.(2.45), **X** and **Y** are known boundary physical quantities (traction or displacement) and unknown boundary quantities (traction or displacement) respectively, **A** is the coefficient matrice of known boundary physical quantities. The unknown physical quantities can be obtained by solving the linear equations.

Taking the computation of the displacement boundary equation in elasticity as an example, the schematic diagram of the computation process can be illustrated in the following figure:

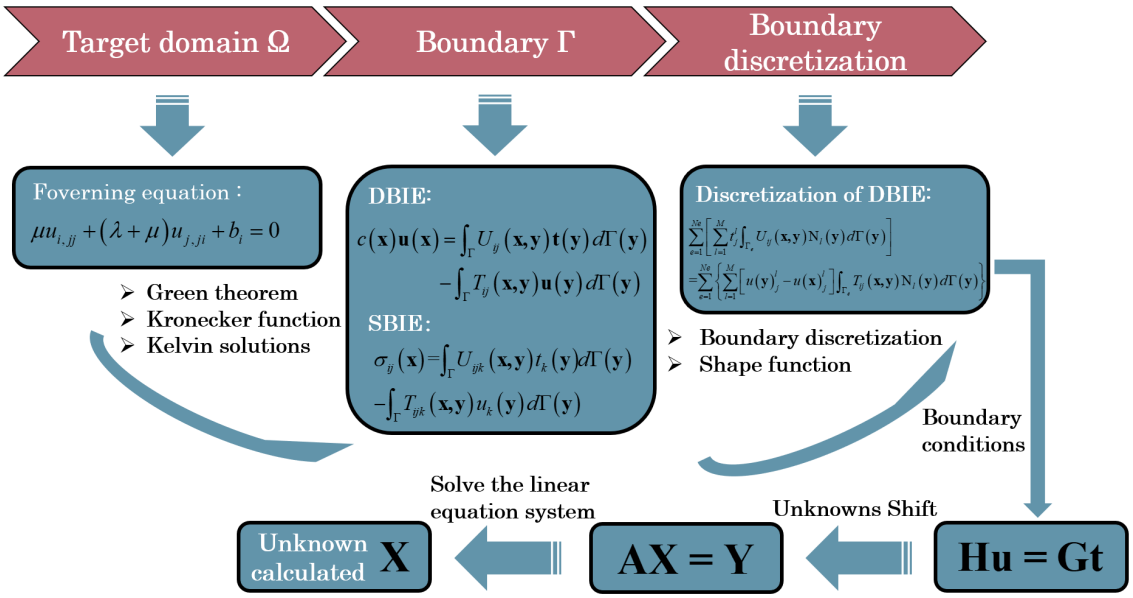

Fig.2.5 Basic computation process of boundary element method

Part II

Application of boundary element method in heat conduction analysis

Chapter 3

The fast multipole method accelerated line integration boundary element method for 3D heat conduction analysis with heat sources

Summary

3D steady heat conduction analysis considering heat source is conducted on the fundamental of BEM in this chapter. Due to considering the heat source, domain integrals appear in heat conduction BIEs which will counteract the well-known merit of the BEM, namely, boundary-only discretisation. To avoid volume discretisation, the enhanced BEM, the line integration BEM (LIBEM) with dimension reduction property is introduced to transfer domain integrals into line integrals. The numerical results prove that the LIBEM is well-performed in convergence and accuracy.

Further, to overcome the shortcoming, high time consumption, of the LIBEM, the FM-LIBEM is proposed to enhance the computation efficiency based on the FMM. According to the numerical results, the FM-LIBEM performs great in reducing computational time and making computing numerical structures with a massive degree of freedom via a personal computer becomes possible. For example, the computer (a 2.6 GHz CPU and 32.0 GB of RAM) used in this research only can calculate models with no more than 50000 elements by the LIBEM, while models with more than 230000 elements are still under the computation capacity when using the FM-LIBEM.

3.1 Introduction

As a common phenomenon in engineering, heat conduction analysis with heat sources also deserves attention. For example, concrete structures can generate heat by themselves during the process of pouring and curing, and this heating process may lead to fractures [4, 114, 115] and break engineering structures [116, 117]. So far, some research are done on heat conduction analysis considering heat source on the fundamental of the BEM. Such as Sekiya et al. [118] conducted the heat conduction analysis considering heat sources via a multiple-reciprocity BEM. Besides, a radial integration polygonal BEM is proposed by Cui et al. [119] for heat conduction analysis.

Due to considering heat sources, domain integrals appear in the BIE of heat conduction. Several previous pieces of research applied the multiple reciprocity method and radial integration method as integral dimension reduction methods. In this research, the LIBEM, is applied to reduce the domain integral dimensionally and the domain integrals can be transferred into line integrals, hence volume discretisation is avoided successfully. LIM is an efficient dimension reduction method as well, unlike RIM, it reduces domain integrals to boundary integrals with 1D integrals based on the divergence theorem in Cartesian coordinates. To deal with singular integrals, the coordinate transformation is exerted. Moreover, LIM also performs well in accuracy and convergence.

However, the time complexity of the LIBEM is $O(NM)$ where N and M are the numbers of nodes and lines, respectively [120-122], which means the computational time will increase sharply with the rise of element number. Thus, the computation of massive or large-scale structures is too time-consuming. Hence, an acceleration algorithm is in need. In this research, the FMM is exerted to couple with the LIBEM as a new method, FM-LIBEM, which can be applied to large-scale computation. The FMM has been applied in many fields by coupling with other mathematic methods since its appearance, like acoustic analysis [123, 124], elasticity analysis [125-127] and electromagnetic

analysis [128, 129]. The FM-LIBEM proposed in this research can enhance computation efficiency without losing accuracy generally. Specifically, the LIM for the computation of domain integrals and the BEM for the computation of traditional boundary integrals can be accelerated by the FMM in this paper.

The detailed theorem and validation of the FM-LIBEM are presented in the following sections. Firstly, the formulas of 3D heat conduction analysis with heat source are presented. In **Section 3.3**, the theorem of the FMM and LIBEM are presented in detail, followed by the procedures for the realization of the FM-LIBEM. Further, in the next section, the accuracy, efficiency and convergence of the FM-LIBEM are testified in the first numerical example, and the latter two examples focus on showing the performance of the FM-LIBEM when it comes to complex models.

3.2 Theorem of 3D heat conduction considering heat sources

For heat conduction analysis of isotropic materials containing heat source, the governing formula is presented as [130]

$$\frac{\partial}{\partial x_i}\left[k\frac{\partial\theta(\mathbf{x})}{\partial x_i}\right]+B(\mathbf{x})=0 \tag{3.1}$$

where k symbolizes thermal conductivity, θ is temperature, $\mathbf{x}$ are the points in the research domain Ω with components x_i, $B(\mathbf{x})$ represents heat source.

And the boundary conditions are set as

$$\begin{cases}\theta(\mathbf{x})=\tilde{\theta}(\mathbf{x}) & on\ \Gamma_\theta\\ q(\mathbf{x})=-k(\mathbf{x})\dfrac{\partial\theta(\mathbf{x})}{\partial\mathbf{n}}=\tilde{q}(\mathbf{x}) & on\ \Gamma_q\end{cases} \tag{3.2}$$

where $q(\mathbf{x})$ symbolizes the heat flux. Γ_θ and Γ_q are the boundary with known temperature and heat flow respectively. $\tilde{\theta}(\mathbf{x})$ and $\tilde{q}(\mathbf{x})$ represent the known temperature and heat flow on Γ_θ and Γ_q respectively. $\mathbf{n}$ symbolizes the outward normal vector on boundary $\Gamma=\Gamma_\theta\cup\Gamma_q$ with its i^{th} component n_i.

By introducing the weight function and divergence theorem, the governing Eq. (3.1) is written as

$$\begin{aligned}c(\mathbf{x})\hat{\theta}(\mathbf{x})=&-\int_\Gamma u^*(\mathbf{x},\mathbf{y})q(\mathbf{y})\mathrm{d}\Gamma(\mathbf{y})-\int_\Gamma q^*(\mathbf{x},\mathbf{y})\hat{\theta}(\mathbf{y})\mathrm{d}\Gamma(\mathbf{y})\\&+\int_\Omega u^*(\mathbf{x},\mathbf{y})B(\mathbf{y})\mathrm{d}\Omega(\mathbf{y})\end{aligned} \tag{3.3}$$

where $\hat{\theta}$ symbolizes the normalized temperature and $\hat{\theta}=k\theta$, and k is the thermal conductivity, c is set to 0.5 and 1.0 respectively for smooth boundary points and internal points, $u^*(\mathbf{x},\mathbf{y})$ and $q^*(\mathbf{x},\mathbf{y})$ are kernel functions [131] and can be found in **Section 2.4**.

There is a domain integral in Eq.(3.3) and can be expressed as follows

$$D_1(\mathbf{x}) = \int_\Omega u^*(\mathbf{x},\mathbf{y}) B(\mathbf{y}) \mathrm{d}\Omega(\mathbf{y}) \tag{3.4}$$

3.3 Line integration method for domain integrals

The LIM is an efficient approach for solving boundary integral equations with domain integrals without volume discretisation. The basic theorem and equations are introduced below [127].

To compute the domain integrals with weakly-singular kernels, the case for domain integrals with continue functions is considered first. By using **Theorem 3.3** in **Appendix**, the domain integrals can be translated into boundary integrals. For simplicity, one can let all the start points of the integral lines on the same plane $\{y_1 = c\}$, i.e. $a(y_2, y_3) = c$, where c is an arbitrary constant value. If one discretises the boundary with N elements, Eq.(3.48) can be rewritten as [127]

$$\int_\Omega f(\mathbf{y}) k(\mathbf{x},\mathbf{y}) \mathrm{d}\Omega = \sum_{i=1}^{N} \int_{\Gamma_i} F(\mathbf{x},\mathbf{y}) n_1(\mathbf{y}) \mathrm{d}\Gamma_i(\mathbf{y}) \tag{3.5}$$

where Γ_i is the ith boundary element and

$$F(\mathbf{x},\mathbf{y}\{y_1,y_2,y_3\}) = \int_c^{y_1} g(\mathbf{t}\{t,y_2,y_3\}) k(\mathbf{x},\mathbf{t}\{t,y_2,y_3\}) \mathrm{d}t, \quad \mathbf{y}\{y_1,y_2,y_3\} \in \Gamma \tag{3.6}$$

The integral on each element in Eq.(3.5) can be computed numerically with Gaussian quadrature. However, the weakly singular integral still exists in Eq.(3.5) and it should be treated carefully. Actually, the integral on an element in Eq.(3.5) is still a domain integral, and the integral area is a volume created by the plane $\{y_1 = c\}$ and the element (see **Fig.3.1**). Then the integrals can be classified into two types: regular integrals and weakly singular integrals (see **Fig.3.1**). Generally speaking, For an element E, the weakly singular integral exists when point $\mathbf{x}$ is in the integral area created by element E, then line $\mathbf{L}\{y_2 = x_2, y_3 = x_3\}$ and E has a cross point $\mathbf{s}$, where $\mathbf{s}$ can be considered as the singular point for the weakly singular integral on

boundary element E (see **Fig.3.2**). The regular integrals can be computed by Gaussian quadrature with weighted integral points directly. The weakly singular point **s** on a boundary element can be eliminated by a coordinate translation and new weighted integral points can be used on the element. Then the domain integral in Eq.(3.5) can be written as

$$\int_{\Omega} f(\mathbf{y}) k(\mathbf{x},\mathbf{y}) \mathrm{d}\Omega = \sum_{i=1}^{M} F^i(\mathbf{x},\mathbf{y}^i) n_1^i(\mathbf{y}^i) w^i \tag{3.7}$$

and

$$F^i(\mathbf{x},\mathbf{y}^i\{y_1^i,y_2^i,y_3^i\}) = \int_c^{y_1^i} g(\mathbf{t}\{t,y_2^i,y_3^i\}) k(\mathbf{x},\mathbf{t}\{t,y_2^i,y_3^i\}) \mathrm{d}t \tag{3.8}$$

where $\mathbf{y}^i\{y_1^i,y_2^i,y_3^i\}$ is the ith boundary integral point, M is the total integral points, w^i and n_1^i are the weight and unit outward normal at y_1-direction of the ith point. By Eqs.(3.7) and (3.8), the domain integral can be computed by the sum of one-dimensional line integrals on straight integral lines finally (see Fig. 3.2). The integral lines are created from the integral points on each boundary element. The lines created from weakly singular integrals can be called singular integral lines.

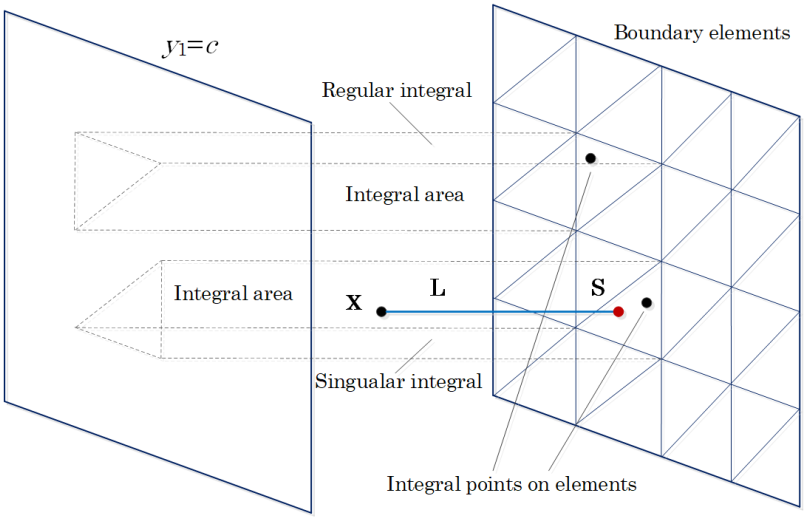

Fig.3.1 Regular integrals and the weakly singular integrals

To compute Eq.(3.8) efficiently, background cells can be used to cut the integral lines into sub-lines (see Fig.3.3) and Eq.(3.7) can be rewritten as

$$\int_{\Omega} f(\mathbf{y}) k(\mathbf{x},\mathbf{y}) \mathrm{d}\Omega = \sum_{i=1}^{M} n_1^i(\mathbf{y}) w^i \int_{L_i} g(\mathbf{y}) k(\mathbf{x},\mathbf{y}) \mathrm{d}y_1 \tag{3.9}$$

where M is the number of total integral sub-lines and L_i is the ith sub-line. n_1^i is and w^i are unit outward normal at y_1-direction and weight of sub-line L_i,

respectively, which are obtained from the corresponding integral points on boundary element.

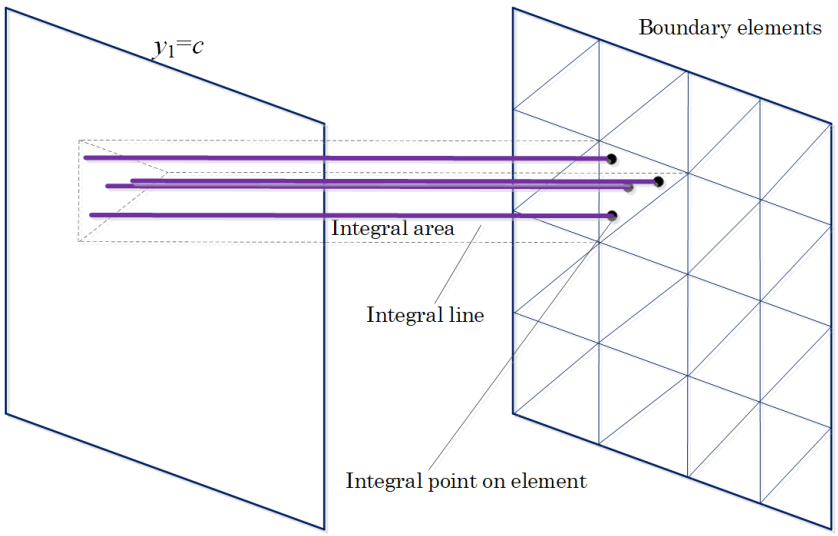

Fig.3.2 Integral lines

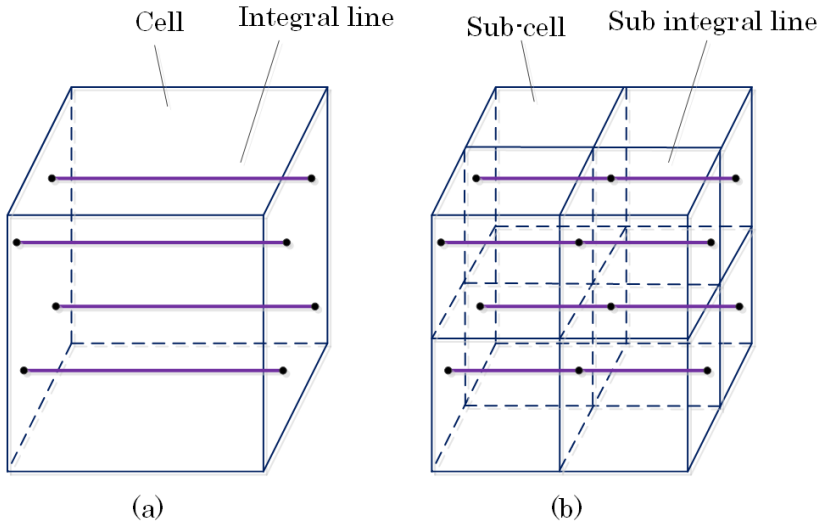

Fig.3.3 Cut and distribute integral lines into cells

The proposed method can be called the line integration method (LIM) and the background cells can be constructed by an adaptive oct-tree structure in a 3D problem. And here are the general steps:

(1) Seek the smallest cube C_0 which can contain Ω, integral lines and boundary nodes.

(2) Define the cube C_0 as level 0, then divide it into 8 cubes of the same size and define them are at level 1, in this way, the sub-cubes (children) at a certain level can be generated by the cube (parent) at the upper level.

(3) Stop the division until the number of the integral lines and boundary

nodes is less than the default numbers respectively.

The childless cube is named a leaf. See **Fig.3.4**, if a cube C shares one or more vertex with another cube (including C) and they are at the same level, then they are defined as neighbours. Besides, a member of the interaction list of C is defined as a cube which is the child of the neighbours of C's parent and has no shared vertex with C. In addition, if a cube is on the same level as C but they are not neighbours, then it is a well-separated cube from cube C. Further, for improving the accuracy and efficiency, the background cells formed by all the cube leaves are applied to divide the integral lines into short ones.

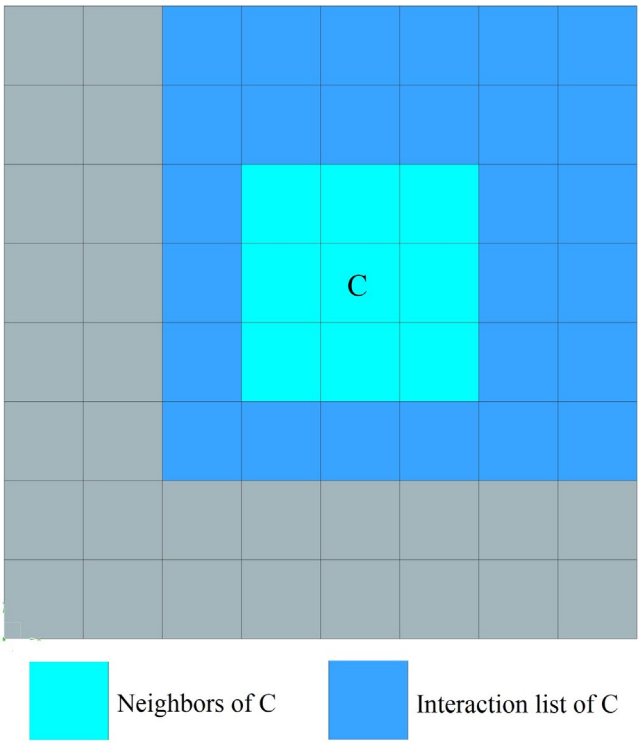

Fig.3.4 The neighbours and interaction list

And here are the application of adaptive oct-tree structure to LIM:

(1) Distribute all the integral lines and nodes into the root cell. All the nodes should be in the root cell and each integral line should also be part or total in the root cell. Keep the part in the root cell for each integral line.

(2) Subdivide the root cell into eight smaller cubes which are on level 1.

(3) Continue dividing in this way, that is, the cells of level l+1 are obtained from level l by subdividing a cell into eight equal cells.

(4) Stop the subdivision of a cell if the number of integral lines in it is less than the prescribed maximum number of lines. While subdividing a cell into eight sub-cells, the nodes and lines in it are distributed into its sub-cells. A line is cut into two lines if it is not total in one sub-cell (see **Fig.3.3**).

(5) Delete the cell if it has no line and node in it.

Now the integrals on sub-lines in background cells can be computed numerically by Gaussian quadrature. The weakly singular lines are also cut into sub-singular lines and distributed into different cells, one can still compute the line integrals with all sub-singular lines. However, the regular sub-integral lines can be used to compute the line integrals if the integral lines are far away from the singular point $\mathbf{x}$, and no singularity exists in this case. One can use the oct-tree structure to judge the distance between a line and point $\mathbf{x}$. If the cell that contains the sub-line is not the neighbour of the cell that contains point $\mathbf{x}$, regular lines can be used, otherwise, singular lines should be used to obtain better accuracy.

By using LIM, the domain integrals can be computed easily. To avoid the judgment of the position of integral points on integral lines, the definition of $f(\mathbf{y})$ can be extended to $\mathbb{R}^3$. And the domain integral in Eq.(3.4) can be transformed into the following form

$$D_1(\mathbf{x}) = \int_\Omega u^*(\mathbf{x},\mathbf{y}) B(\mathbf{y}) \mathrm{d}\Omega(\mathbf{y}) = \sum_{i=1}^{M} n_1^i(\mathbf{y}) w^i \int_{L_i} u^*(\mathbf{x},\mathbf{y}) B(\mathbf{y}) \mathrm{d}y_1 \qquad (3.10)$$

3.4 The fast multipole method accelerated LIBEM

3.4.1 The basic theorem of the FM-LIBEM

Now, considering a domain is subdivided by the oct-tree cubes and a boundary node $\mathbf{x}$ (the vector coordination) is located inside a leaf cube C_P. Two parts need to be computed for $\mathbf{x}$, the domain integrals and the boundary integrals. During the computed procedure, the domain integral is computed with the help of the FMM accelerated LIM, the boundary integrals are computed by the FMM accelerated BEM, and the result of the domain integral is added to the right vector, then the unknowns are computed by the

generalized minimal residual method (GMRES) [132, 133]. In FM-LIBEM, all the integrals are divided into two kinds for a node $\mathbf{x}$, the near integrals (integral points in cubes that are the neighbourhood of C_P and itself) and the far integrals (integral points in cubes that are in the interaction list of C_P and those well-separated from itself), the previous one is computed by the tradition LIBEM directly, while the computation of the latter one is done by the FMM.

(I) Multipole expansion of the fundamental solution

After the adaptive oct-tree is built, assume each cube leaf contains m_d line integral points, then the domain integral in Eq.(3.10) is rewritten as the following format for the cube C_P

$$D_1(\mathbf{x})=\sum_{i=1}^{M} n_1^i(\mathbf{y})\omega^i\int_{L_i} u^*(\mathbf{x},\mathbf{y})B(\mathbf{y})\mathrm{d}L_i(\mathbf{y}) \tag{3.11}$$

where $B(\mathbf{y})$ represents the body force are node $\mathbf{y}$.

As one can see in Eq.(3.11), the kernel function $u^*(\mathbf{x},\mathbf{y})$ only varies with the distance r and its derivatives. An important step of the FMM is separating the points $\mathbf{x}$ and $\mathbf{y}$ apart, see **Fig.3.5**, the spherical coordinates system, $\{\rho,\theta,\phi\}$, is centred at O, $r=\left|\overrightarrow{\mathbf{xy}}\right|$, $\overrightarrow{O\mathbf{x}}=\{\rho_1,\theta_1,\phi_1\}$ and $\overrightarrow{O\mathbf{y}}=\{\rho_2,\theta_2,\phi_2\}$. Hence, the solid harmonic functions, $R_{n,m}$ and $S_{n,m}$, are exerted and they can be written as follow[57]

$$\begin{cases} R_{n,m}\left(\overrightarrow{O\mathbf{x}}\right)=\dfrac{1}{(n+m)!}P_n^m(\cos\theta)e^{im\phi}r^n \\ S_{n,m}\left(\overrightarrow{O\mathbf{x}}\right)=(n-m)!P_n^m(\cos\theta)e^{im\phi}\dfrac{1}{r^{n+1}} \end{cases} \tag{3.12}$$

where P_n^m represents the associated Legendre function.

So the kernel $u^*(\mathbf{x},\mathbf{y})$ can be transformed into the following form for the case $\left|\overrightarrow{O\mathbf{y}}\right|<\left|\overrightarrow{O\mathbf{x}}\right|$ as[57]

$$u^*(\mathbf{x},\mathbf{y})=\frac{1}{4\pi}\sum_{n=0}^{\infty}\sum_{m=-n}^{n}\overline{S_{n,m}\left(\overrightarrow{O\mathbf{x}}\right)}R_{n,m}\left(\overrightarrow{O\mathbf{y}}\right) \tag{3.13}$$

where the superposed bar symbolizes the complex conjugate.

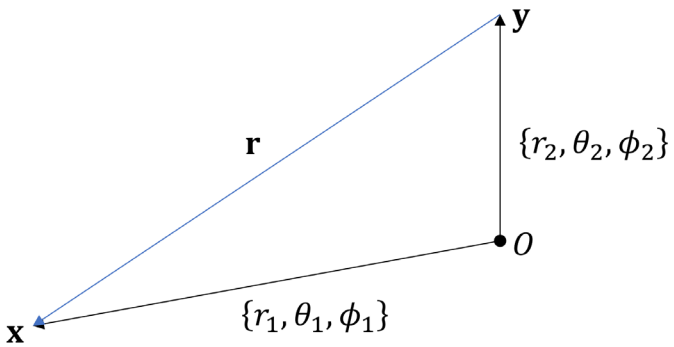

Fig.3.5 Expansion condition of spherical harmonics

(II) Multipole moments

During calculation, the degree expansion p is truncated, setting p=8~10 is enough for better accuracy and efficiency. If p is too large, the computation efficiency will be reduced. With the help of Eq.(3.13), the contribution of a random cube C_Q that is far away from C_P can be written as

$$D_1 = \frac{1}{4\pi}\sum_{n=0}^{p}\sum_{m=-n}^{n}\overline{S_{n,m}}\left(\overrightarrow{O_Q\mathbf{x}}\right)M_{n,m}\left(O_Q\right) \tag{3.14}$$

where O_Q is the centre of cube C_Q, $M_{n,m}\left(O_Q\right)$ is the multipole moments (MM) (see **Fig.3.6**) of D_1 can be expressed as

$$M_{n,m}\left(O_Q\right)=\sum_{i=1}^{m_d} n_1^i\left(\mathbf{y}\right)w^i\int_{L_i}R_{n,m}\left(\overrightarrow{O_Q\mathbf{y}}\right)B\left(O_Q\right)\mathrm{d}L_i\left(O_Q\right) \tag{3.15}$$

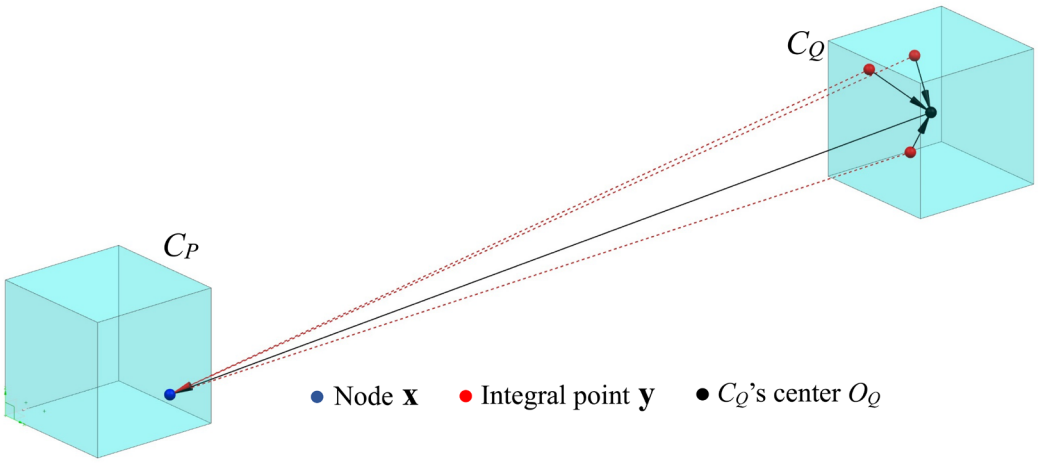

Fig.3.6 Multipole moment

(III) Multipole to multipole translation

Another translation of the FMM that needed to be derived is multipole to multipole (M2M) translation (see **Fig.3.6**), namely, computing the MM from children to their parent cube, taking cube C_Q^{parent} and C_Q as an example, on the fundamental of the property of $R_{n,m}$, expressed as the following equation

$$R_{n,m}\left(\overrightarrow{\mathbf{yx}}\right)=\sum_{n'=0}^{n}\sum_{m'=-n'}^{n'}R_{n',m'}\left(\overrightarrow{\mathbf{y}O}\right)R_{n-n',m-m'}\left(\overrightarrow{\mathbf{x}O}\right) \tag{3.16}$$

One can obtain the M2M as

$$M_{n,m}\left(O_Q^{\text{parent}}\right)=\sum_{n'=0}^{n}\sum_{m'=-n'}^{n'}R_{n',m'}\left(\overrightarrow{O_Q^{\text{parent}}O_Q}\right)M_{n-n',m-m'}\left(O_Q\right) \tag{3.17}$$

(IV) Multipole to local translation

Next, based on the property of the harmonic function $S_{n,m}$, which is expressed as the following equation

$$S_{n,m}\left(\overrightarrow{\mathbf{yx}}\right)=\sum_{n'=0}^{\infty}\sum_{m'=-n'}^{n'}\overline{R_{n',m'}}\left(\overrightarrow{O\mathbf{x}}\right)S_{n+n',m+m'}\left(\overrightarrow{O\mathbf{x}}\right),\ \left|\overrightarrow{O\mathbf{y}}\right|<\left|\overrightarrow{O\mathbf{x}}\right| \tag{3.18}$$

Eq.(3.14) is further written as

$$D_1=\frac{1}{4\pi}\sum_{n'=0}^{p}\sum_{m'=-n'}^{n'}R_{n',m'}\left(\overrightarrow{O_P\mathbf{x}}\right)L_{n',m'}\left(O_p\right) \tag{3.19}$$

where O_P is the center of cube C_P, $L_{n',m'}\left(O_p\right)$ is the local expansion at O_P, and it can be expressed as

$$L_{n',m'}\left(O_p\right)=\sum_{n=0}^{p}\sum_{m=-n}^{n}(-1)^{n'}\overline{S_{n+n',m+m'}}\left(\overrightarrow{O_QO_P}\right)M_{n,m}\left(O_Q\right) \tag{3.20}$$

Eq.(3.20) is named the multipole to local (M2L) translation, plotted as 3..3.7, and it is used for computing the contribution of a cube's interaction list. Then, the transform of the parents of cube C_P and C_Q also is necessary during the procedure of the FMM, assume the parent cube of C_P and C_Q are C_P^{parent} and C_Q^{parent} respectively, and C_Q^{parent} is a member of the interaction list of C_P^{parent}, then the M2L transformation is written as

$$L_{n',m'}\left(O_P^{\text{parent}}\right)=\sum_{n=0}^{\infty}\sum_{m=-n}^{n}(-1)^{n'}\overline{S_{n+n',m+m'}}\left(\overrightarrow{O_Q^{\text{parent}}O_P^{\text{parent}}}\right)M_{n,m}\left(O_Q^{\text{parent}}\right) \tag{3.21}$$

where O_P^{parent} and O_Q^{parent} are the centre of cube C_P^{parent} and C_Q^{parent} respectively.

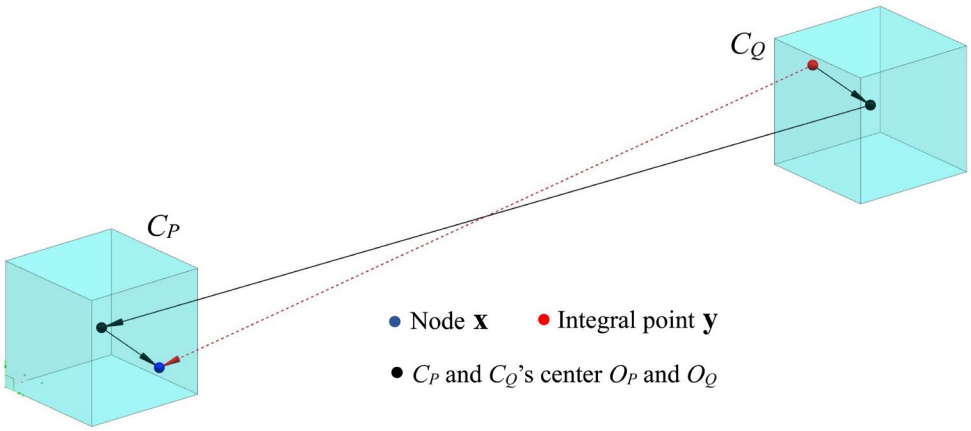

Fig.3.7 M2L translation

(V) Local to local translation

The last step of the FMM is local to local (L2L) translation (see **Fig.3.8**), i.e., transforming the MM from parent to its children, taking cube C_P^{parent} and C_P as an example, with the help of Eq.(3.16), then one can get the L2L translation as below

$$L_{n',m'}\left(O_P\right)=\sum_{n=n'}^{\infty}\sum_{m=-n}^{n}R_{n-n',m-m'}\left(\overrightarrow{O_P^{\text{parent}}O_P}\right)L_{n,m}\left(O_P^{\text{parent}}\right) \tag{3.22}$$

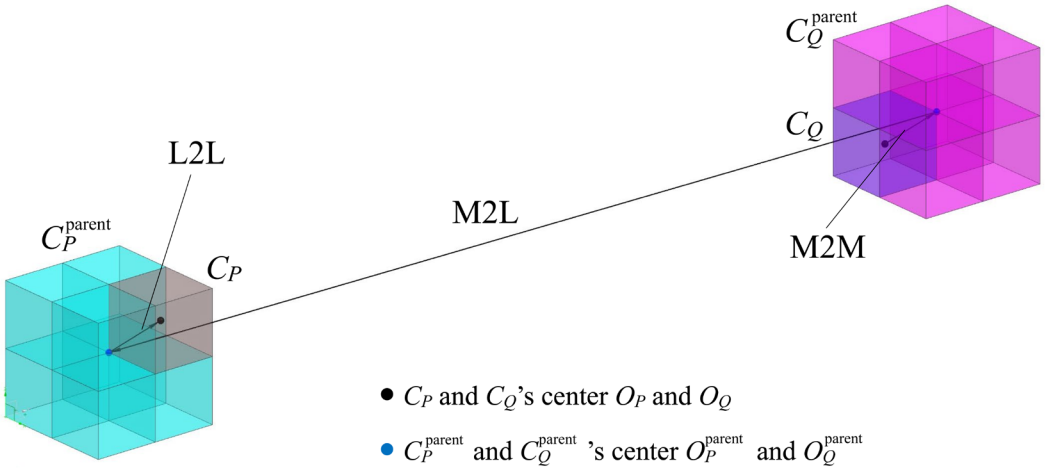

Fig.3.8 M2L, M2M, L2L translations

3.4.2 Steps of the FM-LIBEM

Step 1. Boundary discretisation.

For a given domain, its boundary is discretised into elements by the conventional BEM directly.

Step 2. Integral line creation.

An integral line needed to be created for every integral point on each boundary element, and the corresponding integral point is taken as the endpoint of the integral line. The start point is set by defining s as a constant, which can be the same value for every start point of integral lines for simplicity. Then two kinds of integrals exist for each boundary node $\mathbf{x}$, the regular and singular integral lines. The latter ones are transformed into regular forms by coordination translation.

Step 3. Adaptive oct-tree structure construction and sub-integral line creation.

The procedure for oct-tree structure construction is introduced in **Section**

3.3.2.1, after that, the integral lines are divided into sub-lines with the help of sub-cubes created by the oct-tree.

Step 4. Near integral computation.

For the line integrals transformed from domain integrals, the integrals inside the neighbourhood of a random point **x** are computed directly by the traditional BEM and LIM respectively.

Step 5. Upward pass.

During the upward process, the upward order for computing MM is from the smallest level to level 2. The MM is calculated by Eq.(3.15) for each leaf cube firstly, then via the M2M translation, i.e., Eq.(3.17), the MM of those cubes having children is computed.

Step 6. Downward pass.

In the downward pass, two parts are necessary to consider for calculating the local expansion.

(1) The M2L translation at each level is applied to evaluate the local expansion for a sub-cube from its interaction list by Eq.(3.21).

(2) The second part is calculating the local expansion for the sub-cubes from their parent cube by L2L translation, namely, Eq.(3.22).

Step 7. Far integral computation.

By computing Eq.(3.20), the far integrals are obtained, then add the result of far integrals with the result of near integrals gotten from **Step 4** up.

3.5 Numerical examples

The degree expansion p for the FM-LIBEM is set as 10 in this part. And all the numerical models are computed by a computer assembled with a 2.6 GHz CPU and 32.0 GB of RAM.

To verify the convergence of BEM, the following error calculation formula is introduced to calculate relative errors.

$$R\text{-}Error = \sqrt{\left(\sum_{i=1}^{N}\left(u_i^e - u_i^n\right)^2\right) \Big/ \left(\sum_{i=1}^{N}\left(u_i^e\right)^2\right)} \tag{3.23}$$

where u_i^e and u_i^n are the analytical and numerical results respectively, N

denotes the number of sample points.

3.5.1 A cube with heat sources

This numerical example is the heat conduction analysis of a cube containing a heat source. See **Fig.3.9**, the cube is centered at {2, 2, 2} and bounded by planes {x=0}, {x=4}, {y=0}, {y=4}, {z=0} and {z=4}. The temperature at boundary planes, {z=0} and {z=4} are 0, while the heat flux of the rest boundaries is set to 0. Besides, the value of thermal conductivity is set to 1 W/(m•K). And the expression of heat source is listed as follows

$$B(z)=2e^{-z} \tag{3.24}$$

Hence one can obtain the analytical solution of temperature as the following equation[76]

$$\theta=\frac{1}{2k}\left[4\left(1-e^{-z}\right)-z\left(1-e^{-4}\right)\right] \tag{3.25}$$

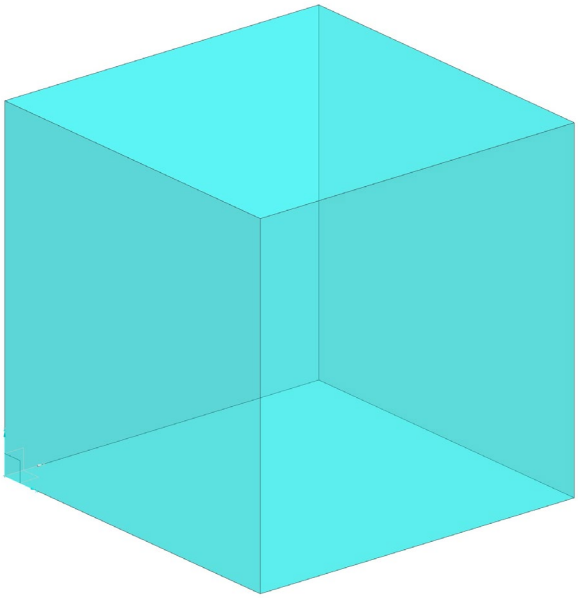

Fig.3.9 The cube model

To prove the developed method is useful for the heat conduction analysis considering the heat source, results of the FM-LIBEM are compared with the analytical result which is expressed as Eq.(3.25). Obviously, the temperature is only related to x-axial, thereby nine internal points are picked for comparison, namely, {2, 2, 0.4}, {2, 2, 0.8}, {2, 2, 1.2}, {2, 2, 1.6}, {2, 2, 2.0}, {2, 2, 2.4}, {2, 2, 2.8}, {2, 2, 3.2}, {2, 2, 3.6}. Besides, in this case, the boundaries of the cube are discretised with 2112 elements. As one can see in **Table 3.1**, the temperature

result of the FM-LIBEM and LIBEM are listed and compared with the analytical results, both of them can present results with high accuracy. In addition, the relative error of the FM-LIBEM and LIBEM is 0.0708% and 0.069% respectively, which means the accuracy of the FM-LIBEM and LIBEM are at the same level.

Besides, to show the convergence of the LIBEM and FM-LIBEM, several boundary discretisation cases are taken for the cube. As **Fig.3.10** plotted, the relative errors of the FM-LIBEM and LIBEM are at the same level and perform great in convergence for cases (a) to (g). While, when it comes to the last two cases with 77460 elements and 120808 elements respectively, the necessary computation demand of the LIBEM is beyond the computation ability, which is still enough for the FM-LIBEM however.

Table 3.1 Result comparison of selected points

Selected points	Temperature (°C)		
	FM-LIBEM	LIBEM	Analytical Results
{2, 2, 0.4}	0.4626	0.4626	0.4630
{2, 2, 0.8}	0.7077	0.7077	0.7087
{2, 2, 1.2}	0.8080	0.8080	0.8086
{2, 2, 1.6}	0.8105	0.8106	0.8109
{2, 2, 2.0}	0.7475	0.7475	0.7476
{2, 2, 2.4}	0.6406	0.6406	0.6405
{2, 2, 2.8}	0.5042	0.5042	0.5040
{2, 2, 3.2}	0.3479	0.3479	0.3478
{2, 2, 3.6}	0.1784	0.1785	0.1783
Relative Error	0.0708%	0.069%	

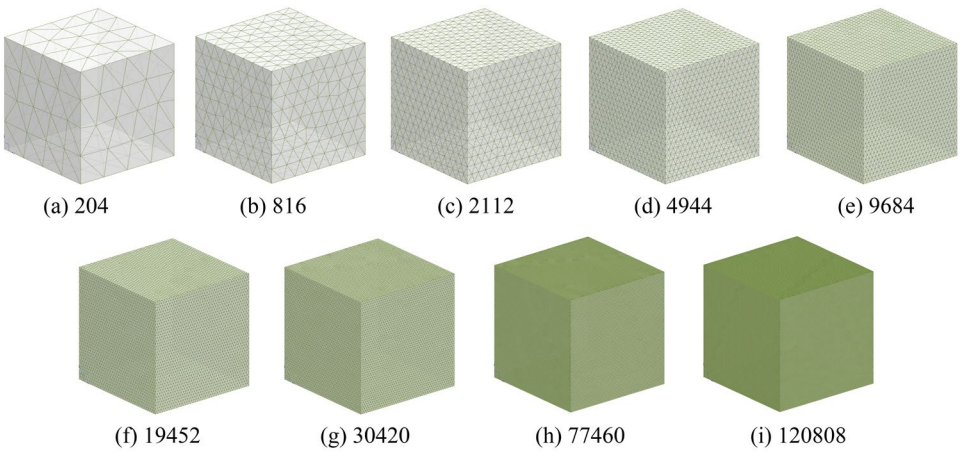

Fig.3.10 The discretised cubes with boundary elements

Further, another key advantage, i.e., the high computational efficiency, of the FM-LIBEM is testified by comparing it to the LIBEM. According to **Fig.3.11**, the computational time of FM-LIBEM is at the same level compared to the LIBEM before the element number reaches about 5000, then the computational time of LIBEM rises sharply with the increase of the element number, while the growth trend of the FM-LIBM is much slower. In addition, when the model is discretised with about 30000 elements, the computing time of FM-LIBM is about 6% of that of LIBEM. Hence, the computational efficiency of FM-LIBEM is much higher than LIBEM.

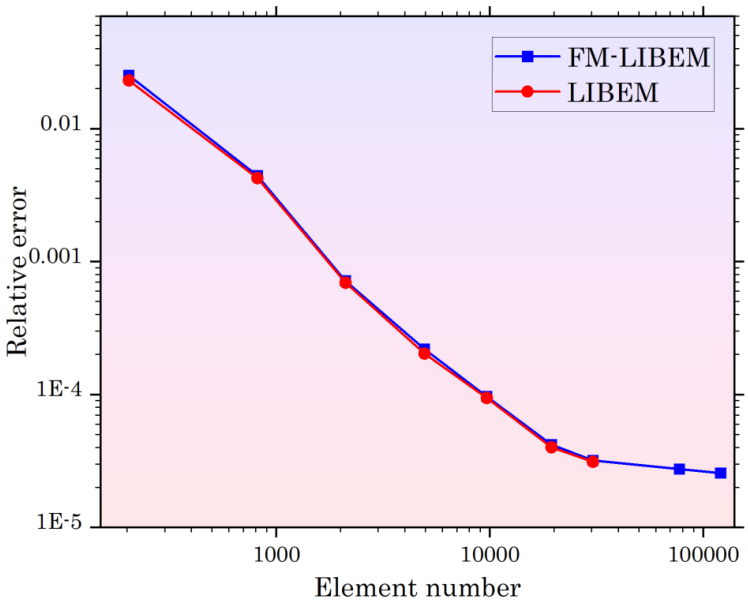

Fig.3.11 Relative errors of the cube in different cases

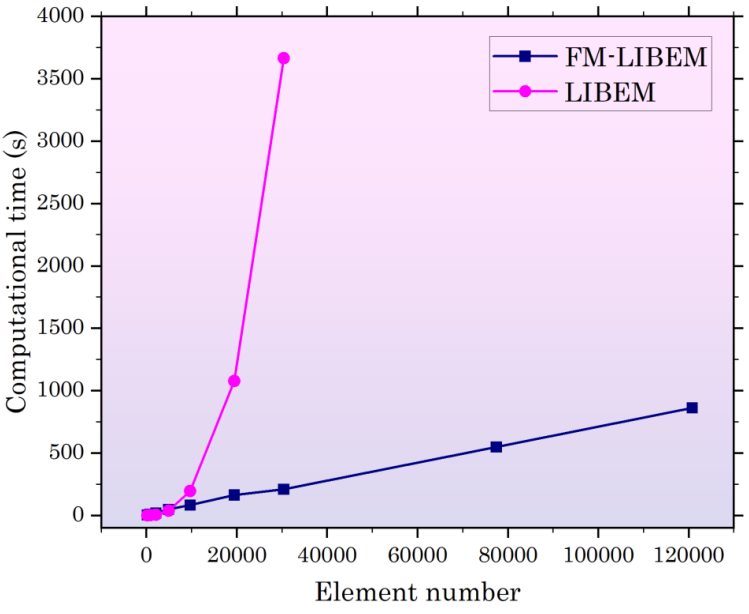

Fig.3.12 Comparison of computational time

3.5.2 A ring flange with heat sources

As one can see in **Fig.3.13**, this ring flange model centres at {0, 0, -2.5} with eight evenly distributed cylindrical holes which is very common in engineering structures, and it is much more complicated than the previous one, the top and bottom faces are planes {z=0} and {z=5}, the rest of the geometrical information can be found in **Fig.3.14** As to the boundary conditions, this model is defined as thermally insulated and the temperature is set to $0\,^{\circ}C$. Besides, the value of thermal conductivity is set to 10 W/(m•K). And the formula for the heat source is displayed below

$$B(z)=10\left[z^2+\sin(z)\right] \tag{3.26}$$

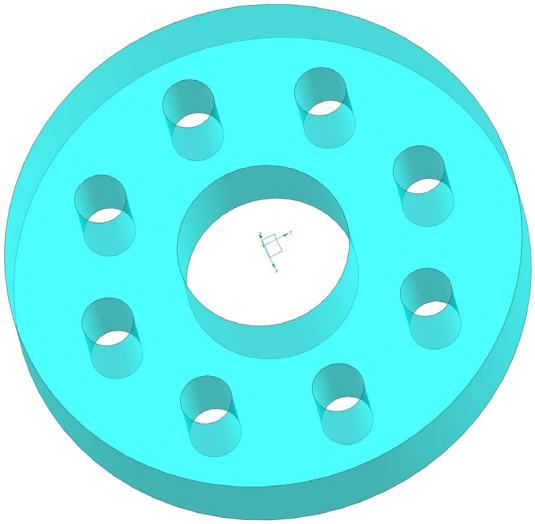

Fig.3.13 The ring flange model

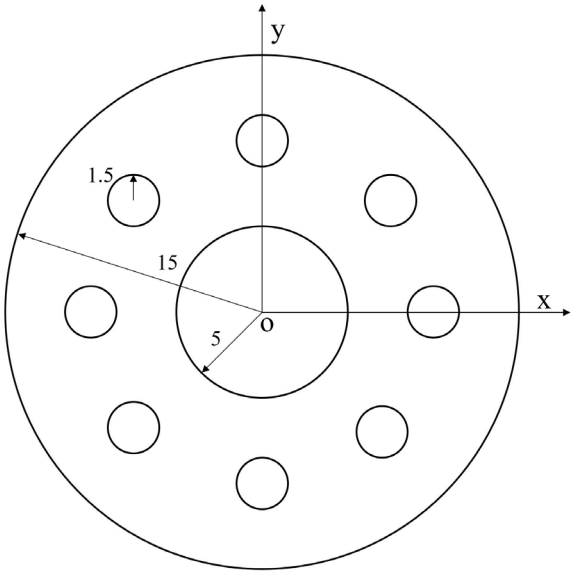

Fig.3.14 Geometry of the ring flange

As there is no analytical solution for this analysis model, the FEM simulation results are taken as a comparison and the FEM model is discretised into 449025 elements. To show the accuracy of the FM-LIBEM, the boundary of this model is discretised into 4806 elements, and 12 points on the line $\{x = 7.5; y = 0.0\}$ are selected for comparison, detailed information can be found in **Table 3.2**. Apparently, the result of the LIBEM and the FM-LIBEM are in high consistency with that of the FEM.

Table 3.2 Result comparison of selected points

Selected points	Temperature (^{o}C)		
	FM-LIBEM	LIBEM	FEM
{7.5, 0, 0.4}	1.5485	1.5481	1.5517
{7.5, 0, 0.8}	3.1703	3.1701	3.1376
{7.5, 0, 1.2}	4.8154	4.8153	4.7590
{7.5, 0, 1.6}	6.4650	6.4651	6.3864
{7.5, 0, 2.0}	8.0580	8.0581	7.9671
{7.5, 0, 2.4}	9.3743	9.3747	9.4193
{7.5, 0, 2.8}	10.7548	10.7547	10.6267
{7.5, 0, 3.2}	11.5355	11.5354	11.4193
{7.5, 0, 3.6}	11.7214	11.7215	11.5507
{7.5, 0, 4.0}	10.8565	10.8568	10.6623
{7.5, 0, 4.4}	8.4153	8.4158	8.2336
{7.5, 0, 4.8}	3.5964	3.5954	3.5183

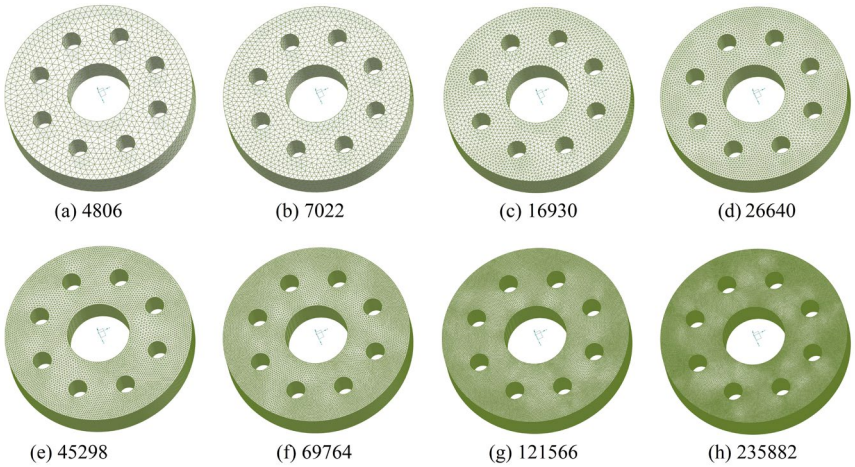

Fig.3.15 The discretised ring flange with boundary elements

Further, to testify the convergence of the FM-LIBEM when it comes to a complex model, the ring flange is discretised into boundary elements in different numbers showing as **Fig.3.15**, two approaches are taken for

convergence analysis, the first one is plotting the relative errors computed by taken the FEM result (discretised by 405314 elements) as a comparison, the second approach is computing the relative errors by taking the next discretisation model as a comparison, for example, for the case, discretised model with 4806 elements, the result of the next case, discretised model with 7022 elements, is the comparison. According to **Fig.3.16**, both the two approaches prove that the FM-LIBEM performs great in convergence.

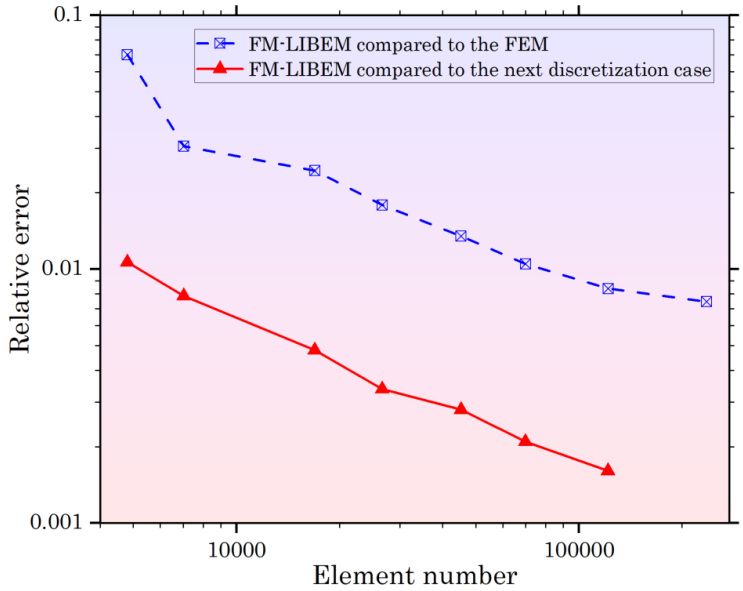

Fig.3.16 Relative errors of the ring flange in different cases

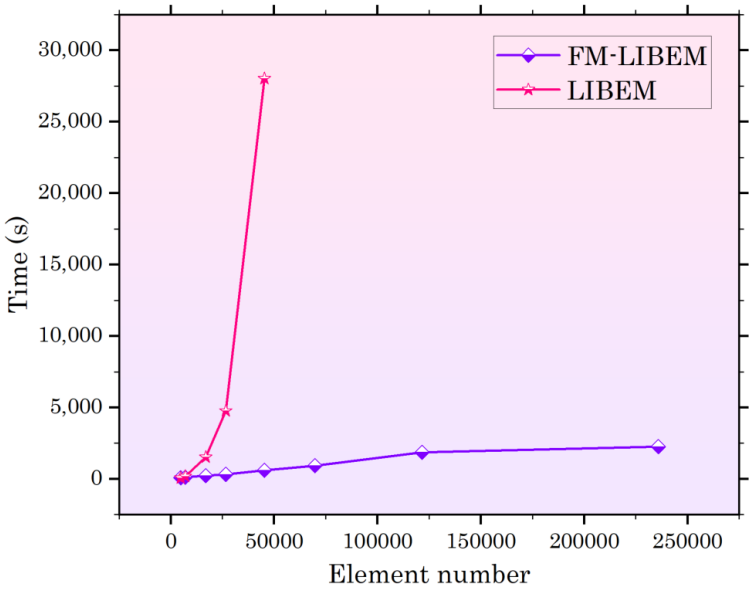

Fig.3.17 Comparison of computational time

Besides, the most important ability of the FM-LIBEM, the computation efficiency, needs to be validated. As **Fig.3.17** shows, the computational time of

the FM-LIBEM is at the same level compared to the LIBEM at first, then the computational time of the LIBEM rises sharply and the cases with more than about 50000 elements are beyond the computation capacity of the computer. While the growth trend of the FM-LIBM is much slower. And for the last case, the discretised model with 235882 elements, the computation time of the FM-LIBEM is 2261 seconds which is only enough for a discretised model with about 18000 elements if computed by LIBEM according to **Fig.3.17**. In addition, when the model is discretised with 45298 elements, the computing time of FM-LIBM is about 2% of that of LIBEM. Hence, the computational efficiency of the FM-LIBEM is still much better than the LIBEM, i.e., the FM-LIBEM is more powerful when it comes to complex models on a large scale.

3.5.3 A cube containing holes with heat sources

As one can see in **Fig.3.18**, centered at {0, 0, 0} and bounded by planes {x=±50}, {y=±50}, {z=±50}, this model is a cube containing eight evenly distributed spherical holes, and its side length is 100, the centers of the eight spherical holes are {25, 25, 25}, {25, -25, 25}, {-25, -25, 25}, {-25, -25, 25}, {25, 25, -25}, {25, -25, -25}, {-25, -25, -25} and {-25, -25, -25}, and their radius is 12.5. As to the boundary conditions, the temperature of this model is set as 0 ^{o}C. In addition, the value of thermal conductivity is 5 W/(m•K). The expression of heat source is set as

$$B(z)=\sin\left[\frac{(z-50)}{50}\right] \tag{3.27}$$

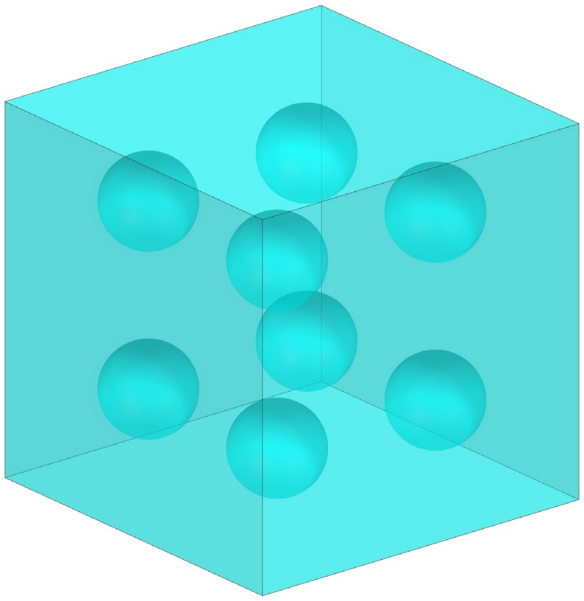

Fig.3.18 The cube with holes

For this model without analytic results, the FEM results are introduced as a comparison and the FEM model is discretised into 385629 elements. To show the accuracy of the FM-LIBEM, the boundary of this model is discretised into 5050 elements, and 41 points evenly distributed on the line {x=50; y=50} with two endpoints, {50,50,-48} and {50,50,148}, are selected for comparison. According to **Fig.3.19**, the results of the LIBEM and the FM-LIBEM are highly consistent with that of the FEM.

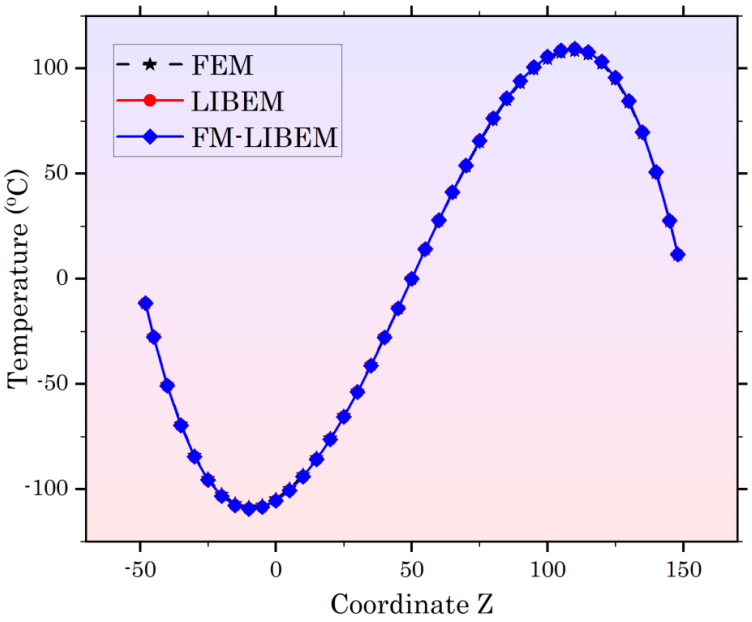

Fig.3.19 Result comparison of selected points

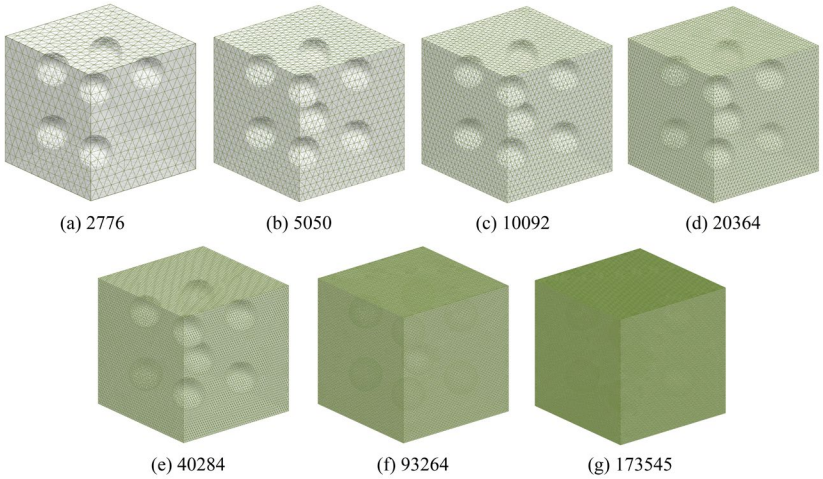

Fig.3.20 The cube with holes discretised with boundary elements

Further, the capacity of the FM-LIBEM and the computation efficiency are validated next. As **Fig.3.20** shows, from 2776 elements to 173545 elements, the model is discretised into elements in different numbers. As **Fig.3.21** plotted, the computational time of the FM-LIBEM is at the same level compared to the LIBEM in the first three cases generally, then the computational time of the LIBEM rises sharply, and in the last two cases with 93264 and 173545 elements respectively are out of the computation capacity of the computer. In contrast, the growth trend of the FM-LIBM is slower. So, this complex model also proves that the computational efficiency of the FM-LIBEM is much better than that of LIBEM.

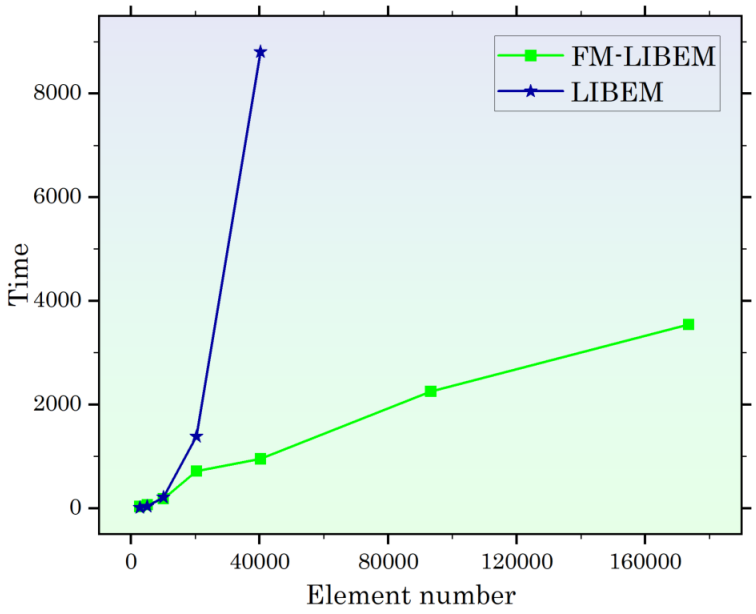

Fig.3.21 Comparison of computational time

Appendix

Theorem 3.1. Suppose Ω is a bounded domain in $\mathbb{R}^3$ with Lipschitz boundary Γ. Assume $f(\mathbf{y})$ is a continuous function defined on the compact $\overline{\Omega}$ and let $g(\mathbf{y})$ be a continuation of $f(\mathbf{y})$ in any box B which containing $\overline{\Omega}$ such that $g(\mathbf{y})$ is bounded and almost everywhere continuous in $B\setminus\overline{\Omega}$. Then for any point $\mathbf{y}\{y_1,y_2,y_3\}\in\overline{\Omega}$, consider the following function

$$F\left(\mathbf{y}\{y_1,y_2,y_3\}\right)=\int_a^{y_1} g\left(\mathbf{t}\{t,y_2,y_3\}\right)\mathrm{d}t,\quad \mathbf{y}\{y_1,y_2,y_3\}\in\overline{\Omega} \tag{3.28}$$

where the value of function $a=a\{y_2,y_3\}$ is finite, $\mathbf{t}\{t,y_2,y_3\}$ is in B. Then vector field can be expressed as

$$\mathbf{F}(\mathbf{y})=F(\mathbf{y})\mathbf{e}_1,\quad \mathbf{y}\in\overline{\Omega} \tag{3.29}$$

which is continuously differentiable with respect to y_1 in $\overline{\Omega}$, where $\mathbf{e}_i$ is the fixed unit basis vector in Cartesian direction, $\mathbf{e}_1=\{1,0,0\}$, and

$$\nabla\cdot\mathbf{F}(\mathbf{y})=f(\mathbf{y}),\quad \mathbf{y}\in\overline{\Omega} \tag{3.30}$$

Poof. Because domain Ω is a bounded domain in $\mathbb{R}^3$, an arbitrary rectangle box B that contains $\overline{\Omega}$ can always be found. Assume the point $\mathbf{y}^0\{a,y_2,y_3\}$ is in box B. Without loss of generality, the prescribed function $f(\mathbf{y})$ can be extended to B and

$$g(\mathbf{y})=\begin{cases} f(\mathbf{y}), & \mathbf{y}\in\overline{\Omega}\\ \chi(\mathbf{y}), & \mathbf{y}\in B\setminus\overline{\Omega}\end{cases} \tag{3.31}$$

where $\chi(\mathbf{y})$ can be any function that is bounded and almost everywhere continuous in $B\setminus\overline{\Omega}$. With the assumption that $f(\mathbf{y})$ is continuous on $\overline{\Omega}$, it follows that $g(\mathbf{y})$ is bounded and almost everywhere continuous in B. This statement implies that $g(\mathbf{y})$ is Riemann integrable in box B. Then functions (3.28) and (3.29) are well defined in B as

$$F\left(\mathbf{y}\{y_1,y_2,y_3\}\right)=\int_a^{y_1} g\left(\mathbf{t}\{t,y_2,y_3\}\right)\mathrm{d}t,\quad \mathbf{y}\{y_1,y_2,y_3\}\in B \tag{3.32}$$

$$\mathbf{F}(\mathbf{y})=F(\mathbf{y})\mathbf{e}_1,\quad \mathbf{y}\in B \tag{3.33}$$

In fact, $F(\mathbf{y})$ is Lipschitz-continuous with respect to y_1 in B and this assertion can be obtained from the following estimate

$$\left|F\left(\mathbf{y}\{y_1+\Delta y_1,y_2,y_3\}\right)-F\left(\mathbf{y}\{y_1,y_2,y_3\}\right)\right|=\left|\int_{y_1}^{y_1+\Delta y_1} g\left(\mathbf{t}\{t,y_2,y_3\}\right)\mathrm{d}t\right| \tag{3.34}$$

and

$$\left|\int_{y_1}^{y_1+\Delta y_1} g\left(\mathbf{t}\{t, y_2, y_3\}\right)\mathrm{d}t\right| \le \Delta y_1 \left\|g_{y_1}\right\|_\infty \tag{3.35}$$

where points $\{y_1+\Delta y_1, y_2, y_3\}$, $\{y_1, y_2, y_3\} \in B$ and

$$\left\|g_{y_1}\right\|_\infty = \sup_{\{y_1, y_2, y_3\}\in B}\left|g\left(\mathbf{y}\{y_1, y_2, y_3\}\right)\right| \tag{3.36}$$

It follows that $F(\mathbf{y})$ is almost everywhere differentiable concerning y_1 on B with

$$\frac{\mathrm{d}F(\mathbf{y})}{\mathrm{d}y_1} = g(\mathbf{y}), \quad \textit{almost everywhere on } B \tag{3.37}$$

In other words, $F(\mathbf{y})$ is differentiable for y_1 on B except on a subset of $B\setminus\bar{\Omega}$ with Lebesgue measure zero, where $g(\mathbf{y})$ has a finite jump. If let point $\mathbf{y}\in\bar{\Omega}$, one can infer that $F(\mathbf{y})$ is continuously differentiable concerning y_1 on $\bar{\Omega}$ and

$$\frac{\mathrm{d}F(\mathbf{y})}{\mathrm{d}y_1} = f(\mathbf{y}), \quad \mathbf{y}\in\bar{\Omega} \tag{3.38}$$

From Eq.(3.33), one can also infer that $\mathbf{F}\left(\mathbf{y}\{y_1, y_2, y_3\}\right)$ is continuous for y_1 in B and

$$\frac{\mathrm{d}\mathbf{F}(\mathbf{y})}{\mathrm{d}y_1} = \frac{\mathrm{d}F(\mathbf{y})}{\mathrm{d}y_1}\mathbf{e}_1, \quad \mathbf{y}\in B \tag{3.39}$$

And the divergence of $\mathbf{F}(\mathbf{y})$ can be written as

$$\nabla\cdot\mathbf{F}(\mathbf{y}) = \frac{\partial F(\mathbf{y})}{\partial y_1}, \quad \mathbf{y}\in B \tag{3.40}$$

Using Eq.(3.37), Eqs.(3.39) and (3.40) can be rewritten as

$$\frac{\mathrm{d}\mathbf{F}(\mathbf{y})}{\mathrm{d}y_1} = g(\mathbf{y})\mathbf{e}_1, \quad \textit{almost everywhere on } B \tag{3.41}$$

$$\nabla\cdot\mathbf{F}(\mathbf{y}) = g(\mathbf{y}), \quad \textit{almost everywhere on } B \tag{3.42}$$

From Eq.(3.41), one can infer that vector field $\mathbf{F}(\mathbf{y})$ is continuously differentiable with respect to y_1 on B except on subset of $B\setminus\bar{\Omega}$ with Lebesgue measure zero, where $g(\mathbf{y})$ has a finite jump. And from Eq.(3.42), one can further infer that the divergence of vector field $\mathbf{F}(\mathbf{y})$ is continuous for $\mathbf{y}$ almost everywhere on B except for the subset of $B\setminus\bar{\Omega}$ with Lebesgue measure zero. From these statements and letting $\mathbf{y}\in\bar{\Omega}$, it follows that $\mathbf{F}(\mathbf{y})$ is continuous with respect to y_1 and continuously differentiable for y_1. Then,

$$\frac{\mathrm{d}\mathbf{F}(\mathbf{y})}{\mathrm{d}y_1} = f(\mathbf{y})\mathbf{e}_1, \quad \mathbf{y}\in\bar{\Omega} \tag{3.43}$$

Similarly, the divergence of $\mathbf{F}(\mathbf{y})$ in $\bar{\Omega}$ can be obtained as

$$\nabla \cdot \mathbf{F}(\mathbf{y}) = f(\mathbf{y}), \quad \mathbf{y} \in \bar{\Omega} \tag{3.44}$$

Then the proof of theorem 3.1 is completed.

Remark 1. The integral in Eq.(3.28) is on a straight line $\mathbf{L}\{y_2, y_3\}$ from the start point $\mathbf{y}^0\{a(y_2, y_3), y_2, y_3\}$ to the target point $\mathbf{y}\{y_1, y_2, y_3\} \in \bar{\Omega}$. The start point $\mathbf{y}^0$ is an arbitrary point on the line but should be the same for any target point $\mathbf{y}$ on the same line, in other words, once the start point $\mathbf{y}^0$ is specified for a target point $\mathbf{y}$, all the other target points on that line should use the same start point $\mathbf{y}^0$ (see **Fig.3.21**). This condition should be satisfied for a simply connected convex region and it can also be applied in multiply connected regions and non-convex regions. However, for a multiply connected region or a non-convex region, this condition is not mandatory since one can always subdivide a multiply connected region or non-convex region into simply connected convex regions (see **Fig.3.22**).

Remark 2. The location of the start point $\mathbf{y}^0$ for a line $\mathbf{L}$ is arbitrary, it can be inside or outside the domain or on the boundary (see **Figs.3.22** and **3.23**).

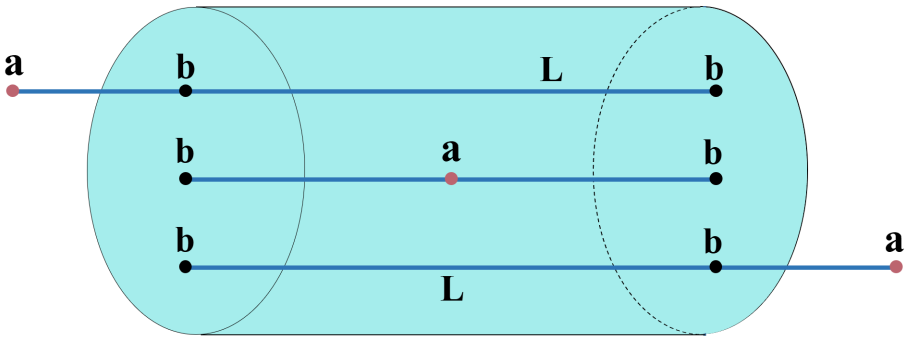

● Start point ● Target point

Fig.3.22 Start point of an integral line

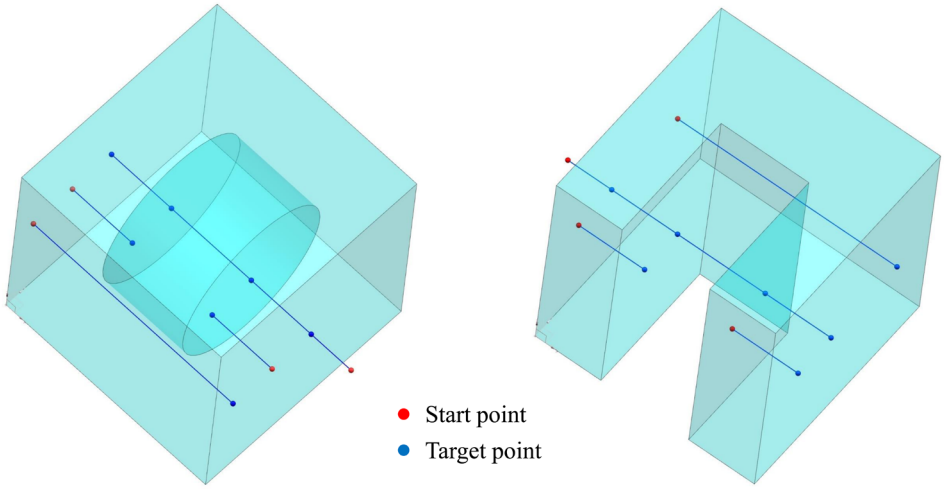

(a) Multi-connected region (b) Non-convex region

Fig.3.23 Integral lines in non-convex and multiply-connected region

Theorem 3.2 Suppose Ω is a bounded domain in $\mathbb{R}^3$ with Lipschitz boundary Γ. Assume $f(\mathbf{y})$ is a continuous function defined on the compact $\bar{\Omega}$ and let $g(\mathbf{y})$ be a continuation of $f(\mathbf{y})$ in any box B which containing $\bar{\Omega}$ and such that $g(\mathbf{y})$ is bounded and almost everywhere continuous in $B\setminus\bar{\Omega}$. Then for any point $\mathbf{y}\{y_1,y_2,y_3\}\in\bar{\Omega}$, consider the following function

$$F\left(\mathbf{y}\{y_1,y_2,y_3\}\right)=\int_a^{y_1} g\left(\mathbf{t}\{t,y_2,y_3\}\right)\mathrm{d}t,\quad \mathbf{y}\{y_1,y_2,y_3\}\in\bar{\Omega} \tag{3.45}$$

where the value of function $a=a\{y_2,y_3\}$ is finite, $\mathbf{t}\{t,y_2,y_3\}$ is in B, then

$$\int_\Omega f(\mathbf{y})\mathrm{d}\Omega(\mathbf{y})=\oint_\Gamma F(\mathbf{y})n_1(\mathbf{y})\mathrm{d}\Gamma(\mathbf{y}) \tag{3.46}$$

where n_1 is the component of the unit outward normal $\mathbf{n}$ on Γ at direction of y_1-axis.

Proof. From Theorem 3.1, one can infer that there exists a vector field $\mathbf{F}(\mathbf{y})$ in $\bar{\Omega}$ expressed as Eq.(3.29) such that it satisfies Eq.(3.30). Thus, by applying the divergence theorem and using Eq.(3.45), one can obtain Eq.(3.29) directly.

By using Theorem 3.2, the domain integrals with the continue function $f(\mathbf{y})$ can be translated into boundary integrals by Eq.(3.46). Similar results can be obtained for domain integrals with weakly-singular kernels. Kernel $k(\mathbf{x},\mathbf{y})$ is said to be weakly singular in Ω if it is defined and continuous for all $\mathbf{x},\mathbf{y}\in\Omega$, $\mathbf{x}\neq\mathbf{y}$, and there exists a positive constant C_1 such that

$$|k(\mathbf{x},\mathbf{y})|\le C_1 r^{-\beta},\quad 0\le\beta<3 \tag{3.47}$$

for all $\mathbf{x},\mathbf{y}\in\Omega$, $\mathbf{x}\neq\mathbf{y}$, where $r=|\mathbf{x}-\mathbf{y}|$.

Theorem 3.3. Suppose Ω is a bounded domain in $\mathbb{R}^3$ with Lipschitz boundary Γ. Assume $f(\mathbf{y})$ is a continuous function defined on the compact $\bar{\Omega}$ and let $g(\mathbf{y})$ be a continuation of $f(\mathbf{y})$ in any box B which containing $\bar{\Omega}$ and such that $g(\mathbf{y})$ is bounded and almost everywhere continuous in $B\setminus\bar{\Omega}$. Let point $\mathbf{x}$ be a fixed point in $\mathbb{R}^3$ and function $k(\mathbf{x},\mathbf{y})$ be a weakly singular kernel centred at point $\mathbf{x}$ in box B. Then for any point $\mathbf{y}\{y_1,y_2,y_3\}\in\bar{\Omega}$, consider the following function

$$F\left(\mathbf{x},\mathbf{y}\{y_1,y_2,y_3\}\right)=\int_a^{y_1} g\left(\mathbf{t}\{t,y_2,y_3\}\right)k\left(\mathbf{x},\mathbf{t}\{t,y_2,y_3\}\right)\mathrm{d}t,\quad \mathbf{y}\{y_1,y_2,y_3\}\in\bar{\Omega} \tag{3.48}$$

where the value of function $a=a\{y_2,y_3\}$ is finite, $\mathbf{t}\{t,y_2,y_3\}$ is in B, then

$$\int_\Omega f(\mathbf{y})k(\mathbf{x},\mathbf{y})\mathrm{d}\Omega(\mathbf{y})=\oint_\Gamma F(\mathbf{x},\mathbf{y})n_1(\mathbf{y})\mathrm{d}\Gamma(\mathbf{y}) \tag{3.49}$$

where n_1 is the component of the unit outward normal $\mathbf{n}$ on Γ at direction of y_1-axis.

Proof. From the assumption of the theorem, $g(\mathbf{y})$ is bounded and almost everywhere continuous in box B and one can introduce a quantity as

$$\|g\|_\infty=\sup_{\mathbf{y}\in B}|g(\mathbf{y})| \tag{3.50}$$

Then one can estimate Eq.(3.48) as

$$|F(\mathbf{x},\mathbf{y})|\le C_1\|g\|_\infty\int_a^{y_1} r_t^{-\beta}\mathrm{d}t,\quad \mathbf{y}\{y_1,y_2,y_3\}\in B \tag{3.51}$$

where C_1 is a positive constant and $r_t=|\mathbf{x}-\mathbf{t}|$, $0\le\beta<3$.

The weakly singular integral can be written as

$$\int_\Omega f(\mathbf{y})k(\mathbf{x},\mathbf{y})\mathrm{d}\Omega(\mathbf{y})=\int_{\Omega\setminus\Omega_\varepsilon} f(\mathbf{y})k(\mathbf{x},\mathbf{y})\mathrm{d}\Omega(\mathbf{y})+\int_{\Omega_\varepsilon} f(\mathbf{y})k(\mathbf{x},\mathbf{y})\mathrm{d}\Omega(\mathbf{y}) \tag{3.52}$$

where Ω_ε is a small ball centred at singular point $\mathbf{x}$ (see **Fig.3.24** (a)).

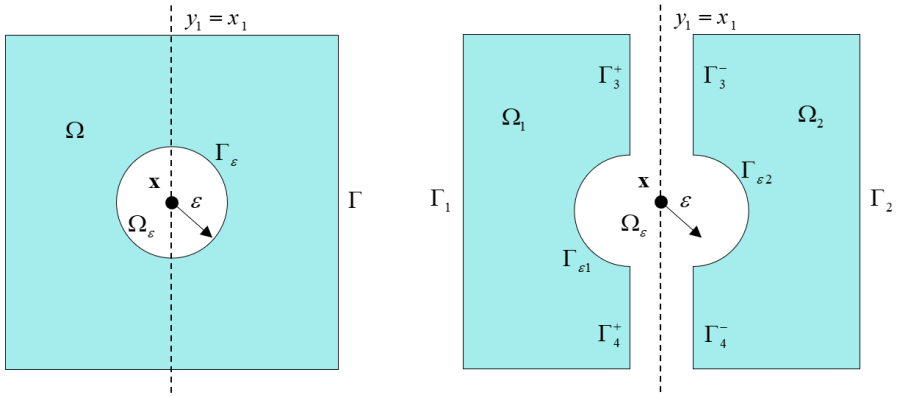

(a) Weakly-singular integration at $\mathbf{x}$ (b) Subdivide the region at $\mathbf{x}$

Fig.3.24 Weakly singular integral

To compute the first part in Eq.(3.52), one can divide the integrated region

into two sub-regions by plane $\{y_1 = x_1\}$ as shown in **Fig.3.24** (b). Then

$$\int_{\Omega\setminus\Omega_\varepsilon} f(\mathbf{y})k(\mathbf{x},\mathbf{y})\mathrm{d}\Omega = \int_{\Omega 1} f(\mathbf{y})k(\mathbf{x},\mathbf{y})\mathrm{d}\Omega(\mathbf{y}) + \int_{\Omega 2} f(\mathbf{y})k(\mathbf{x},\mathbf{y})\mathrm{d}\Omega(\mathbf{y}) \quad (3.53)$$

where $\Omega\setminus\Omega_\varepsilon = \Omega_1 \bigcup \Omega_2$. The integrals for region Ω_1 and Ω_2 have no singularity and one can have the following equation by applying Theorem 3.2.

$$\begin{aligned}&\int_{\Omega 1} f(\mathbf{y})k(\mathbf{x},\mathbf{y})\mathrm{d}\Omega(\mathbf{y}) = \int_{\Gamma_1} F(\mathbf{x},\mathbf{y})n_1(\mathbf{y})\mathrm{d}\Gamma(\mathbf{y})\\ &+\int_{\Gamma_3^+ + \Gamma_4^+} F(\mathbf{x},\mathbf{y})n_1(\mathbf{y})\mathrm{d}\Gamma(\mathbf{y}) + \int_{\Gamma_{\varepsilon 1}} F(\mathbf{x},\mathbf{y})n_1(\mathbf{y})\mathrm{d}\Gamma(\mathbf{y})\end{aligned} \quad (3.54)$$

From Eq.(3.51), the last integral in Eq.(3.54) has

$$\left|\int_{\Gamma_{\varepsilon 1}} F(\mathbf{x},\mathbf{y})n_1(\mathbf{y})\mathrm{d}\Gamma(\mathbf{y})\right| \le C_1 \|g\|_\infty \int_{\Gamma_{\varepsilon 1}} n_1(\mathbf{y}) \int_a^{y_1} r_t^{-\beta}\mathrm{d}t\mathrm{d}\Gamma(\mathbf{y}), \quad \mathbf{y}\{y_1,y_2,y_3\} \in B \quad (3.55)$$

If the start points $\mathbf{y}^0\{a,y_2,y_3\}$ of the integral lines for $\Gamma_{\varepsilon 1}$ satisfy $a < y_1$, where points $\mathbf{y}\{y_1,y_2,y_3\}$ are on $\Gamma_{\varepsilon 1}$, then

$$\int_a^{y_1} r_t^{-\beta}\mathrm{d}t = -\int_{r_1}^{\varepsilon} \frac{r_t^{1-\beta}}{\sqrt{r_t^2 - (y_2-x_2)^2 - (y_3-x_3)^2}}\mathrm{d}r_t, \quad \mathbf{y}\{y_1,y_2,y_3\} \in \Gamma_{\varepsilon 1} \quad (3.56)$$

where

$$\varepsilon = |\mathbf{x}-\mathbf{y}| \quad (3.57)$$

$$r_1 = |\mathbf{x}-\mathbf{y}^0| \quad (3.58)$$

The integrated function in Eq.(3.56) is also a weakly singular kernel and there exists a positive constant C_2 such that

$$\left|\frac{r_t^{1-\beta}}{\sqrt{r_t^2 - (y_2-x_2)^2 - (y_3-x_3)^2}}\right| \le C_2 r_t^{-\beta}, \quad 0 \le \beta < 3 \quad (3.59)$$

Then from Eq.(3.56), one can have

$$\left|\int_a^{y_1} r_t^{-\beta}\mathrm{d}t\right| \le C_2 \left|\int_{r_1}^{\varepsilon} r_t^{-\beta}\mathrm{d}r_t\right| = C_2 \left|\frac{\varepsilon^{1-\beta} - r_1^{1-\beta}}{1-\beta}\right|, \quad \mathbf{y}\{y_1,y_2,y_3\} \in \Gamma_{\varepsilon 1} \quad (3.60)$$

Then the last integral in Eq.(3.54) has

$$\left|\int_{\Gamma_{\varepsilon 1}} F(\mathbf{x},\mathbf{y})n_1(\mathbf{y})\mathrm{d}\Gamma(\mathbf{y})\right| \le C_1 C_2 \|g\|_\infty \int_0^\pi \int_0^\pi \varepsilon^2 n_1 \left|\frac{\varepsilon^{1-\beta} - r_1^{1-\beta}}{1-\beta}\right| \sin\theta \mathrm{d}\theta\mathrm{d}\varphi \quad (3.61)$$

where θ and φ are polar coordinates of the point, and one can finally obtain that

$$\lim_{\varepsilon\to 0} \int_{\Gamma_{\varepsilon 1}} F(\mathbf{x},\mathbf{y})n_1(\mathbf{y})\mathrm{d}\Gamma(\mathbf{y}) = 0 \quad (3.62)$$

Similarly, if the start points $\mathbf{y}^0\{a,y_2,y_3\}$ of the integral lines for $\Gamma_{\varepsilon 2}$ satisfy $a > y_1$, where points $\mathbf{y}\{y_1,y_2,y_3\}$ are on $\Gamma_{\varepsilon 2}$, then

$$\int_{\Omega_2} f(\mathbf{y})k(\mathbf{x},\mathbf{y})\mathrm{d}\Omega(\mathbf{y}) = \int_{\Gamma_2} F(\mathbf{x},\mathbf{y})n_1(\mathbf{y})\mathrm{d}\Gamma(\mathbf{y}) + \int_{\Gamma_3^- + \Gamma_4^-} F(\mathbf{x},\mathbf{y})n_1(\mathbf{y})\mathrm{d}\Gamma(\mathbf{y}) + \int_{\Gamma_{\varepsilon 2}} F(\mathbf{x},\mathbf{y})n_1(\mathbf{y})\mathrm{d}\Gamma(\mathbf{y}) \tag{3.63}$$

$$\lim_{\varepsilon\to 0}\int_{\Gamma_{\varepsilon 2}} F(\mathbf{x},\mathbf{y})n_1(\mathbf{y})\mathrm{d}\Gamma(\mathbf{y}) = 0 \tag{3.64}$$

Since the start points of the integral lines for points on Γ_3^+ and Γ_3^- can be arbitrary, one can use the same start points of the integral lines for target points on Γ_3^+ and Γ_3^-, Similar assumption can be applied for Γ_4^+ and Γ_4^- , then one can have

$$\int_{\Gamma_3^+ + \Gamma_4^+} F(\mathbf{x},\mathbf{y})n_1(\mathbf{y})\mathrm{d}\Gamma(\mathbf{y}) + \int_{\Gamma_3^- + \Gamma_4^-} F(\mathbf{x},\mathbf{y})n_1(\mathbf{y})\mathrm{d}\Gamma(\mathbf{y}) = 0 \tag{3.65}$$

Then Eq.(3.52) can be written as

$$\int_{\Omega} f(\mathbf{y})k(\mathbf{x},\mathbf{y})\mathrm{d}\Omega(\mathbf{y}) = \int_{\Gamma_1} F(\mathbf{x},\mathbf{y})n_1(\mathbf{y})\mathrm{d}\Gamma(\mathbf{y}) + \int_{\Gamma_2} F(\mathbf{x},\mathbf{y})n_1(\mathbf{y})\mathrm{d}\Gamma(\mathbf{y}) + \int_{\Gamma_{\varepsilon 1}} F(\mathbf{x},\mathbf{y})n_1(\mathbf{y})\mathrm{d}\Gamma(\mathbf{y}) + \int_{\Gamma_{\varepsilon 2}} F(\mathbf{x},\mathbf{y})n_1(\mathbf{y})\mathrm{d}\Gamma(\mathbf{y}) + \int_{\Omega_\varepsilon} f(\mathbf{y})k(\mathbf{x},\mathbf{y})\mathrm{d}\Omega(\mathbf{y}) \tag{3.66}$$

The last domain integral in Eq.(3.66) can be computed as

$$\begin{aligned}\left|\int_{\Omega_\varepsilon} f(\mathbf{y})k(\mathbf{x},\mathbf{y})\mathrm{d}\Omega(\mathbf{y})\right| &\le C_1\|g\|_\infty \int_{\Omega_\varepsilon} r^{-\beta}\mathrm{d}\Omega(\mathbf{y}) \\ &= C_1\|g\|_\infty \int_0^{2\pi}\int_0^{\pi}\int_0^{\varepsilon} r^{2-\beta}\sin\theta\mathrm{d}r\mathrm{d}\theta\mathrm{d}\varphi \\ &= C_1\|g\|_\infty \int_0^{2\pi}\int_0^{\pi}\frac{\varepsilon^{3-\beta}}{3-\beta}\sin\theta\mathrm{d}r\mathrm{d}\theta\mathrm{d}\varphi\end{aligned} \tag{3.67}$$

where $\{r,\theta,\phi\}$ are the polar coordinates of the point, $0 \le \beta < 3$. From Eq.(3.67), one can also obtain that

$$\lim_{\varepsilon\to 0}\int_{\Omega_\varepsilon} f(\mathbf{y})k(\mathbf{x},\mathbf{y})\mathrm{d}\Omega(\mathbf{y}) = 0 \tag{3.68}$$

At last, taking the limit as $\varepsilon \to 0$ in Eq.(3.52) one can have

$$\begin{aligned}\int_{\Omega} f(\mathbf{y})k(\mathbf{x},\mathbf{y})\mathrm{d}\Omega(\mathbf{y}) &= \lim_{\varepsilon\to 0}\int_{\Omega\setminus\Omega_\varepsilon} f(\mathbf{y})k(\mathbf{x},\mathbf{y})\mathrm{d}\Omega(\mathbf{y}) + \lim_{\varepsilon\to 0}\int_{\Omega_\varepsilon} f(\mathbf{y})k(\mathbf{x},\mathbf{y})\mathrm{d}\Omega(\mathbf{y}) \\ &= \oint_{\Gamma} F(\mathbf{x},\mathbf{y})n_1(\mathbf{y})\mathrm{d}\Gamma(\mathbf{y})\end{aligned} \tag{3.69}$$

For the case when the weakly singular point is on the boundary, a similar method can be used to prove the theorem.

Chapter 4

An AOIMLS enhanced LIBEM for solving 3D non-homogeneous heat conduction problems with heat sources

Summary

In this chapter, a novel BEM is proposed to solve non-homogeneous heat conduction problems with heat sources. Apart from heat sources the non-homogeneous thermal conductivity can also result in domain integrals in BIEs. To avoid losing the well-known advantage of BEM, boundary-only discretisation, LIBEM is applied to reduce the domain integrals dimensionally. However, LIMBEM only can deal with domain integrals with known integrand function, i.e., the domain integrals caused by heat sources with known function can be computed directly. While the domain integral caused by non-homogeneous thermal conductivity contains an unknown integrand function related to the regularized temperature that is beyond the capability of the LIBEM. Thereby a novel adaptive orthogonal interpolating moving least-square method (AOIMLS) enhanced LIBEM is proposed to deal with the case when the BIEs contain domain integrals with unknown functions, as all the necessary temperature values for the integral points in LIM can be interpolated from discretised nodes by AOIMLS.

4.1 Introduction

Many numerical methods are exerted to solve heat conduction problems, like FEM [134-136] and the meshless method [137-139]. As a semi-analytical and dimension reduction method, BEM [30, 140] is also considered a possible approach for heat conduction analysis. Fruitful achievements on heat conduction problems with BEM have been obtained. Gao developed a new meshless BEM for non-homogeneous heat conduction problems containing heat sources [141]. In 2015, Yang et al. presented a new approach for heat conduction problems with a variable thermal coefficient [142].

It is worth mentioning that a key problem for BEM when it comes to heat conduction problems is domain integrals appearing in BIEs, which result in losing the advantage, boundary-only discretisation, of BEM. Including the research mentioned earlier, different kinds of methods are applied for treating domain integrals, like the frequently used RIM [16, 119, 143, 144], DRM [70, 145-148] and MRM [149, 150]. LIM [77, 78] is proposed by Wang based on the divergence theorem and applied in this chapter. LIM can transform domain integrals to boundary integrals with 1D integrals based on the divergence theorem in Cartesian coordinates and the coordinate transformation is exerted to deal with singular integrals. Proved by many researchers, LIM can reduce domain integrals dimensionally and can be coupled with BEM perfectly as LIBEM. In the current research, all the domain integrals with known functions are solved by the LIBEM. But the LIBEM cannot treat domain integrals with unknown functions that are caused by the non-homogeneous thermal conductivity [151] in heat conduction BIEs. As the frequently used approximation method, the moving-least square (MLS) [37, 152] is very popular for many years and various improved MLS are proposed [153, 154]. In this study, the AOIMLS [39] is introduced to combine with the LIBEM as a new LIBEM with approximation property, for solving the domain integrals with unknown functions. The new LIBEM with AOIMLS has at least three advantages. Firstly, the shape function of AOIMLS owns the delta function property which makes it possible

to interpolate the field from only discrete nodes. Secondly, the AOIMLS can circumvent the ill-condition moment matrix adaptively which ensures the stability of this approximation method. Thirdly, compared to other approximation methods, such as RBFs [155, 156], the computation of the inverse coefficient matrix during approximation is not necessary for this new method.

This chapter is organized as below, the BIEs for non-homogeneous heat conduction problems containing heat generation are introduced first, followed by the proposal and detailed description of the novel AOIMLS enhanced LIBEM. As the LIBME is applied to heat conduction analysis for the first time, hence, to prove the accuracy and convergence of the LIBEM, in **Section 4.4**, the thermal conductivity is defined as constant in heat conduction problems in 2nd numerical example. Further, the efficiency and accuracy of the new AOIMLS enhanced LIBEM for non-homogeneous heat conduction problems containing heat sources are testified by another numerical example.

4.2 Formulas of non-homogeneous heat conduction

Heat conduction problems are common in engineering analysis, and some special materials, like non-homogeneous materials, own variable thermal conductivity which is a function of spatial coordinates. Further, some structures contain heat sources which can change temperature distribution and is worth the attention of researchers and engineers as well. The necessary theorems for those two problems are introduced below.

For non-homogeneous materials with heat generation, the governing equation is expressed as

$$\frac{\partial}{\partial x_i}\left[T(\mathbf{x})\frac{\partial \theta(\mathbf{x})}{\partial x_i} \right] + B(\mathbf{x}) = 0 \tag{4.1}$$

where the thermal conductivity $T(\mathbf{x})$ is a function of spatial coordinates, $B(\mathbf{x})$ represents the heat source, θ is temperature, $\mathbf{x}$ and $\mathbf{y}$ shown in the later formulas are the points in the research domain Ω with components x_i and y_i, $i = 1, 2, 3$.

And the boundary conditions can be set as

$$\begin{cases} \theta(\mathbf{x})=\tilde{\theta}(\mathbf{x}) \\ q(\mathbf{x})=-T(\mathbf{x})\dfrac{\partial\theta(\mathbf{x})}{\partial\mathbf{n}}=\tilde{q}(\mathbf{x}) \end{cases} \tag{4.2}$$

where $q(\mathbf{x})$ is heat flux on the boundary and $\mathbf{n}$ is the unit outward normal of the boundary.

By introducing the weight function, subsection integral method and divergence theorem, the governing equation (4.1) is written as the following integral equation and the detailed derivation process can be found in [141].

$$\begin{aligned} c(\mathbf{x})\hat{\theta}(\mathbf{x})=&-\int_{\Gamma}u^{*}(\mathbf{x},\mathbf{y})q(\mathbf{y})\mathrm{d}\Gamma(\mathbf{y})-\int_{\Gamma}q^{*}(\mathbf{x},\mathbf{y})\hat{\theta}(\mathbf{y})\mathrm{d}\Gamma(\mathbf{y}) \\ &+\int_{\Omega}u^{*}(\mathbf{x},\mathbf{y})B(\mathbf{y})\mathrm{d}\Omega(\mathbf{y})+\int_{\Omega}\varpi(\mathbf{x},\mathbf{y})\hat{\theta}(\mathbf{y})\mathrm{d}\Omega(\mathbf{y}) \end{aligned} \tag{4.3}$$

where $\hat{\theta}$ is the normalized temperature and $\hat{\theta}=T(\mathbf{x})\theta$ where $T(\mathbf{x})$ represents thermal conductivity which changes with coordinates. c=1/2 for smooth boundary points and c=1 for internal points, $u^{*}(\mathbf{x},\mathbf{y})$ and $q^{*}(\mathbf{x},\mathbf{y})$ are Green functions [157].

Moreover, $\varpi(\mathbf{x},\mathbf{y})$ can be written as

$$\varpi(\mathbf{x},\mathbf{y})=u^{*}_{,i}(\mathbf{x},\mathbf{y})\hat{T}_{,i}(\mathbf{x}) \tag{4.4}$$

with

$$u^{*}_{,i}(\mathbf{x},\mathbf{y})=-\frac{r_{,i}}{4\pi r^{2}} \tag{4.5}$$

$$\hat{T}(\mathbf{x})=\ln T(\mathbf{x}) \tag{4.6}$$

As one can see in Eq.(4.3), two domain integrals can be found and expressed as follows

$$D_{1}=\int_{\Omega}u^{*}(\mathbf{x},\mathbf{y})B(\mathbf{y})\mathrm{d}\Omega(\mathbf{y}) \tag{4.7}$$

$$D_{2}=\int_{\Omega}\omega(\mathbf{x},\mathbf{y})\hat{\theta}(\mathbf{y})\mathrm{d}\Omega(\mathbf{y}) \tag{4.8}$$

The domain integral in Eq.(4.7) is relative to the heat generation, and the function $B(\mathbf{y})$ is always known, hence the domain integral in Eq. (4.7) can be treated with the traditional LIM, while the function $\hat{\theta}(\mathbf{x})$ in the domain integral in Eq.(4.8) is unknown and cannot be computed by LIM directly and the new solution will be introduced next.

4.3 The adaptive orthogonal IMLS

In this section, a detailed introduction to the theorem of AOIMLS and the

development history of MLS [158-160] will be given. The reason why this algorithm needs to be introduced is that LIM only can perform dimensionality reduction transformation on domain integrals with a known integrand function while dealing with domain integrals with an unknown integrand function is beyond the ability of LIM. Therefore, an interpolation algorithm, AOIMLS, is needed to approximate the unknown values at the nodes created by LIM.

4.3.1 Development of the moving least squares method

MLS is a very popular approximation method for scattered data and has been applied to many fields, such as function approximation, surface construction, and many meshless methods such as boundary point method, hybrid boundary point method, Galerkin boundary point method, and boundary surface method. Numerous studies have demonstrated that MLS is a very powerful interpolation approximation method with high accuracy. In recent years, there are also some improvements in MLS, such as the generalized moving least squares (GMLS) method, the generalized moving least square reproducing kernel method and generalized interpolating moving least squares.

There are two difficulties in the implementation of the MLS method: (1) the shape function obtained by MLS does not have the property of delta function, which makes it difficult to impose boundary conditions; (2) when calculating the shape function, the moment matrix needs to be inversed and the moment matrix may be singular, and the reasons mainly are the quality of the data point set is ill or there are few points in the local support domain.

Lancaster et al. [161] further developed an interpolating moving least squares (IMLS) method and applied it to some mesh-free methods. However, since a specific singular function is used as the weight function, the moment matrix is singular, and the inverse of the singular matrix needs to be calculated, which leads to a reduction in calculation efficiency. In order to overcome the shortcomings in MLS and IMLS, Wang et al. [39, 162] recently proposed an improved interpolated moving least squares (IIMLS) method.

Compared with MLS, the shape function obtained by IIMLS owns the characteristic of the delta function, which ensures a much easier boundary conditions implementation for meshless methods. In addition, different from the IMLS method, there is no restriction on the weight function used in IIMLS and any weight function used in MLS can be directly used in IIMLS which has been applied to some meshless methods, such as the improved interpolation element free Galerkin method, and the improved interpolation boundary element free method. However, the second problem still exists in IIMLS, even if non-singular weight functions are used, in some cases, the moment matrix may still be singular.

To solve the problem that the moment matrix may be singular or ill-conditioned, some techniques have been proposed. However, very few techniques are introduced in the MLS method to deal with the singular moments, such as coordinate transformation perturbation of nodal positions, and matrix triangularization algorithm. Chowdhury et al. [163, 164] proposed an improved moving least squares (MMLS) method, which avoids the singularity of the moment matrix of the higher-order basis function by adding additional constraints to the error function. Wang et al. proposed a regularized MLS and regularized IIMLS that can completely avoid singular moment matrices, even if there is only one node in the support domain. However, this requires a new regularization factor, which will significantly affect the accuracy of the method.

The weighted orthogonal basis function can be used for the MLS approximation. The inverse of the moment matrix can be avoided by constructing the diagonal matrix which can improve the accuracy of MLS approximation in most cases. However, if the moment matrix is singular or ill-conditioned, the weighted orthogonal basis function cannot change the properties of the moment matrix. In this case, some values of the diagonal matrix in the moment matrix are zero or very close to zero, which may lead to inaccurate results.

This chapter adopts an adaptive orthogonal IIMLS method proposed by Wang et al. [39, 162] which can effectively avoid singular or ill-conditioned

moment matrix. The following are the specific steps: firstly, the weighted orthogonal basis function is constructed based on IIMLS approximation to achieve the orthogonal IIMLS approximation; then, the adaptive scheme is realized by ignoring the contribution of elements which are equal to or close to zero in the new diagonal moment matrix. This process can also be interpreted as ignoring the corresponding basis function that leads to singularity. However, if the traditional basis function is directly used, the calculation result may be unstable, mainly because the node spacing is very small, making the size of some diagonal elements close to zero. Therefore, the method uses the translated and scaled polynomial basis function proposed by Mirzaei [165] as the original basis function to improve the stability of the proposed method.

4.3.2 Basic theorem of AOIMLS

Suppose there exist two points $\mathbf{x}\{x_1, x_2, x_3\}$ and $\mathbf{y}\{y_1, y_2, y_3\}$ in a bounded region Ω, and $\mathbf{x}, \mathbf{y} \in R(\mathbf{x})$, where $R(\mathbf{x})$ is a local support domain centred at $\mathbf{x}$, and a basis function, $s_j(\mathbf{x}, \mathbf{y})\big|_{j=1}^{m}$ is defined as

$$s_j(\mathbf{x}, \mathbf{y}) = p_j(\mathbf{y}) - \sum_{i=1}^{n} o(\mathbf{x}, \mathbf{y}_i)\, p_j(\mathbf{y}_i) \tag{4.9}$$

where m represents the number of basis functions, $\mathbf{y}_i$ denotes the nodes, and the specific expression of $o(\mathbf{x}, \mathbf{y}_i)$ is

$$o(\mathbf{x}, \mathbf{y}_i) = \begin{cases} \dfrac{d(\mathbf{x}, \mathbf{y}_i)}{\sum_{k=1}^{e} d(\mathbf{x}, \mathbf{y}_k)}, & \mathbf{x} \in R(\mathbf{y}_i) \\ 0, & \mathbf{x} \notin R(\mathbf{y}_i) \end{cases} \tag{4.10}$$

and

$$d(\mathbf{x}, \mathbf{y}_i) = \frac{\Pi_{i=1, i\neq k}^{n} \| \mathbf{x} - \mathbf{y}_i \|^2}{\Pi_{i=1, i\neq k}^{n} \| \mathbf{y}_k - \mathbf{y}_i \|^2} \tag{4.11}$$

where d=1 when n=1, $p_j(\mathbf{x}, \mathbf{y})\big|_{j=1}^{m}$ represents a series of known functions, and the specific expressions can be found in previous studies [39, 162].

The orthogonalized basis functions with a given weight function $w(\mathbf{x})$ based on the Gram-Schmidt orthogonalization can be defined as

$$\overline{s}_1(\mathbf{x}, \mathbf{y}) = s_1(\mathbf{x}, \mathbf{y}) \equiv 0 \tag{4.12}$$

$$\overline{s}_2(\mathbf{x}, \mathbf{y}) = s_2(\mathbf{x}, \mathbf{y}) \tag{4.13}$$

$$\overline{s}_i(\mathbf{x},\mathbf{y})=s_i(\mathbf{x},\mathbf{y})-\sum_{k=2}^{i-1}\frac{\overline{s}_k(\mathbf{x},\mathbf{y})(s_i,\overline{s}_k)_{\mathbf{x}}}{(\overline{s}_k,\overline{s}_k)_{\mathbf{x}}} \tag{4.14}$$

where $s_i(\mathbf{x},\mathbf{y})$ and $(\cdot,\cdot)_{\mathbf{x}}$ are basis functions and inner product defined given in [39], respectively.

Hence, a given function $u(\mathbf{x})$, and its local approximation function $\tilde{u}^h(\mathbf{x},\mathbf{y})$ can be defined as

$$\tilde{u}^h(\mathbf{x},\mathbf{y})=\overline{\mathbf{s}}(\mathbf{x},\mathbf{y})\overline{\mathbf{A}}^{-1}(\mathbf{x})\overline{\mathbf{D}}(\mathbf{x})\mathbf{u} \tag{4.15}$$

where

$$\overline{\mathbf{s}}(\mathbf{x},\mathbf{y})=\left[\overline{s_2}(\mathbf{x},\mathbf{y}),\ \overline{s_3}(\mathbf{x},\mathbf{y}),\ \cdots,\ \overline{s_m}(\mathbf{x},\mathbf{y})\right] \tag{4.16}$$

$$\overline{\mathbf{A}}^{-1}(\mathbf{x})=\begin{bmatrix} 1/(\overline{s_2},\overline{s_2})_{\mathbf{x}} & 0 & \cdots & 0 \\ 0 & 1/(\overline{s_3},\overline{s_3})_{\mathbf{x}} & \cdots & 0 \\ \vdots & \vdots & \ddots & \vdots \\ 0 & 0 & \cdots & 1/(\overline{s_m},\overline{s_m})_{\mathbf{x}} \end{bmatrix} \tag{4.17}$$

$$\overline{\mathbf{D}}(\mathbf{x})=\mathbf{Q}^{\mathrm{T}}(\mathbf{x})\mathbf{W}(\mathbf{x})\left[\mathbf{I}-\mathbf{S}(\mathbf{x})\right] \tag{4.18}$$

and

$$\mathbf{Q}(\mathbf{x})=\begin{bmatrix} \overline{s_2}(\mathbf{x},\mathbf{y}_1) & \overline{s_3}(\mathbf{x},\mathbf{y}_1) & \cdots & \overline{s_m}(\mathbf{x},\mathbf{y}_1) \\ \overline{s_2}(\mathbf{x},\mathbf{y}_2) & \overline{s_3}(\mathbf{x},\mathbf{y}_2) & \cdots & \overline{s_m}(\mathbf{x},\mathbf{y}_2) \\ \vdots & \vdots & \ddots & \vdots \\ \overline{s_2}(\mathbf{x},\mathbf{y}_2) & \overline{s_3}(\mathbf{x},\mathbf{y}_2) & \cdots & \overline{s_m}(\mathbf{x},\mathbf{y}_n) \end{bmatrix} \tag{4.19}$$

$$\mathbf{W}(\mathbf{x})=\begin{bmatrix} w(\mathbf{x}-\mathbf{y}_1) & 0 & \cdots & 0 \\ 0 & w(\mathbf{x}-\mathbf{y}_2) & \cdots & 0 \\ \vdots & \vdots & \ddots & \vdots \\ 0 & 0 & \cdots & w(\mathbf{x}-\mathbf{y}_n) \end{bmatrix} \tag{4.20}$$

$$\mathbf{S}(\mathbf{x})=\left[s(\mathbf{x},\mathbf{y}_1),\ s(\mathbf{x},\mathbf{y}_2),\ \cdots,\ s(\mathbf{x},\mathbf{y}_n)\right] \tag{4.21}$$

$$\mathbf{u}(\mathbf{x})=\left[u(\mathbf{x},\mathbf{y}_1),\ u(\mathbf{x},\mathbf{y}_2),\ \cdots,\ u(\mathbf{x},\mathbf{y}_n)\right]^{\mathrm{T}} \tag{4.22}$$

where $\mathbf{I}$ is the $n\times n$ identity matrix.

Let $\mathbf{x}=\mathbf{y}$, the global approximation of $u(\mathbf{x})$ can be written as

$$u(\mathbf{x})=\boldsymbol{\varphi}(\mathbf{x})\mathbf{u} \tag{4.23}$$

and

$$\boldsymbol{\varphi}(\mathbf{x})=\overline{s}(\mathbf{x},\mathbf{x})\overline{\mathbf{A}}^{-1}(\mathbf{x})\overline{\mathbf{C}}(\mathbf{x})\mathbf{u}+\mathbf{o}(\mathbf{x})\mathbf{u} \tag{4.24}$$

where the elements of $\boldsymbol{\varphi}(\mathbf{x})$ can be expressed as

$$\varphi_i(\mathbf{y})=\sum_j^n\left[\delta_{ij}-o\left(\mathbf{x},\mathbf{y}_i\right)\right]w\left(\mathbf{x},\mathbf{y}_j\right)\frac{\sum_{k=2}^m\overline{s}_k\left(\mathbf{x},\mathbf{x}\right)\overline{s}_k\left(\mathbf{x},\mathbf{y}_j\right)}{\left(\overline{s}_k,\overline{s}_k\right)_{\mathbf{x}}}+o\left(\mathbf{x},\mathbf{y}_i\right) \tag{4.25}$$

4.4 The novel AOIMLS enhanced LIBEM

The AOIMLS is a high-accuracy approximation scheme and can avoid ill-condition matrix adaptively, besides it owns delta function property which ensures it can interpolate the field based on discretise nodes.

4.4.1 Dimensionally reduction of domain integrals

The derivation process and gist core of LIM have been addressed in detail in **Chapter 3** which readers can refer to. Here the theorem of AOIMLS enhanced LIBEM is introduced.

Eq.(4.7) can be dimensionally reduced in the case that heat conduction analysis with known heat sources, i.e., domain integrals with known functions. So, Eq. (4.7) is written in the following form

$$D_1=\int_\Omega u^*\left(\mathbf{x},\mathbf{y}\right)B\left(\mathbf{y}\right)\mathrm{d}\Omega\left(\mathbf{y}\right)=\sum_{i=1}^N n_{y_1}^i\left(\mathbf{y}\right)\omega^i\int_{L_i}u^*\left(\mathbf{x},\mathbf{y}\right)B\left(\mathbf{y}\right)\mathrm{d}y_1 \tag{4.26}$$

Based on the shape function of AOIMLS, the unknown integrand function in domain integrals can be written as the following equation

$$f_l\left(\mathbf{y}\right)=\sum_{j=0}^N\varphi_j\left(\mathbf{y}\right)f_l^j \tag{4.27}$$

where f_j is the function value at the j^{th} node and N represents the number of nodes on the boundary.

In fact, when calculating Eq.(4.25), a local influence domain exists for each node, when the j^{th} node is in the local influence domain, $\varphi_j(\mathbf{y})\neq 0$. If the integral point $\mathbf{y}$ is on the boundary, the calculation can be performed directly. However, in LIM, the integration point may be outside the solution domain, for this case, since the value of the integral kernel function outside the domain has little effect on the final calculation result, Eq.(4.25) can be used to approximate the unknown function value.

The accuracy of the above procedure may be affected when approximating the integral points outside the solution domain, but it is more convenient to do

so without distinguishing the location of integral points. In addition, AOIMLS is a local approximation method, so it is more suitable for large-scale computational problems.

Therefore, domain integrals with unknown integrand functions can be rewritten as

$$\int_{\Omega} G(\mathbf{x},\mathbf{y}) f(\mathbf{y}) \mathrm{d}\Omega(\mathbf{y}) = \sum_{k=1}^{N} \sum_{i=1}^{M} n_{y_1}^{i}(\mathbf{y}) w^{i} \int_{L_i} G(\mathbf{x},\mathbf{y}) \varphi_k(\mathbf{y}) \mathrm{d}y_1 f_k \tag{4.28}$$

where f_k is the value of kth nodes in the domain Ω.

The shape function in Eq.(4.28), owns the following merits:

Property.1. Reduce the domain integrals to boundary integrals dimensionally. As shown in Eq.(4.28), as a dimension reduction method, it can treat domain integrals efficiently without losing the merit of BEM.

Property.2. Interpolating property. For shape function on nodes, it has

$$\varphi_i(\mathbf{y}_j) = \delta_{ij} \tag{4.29}$$

Property.3. Reproduction.

$$\sum_{i=1}^{n} \varphi_i(\mathbf{x}) p_j(\mathbf{y}_i) = p_j(\mathbf{x}) \tag{4.30}$$

Property.4. None singular moment matrix. Singular or ill-condition moment matrix can be adaptively avoided as the term $\overline{s}_k(\mathbf{x},\mathbf{x})\overline{s}_k(\mathbf{x},\mathbf{y}_j)/(\overline{s}_k,\overline{s}_k)_{\mathbf{x}}$ in Eq.(4.14) is ignored if $(\overline{s}_k,\overline{s}_k)_{\mathbf{x}}$=0 or $(\overline{s}_k,\overline{s}_k)_{\mathbf{x}} < \tau$ and τ is a specified small tolerance.

Hence, the domain integral in Eq.(4.8) can be written as

$$D_2 = \int_{\Omega} \omega(\mathbf{x},\mathbf{y}) \hat{\theta}(\mathbf{y}) d\Omega(\mathbf{y}) = \sum_{k=1}^{N} \sum_{i=1}^{M} n_{y_1}^{i}(\mathbf{y}) w^{i} \int_{L_i} \beta\omega(\mathbf{x},\mathbf{y}) \varphi_k(\mathbf{y}) \mathrm{d}y_1 \hat{\theta}_k \tag{4.31}$$

where $\hat{\theta}_k$ is the regularized temperature value of kth nodes in the domain Ω.

4.4.2 Discretisation of the heat conduction BIEs

Discretizing Eq.(4.3) with boundary elements as in traditional BEM, one can obtain

$$\hat{\mathbf{H}}\hat{\mathbf{c}} - \hat{\mathbf{G}}\hat{\mathbf{q}} = \hat{\mathbf{z}}_{\mathrm{b}} + \hat{\mathbf{M}}\mathbf{c} \tag{4.32}$$

where matrices $\hat{\mathbf{H}}$ and $\hat{\mathbf{G}}$ are the $N_b \times N_b$ coefficient matrices obtained from integrals on boundary elements as in traditional BEM. $\hat{\mathbf{z}}_{\mathrm{b}}$ is the known column vector and originated from heat generation, $\mathbf{c}$ is the regularized

temperature values of all nodes and

$$\mathbf{c}=\left[\hat{\mathbf{c}} \quad \tilde{\mathbf{c}}\right]^{\mathrm{T}} \tag{4.33}$$

where $\hat{\mathbf{c}}$ and $\tilde{\mathbf{c}}$ are nodal values of boundary and internal points and

$$\hat{\mathbf{c}}=\left[\hat{c}^1 \quad \cdots \quad \hat{c}^i \quad \cdots \quad \hat{c}^{N_b}\right]^{\mathrm{T}} \tag{4.34}$$

$$\tilde{\mathbf{c}}=\left[\tilde{c}^1 \quad \cdots \quad \tilde{c}^i \quad \cdots \quad \tilde{c}^{N_c}\right]^{\mathrm{T}} \tag{4.35}$$

Besides, $\hat{\mathbf{q}}$ is the heat flux values on N_b boundary nodes and can be written as

$$\hat{\mathbf{q}}=\left[\hat{q}^1 \quad \cdots \quad \hat{q}^i \quad \cdots \quad \hat{q}^{N_b}\right]^{\mathrm{T}} \tag{4.36}$$

$\hat{\mathbf{M}}$ is a $N_b \times N$ matrix defined as

$$[\hat{\mathbf{M}}]_{kl}=\sum_{i=1}^{M} n_{y_1}^i(\boldsymbol{\xi}) w^i \int_{L_i} \Phi_m(\mathbf{y}) \omega(\mathbf{x}_k, \mathbf{y}) \mathrm{d}y_1 \tag{4.37}$$

where $\mathbf{x}_k$ are boundary nodes and k is from 1 to N_b, m is from 1 to N. $\Phi_m(\mathbf{y})$ is the shape functions of AOIMLS. And $N=N_b+N_c$ is the total number of nodes on the domain, where N_c is the number of nodes in domain Ω.

Eq.(4.32) cannot be solved since the number of unknowns is more than the number of equations, and N_c additional equations are needed. For the nodes in Ω, applying the integral Eq. (4.3), one can have

$$\tilde{\mathbf{c}}+\tilde{\mathbf{H}}\hat{\mathbf{c}}-\tilde{\mathbf{G}}\hat{\mathbf{q}}=\tilde{\mathbf{z}}_{\mathrm{b}}+\tilde{\mathbf{M}}\mathbf{u} \tag{4.38}$$

where $\tilde{\mathbf{H}}$ and $\tilde{\mathbf{G}}$ are $N_c \times N_b$ matrices obtained by integrals on boundary elements and the source points are internal nodes.

$\tilde{\mathbf{M}}$ is a $N_c \times N$ matrix defined as Eq.(4.37) and the difference is ς_k are integral nodes.

Then from Eqs.(4.32) and(4.38), one can have

$$\begin{bmatrix}\hat{\mathbf{H}} & \mathbf{0}\\ \tilde{\mathbf{H}} & \mathbf{I}\end{bmatrix}\begin{bmatrix}\hat{\mathbf{c}}\\ \tilde{\mathbf{c}}\end{bmatrix}-\begin{bmatrix}\hat{\mathbf{G}}\\ \tilde{\mathbf{G}}\end{bmatrix}[\hat{\mathbf{q}}]=\begin{bmatrix}\hat{\mathbf{z}}_{\mathrm{b}}\\ \tilde{\mathbf{z}}_{\mathrm{b}}\end{bmatrix}+\begin{bmatrix}\hat{\mathbf{M}}\\ \tilde{\mathbf{M}}\end{bmatrix}\mathbf{c} \tag{4.39}$$

Let

$$\mathbf{H}'=\begin{bmatrix}\hat{\mathbf{H}} & \mathbf{0}\\ \tilde{\mathbf{H}} & \mathbf{I}\end{bmatrix} \tag{4.40}$$

$$\mathbf{M}=\begin{bmatrix}\hat{\mathbf{M}}\\ \tilde{\mathbf{M}}\end{bmatrix} \tag{4.41}$$

$$\mathbf{H}=\mathbf{H}'+\mathbf{M} \tag{4.42}$$

where $\mathbf{H}'$, $\mathbf{M}$ and $\mathbf{H}$ are $N \times N$ matrix.

Then one can simply write Eq.(4.39) as

$$\mathbf{Hu}-\mathbf{G}\hat{\mathbf{q}}=\mathbf{y}_{\mathrm{b}} \tag{4.43}$$

where $\mathbf{G}$ is a $N\times N_b$ matrix and $\mathbf{u}$ are the displacements of the boundary and internal nodes. Then one can assemble Eq.(4.43) as the traditional BEM.

4.5 Numerical examples

To testify to the efficiency and correctness of the AOIMLS enhanced LIBEM for 3D thermo-elastic problems and non-homogeneous heat conduction problems containing heat generation, several examples are simulated and analyzed. The first example targets to prove the accuracy of LIBEM for homogeneous heat conduction problems with heat sources respectively by comparing the results with the analytical solution. Further, the second example, a flange plate, is used to prove the AOIMLS enhanced LIBEM has the ability for calculating the steady non-homogeneous heat conduction problems containing heat generation by comparing it with FEM analysis.

Besides, the relative error used in this section is defined in Section 3.5.

4.5.1 A cube

This numerical example is about a cube subjected to heat conduction and a heat source. The cube, centred at {0.5, 0.5, 0.5}, is bounded by the planes, $x=0$, $y=0$, $z=0$, $x=1$, $y=1$ and $z=1$, i.e., the side length of this cube is 1m. The temperatures at $x=0$ and $x=1$ are zero, while the other boundaries are set as the heat flux $q=0$. Besides, the thermal conductivity is a constant, T=0.01 W/(m•K). The heat generation is set as follows[73, 134, 141]

$$Q(x)=Q_0e^{-x} \tag{4.44}$$

where Q_0 is a constant and is set as 1.

Hence one can obtain the analytical solution of temperature as the following equation[73, 134, 141]

$$\theta=\frac{Q_0}{kL}\left[L\left(1-e^{-x}\right)-x\left(1-e^{-L}\right)\right] \tag{4.45}$$

For proving the developed method is useful for the heat conduction problems containing heat generation, the results of the developed method is compared with analytical solution in Eq.(4.45). As one can observe, the

temperature is only related to x-axial, so nine internal points are picked for comparison, namely, {0.1, 0.5, 0}, {0.2, 0.5, 0}, {0.3, 0.5, 0}, {0.4, 0.5, 0}, {0.5, 0.5, 0}, {0.6, 0.5, 0}, {0.7, 0.5, 0}, {0.8, 0.5, 0}, {0.9, 0.5, 0}. The boundaries of the cube are discretised with 1258 elements, as is shown in **Fig.4.1**.

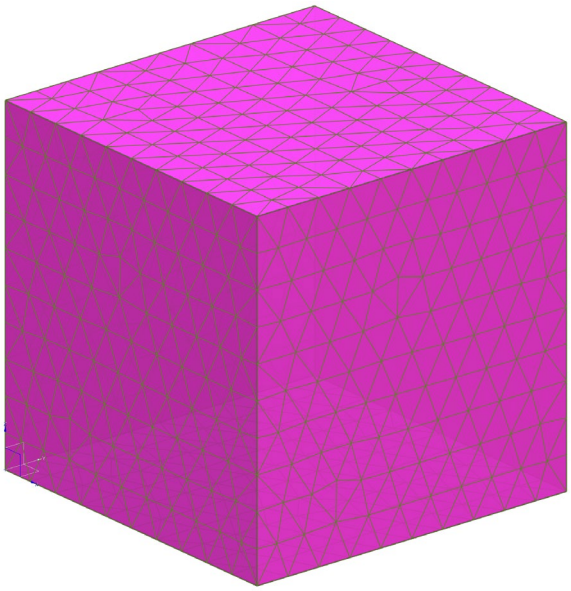

Fig.4.1 The cube with 1258 boundary elements

Then the result of the developed method is compared with the analytical solution, as one can see in **Fig.4.2**, the temperature rise with the increase of *x*-axial, then decreased. In addition, the numerical solution is consistent with the analytical solution. With the error estimation formula, the relative error is computed in this condition and the result is 0.7246% which indicates that the numerical result is in high accuracy. Besides, as one can see in **Fig.4.3**, the length of red bars represents the relative error of discretised nodes, the closer the position of the discretised node is to the boundary, the higher the relative error is. Besides, the maximum value of relative errors is 0.6.

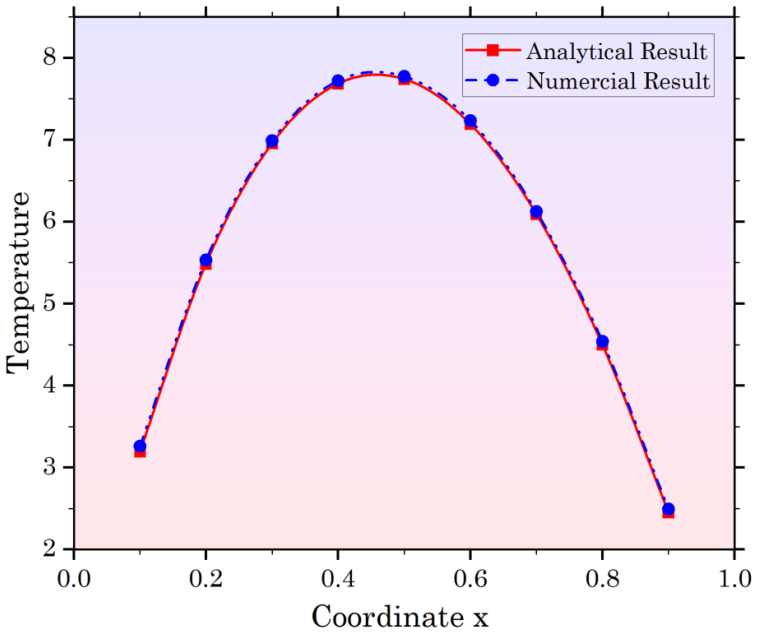

Fig.4.2 Comparison of numerical results with the analytical solution

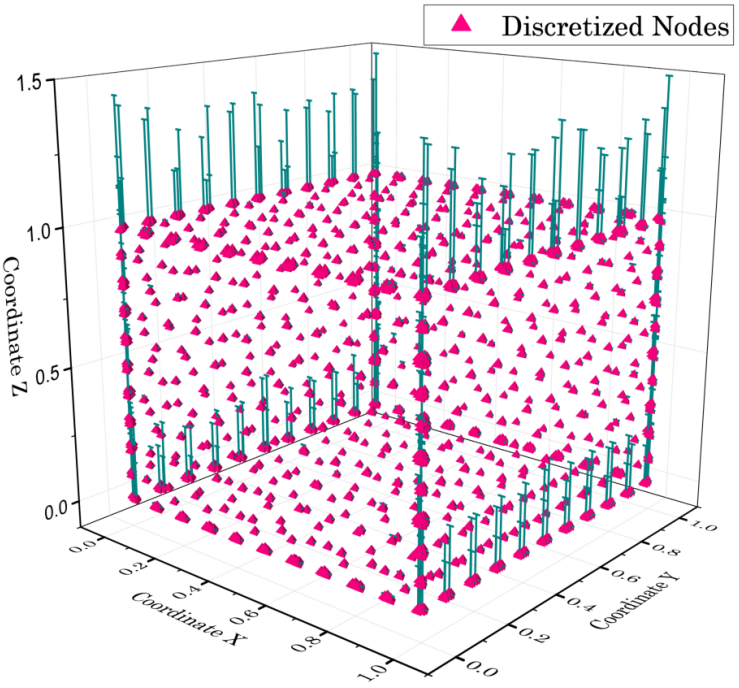

Fig.4.3 Relative error distribution of temperature (°C)

Furthermore, according to **Fig.4.4**, clearly, the relative error shows a downward trend with the increase of boundary element amount in the logarithmic coordinate system on the whole, which proves the convergence of the LIBEM.

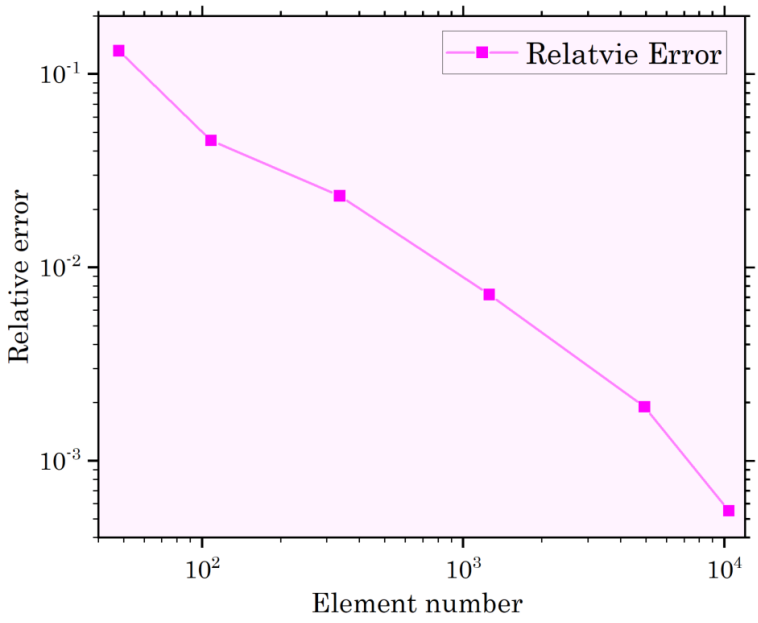

Fig.4.4 Relative error of temperature

4.5.2 A flange plate

This complex model is simulated for testifying that the proposed method is accurate and practicable when it comes to complex models, the geometrical parameters are clearly shown in **Figs.4.5** and **4.6**, besides, the height of the model is $5mm$, and the eight cylinders are evenly distributed. The surfaces, $z=0mm$ and $z=5mm$ are set with temperatures, 10 ^{o}C and 100 ^{o}C respectively. All the other faces are defined as thermally insulated. Moreover, to approximate the unknowns involved in domain integrals, 1952 points are distributed inside the model.

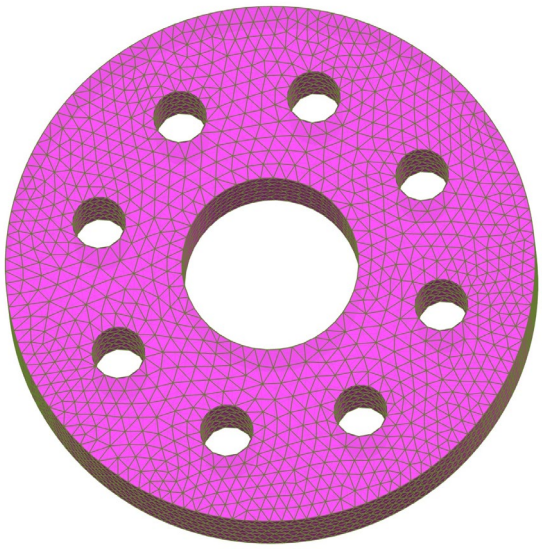

Fig.4.5 The discretised complex model

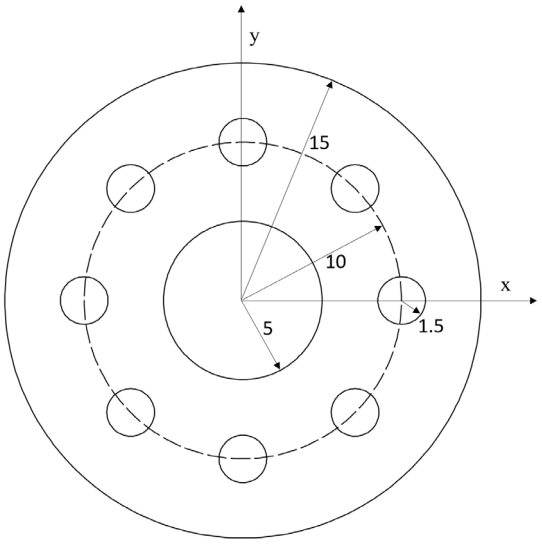

Fig.4.6 Plane graph of the complex model

In order to make this example more complicated, the various thermal conductivity is defined as a multi-modal function (see **Fig.4.7**) and expressed as

$$T(x,z)=100\cos\left(\frac{x}{3}\right)\cos\left(\frac{z}{3}\right) \tag{4.46}$$

and the heat generation is simply defined as 1.

To prove the accuracy of the proposed mathematic method, the FEM analysis is taken for comparison and the results on the selected straight line whose endpoints are {7, 0, 0} and {7, 0, 5}, are extracted and plotted in **Fig.4.8**. Apparently, the results obtained by the proposed method is highly consistent with the FEM simulation.

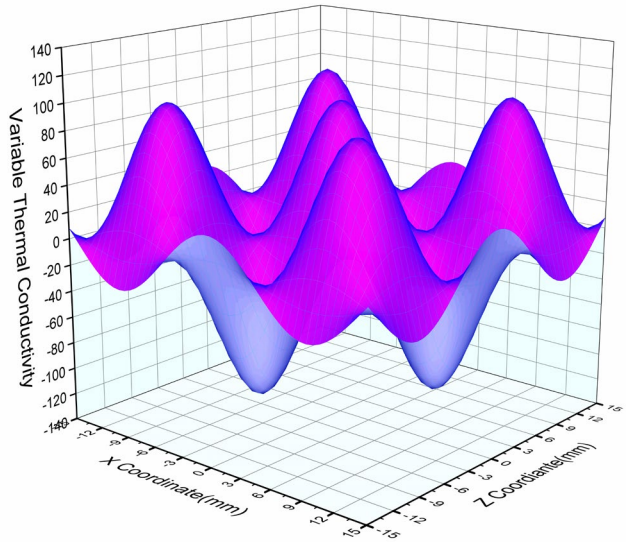

Fig.4.7 The multi-modal function of thermal conductivity

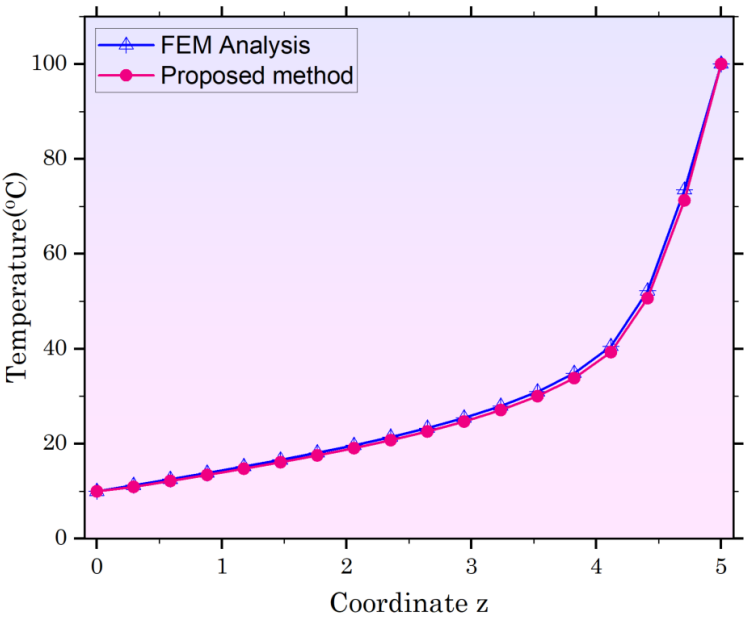

Fig.4.8 Comparison of the proposed method and FEM

Part III

Application of boundary element method in thermoelastic fracture analysis

Chapter 5

NURBS-enhanced line integration BEM for thermo-elastic problems considering the gravity load

Summary

This chapter is aimed at solving 2D thermo-elastic problems with the gravity load by LIBEM. The boundary-only discretisation, as one of the significant advantages of BEM, will disappear due to considering the thermal and gravity loads which result in domain integrals. Hence, the LIBEM, owning the dimension reduction ability, is introduced to reduce domain integrals dimensionally to ensure that no domain discretisation during the numerical calculation. Furthermore, as a well-known isogeometric characterization method, the non-uniform rational B-spline (NURBS), is exerted during geometrical construction. Thus, the boundary shape of the numerical models will not change during the refinement and the error of model discretisation will be prevented. It is worth mentioning that, to ensure boundary conditions are imposed without difficulty, the field approximation is conducted by the lagrangian basis functions (LBFs) which owns the characteristic of the Kronecker delta function.

5.1 Introduction

Generally, many engineering structures withstand thermal and gravity loads [6]. Gravity is a basic load for every engineering structure on earth and it can bring inner stress and strain changes to engineering structures, and the gravity load is a key factor for the design of engineering structures, like buildings and dams. The thermal load [166-168], which has drawn much attention of many researchers for a long time, is a vital factor that leads to fractures [169, 170] or damage in structures [114, 171], especially those mass concrete structures, like concrete dams, concrete foundation, column structure in buildings and so on. Hence, it is rather important to obtain thermal stress under different conditions in numerical simulation accurately. For that purpose, many numerical methods are developed, like the widely used FEM, boundary node method (BNM) [42, 172-174], boundary face method (BFM) [175], boundary element-free method (BEFM) [37, 176, 177], indirect boundary element method (IBEM) [178, 179]. The BEM, which owns the well-known advantage that only the boundary needed to be discretised, is taken as the basic analysis method in this research. In recent years, several researchers have conducted their investigations on thermo-elastic problems based on BEM [75, 180-182]. For example, Zhang et al.[183] developed research on solving thin-structure thermo-elastic problems. Gao also did lots of research on thermal stress a semi-analytical technique [184].

For thermal load and gravity considered elastic problems, the traditional BEM cannot be applied directly because the domain integrals [127, 185, 186] appear in the BIEs. In this research, based on the divergence theorem [187, 188], the LIBEM [57, 189, 190] is exerted to reduce the domain integrals dimensionally and the coordinate transformation is exerted to deal with singular integrals. Further, for guaranteeing the precision of LIBEM, the adaptive background cells [191, 192] are applied for subdividing the initial integral lines into short ones, so the domain integrals can be obtained by adding up sub-line integrals.

For traditional BEM, before simulation, constructing the model, meshing the model and imposing the boundary conditions are necessary preparation

items [31, 49, 193]. The model meshing procedure may lead to errors as the mesh may be twisted or the operators are not experienced enough. Hence, in order to keep the model geometrically accurate during all the pre-processing procedures, based on the idea of Isogeometric analysis (IGA) [194, 195], the NURBS [49, 190, 196] is introduced for the geometric reconstruction of numerical models in this research. However, when it comes to field approximation, there is an evident difference between some previous IGA-based BEM research and this paper, i.e., the IGA-based BEM exerts the same basis functions in geometric construction and field approximation [197-199], like the B-spline or NURBS basis functions. In this research, the field approximation is done with the help of the LBFs [200] with the property of Kronecker delta, which can lead to a range of benefits, mainly including ensuring the NURBS-enhanced LIBEM to set boundary conditions, deal with singular integrals and couple with other high-performance algorithms easily [4, 193, 201].

In the current study, the BIEs for thermo-elastic problems with the gravity load are introduced in **Section 5.2**. In the next section, a detailed description of the NURBS theorem is presented, followed by the introduction of geometry construction and field approximation. Then, the LIBEM is described in detail in **Section 5.4**. To prove the accuracy and merits of the NURBS-enhanced LIBEM, three examples are analyzed in the last section.

5.2 The BIEs for thermo-elastic problems considering gravity

The governing equation for elastic problems considering the thermal and gravity load is written below [202]

$$(\lambda+\mu)u_{j,ji}(\mathbf{x},\mathbf{y})+\mu u_{i,jj}(\mathbf{x},\mathbf{y})-\frac{\lambda(1+\nu)}{\nu}\beta\theta_{,i}(\mathbf{x})+b_i(\mathbf{x})=0 \qquad i,j=1,2 \tag{5.1}$$

where $u_{j,ji}$ and $u_{i,jj}$ are the derivatives of displacement u, Ω is the domain of the problems bounded with boundary Γ, $\mathbf{x}\{x_1,x_2\}$ and $\mathbf{y}\{y_1,y_2\}$ are points in Ω, μ and λ are the Lame constants, ν represents the Poisson's ratio, θ represents temperature, $\theta_{,i}$ are the partial derivatives of θ with respect to x_i, β is thermal expansion coefficient.

5.2.1 The displacement boundary integral equation

By Bett's reciprocal theorem, the following BIE can be derived from Eq.(5.1) as below [184]

$$\begin{aligned} c_{ij}(\mathbf{x})u_i(\mathbf{x}) = &\int_\Gamma U_{ij}(\mathbf{x},\mathbf{y})\mathbf{t}_j(\mathbf{y})d\Gamma(\mathbf{y}) - \int_\Gamma T_{ij}(\mathbf{x},\mathbf{y})\mathbf{u}_j(\mathbf{y})\mathrm{d}\Gamma(\mathbf{y}) \\ &- \int_\Omega \beta\Phi_i(\mathbf{x},\mathbf{y})\theta(\mathbf{y})\mathrm{d}\Omega(\mathbf{y}) + \int_\Omega U_{ij}(\mathbf{x},\mathbf{y})G_j(\mathbf{y})\mathrm{d}\Omega(\mathbf{y}) \end{aligned} \tag{5.2}$$

where $U_{ij}(\mathbf{x},\mathbf{y})$ and $T_{ij}(\mathbf{x},\mathbf{y})$ are Kelvin functions and given in **Chapter 2**, and

$$\Phi_i(\mathbf{x},\mathbf{y}) = \frac{-2(1+\nu)r_{,i}}{A_1 r} \tag{5.3}$$

Obviously, two domain integrals appear in Eq.(5.2), namely,

$$D_1 = \int_\Omega U_{ij}(\mathbf{x},\mathbf{y})G_j(\mathbf{y})\mathrm{d}\Omega(\mathbf{y}) \tag{5.4}$$

$$D_2 = \int_\Omega \beta\Phi_i(\mathbf{x},\mathbf{y})\theta(\mathbf{y})\mathrm{d}\Omega(\mathbf{y}) \tag{5.5}$$

5.2.2 Boundary integral equation for internal stress

Combining Eq.(5.2) with the following equation, which is called the strain-displacement relationship

$$\varepsilon_{ij}(\mathbf{x},\mathbf{y}) = \frac{1}{2}\left[u_{i,j}(\mathbf{x},\mathbf{y}) + u_{j,i}(\mathbf{x},\mathbf{y})\right] \tag{5.6}$$

Hence, the BIE of stresses can be written as

$$\begin{aligned} \sigma_{ij}(\mathbf{x}) = &\int_\Gamma U_{ijk}(\mathbf{x},\mathbf{y})t_k(\mathbf{y})\mathrm{d}\Gamma(\mathbf{y}) - \int_\Gamma \mathrm{T}_{ijk}(\mathbf{x},\mathbf{y})u_k(\mathbf{y})\mathrm{d}\Gamma(\mathbf{y}) \\ &+ \int_\Omega \beta\Psi_{ij}(\mathbf{x},\mathbf{y})\theta(\mathbf{y})\mathrm{d}\Omega(\mathbf{y}) + \int_\Omega U_{ijk}(\mathbf{x},\mathbf{y})G_j(\mathbf{y})\mathrm{d}\Omega(\mathbf{y}) \\ &- b\beta\delta_{ij}\theta(\mathbf{x}) \end{aligned} \tag{5.7}$$

where

$$\begin{cases} \Psi_{ij}(\mathbf{x},\mathbf{y}) = \dfrac{-4\mu(1+\nu)\left[\delta_{ij} - 2r_{,i}r_{,j}\right]}{A_1 r^2} \\ b = \mu\dfrac{1+\nu}{1-\nu} \end{cases} \tag{5.8}$$

The first domain integral term of Eq.(5.5) has a strong singularity, to deal with this problem, one can refer to ref.[184] to regularize Eq.(5.5). After a series of similar transformations, Eq.(5.7) can be rewritten as

$$\begin{aligned} \sigma_{ij}(\mathbf{x}) = &\int_\Gamma U_{ijk}(\mathbf{x},\mathbf{y})t_k(\mathbf{y})\mathrm{d}\Gamma(\mathbf{y}) - \int_\Gamma \mathrm{T}_{ijk}(\mathbf{x},\mathbf{y})u_k(\mathbf{y})\mathrm{d}\Gamma(\mathbf{y}) \\ &+ \int_\Gamma \beta r_{,m}n_m \ln\left(r^r\right)\Psi_{ij}(\mathbf{x},\mathbf{y})\theta(\mathbf{y})\mathrm{d}\Gamma(\mathbf{y}) + \int_\Omega \beta\Psi_{ij}(\mathbf{x},\mathbf{y})\theta(\mathbf{y})\mathrm{d}\Omega(\mathbf{y}) \\ &- \int_\Omega \beta\Psi_{ij}(\mathbf{x},\mathbf{y})\theta(\mathbf{x})\mathrm{d}\Omega(\mathbf{y}) + \int_\Omega U_{ijk}(\mathbf{x},\mathbf{y})G_j(\mathbf{y})\mathrm{d}\Omega(\mathbf{y}) - \beta b\delta_{ij}\theta(\mathbf{x}) \end{aligned} \tag{5.9}$$

Now, the above Eqs.(5.2) and (5.9) can be calculated numerically with Gauss quadrature formulae.

In Eq.(5.9), another three domain integrals can be written as follows

$$D_3 = \int_\Omega \beta \Psi_{ij}(\mathbf{x},\mathbf{y})\theta(\mathbf{y})\mathrm{d}\Omega(\mathbf{y}) \tag{5.10}$$

$$D_4 = \int_\Omega \beta \Psi_{ij}(\mathbf{x},\mathbf{y})\theta(\mathbf{x})\mathrm{d}\Omega(\mathbf{y}) \tag{5.11}$$

$$D_5 = \int_\Omega U_{ijk}(\mathbf{x},\mathbf{y})G_j(\mathbf{y})\mathrm{d}\Omega(\mathbf{y}) \tag{5.12}$$

To keep the advantage of BEM, one has to reduce all the domain integrals dimensionally by LIM which is described in **Section 3.3**.

Furthermore, it needs to make clear that all the formulations are solved by introducing the following boundary conditions

$$u_i = \overline{u}_i(\mathbf{x}), \quad \mathbf{x} \in \Gamma \tag{5.13}$$

or

$$\sigma_{ij} n_j = \overline{t}_i(\mathbf{x}), \quad \mathbf{x} \in \Gamma \tag{5.14}$$

where σ_{ij} represent the boundary stresses, $\overline{u}_i(\mathbf{x})$ and $\overline{t}_i(\mathbf{x})$ represent the known boundary functions.

5.3 Theorem of NURBS and geometry reconstruction

In this section, the theorem of NURBS is described first, and then the geometry reconstruction and field approximation are introduced.

The geometric models of engineering structures can generally be classified into two types: (1) simple curves or surfaces, whose mathematical expressions can be easily obtained, such as circles, cylinders, spheres, cuboids, etc. In reality, most engineering structures are also composed of or a combination of analytical curves and surfaces; (2) the structure with complex change, which is difficult to describe by analytical curves and surfaces. For some engineering and industrial products with high precision and complex shapes, such as aircraft and ship parts, as well as the improvement and optimization process of complex models and mass production, a scientific and accurate mathematical expression method is urgently needed. In addition, it is unrealistic for the design and construction of large-scale and complex structures to rely on manual calculation, adjustment and recording. Therefore, only a mathematical

expression method of curves and surfaces that is suitable for computer processing and can meet the effectiveness and accuracy of shape expression is vital and can be widely used.

In 1963, Ferguson, who worked at Boeing, proposed a method of using the vector function of parameters to express the shape of product structure. The cubic parametric curve is introduced first and the Ferguson cubic surface, which is composed of the combined curve, the position vector of the four corners and the tangential vector of the two directions, is defined. In the following year, Coons of the Massachusetts Institute of Technology (MIT) proposed a more general description method that can express a surface sheet by using the four boundaries of a closed curve. However, there are disadvantages of the two methods addressed above, i.e., connection and difficulty in controlling shapes. In the same year, the spline function is proposed to solve the problem of connection and used parametric form to represent curves and surfaces. However, it is difficult to adjust the local shape. In 1971, Bezier of Renault company addressed an approach to control curves and surfaces by using polygons which have been widely used in the engineering industry, but the drawback is that the geometry can not be modified and connected locally still exists.

A year later, Boor proposed the theory of B-splines, and then based on the improvements and updates of several researchers, Versprille proposed NURBS in 1975, which included rational and irrational Bezier curves and irrational B-splines. In 1991, NURBS was designated by the International Standards Organization (ISO) as the only mathematical method for the geometry of industrial products.

NURBS can be specifically interpreted as:

(1) Non-uniform: the distances between the nodes of the curves are not equal to each other, so the influential domain of each control vertex can be manipulated, and it owns the property of local support and modification;

(2) Rational: the control points are weighted, and each curve described by NURBS can be expressed by mathematical formulas;

(3) B-spline: it is developed from non-rational B-spline curves and surfaces, and takes B-spline as the basis function, which well retains the advantages of non-rational B-spline.

In addition, the following are the advantages and disadvantages of NURBS:

(1) Advantages: It can not only represent elementary analytic curves and surfaces in the form of mathematical expressions, but also accurately and effectively represent complex curves and surfaces; by modifying control points and weights, local modifications of geometry can be performed, and greater flexibility can be performed during geometric design; the expression of geometry is invariant when performing transformations such as scaling, rotation, shearing, translation, and perspective projection; NURBS is the promotion and improvement of non-rational B-splines, rational and non-rational Bezier curve and keeps the advantages of the above three methods; explicit geometric expressions can be obtained by NURBS, which is very friendly to design engineers.

(2) Disadvantages: The first obvious drawback is that additional data storage is still needed when describing simple curves and surfaces. For example, to express a circle, a circumscribed square is required as a control polygon, so at least 10 nodes and 7 control points are required. While the traditional method only needs to store three kinds of data: the radius, the coordinates of the centre and the normal vector perpendicular to the surface of the circle; besides, inappropriate weights may lead to unsatisfactory parameterization, and then the curve or surface cannot be accurately expressed; moreover, in some aspects, it is simpler and more convenient to use traditional techniques, such as compute the intersection between surfaces.

5.3.1 Introduction of the Bezier Curve

NURBS is based on the generalization of the Bezier curve theory. In other words, the Bezier curve theory is a special case of NURBS.

The definition of an irrational Bezier curve of order n can be expressed as:

$$C(\tau)==\sum_{i=0}^{n} B_{i,n}(\tau)P_i \quad 0\le\tau\le 1 \tag{5.15}$$

where P_i is the control point, $B_{i,n}$ is the classical Bernstein polynomial of order n and the expression is

$$B_{i,n}(\tau)=\frac{n!}{i!(n-i)!}\tau'(1-\tau)^{n-i} \tag{5.16}$$

However, although there are many advantages of polynomials, irrational Bezier curves can not describe quadratic curves, and there will be problems when expressing many typical and important curves and surfaces. Taking the unit circle with the centre at the origin as an example, the counterproof method is adopted. It is assumed that the circle is represented by the following polynomial:

$$x(\tau)=a_0+a_1\tau+\cdots+a_n\tau^n \tag{5.17}$$

$$y(\tau)=b_0+b_1\tau+\cdots+b_n\tau^n \tag{5.18}$$

Due to $x^2+y^2=1$, the following can be obtained

$$\begin{aligned}0&=\left(a_0+a_1\tau+\cdots+a_n\tau^n\right)^2+\left(b_0+b_1\tau+\cdots+b_n\tau^n\right)^2-1\\&=\left(a_0^2+b_1^2-1\right)+2\left(a_0a_1+b_0b_1\right)\tau+\left(a_1^2+2a_0a_2+b_1^2+2b_0b_2\right)\tau^2\\&\quad+\cdots+\left(a_{n-1}^2+2a_{n-2}a_n+b_{n-1}^2+2b_{n-2}b_n\right)\tau^{2n-2}\\&\quad+2\left(a_na_{n-1}+b_nb_{n-1}\right)\tau^{2n-1}+\left(a_n^2+b_n^2\right)\tau^{2n}\end{aligned} \tag{5.19}$$

The above formula should be right for an arbitrary τ, so all the coefficients at the right of the above formula must be zero. It can be deduced that for $i=1,2,3,\cdots,n$, one can have $a_i=0$, $b_i=0$. Obviously, the expression is not the unit circle, which is inconsistent with the assumption.

Therefore, the rational Bezier curve theory came into being. The rational function is the ratio of two polynomials. The expression of rational Bezier curve theory is defined as follows

$$C(\tau)=\frac{\sum_{i=0}^{n} B_{i,n}(\tau)w_iP_i}{\sum_{i=0}^{n} B_{i,n}(\tau)w_i} \quad 0\le\tau\le 1 \tag{5.20}$$

where the definition of P_i and $B_{i,n}$ are not changed, w_i is the weight factor. The larger the weight factor is, the curve will be pushed away from the corresponding control point, and vice versa.

5.3.2 The basic functions of B-spline

Because local control is not easy for the Bezier curve which limits its development, the B-spline curve is gradually popular. Compared with Bezier curves, which define the basis function in $[u_0, u_m]$, the basis function for the B-spline curve is defined in the limited subinterval, and the B-spline curve is defined as follows:

$$C(\tau) = \sum_{i=0}^{n} R_{i,p} P_i \qquad a \le \tau \le b \tag{5.21}$$

where $R_{i,p}$ represent the B-spline basis function in p order.

Assuming that the sequence $\Lambda=[\tau_0, \tau_1, \cdots, \tau_n]$ is a series of real numbers with the property $\tau_{i+1} \ge \tau_i$. The B-spline basis function of degree p is defined below by the recursive formula

$$\begin{cases} Q_{i,0}(\tau) = \begin{cases} 1, \tau_i \le \tau \le \tau_{i+1} \\ 0, \ otherwise \end{cases} \\ Q_{i,p}(\tau) = \dfrac{\tau - \tau_i}{\tau_{i+p} - \tau_i} Q_{i,p-1}(\tau) + \dfrac{\tau_{i+p+1} - \tau}{\tau_{i+p+1} - \tau_{i+1}} Q_{i+1,\rho-1}(\tau) \\ i = 0, 1, \cdots, n, \quad \tau_i \le \tau_{i+1} \\ Set \ \dfrac{0}{0} = 0 \end{cases} \tag{5.22}$$

where the nodal vector is aperiodic and non-uniform and written as follows

$$\Lambda = \left\{ \underbrace{a, \cdots, a}_{p+1}, \tau_{p+1}, \cdots, \tau_{m-p+1}, \underbrace{b, \cdots, b}_{p+1} \right\} \tag{5.23}$$

Generally speaking, $a = 0$, $b = 1$ in the application.

5.3.3 The basic functions of NURBS

In order to describe the quadratic curve, the B-spline curve is generalized to obtain a non-uniform rational B-spline curve, which is defined as:

$$C(\tau) = \sum_{i=0}^{n} R_{i,p}(\tau) P_i \tag{5.24}$$

$$R_{i,p}(\tau) = \frac{Q_{i,p}(\tau) w_i}{\sum_{j=0}^{n} Q_{j,p}(\tau) w_j} \tag{5.25}$$

where w_0 and w_n are positive numbers to avoid the denominator equaling zero and make sure that curves do not degenerate to a point, $Q_{i,p}$ are pth degree basis functions.

5.3.4 Properties of NURBS basis functions

The basic properties of NURBS are introduced below and one can find the detailed derivation process in the references [49, 190, 196].

Property.1 Nonnegativity: for any given i, p, $R_{i,p}(\tau) \geq 0$.

Property.2 Partition of unity: $\sum_{i=0}^{n} R_{i,p}(\tau)=1$.

Property.3 Local support: for $\tau \notin [\tau_i, \tau_{i+p+1}]$, $R_{i,p}(\tau)=0$. In addition, for any given knot span, p+1 of the $R_{i,p}(\tau)$ should be non-zero at most.

Property.4 The weights w_i only exert their influence on the curve shape in span $[\tau_i, \tau_{i+p+1}]$.

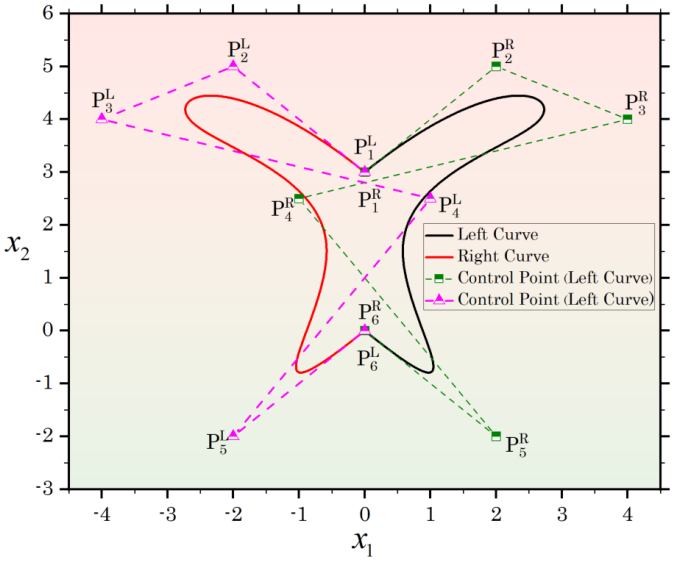

Fig.5.1 NURBS curves with $p=3$

Property.5 The higher the pth is, the farther away the control point is from the curve. **Figs.5.1** and **5.2** show the irregular and symmetrical NURBS curves, both two curves are based on the same control points.

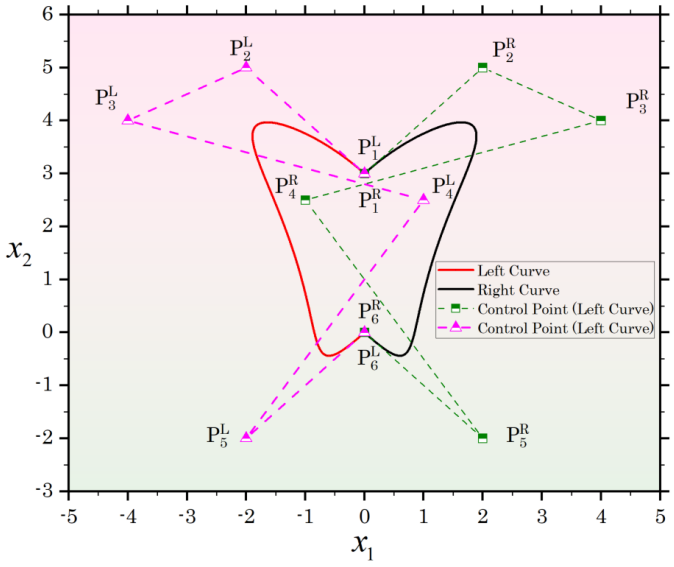

Fig.5.2 NURBS curves with $p = 5$

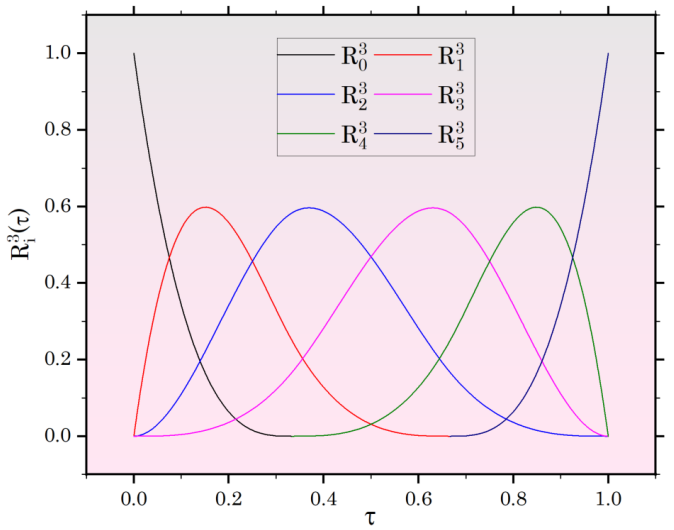

Fig.5.3 NURBS basis functions with $p = 3$

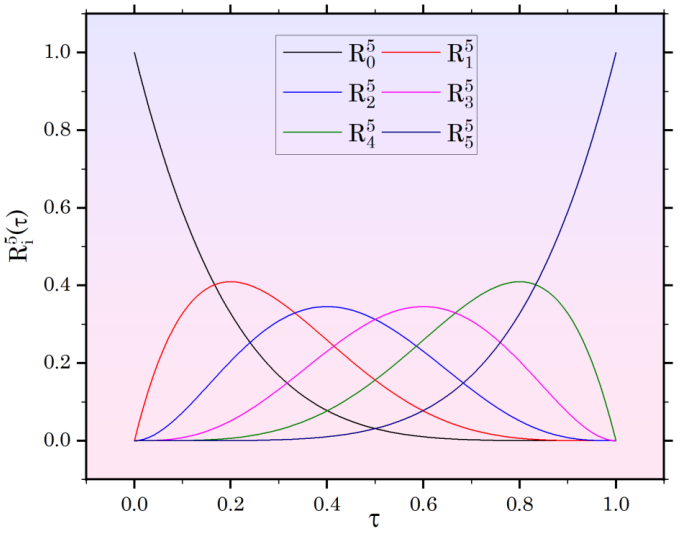

Fig.5.4 NURBS basis functions with $p = 5$

The ones of left curves are $P_1^L=\{0,3\}$, $P_2^L=\{-2,5\}$, $P_3^L=\{-4,4\}$, $P_4^L=\{1,2.5\}$, $P_5^L=\{-2,-2\}$, $P_6^L=\{0,0\}$, the control points of right curves are $P_1^R=\{0,3\}$, $P_2^R=\{2,5\}$, $P_3^R=\{4,4\}$, $P_4^R=\{-1,2.5\}$, $P_5^R=\{2,-2\}$, $P_6^R=\{0,0\}$. **Fig.5.1** displays the $p=3$ degree curve and its basis functions are presented in **Fig.5.3**. **Fig.5.2** shows the $p=5$ degree curve and its basis functions are presented in **Fig.5.4**. Hence, the higher the degree pth is, the farther away the control point is from the curve, and vice versa.

5.3.5 Geometric meaning of weighting factors

For NURBS curves, w_i can only affect part of the shape of the curve. When τ is the same, with the change of w_i, $P(\tau)$ is on the same straight line, as shown in Fig.5.5. When $w_i \to +\infty$, $R_{i,p}(u)=1$, $P(\tau)$ is vertex P_i; when $w_i=0$, $R_{i,p}(u)=0$, $P(\tau)$ is vertex B; and when $w_i \neq 0,1$, $P(u)$ is vertex B_i.

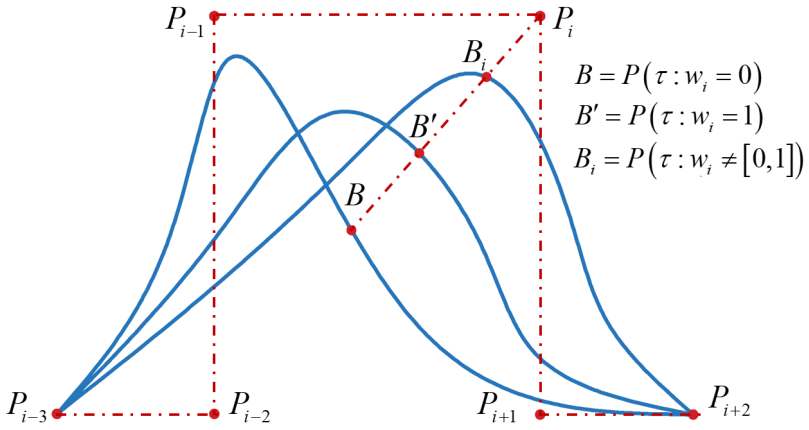

Fig.5.5 Geometric meaning of weighting factors

When all vertices and weighting factors do not change, the calculation formula of $R_{i,p}(u)$ changes from Eq.(5.25) to Eq.(5.16), let

$$\begin{cases} \alpha = R_{i,p}(\tau) = \dfrac{N_{i,p}(\tau)}{\sum\limits_{i\neq m=0}^{n} \omega_m N_{m,p}(\tau) + N_{i,p}(\tau)} & (\omega_i = 1) \\ \beta = R_{i,p}(\tau) = \dfrac{\omega_i N_{i,p}(\tau)}{\sum\limits_{i\neq m=0}^{n} \omega_m N_{m,p}(\tau) + N_{i,p}(\tau)} & (\omega_i \neq [0,1]) \end{cases} \tag{5.26}$$

Then the cross-ratio of the four points (P_i, B_i, B', B) can be obtained as

$$\frac{1-\alpha}{\alpha} : \frac{1-\beta}{\beta} = \frac{\sum\limits_{i\neq m=0}^{n} \omega_m N_{m,p}(\tau)}{N_{i,p}(\tau)} : \frac{\sum\limits_{i\neq m=0}^{n} \omega_m N_{m,p}(\tau)}{\omega_i N_{m,p}(\tau)} = \omega_i \tag{5.27}$$

It can be seen that the geometric meaning of w_i is: w_i is the value of the intersection ratio of the corresponding four points in the case that w_i is $+\infty$,0,1 and $w_i \neq 0,1$ respectively; when w_i increases, B_i approaches P_i; while when w_i decreases, B_i moves away from P_i.

5.3.6 Geometry reconstruction and field approximation

5.3.3.1 Geometry reconstruction

For most numerical simulation methods, geometry reconstruction and element discretisation are vital factors influencing the simulation. With the help of NURBS, discretisation errors can be avoided. Define an increasing and unique knot vector as $\Pi=\{s_1, s_2, \cdots, s_n\}$, then the NURBS boundary is discretised into isogeometric boundary elements as

$$\Gamma=\sum_{i=0}^{n-1}\Gamma_i\left[s_i, s_{i+1}\right] \tag{5.28}$$

where Γ_i is the ith element with its local parameter span $\left[s_i, s_{i+1}\right]$ which is shown in **Fig.5.6**.

(a) Global space (b) Parameter space

Fig.5.6 Isogeometric elements on the boundary

Hence, the NURBS-based geometry reconstruction can be expressed as the following

$$\mathbf{y}(\tau)=\sum_{i=0}^{m}\mathbf{R}_{i,p}(\tau)\mathbf{P}_i \tag{5.29}$$

Then, Eq.(5.2) can be discretised as

$$\begin{aligned} c_{ij}(\mathbf{x})u_i(\mathbf{x})=&\sum_{k=0}^{n-1}\int_{\Gamma_k}U_{ij}\left[\mathbf{x},\mathbf{y}(\tau)\right]t_j\left[\mathbf{y}(\tau)\right]J_{ac}\mathrm{d}\Gamma(\tau) \\ &-\sum_{k=0}^{n-1}\int_{\Gamma_k}T_{ij}\left[\mathbf{x},\mathbf{y}(\tau)\right]u_j\left[\mathbf{y}(\tau)\right]J_{ac}\mathrm{d}\Gamma(\tau)+D_1+D_2 \end{aligned} \tag{5.30}$$

where τ is the parameter relevant to ς, and the Jacob coefficient is written as

$$J_{ac}=\left[\left(\frac{\partial y_1}{\partial\tau}\right)^2+\left(\frac{\partial y_2}{\partial\tau}\right)^2\right]^{1/2} \tag{5.31}$$

5.3.3.2 Field approximation

For an element, the field approximation is conducted in the parameter space, then the node collocation is done. $u(\mathbf{x})$ and $t(\mathbf{x})$ of boundary nodes on the Γ_n are approximated as below

$$u_i(\mathbf{x}) = u_i\left\{\mathbf{x}\left[\tau(\eta)\right]\right\} = \sum_{m=0}^{k_n} \xi_n^m(\eta) u_i^{n,m} \tag{5.32}$$

$$t_i(\mathbf{x}) = t_i\left\{\mathbf{x}\left[\tau(\eta)\right]\right\} = \sum_{m=0}^{k_n} \xi_n^m(\eta) t_i^{n,m} \tag{5.33}$$

where $i = 1,2$, $\eta \in [-1, 1]$ represents the local coordinate of Γ_n, $u_i^{n,m}$ and $t_i^{n,m}$ are the displacement and traction for node η_n^m on the discretised boundary Γ_n, ξ_n^m symbolizes the shape function on the boundary Γ_n with $k_n + 1$ nodes. For liner element, ξ_n^m can be written as

$$\xi_n^0(\eta) = \frac{1-\eta}{2} \tag{5.34}$$

$$\xi_n^1(\eta) = \frac{1+\eta}{2} \tag{5.35}$$

on Γ_n, while, $\xi_n^m = 0$ for $\tau \notin \Gamma_n$.

Hence, Eq.(5.30) can be written in the following form by substituting the displacement and tractions in Eqs.(5.32) and (5.33)

$$\begin{aligned} c_{ij}(\mathbf{x}) u_i(\mathbf{x}) = & \sum_{l=0}^{n-1} \int_{\Gamma_l} U_{ij}\left\{\mathbf{x}, \mathbf{y}\left[\tau(\eta)\right]\right\} \sum_{m=0}^{k_n} \xi_l^m(\eta) t_i^{l,m} J_{ac}^1 J_{ac} \mathrm{d}\Gamma(\eta) \\ & - \sum_{l=0}^{n-1} \int_{\Gamma_l} T_{ij}\left\{\mathbf{x}, \mathbf{y}\left[\tau(\eta)\right]\right\} \sum_{m=0}^{k_n} \xi_l^m(\eta) u_i^{l,m} J_{ac}^1 J_{ac} \mathrm{d}\Gamma(\eta) + D_1 + D_2 \end{aligned} \tag{5.36}$$

where

$$J_{ac}^1 = \frac{\mathrm{d}\tau}{\mathrm{d}\eta} \tag{5.37}$$

5.4 The line integration BEM

To keep the advantage of boundary-only discretisation, the LIBEM is introduced. All the domain integrals can be dimensionally reduced to dimensionally. The basic theorem and equations are introduced below and one can find the detailed derivation process in ref. [57, 189, 190].

Based on LIM, the LIBEM is introduced to deal with domain integrals by reducing them into boundary integrals. So, Eqs.(5.4), (5.5), (5.10), (5.11) and

(5.12) can be transformed as

$$D_1 = \int_\Omega U_{ij}(\mathbf{x},\mathbf{y}) G_j(\mathbf{y}) \mathrm{d}\Omega(\mathbf{y}) = \sum_{m=0}^{M} n_{y_1}^m(\mathbf{y}) w^m J_{ac}^m \int_{L_m} U_{ij}(\mathbf{x},\mathbf{y}) G_j(\mathbf{y}) \mathrm{d}y_1 \tag{5.38}$$

$$D_2 = \int_\Omega \beta\Phi_i(\mathbf{x},\mathbf{y}) \theta(\mathbf{y}) \mathrm{d}\Omega(\mathbf{y}) = \sum_{m=0}^{M} n_{y_1}^m(\mathbf{y}) w^m J_{ac}^m \int_{L_m} \beta\Phi_i(\mathbf{x},\mathbf{y}) \theta(\mathbf{y}) \mathrm{d}y_1 \tag{5.39}$$

$$D_1 = \int_\Omega U_{ij}(\mathbf{x},\mathbf{y}) G_j(\mathbf{y}) \mathrm{d}\Omega(\mathbf{y}) = \sum_{m=0}^{M} n_{y_1}^m(\mathbf{y}) w^m J_{ac}^m \int_{L_m} U_{ij}(\mathbf{x},\mathbf{y}) G_j(\mathbf{y}) \mathrm{d}y_1 \tag{5.40}$$

$$D_4 = \int_\Omega \beta\Psi_{ij}(\mathbf{x},\mathbf{y}) \theta(\mathbf{x}) \mathrm{d}\Omega(\mathbf{y}) = \sum_{m=0}^{M} n_{\varsigma_1}^m(\boldsymbol{\varsigma}) w^m J_{ac}^m \int_{L_m} \beta\Psi_{ij}(\mathbf{x},\mathbf{y}) \theta(\mathbf{x}) \mathrm{d}y_1 \tag{5.41}$$

$$D_5 = \int_\Omega U_{ijk}(\mathbf{x},\mathbf{y}) G_j(\mathbf{y}) \mathrm{d}\Omega(\mathbf{y}) = \sum_{m=0}^{M} n_{\varsigma_1}^m(\mathbf{y}) w^m J_{ac}^m \int_{L_m} U_{ijk}(\mathbf{x},\mathbf{y}) G_j(\mathbf{y}) \mathrm{d}y_1 \tag{5.42}$$

Obviously, the domain integrals are avoided and can be computed with one-dimensional integrations.

5.5 Numerical examples

The examples in this section are simulated and analyzed to prove the accuracy and efficiency of the NURBS-LIBEM. The first numerical example targets showing the model reconstruction process based on NURBS and the correctness of the NURBS-LIBEM when dealing with thermo-elastic problems. Further, the gravity load is involved in the second example and the results prove the correctness of the NURBS-LIBEM as well. Furthermore, to prove that the NURBS-LIBEM is also efficient when dealing with complex models, the last model is presented and analyzed.

5.5.1 A beam considering thermal load

This example aims to show the process of geometry reconstruction with the NURBS theorem and prove that the NURBS-LIBEM can be applied to compute the stress and displacement of models under thermo-elasticity accurately.

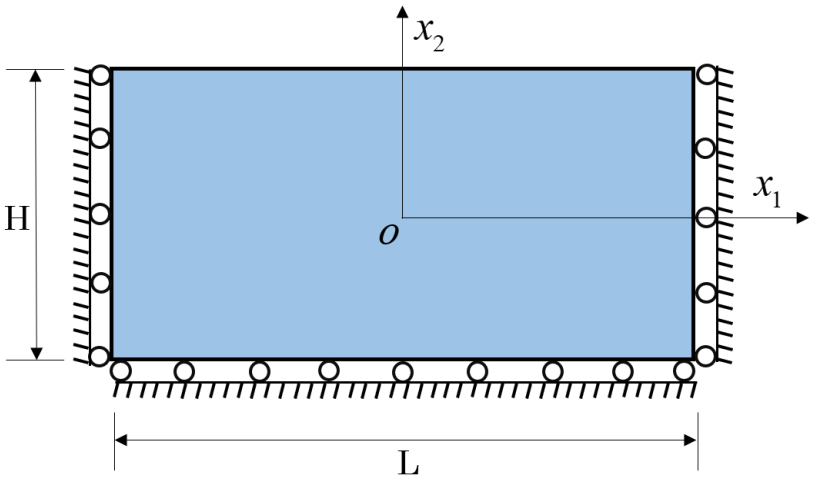

Fig.5.7 A beam considering thermal load

Table 5.1 Parameters of the beam

Length	L=2m
Width	H=1m
Poisson's ratio	v=0.3
Young's Modulus	E=10000Mpa
Thermal distribution	$\theta = 40x_2^2 - 60x_2$
Coefficient of thermal expansion	$\beta = 0.00001K^{-1}$

As one can see, the boundary condition is shown in **Fig.5.7**, The relevant geometric and mechanical parameters and the thermal distribution of this beam are shown in **Table 5.1**. Besides, this model is constructed with 4 separate and open NURBS curves which are shown in **Table 5.2** with their necessary data.

The analytical result of the displacement u_2 and stress σ_{11} are written below [184]

$$u_2(x_2) = \frac{1+v}{1-v}\beta\left\{\frac{40}{3}\left[x_2^3 + (H/2)^3\right] - 30\left[x_2^2 - (H/2)^2\right]\right\} \tag{5.43}$$

$$\sigma_{11} = -\frac{E}{1-v}\beta\theta \tag{5.44}$$

This model is discretised with 400 elements, to analyze the accuracy of NURBS-LIBEM, six points on the line $x_1 = 0$ are selected. The comparison of the displacement and inner stress is shown in **Table 5.3** and **Table 5.4**. It is clear to see that NURBS-LIBEM shows a high agreement with the exact solution. Calculated by the error estimation formula, the relative error of u_2 and σ_{11} are 3.2652×10^{-5} and 1.008×10^{-4}, which are rather low evidently.

Table 5.2 Parameters of NURBS curves for the beam

Curve endpoints	Knot vector	Control points	Weights
(-1, -0.5), (-1, 0.5)	0.0, 0.0, 0.0, 0.0, 1.0, 1.0, 1.0, 1.0	(-1.0, -0.5); (-1.0, -0.17); (-1.0, -0.17); (-1.0, 0.5)	1.0, 1.0, 1.0, 1.0
(-1, 0.5), (1, 0.5)	0.0, 0.0, 0.0, 0.0, 1.0, 1.0, 1.0, 1.0	(-1.0, 0.5); (-0.33, 0.5); (-0.33, 0.5); (1.0, 0.5)	1.0, 1.0, 1.0, 1.0
(1, 0.5), (-1, 0.5)	0.0, 0.0, 0.0, 0.0, 1.0, 1.0, 1.0, 1.0	(1.0, 0.5); (1.0, -0.17); (1.0, -0.17); (1.0, -0.5)	1.0, 1.0, 1.0, 1.0
(1, -0.5), (-1, -0.5)	0.0, 0.0, 0.0, 0.0, 1.0, 1.0, 1.0, 1.0	(1.0, -0.5); (0.33, -0.5); (-0.33, -0.5); (-1.0, -0.5)	1.0, 1.0, 1.0, 1.0

Table 5.3 The displacement $u_2\left(\times 10^{-5}\right)$ (MPa)

x_2/m	Analytical Results/m	LI-BEM/m
-0.375	7.88319	7.88311
-0.25	13.15476	13.1546
-0.125	16.10491	16.1047
0	17.02381	17.0235
0.125	16.20164	16.2012
0.25	13.92857	13.9279
0.375	10.49479	10.494

Table 5.4 The inner stress σ_{11} (MPa)

x_2/m	Analytical Results /MPa	LI-BEM/MPa
-0.375	-4.01786	-4.01819
-0.25	-2.50000	-2.5003
-0.125	-1.16071	-1.16098
0	0.00000	-0.00021
0.125	0.98214	0.981994
0.25	1.78571	1.78564
0.375	2.41071	2.41072

To figure out the trend of the displacement u_2 and the stress σ_{11}, **Figs.5.8** and **5.9** are drawn based on the 101 points pick from the line $x_1 = 0$. From **Fig.5.8**, one can see that the stress σ_{11} increases gradually with the increase of coordinates. And **Fig.5.9** shows that the displacement u_2 rises sharply with the increase of coordinate y firstly, then decreases slowly after reaching a peak. All in all, this numerical model shows the accuracy and efficiency of NURBS-LIBEM.

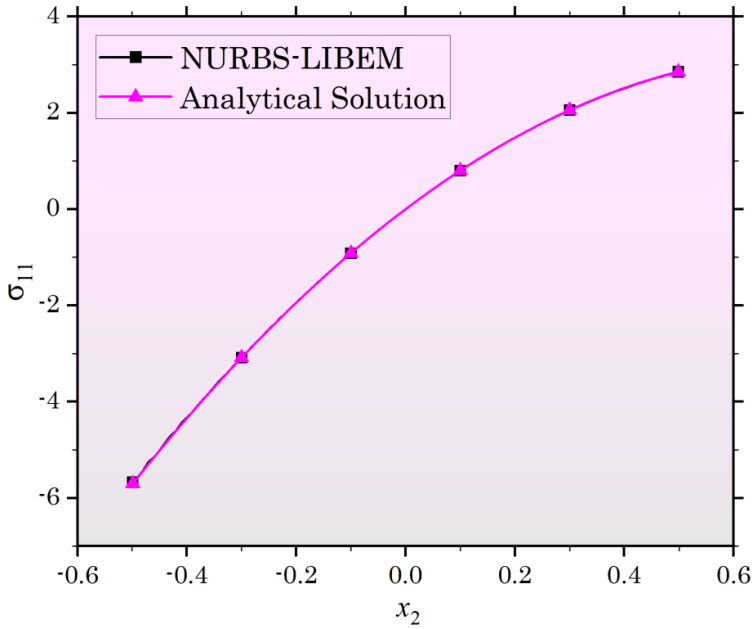

Fig.5.8 Comparison of σ_{11} with analytical results (Mpa)

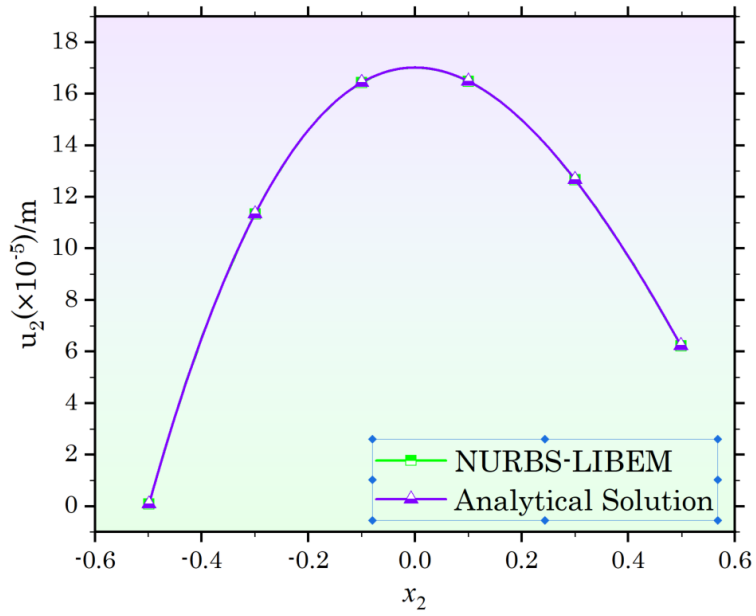

Fig.5.9 Comparison between u_2 and analytical results

Further, to prove the NURBS-LIBEM is convergent, as listed in **Table 5.5**, the model is discretised by boundary elements in different numbers. The displacement is taken as the analysis object and the same eight internal points are chosen, then one can obtain **Fig.5.10**. It is clear to see that the relative error decreases straight down with the increase of element number in the logarithmic coordinate system, which means the convergence of the NURBS-LIBEM is excellent. Besides, it is worth mentioning that the relative error of the displacement u_2 is smaller than that of the stress σ_{11} in any case.

Table 5.5 Different numbers of boundary elements

Cases	1	2	3	4	5	6	7
Element Number	20	40	80	160	320	640	1280

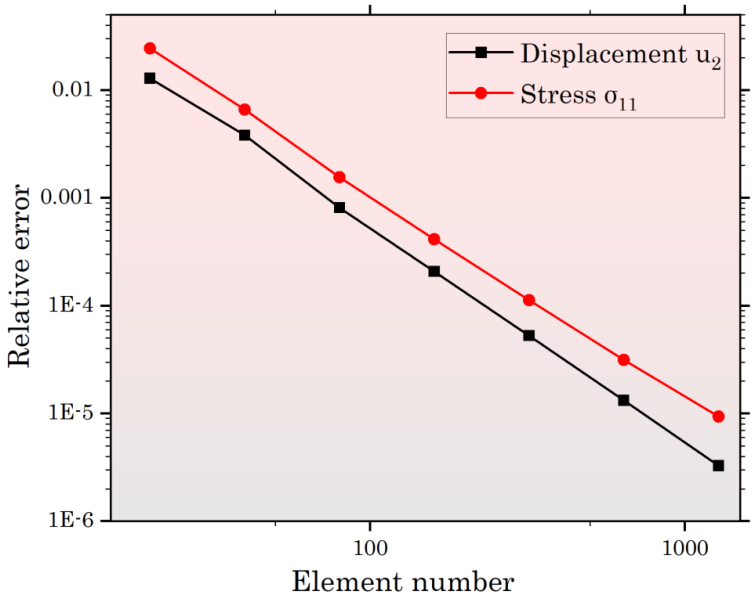

Fig.5.10 Relative error of u_2 and σ_{11}

5.5.2 A ring considering thermal and gravity loads

As one can see in **Fig.5.11**, the ring model is under uniform pressure. Obviously, it is a symmetrical model, hence, one can simplify the ring model and the simplified model is displayed in **Fig.5.12**. And the relevant parameters are listed in **Table 5.6**.

Table 5.6 Parameters of the ring

The outer radius	b=2
The inner radius	a=1
Young's Modulus	E=2.5
Poisson's ratio	v=0.3
Uniformly pressure	P=1.0
Acceleration of Gravity	g=10
Thermal distribution	θ=50 ^oC
Coefficient of thermal expansion	$\beta = 0.0001K^{-1}$

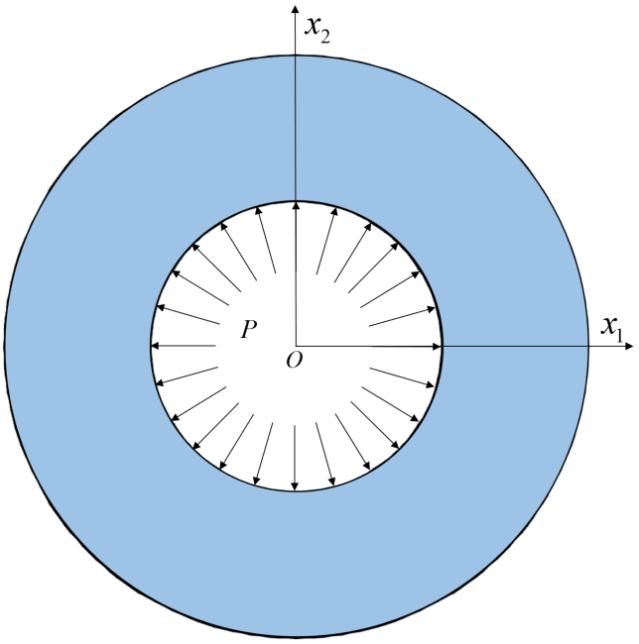

Fig.5.11 A ring model

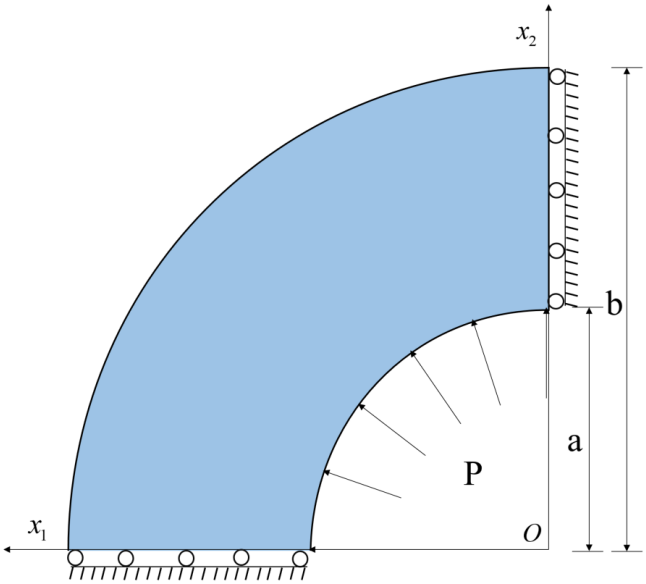

Fig.5.12 The simplified ring model

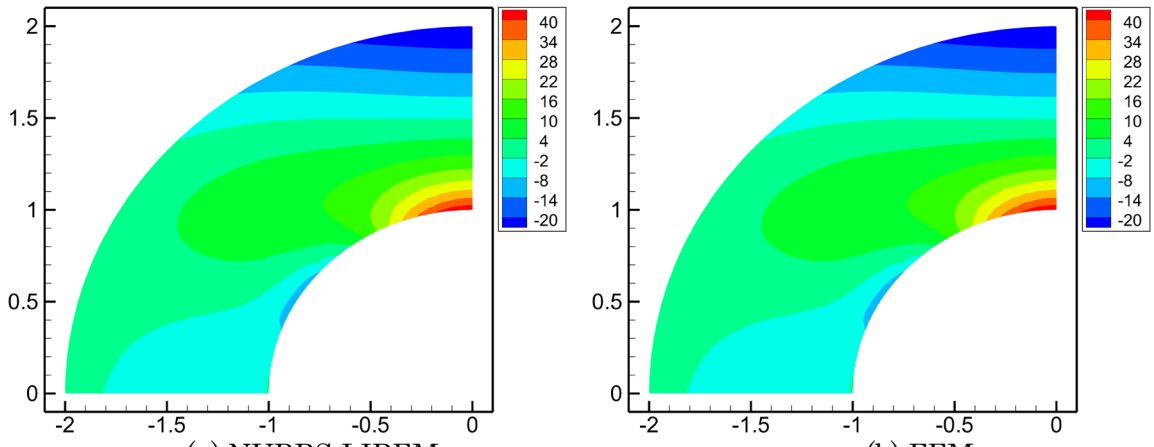

(a) NURBS-LIBEM (b) FEM

Fig.5.13 The contour map of σ_{11} (Mpa)

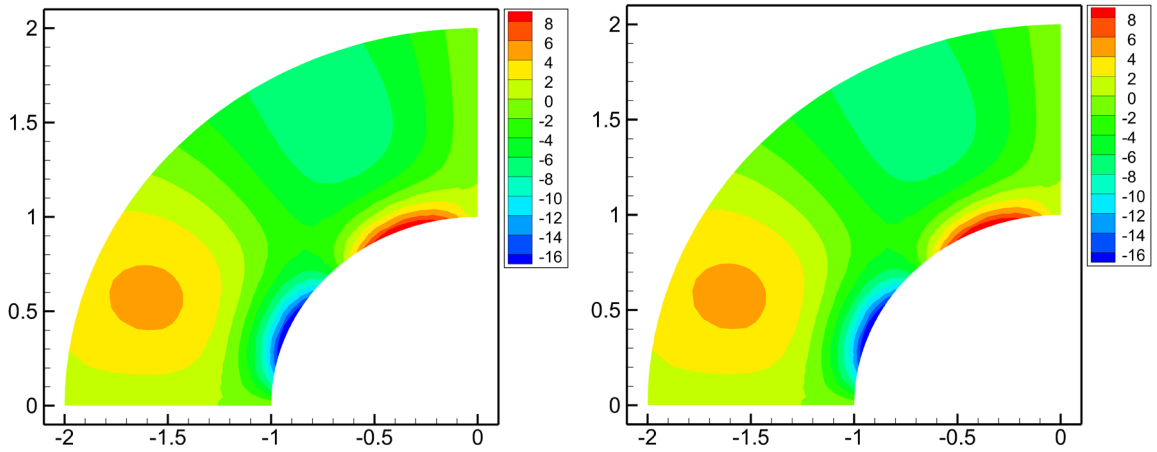

(a) NURBS-LIBEM (b) FEM

Fig.5.14 The contour map of σ_{12} (Mpa)

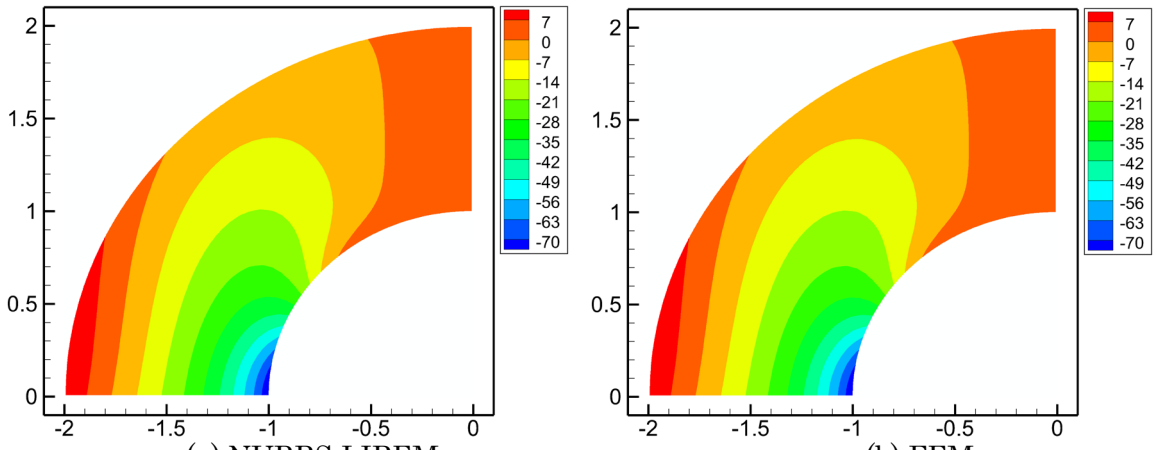

(a) NURBS-LIBEM (b) FEM

Fig.5.15 The contour map of σ_{22} (Mpa)

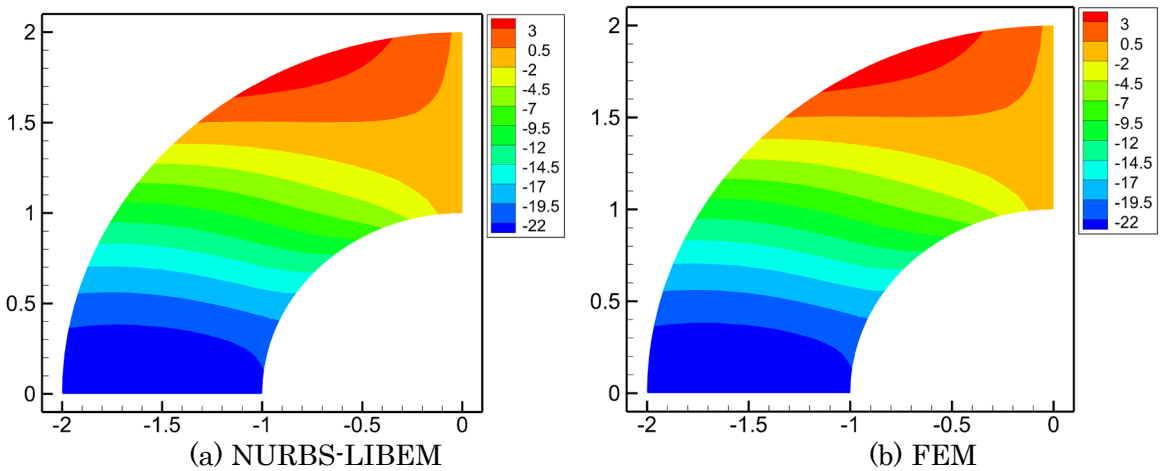

(a) NURBS-LIBEM (b) FEM

Fig.5.16 The contour map of u_1 (mm)

The boundary is discretised by 200 elements. No analytical solution is found for this numerical example, so the FEM simulation is carried out for comparison with the NURBS-LIBEM. As one can see, **Figs.5.13-17** show the comparison of the results of σ_{11}, σ_{12}, σ_{22}, u_1 and u_2. The contour map can tell

that the result of the NURBS-LIBEM highly agrees with the FEM results.

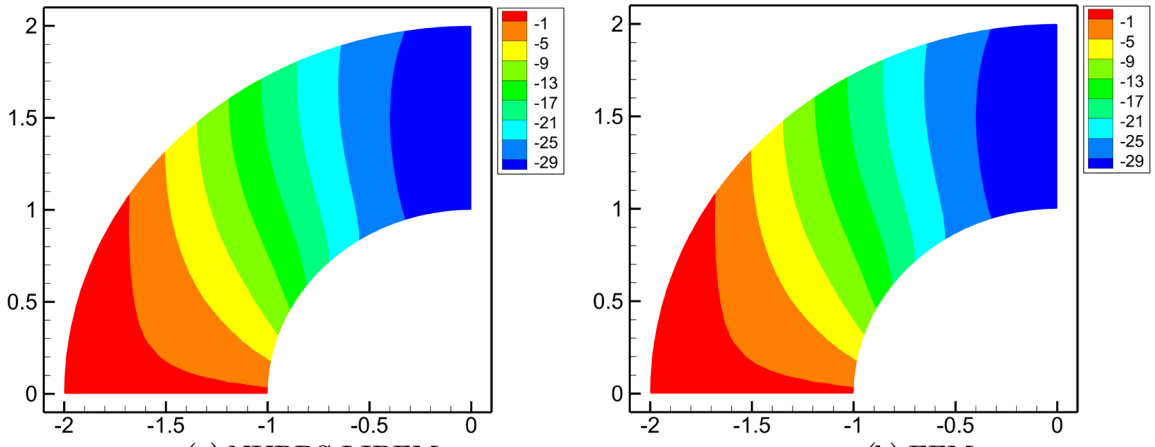

(a) NURBS-LIBEM (b) FEM

Fig.5.17 The contour map of u_2 (mm)

5.5.3 A complex model under thermal and gravity loads

To prove the correctness of NURBS-LIBEM when it comes to complex numerical models, this example is presented. The relevant parameters are shown in **Table 5.7**. Besides, one can refer to **Fig.5.18** for detailed boundary conditions of the complex model.

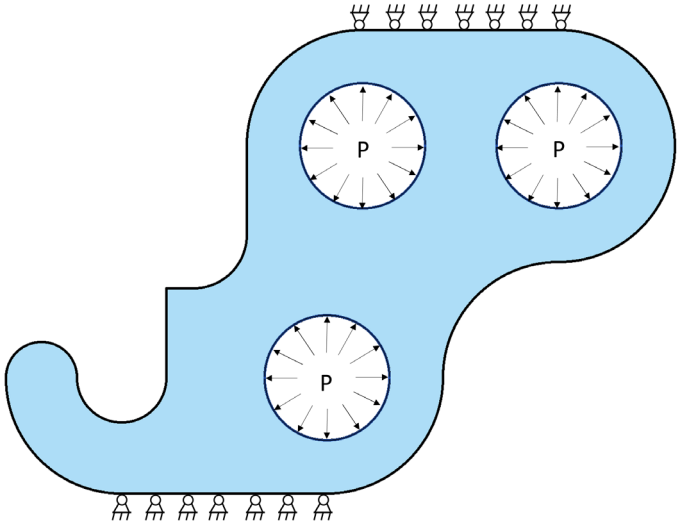

Fig.5.18 A complex model

Table 5.7 Parameters of the complex model

Young's Modulus	E=2.5
Poisson's ratio	v=0.3
Pressure	P=1.0
Gravity	g=10
Thermal distribution	θ=500 $^{\circ}C$
Coefficient of thermal expansion	$\beta = 0.0001K^{-1}$

According to **Figs.5.19** and **5.20**, the displacement u_1 and u_2 are shown by the contour map, and it is clear that the NURBS-LIBEM shows a great agreement with the FEM results. Moreover, the complex model is discretised by 800 elements, while discretised by FEM with 4407 elements, which is a much larger number. However, the results show a high coincidence, hence the high accuracy of BEM is proved by comparing it with FEM again. Further, this example proves that this new method can be widely used in complicated models under complicated conditions.

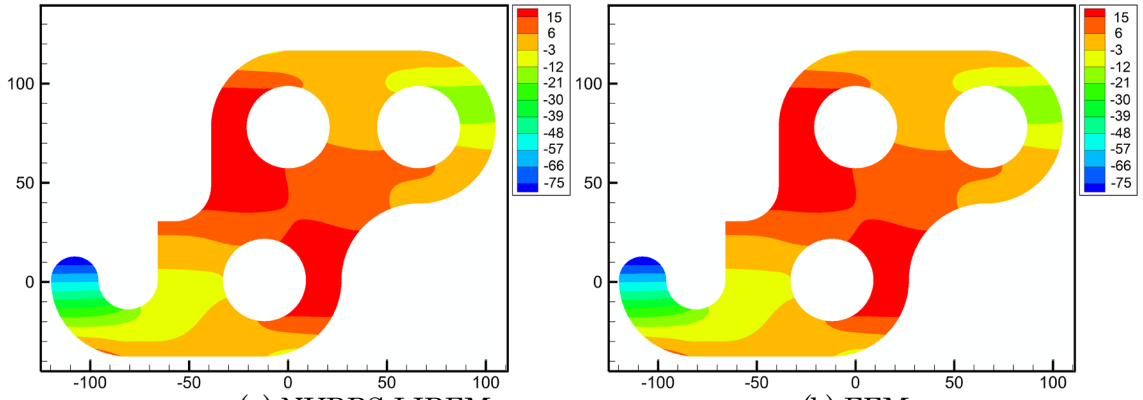

(a) NURBS-LIBEM (b) FEM

Fig.5.19 The contour map of $u_1\left(\times 10^3\right)$

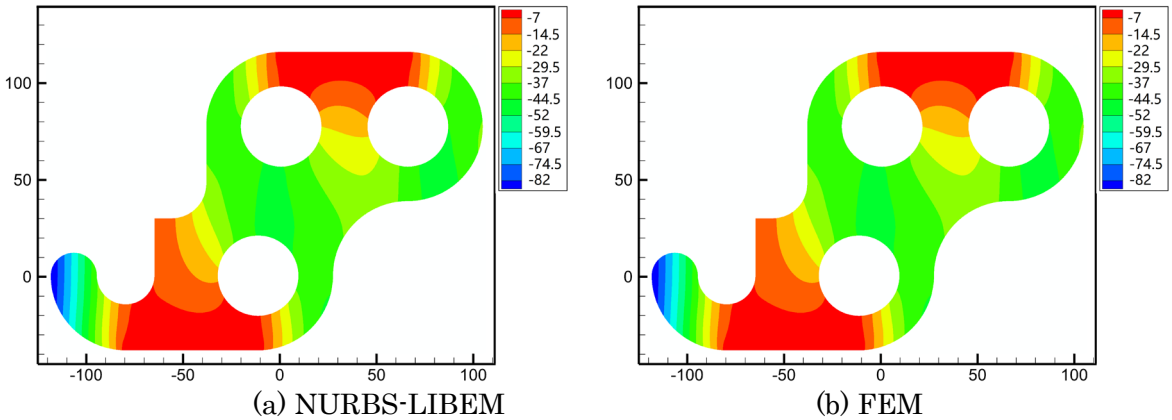

(a) NURBS-LIBEM (b) FEM

Fig.5.20 The contour map of $u_2\left(\times 10^3\right)$

Chapter 6

Solving 3D thermoelastic problems by the AOIMLS enhanced LIBEM

Summary

In this chapter, the AOIMLS enhanced LIBEM is applied to solve 3D thermo-elastic problems. When it comes to the case, only temperature boundary conditions are known which means the integrand functions in domain integrals are unknwon, the LIBEM can not be applied to transform domain integrals into boundary integrals directly. Thereby the AOIMLS enhanced LIBEM is proposed for dealing with the case when the BIEs contain domain integrals with unknown functions, as all the necessary temperature values for the integral points in LIM can be interpolated from discretise nodes by AOIMLS. In addition, the accuracy of the AOIMLS enhanced LIBEM is testified by numerical examples.

6.1 Introduction

Thermo-elastic problems [8, 9] are rather common in engineering structures. Thermo-elasticity is an important branch of solid mechanics as thermal stress [10, 11] can appear frequently whenever the structures, like engines or concrete components are enduring thermal shock or cooling while their expansion or volume reduction is restricted, which may further result in changes in mechanical behaviour, even failure.

This paper is organized as below, the BIEs for 3D thermo-elastic BIEs for displacement and internal stress, followed by the dimensional reduction of domain integrals by AOIMLS enhanced LIBEM. As the LIBME is applied to 3D thermo-elastic problems for the first time, hence, to prove the accuracy and convergence of the LIBEM, in **Section 6.4**, thermal distribution is set as known for thermo-elastic problems in the first numerical example. Further, the efficiency and accuracy of the new AOIMLS enhanced LIBEM for thermo-elastic problems are testified by the other numerical example.

6.2 Formulas of thermo-elastic problems

The governing equation of thermo-elastic problems can be written as follows

$$\begin{aligned}(\lambda+\mu)u_{j,ji}(\mathbf{x},\mathbf{y})+\mu u_{i,jj}(\mathbf{x},\mathbf{y})-\frac{\beta\lambda(1+\nu)}{\nu}\theta_{,i}(\mathbf{y})=0\\ i,j=1,\ 2,\ 3;\ \mathbf{x},\mathbf{y}\in\Omega\end{aligned} \tag{6.1}$$

where $u_{i,jj}$ and $u_{i,jj}$ symbolize the derivatives of displacement u, $i,j=1,2,3$, β symbolizes the coefficient of thermal expansion, θ represents temperature.

Based on Bett's reciprocal theorem, one can deduce the following regularized displacement BIE [203]

$$\begin{aligned}c_{ij}(\mathbf{x})u_i(\mathbf{x})=&\int_\Gamma U_{ij}(\mathbf{x},\mathbf{y})t_j(\mathbf{y})\mathrm{d}\Gamma(\mathbf{y})-\int_\Gamma T_{ij}(\mathbf{x},\mathbf{y})u_j(\mathbf{y})\mathrm{d}\Gamma(\mathbf{y})\\ &-\beta\int_\Omega \Phi_i(\mathbf{x},\mathbf{y})\theta(\mathbf{y})\mathrm{d}\Omega(\mathbf{y})\end{aligned} \tag{6.2}$$

and the regularized inner stress BIE can be obtained based on the strain-displacement relationship as below

$$\begin{aligned}\sigma_{ij}(\mathbf{x})=&\int_{\Gamma}U_{ijk}(\mathbf{x},\mathbf{y})t_k(\mathbf{y})\mathrm{d}\Gamma-\int_{\Gamma}\mathrm{T}_{ijk}(\mathbf{x},\mathbf{y})u_k(\mathbf{y})\mathrm{d}\Gamma\\&+\beta\theta(\mathbf{y})\int_{\Gamma}r_{,\mathrm{m}}n_m\ln(r^r)\varphi_{ij}(\mathbf{x},\mathbf{y})\mathrm{d}\Gamma(\mathbf{y})\\&+\int_{\Omega}\beta\varphi_{ij}(\mathbf{x},\mathbf{y})\theta(\mathbf{y})\mathrm{d}\Omega(\mathbf{y})\\&-\int_{\Omega}\beta\varphi_{ij}(\mathbf{x},\mathbf{y})\theta(\mathbf{x})\mathrm{d}\Omega(\mathbf{y})\\&-\delta_{ij}\beta b\theta(\mathbf{x})\end{aligned}\tag{6.3}$$

where the Kronecker symbol δ_{ij} can be written as

$$\delta_{ij}=\begin{cases}1 & i=j\\0 & i\neq j\end{cases}\tag{6.4}$$

and

$$r_{,i}=\frac{\partial r}{\partial\varsigma_i}\tag{6.5}$$

further, μ and λ are the Lame constants, v represents the Poisson ratio. And

$$\psi_i(\mathbf{x},\mathbf{y})=\frac{-(1+\nu)r_{,i}}{4\pi(1-\nu)r^2}\tag{6.6}$$

$$\phi_{ij}(\mathbf{x},\mathbf{y})=\frac{-\mu(1+\nu)}{2\pi(1-\nu)r^3}(\delta_{ij}-3r_{,i}r_{,j})\tag{6.7}$$

With Eq.(6.2), one can obtain the displacement for both internal and boundary points, and the stress of internal points can be got by Eq.(6.3). Clearly, there are three domain integrals in Eqs.(6.2) and (6.3) which can be written as

$$D_1=\int_{\Omega}\beta\psi_i(\mathbf{x},\mathbf{y})\theta(\mathbf{y})\mathrm{d}\Omega(\mathbf{y})\tag{6.8}$$

$$D_2=\int_{\Omega}\beta\phi_{ij}(\mathbf{x},\mathbf{y})\theta(\mathbf{y})\mathrm{d}\Omega(\mathbf{y})\tag{6.9}$$

$$D_3=\int_{\Omega}\beta\phi_{ij}(\mathbf{x},\mathbf{y})\theta(\mathbf{x})\mathrm{d}\Omega(\mathbf{y})\tag{6.10}$$

Here, two conditions should be considered, the first one is that the temperature distribution is known, i.e., the functions in domain integrals in Eqs.(6.8), (6.9) and (6.10) are known, hence, one can compute the above three domain integrals with LIM directly. The second condition is that the temperature distribution is unknown, one needs to simulate the thermal field by heat conduction BIEs at first, and then one can obtain the temperature value of pre-defined nodes both in the domain and on boundaries. But it is not realistic to compute all the necessary values for line integration points, thereby the AOIMLS enhanced LIBEM is needed for this case, i.e., the domain

integrals with unknown functions. The two conditions are considered and analyzed in **Section 6.4**.

6.3 The AOIMLS enhanced LIBEM

Eq.(3.9) can be applied for the case, thermo-elasticity analysis with known temperature distribution, i.e., domain integrals with known function. So, Eqs.(6.8), (6.9) and (6.10) are written in the following form

$$D_1=\int_\Omega \beta\psi_i(\mathbf{x},\mathbf{y})\theta(\mathbf{y})\mathrm{d}\Omega(\mathbf{y})=\sum_{i=1}^{M} n_{y_1}^i(\mathbf{y})\omega^i\beta\int_{L_i}\psi_i(\mathbf{x},\mathbf{y})\theta(\mathbf{y})\mathrm{d}y_1 \tag{6.11}$$

$$D_2=\int_\Omega \beta\phi_{ij}(\mathbf{x},\mathbf{y})\theta(\mathbf{y})\mathrm{d}\Omega(\mathbf{y})=\sum_{i=1}^{M} n_{y_1}^i(\mathbf{y})\omega^i\beta\int_{L_i}\phi_{ij}(\mathbf{x},\mathbf{y})\theta(\mathbf{y})\mathrm{d}y_1 \tag{6.12}$$

$$D_3=\int_\Omega \beta\phi_{ij}(\mathbf{x},\mathbf{y})\theta(\mathbf{x})\mathrm{d}\Omega(\mathbf{y})=\sum_{i=1}^{M} n_{y_1}^i(\mathbf{y})\omega^i\beta\int_{L_i}\phi_{ij}(\mathbf{x},\mathbf{y})\theta(\mathbf{x})\mathrm{d}y_1 \tag{6.13}$$

If the temperature distribution is unknown, then the domain integral in Eqs.(6.11), (6.12) and (6.13) can be dimensionally reduced by the AOIMLS enhanced LIBEM to the following forms

$$D_1=\int_\Omega \beta\psi_i(\mathbf{x},\mathbf{y})\theta(\mathbf{y})\mathrm{d}\Omega(\mathbf{y})=\sum_{k=1}^{N}\sum_{i=1}^{M} n_{y_1}^i(\mathbf{y})\omega^i\beta\int_{L_i}\psi_i(\mathbf{x},\mathbf{y})\varphi_k(\mathbf{y})\mathrm{d}y_1\theta_k(\mathbf{y}) \tag{6.14}$$

$$D_2=\int_\Omega \beta\phi_{ij}(\mathbf{x},\mathbf{y})\theta(\mathbf{y})\mathrm{d}\Omega(\mathbf{y})=\sum_{k=1}^{N}\sum_{i=1}^{M} n_{y_1}^i(\mathbf{y})\omega^i\beta\int_{L_i}\phi_{ij}(\mathbf{x},\mathbf{y})\varphi_k(\mathbf{y})\mathrm{d}y_1\theta_k(\mathbf{y}) \tag{6.15}$$

$$D_3=\int_\Omega \beta\phi_{ij}(\mathbf{x},\mathbf{y})\theta(\mathbf{x})\mathrm{d}\Omega(\mathbf{y})=\sum_{k=1}^{N}\sum_{i=1}^{M} n_{y_1}^i(\mathbf{y})\omega^i\beta\int_{L_i}\phi_{ij}(\mathbf{x},\mathbf{y})\varphi_k(\mathbf{y})\mathrm{d}y_1\theta_k(\mathbf{x}) \tag{6.16}$$

6.4 Numerical examples

To testify to the efficiency and correctness of the AOIIMLS enhanced LIBEM for 3D thermo-elastic problems, two numerical examples are calculated and analyzed. The first example target proving the accuracy of LIBEM for 3D thermo-elastic problems with known temperature distribution by comparing the results with the analytical solution. Further, the second complicated example, a torus, is used to prove the AOIIMLS enhanced LIBEM has the ability for simulating thermo-elastic problems with unknown temperature distribution by comparing it with FEM analysis. It is worth mentioning that in this section, all the examples are built in the Cartesian coordinate system.

Besides, the relative error used in this section is defined in Section 3.5.

6.4.1 A cube under thermal load

In this example, centred at {0, 0, 0} in the Cartesian coordinate system and bounded by the planes $x=\pm 1$, $y=\pm 1$ and $z=\pm 1$, a cube bearing thermal stress is considered (see **Fig.6.1**), and its geometrical and mechanical parameters are listed in **Table 6.1** respectively. The cube is set with a free upper plane, $z=1$ and the other five bounded planes are supported with a roller condition.

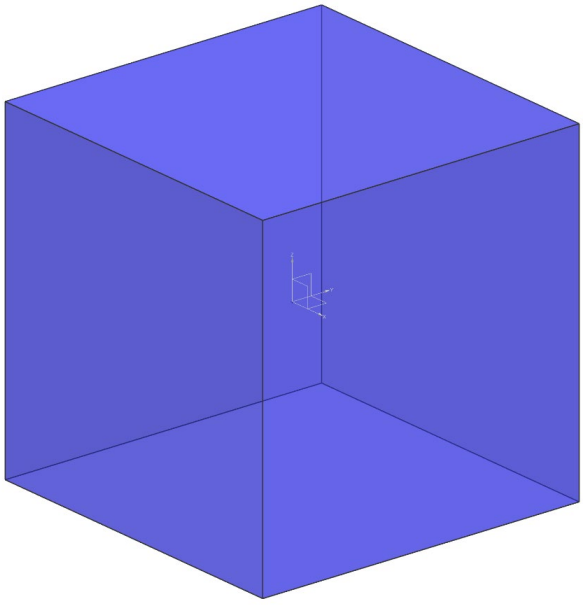

Fig.6.1 A cube under thermal load

Without losing generalization, for an isotropic rectangular or cuboid with θ_1 at the upper boundary, θ_2 at the below boundary, the temperature distribution can be given as below [204]

$$\theta=C_1 z^2+C_2 z+C_3 \tag{6.17}$$

where $C_1=\dfrac{(\theta_1+\theta_2)}{L^2}$, $C_2=\dfrac{(\theta_1-\theta_2)}{L}$ $C_3=2\theta_1+\theta_2$.

For simplicity, the temperature distribution in this example is presented in **Table 6.1**. And one can obtain the analytical solution of its displacement and stress as

$$u_z(z)=\frac{1+v}{1-v}\beta\left\{\frac{1}{3}C_1\left[z^3+(L/2)^3\right]+\frac{1}{2}C_2\left[z^2-(L/2)^2\right]+C_3\left[z+L/2\right]\right\} \tag{6.18}$$

$$\sigma_x=-\frac{E}{1-v}\beta\theta \tag{6.19}$$

Table 6.1 Parameters of the cube

Side length	L=2m
Poisson's ratio	v=0.3
Young's Modulus	E=10000Mpa
Temperature distribution	$\theta=z^2+10z$
Thermal expansion coefficient	$\beta=0.00001K^{-1}$

In order to show the accuracy of the LIBEM, eight points, (0, 0, -0.8), (0, 0, -0.6), (0, 0, -0.4), (0, 0, -0.2), (0, 0, 0.0), (0, 0, 0.2), (0, 0, 0.4), (0, 0, 0.6) and (0, 0, 0.8) are selected for comparing their displacement and stress with the analytical solution. See **Fig.6.2**, obviously, the result of the proposed method agrees with the analytical solution very well at the selected internal points. It is worth mentioning that the boundaries of the cube are discretised with 612 elements. Hence, this demonstrates that the developed method can be used for calculating thermo-elastic problems and presenting satisfying results. Furthermore, as one can see in **Fig.6.3**, the length of red bars represents the relative error of discretised nodes, clearly, the closer the position of the discretised node is to the boundary, the higher the relative error is. In addition, the maximum value of relative errors is 0.42.

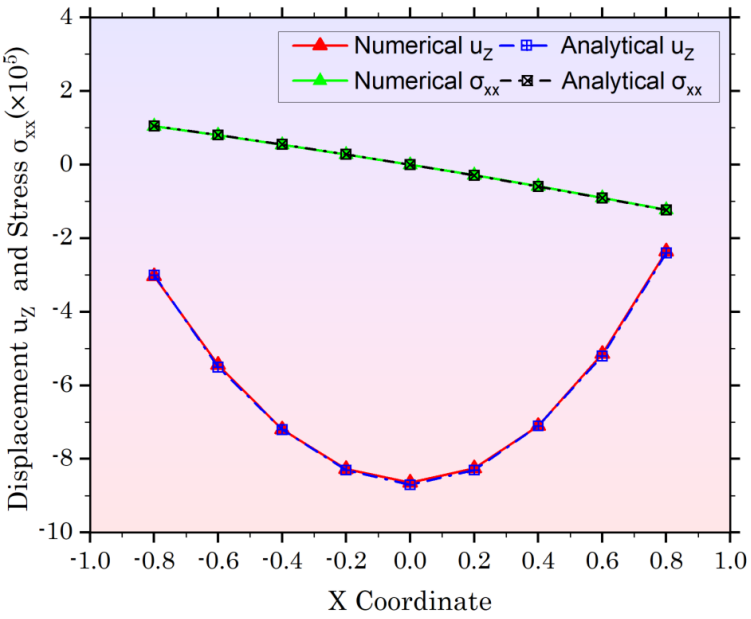

Fig.6.2 Comparison of displacement and stress

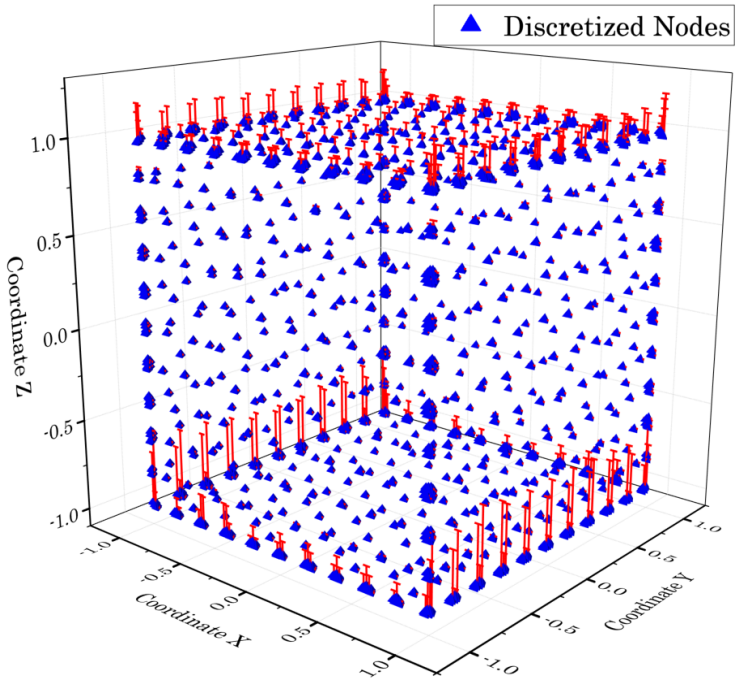

Fig.6.3 Relative error distribution of displacement

Further, to show the convergence of the LIBEM, the bounded planes of the cube are discretised with elements in different amounts as shown in **Fig.6.4**. The displacement u_z is taken as the analysis object and the same eight internal points are chosen, and the relative error is calculated, and one can obtain **Fig.6.5**. It is clearly shown that, in the logarithmic coordinate system, with the increase of boundary element amount, the relative error decreases straight down, which means the convergence of the LIBEM is excellent. It is worth mentioning that the relative error is 1.23%, which is satisfying when the boundaries are discretised by only 204 elements.

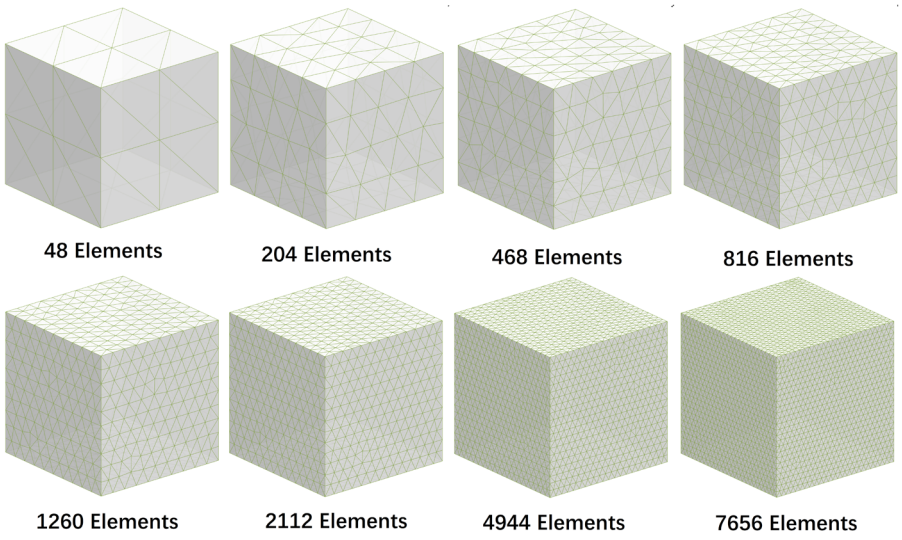

Fig.6.4 Boundary discretisation with different amounts of elements

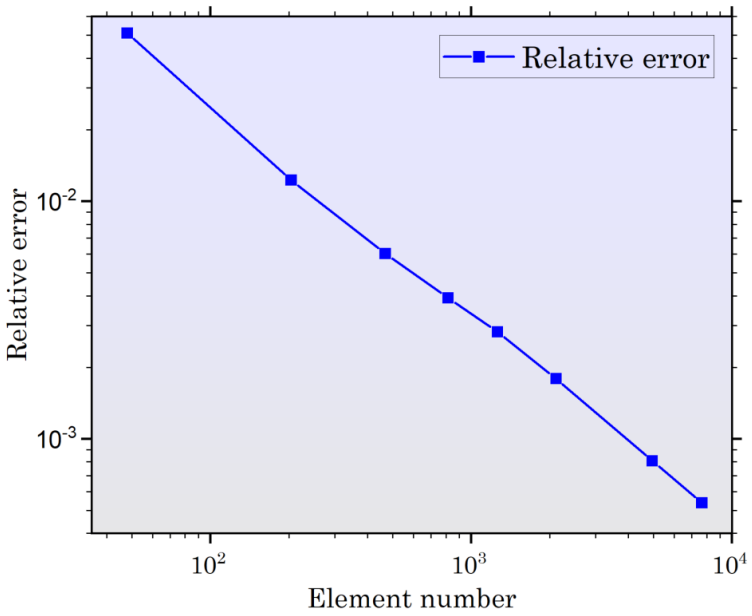

Fig.6.5 Relative error of displacement u_z

6.4.2 A torus under thermal load

For proving the correctness of the new AOIMLS enhanced LIBEM for thermo-elasticity when it comes to unknown temperature distribution, a torus (see **Fig.6.6**) under unknown temperature distribution is considered. This model is symmetric about the plane $z=0$, and the necessary geometry information of this model can be seen in **Figs.6.6** and **6.7**.

In addition, the geometrical and mechanical parameters are shown in **Table 6.2**. As to the boundary condition of this numerical model, the temperature of the inner and outer curved surfaces are set at 0 °C and 100 °C respectively, the other two sides are defined as thermal insulated.

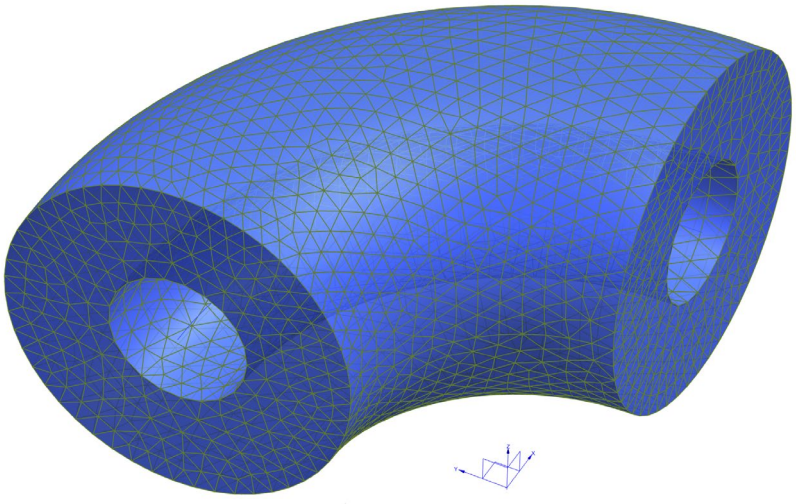

Fig.6.6 A torus bearing thermal load

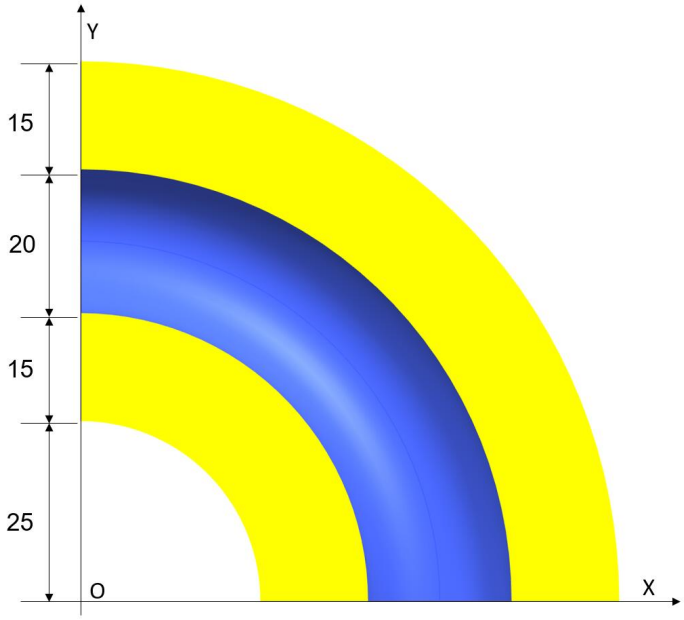

Fig.6.7 Geometry information of the torus

During thermo-elasticity analysis, the inner and outer curved surfaces are free while the other two surfaces of the torus are fixed. And the basic mechanic parameters are listed in **Table 6.2**. Also, to approximate the unknowns involved in domain integrals, 1632 points are distributed inside the model.

Table 6.2 Parameters of the cylinder

Poisson's ratio	v=0.35
Young's modulus	E=1000Mpa
Thermal conductivity	T=10 W/(m·K)
Thermal expansion coefficient	β =0.00002K^{-1}

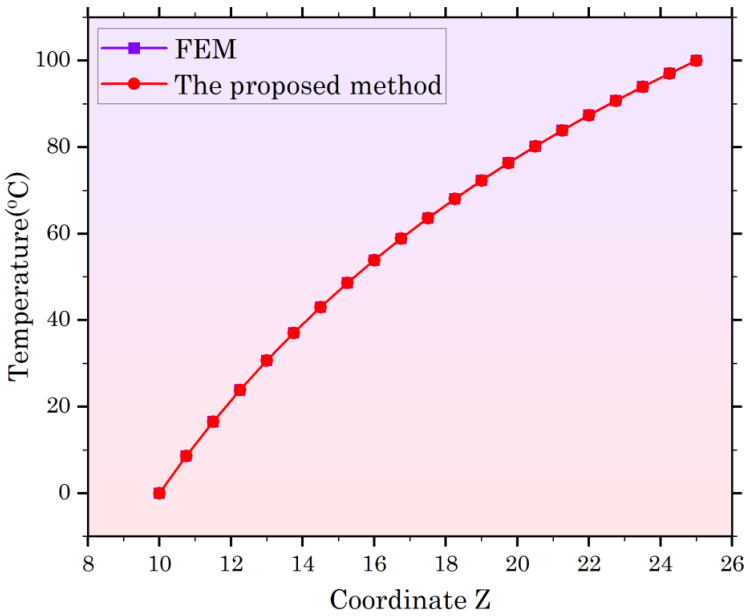

Fig.6.8 The temperature distribution

As there is no analytical solution to this example, the results of the developed method are compared with the FEM analysis. Firstly, the results of heat conduction simulation are analyzed, and a set of nodes are picked along a straight line with two endpoints {0, 0, 10} and {0, 0, 25}. As one can see in **Fig.6.8**, the temperature value increases stably and the proposed method is highly consistent with the FEM.

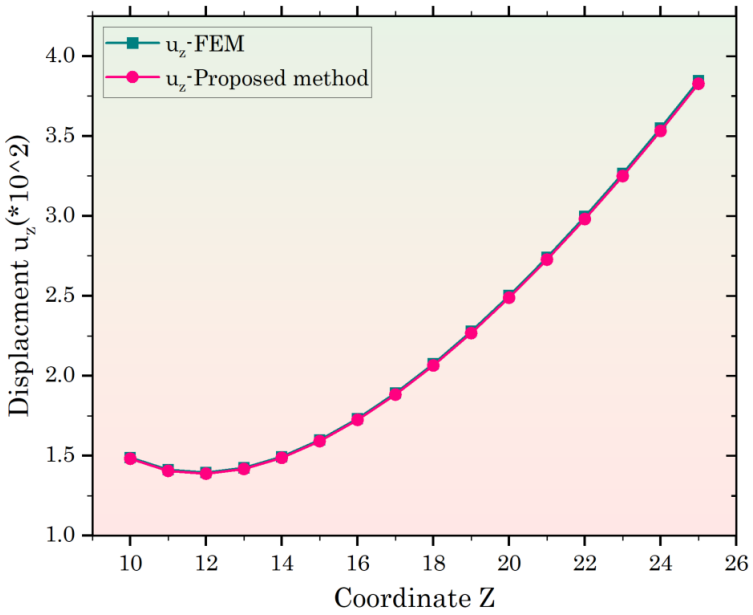

Fig.6.9 Comparison of displacement u_z

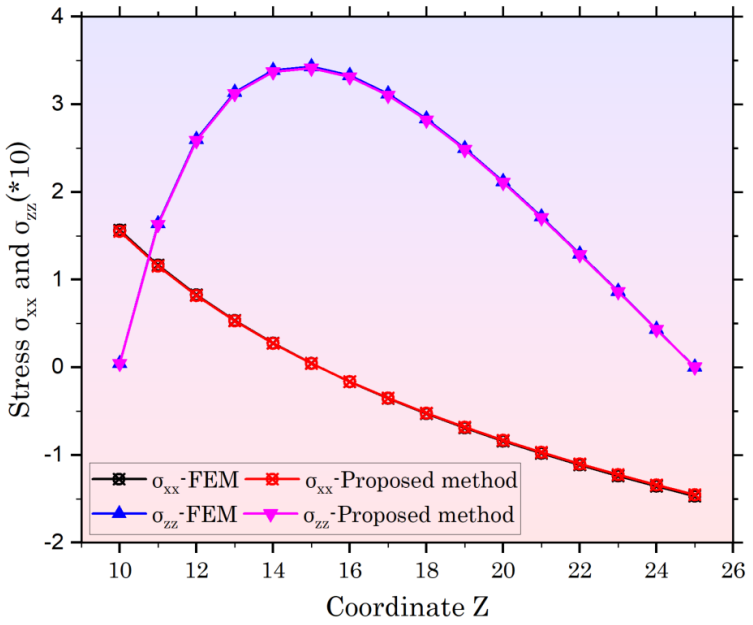

Fig.6.10 Comparison of stress

Further, the results, both the displacement and stress are analyzed. As one can see, in **Fig.6.9**, the displacement u_z decreases slightly at the beginning

followed by a stable increase with the increase of coordinate *z*. According to **Fig.6.10**, the stress σ_{xx} and σ_{zz} show a different trend, σ_{xx} decreasing stably, while σ_{zz} showing a rising trend before decreasing. All in all, the results of the developed method highly agree with the FEM.

Chapter 7

Formulations of displacement discontinuity method for crack problems based on boundary element method

Summary

In this chapter, formulations of the displacement discontinuity method (DDM) for crack problems based on BEM are proposed in finite domains. Four different boundary element methods, i.e., the conventional direct displacement boundary element method (CBEM), the hyper-singular traction direct boundary element (HBEM), the displacement discontinue indirect boundary element method (DD-IBEM), and the fictitious stress indirect boundary element method (FS-IBEM), are considered. The original two indirect boundary element methods are unstable and may obtain inaccurate results, and a new modified method is applied to improve the accuracy. Numerical examples have been proposed to demonstrate the accuracy of the proposed methods.

7.1 Introduction

For engineering structures, crack problems [205-207] is rather common and can result in structural failure if not treated cautiously [208, 209]. Thus, carrying out research on the features and behaviours of cracks that existed in engineering materials is vital. Actually, many types of research have been carried out by researchers with various methods, such as the FEM, extend FEM [210], boundary node method [211, 212], cellular automaton method [213, 214] and so on.

Moreover, BEM has drawn the attention of people as well which converts the governing differential equation into a boundary integral equation based on Green's formula and kelvin's fundamental solution to the problem. And it presents its advantages, like boundary-only discretisation, compared to other numerical methods. The BEM theory for elastic problems can be divided into two basic methods, the direct BEM and indirect BEM, both based on kelvin's fundamental solution. The direct BEM is used to calculate the unknown displacement and traction on the boundary with the known boundary conditions, further, the displacement and stress of the inner field can be computed. While, the indirect BEM, which mainly includes FSM and DDM, is based on Kelvin's fundamental solution and the distribution density function of hypothetical virtual values on the boundary, the boundary distribution density function itself has no specific physical meaning. However, Zhang et al. pointed out that the indirect BEM cannot give accurate results sometimes [215], due to the rigid displacement is not subtracted from the displacement field. To gain more exact data, a new modified indirect BEM is proposed in this chapter.

For solving crack problems based on BEM, lots of methods are devised, like the dual boundary element method, the Green's function method, the sub-regions method and the DDM. The dual boundary element method can also be applied to crack methods [216-218], and its theorem was presented by Hong and Chen [219]. Romlay et al. [220] used the dual boundary element method to solve the crack propagation problem latterly. For Green's function method [221], it can

only be used for a single straight traction-free crack. And the main weakness of the sub-regions method [222] is that the introduction of artificial boundaries is not unique, therefore, it cannot be easily implemented into an automatic procedure. The DDM, systematically developed by Crouch [223] to solve 2D elastic crack problems, is rather popular in that field since its creation. Liu and Li [97] have proved the equivalence of DDM and BEM for crack problems. Furthermore, the propagation of cracks is studied by DDM as well.

In this research, four kinds of BIEs for crack problems are proposed based on DDM. The first two BIEs, called CBEM and HBEM, both originated from direct BEM and DDM. The latter two, DD-IBEM and FS-IBEM are derived from the indirect BEM and DDM. All these four BIEs will be described particularly in **Sections 7.2** and **7.3**. In addition, the result of the indirect BEM is not satisfying, therefore, a new modified indirect BEM (M-DD-IBEM and M-FS-IBEM) is introduced (seeing **Section 7.3.3**), compared to the theoretical result in **Section 7.4.1**, one can notice that the result improved apparently. But it must be committed that the indirect BEM is not as good as the direct BEM in the aspect of accuracy and stability. And the indirect BEM is very sensitive to boundary conditions.

7.2 The direct BIEs

In this section, the BIEs for direct BEM for 2D elasticity problems are introduced, and the indirect BIEs with cracks are derived from direct BEM.

Suppose Ω is a bounded domain with boundary $\partial\Omega = \Gamma$ and crack area V with crack surface $S = S^+ \bigcup S^-$ in $\mathbb{R}^2$ (see **Fig.7.1**). The whole space $\mathbb{R}^2$ can be partitioned into three domains as: (I) Ω with boundary $\Gamma \bigcup S$; (II) Ω^∞ with boundary Γ and (III) V with boundary S. Then BIEs can be obtained separately for these three domains and BIEs for domain (I) and (II) are applied to obtain the BIEs for crack problems.

7.2.1 BIE for domain (I)

For elasticity problems, one can suppose $\sigma_{ij,j}(\mathbf{x}) = 0$ on Ω, where $\boldsymbol{\sigma}$ are the stress tensor. Then one can have the well-known conventional boundary

integral equation as

$$\int_{\Gamma\cup S}\left[U_{ij}(\mathbf{x},\mathbf{y})t_j(\mathbf{y})-T_{ij}(\mathbf{x},\mathbf{y})u_j(\mathbf{y})\right]\mathrm{d}\Gamma(\mathbf{y})=\begin{cases}u_i(\mathbf{x}), & \mathbf{x}\in\Omega\\ c_{ij}(\mathbf{x})u_i(\mathbf{x}), & \mathbf{x}\in\Gamma\cup S\\ \mathbf{0}, & \mathbf{x}\in\Omega^{\infty}\cup V\end{cases}\qquad(7.1)$$

where point $\mathbf{x},\mathbf{y}\in\mathbb{R}^2$, $2\pi\cdot c_{ij}(\mathbf{x})$ is the interior boundary angle at $\mathbf{x}$ and $c_{ij}(\mathbf{x})=0.5$ if the position of $\mathbf{x}$ is smooth. $u_i(\mathbf{x})$ and $t_i(\mathbf{y})$ are the displacement and traction.

The corresponding BIE for direct traction (hyper singular) BEM is

$$\int_{\Gamma\cup S}\left[K_{ik}(\mathbf{x},\mathbf{y})t_k(\mathbf{y})-H_{ik}(\mathbf{x},\mathbf{y})u_k(\mathbf{y})\right]\mathrm{d}\Gamma(\mathbf{y})=\begin{cases}t_j(\mathbf{x}), & \mathbf{x}\in\Omega\\ c_{ij}(\mathbf{x})t_j(\mathbf{x}), & \mathbf{x}\in\Gamma\cup S\\ \mathbf{0}, & \mathbf{x}\in\Omega^{\infty}\cup V\end{cases}\qquad(7.2)$$

where $n_i(\mathbf{y})$ is the unit outward normal and $\Omega^{\infty}=\mathbb{R}^2\setminus\bar{\Omega}$, $\bar{\Omega}=\Omega\cup\Gamma\cup V\cup S$.

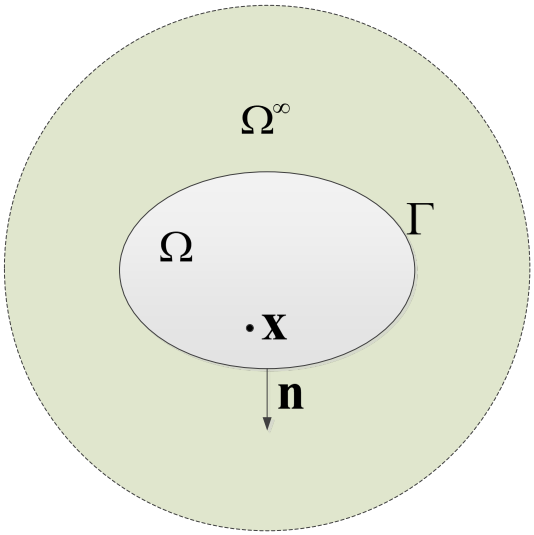

Fig.7.1 Bounded domain in 2D

7.2.2 BIE for domain (II)

Domain (II) Ω^{∞} can be considered as an exterior problem with control function $\sigma^{\mathrm{ex}}_{ij,j}(\mathbf{x})=0$ on Ω^{∞}, where $\sigma^{\mathrm{ex}}_{ij,j}(\mathbf{x})$ are the relative stress. Suppose

$$\sup_{\mathbf{x}\in\bar{\Omega}^{\infty}}|u_{ij}(\mathbf{x})|<\infty\qquad(7.3)$$

where $\bar{\Omega}^{\infty}=\Omega^{\infty}\bigcup\Gamma$. The displacements $u_{ij}^{\mathrm{ex}}(\infty)$ are displacements at points when $\mathbf{x}$ tend to ∞, are assumed to be zero usually which can lead to unacceptably inaccurate results, this will be discussed in **Section 7.3.3**, and then,

$$\int_{\Gamma\cup S}\left[\widehat{U}_{ij}\left(\mathbf{x},\mathbf{y}\right)t_j^{ex}\left(\mathbf{y}\right)-\widehat{T}_{ij}\left(\mathbf{x},\mathbf{y}\right)u_j^{ex}\left(\mathbf{y}\right)\right]\mathrm{d}\Gamma\left(\mathbf{y}\right)$$
$$=\begin{cases}u_i^{ex}\left(\mathbf{x}\right)-u_{ij}{}^{\mathrm{ex}}\left(\infty\right), & \mathbf{x}\in\Omega^{\infty}\\ \left[1-c_{ij}\left(\mathbf{x}\right)\right]u_i^{ex}\left(\mathbf{x}\right)-u_{ij}{}^{\mathrm{ex}}\left(\infty\right), & \mathbf{x}\in\Gamma\\ \mathbf{0}, & \mathbf{x}\in\Omega\cup V\cup S\end{cases} \tag{7.4}$$

and

$$\int_{\Gamma\cup S}\left[\widehat{K}_{ik}\left(\mathbf{x},\mathbf{y}\right)t_k^{ex}\left(\mathbf{y}\right)-\widehat{H}_{ik}\left(\mathbf{x},\mathbf{y}\right)\left(\mathbf{y}\right)u_k^{ex}\right]\mathrm{d}\Gamma\left(\mathbf{y}\right)=\begin{cases}[1-c_{ij}\left(\mathbf{x}\right)]t_j^{ex}\left(\mathbf{x}\right), & \mathbf{x}\in\Gamma\\ \mathbf{0}, & \mathbf{x}\in\Omega\cup V\cup S\end{cases} \tag{7.5}$$

where one can obtain

$$\begin{cases}\widehat{U}_{ij}\left(\mathbf{x},\mathbf{y}\right)=U_{ij}\left(\mathbf{x},\mathbf{y}\right)\\ \widehat{T}_{ij}\left(\mathbf{x},\mathbf{y}\right)=-T_{ij}\left(\mathbf{x},\mathbf{y}\right)\\ \widehat{K}_{ik}\left(\mathbf{x},\mathbf{y}\right)=-K_{ik}\left(\mathbf{x},\mathbf{y}\right)\\ \widehat{H}_{ik}\left(\mathbf{x},\mathbf{y}\right)=H_{ik}\left(\mathbf{x},\mathbf{y}\right)\end{cases} \tag{7.6}$$

Then Eqs.(7.4) and (7.5) can be written as

$$\int_{\Gamma\cup S}\left[U_{ij}\left(\mathbf{x},\mathbf{y}\right)t_j^{ex}\left(\mathbf{y}\right)+T_{ij}\left(\mathbf{x},\mathbf{y}\right)u_j^{ex}\left(\mathbf{y}\right)\right]\mathrm{d}\Gamma\left(\mathbf{y}\right)$$
$$=\begin{cases}u_i^{ex}\left(\mathbf{x}\right)-u_{ij}{}^{\mathrm{ex}}\left(\infty\right), & \mathbf{x}\in\Omega^{\infty}\\ \left[1-c_{ij}\left(\mathbf{x}\right)\right]u_i^{ex}\left(\mathbf{x}\right)-u_{ij}{}^{\mathrm{ex}}\left(\infty\right), & \mathbf{x}\in\Gamma\\ \mathbf{0}, & \mathbf{x}\in\Omega\cup V\cup S\end{cases} \tag{7.7}$$

and

$$\int_{\Gamma\cup S}-\left[K_{ik}\left(\mathbf{x},\mathbf{y}\right)t_k^{ex}\left(\mathbf{y}\right)+H_{ik}\left(\mathbf{x},\mathbf{y}\right)\left(\mathbf{y}\right)u_k^{ex}\right]\mathrm{d}\Gamma\left(\mathbf{y}\right)=\begin{cases}[1-c_{ij}\left(\mathbf{x}\right)]t_j^{ex}\left(\mathbf{x}\right), & \mathbf{x}\in\Gamma\\ \mathbf{0}, & \mathbf{x}\in\Omega\cup V\cup S\end{cases} \tag{7.8}$$

7.3 BIEs for general DDM

Four types of boundary integral equations for DDM are obtained in this section.

7.3.1 The direct BEM and DDM

For points $\mathbf{x}\in\Omega$, if S^- is collapsed onto S^+, Eq.(7.1) can be written as

$$u_i\left(\mathbf{x}\right)=\int_{\Gamma}\left[U_{ij}\left(\mathbf{x},\mathbf{y}\right)t_j\left(\mathbf{y}\right)-T_{ij}\left(\mathbf{x},\mathbf{y}\right)u_j\left(\mathbf{y}\right)\right]\mathrm{d}\Gamma\left(\mathbf{y}\right)$$
$$+u_i\left(\mathbf{x}\right)|\,\mathbf{y}^+ + \lim_{S^-\to S^+}u_i\left(\mathbf{x}\right)|\,\mathbf{y}^- \tag{7.9}$$

and

$$u_i\left(\mathbf{x}\right)|\,\mathbf{y}^+=\int_{S^+}U_{ij}\left(\mathbf{x},\mathbf{y}^+\right)t_j\left(\mathbf{y}^+\right)\mathrm{d}\Gamma\left(\mathbf{y}^+\right)-\int_{S^+}T_{ij}\left(\mathbf{x},\mathbf{y}^+\right)u_j\left(\mathbf{y}^+\right)\mathrm{d}\Gamma\left(\mathbf{y}^+\right) \tag{7.10}$$

where $\mathbf{y}^+$ and $\mathbf{y}^-$ are points on S^+ and S^-, respectively. Replace the superscript "-" with the superscript"+" in $u_i(\mathbf{x})|\mathbf{y}^+$, and $u_i(\mathbf{x})|\mathbf{y}^-$ can be obtained.

Since $U_{ij}(\mathbf{x},\mathbf{y}^+)=U_{ij}(\mathbf{x},\mathbf{y}^-)$ and $T_{ij}(\mathbf{x},\mathbf{y}^+)=-T_{ij}(\mathbf{x},\mathbf{y}^-)$, Eq.(7.9) can be reduced to

$$u_i(\mathbf{x})=\int_\Gamma\left[U_{ij}(\mathbf{x},\mathbf{y})t_j(\mathbf{y})-T_{ij}(\mathbf{x},\mathbf{y})u_j(\mathbf{y})\right]\mathrm{d}\Gamma(\mathbf{y})+u_j^*(\mathbf{x})|\mathbf{y}^+ \tag{7.11}$$

where

$$u_j^*(\mathbf{x})|\mathbf{y}^+=\int_{S^+}U_{ij}(\mathbf{x},\mathbf{y}^+)\sum t_j(\mathbf{y})\mathrm{d}\Gamma(\mathbf{y}^+)-\int_{S^+}T_{ij}(\mathbf{x},\mathbf{y}^+)\Delta u_j(\mathbf{y})\mathrm{d}\Gamma(\mathbf{y}) \tag{7.12}$$

and

$$\sum t_j(\mathbf{y})=t_j(\mathbf{y}^+)+t_j(\mathbf{y}^-) \tag{7.13}$$

$$\Delta u_j(\mathbf{y})=u_j(\mathbf{y}^+)-u_j(\mathbf{y}^-) \tag{7.14}$$

A similar equation can be obtained for the case $\mathbf{x}\in\Gamma$.

For points $\mathbf{x}\in S$, if S^- is collapsed onto S^+,

$$\begin{aligned}c_{ij}(\mathbf{x}^+)u_j(\mathbf{x}^+)=&\int_\Gamma\left[U_{ij}(\mathbf{x}^+,\mathbf{y})t_j(\mathbf{y})-T_{ij}(\mathbf{x}^+,\mathbf{y})u_j(\mathbf{y})\right]\mathrm{d}\Gamma(\mathbf{y})\\&+u_i(\mathbf{x}^+)|\mathbf{y}^+ +\lim_{S^-\to S^+}u_i(\mathbf{x}^+)|\mathbf{y}^-\end{aligned} \tag{7.15}$$

$$\begin{aligned}c_{ij}(\mathbf{x}^-)u_j(\mathbf{x}^-)=&\int_\Gamma\left[U_{ij}(\mathbf{x}^-,\mathbf{y})t_j(\mathbf{y})-T_{ij}(\mathbf{x}^-,\mathbf{y})u_j(\mathbf{y})\right]\mathrm{d}\Gamma(\mathbf{y})\\&+u_i(\mathbf{x}^-)|\mathbf{y}^+ +\lim_{S^-\to S^+}u_i(\mathbf{x}^-)|\mathbf{y}^-\end{aligned} \tag{7.16}$$

Eqs.(7.15) and (7.16) are equal and can be reduced to one equation as

$$\sum u_i(\mathbf{x})=\int_\Gamma\left[U_{ij}(\mathbf{x}^+,\mathbf{y})t_j(\mathbf{y})-T_{ij}(\mathbf{x}^+,\mathbf{y})u_j(\mathbf{y})\right]\mathrm{d}\Gamma(\mathbf{y})+u_i^*(\mathbf{x}^+)|\mathbf{y}^+ \tag{7.17}$$

where

$$\begin{aligned}\sum u_i(\mathbf{x})&=c_{ij}(\mathbf{x}^+)u_j(\mathbf{x}^+)+[1-c_{ij}(\mathbf{x}^+)]u_j(\mathbf{x}^-)\\&=u_i(\mathbf{x}^-)+c_{ij}(\mathbf{x}^+)\Delta u_j(\mathbf{x})\\&=u_i(\mathbf{x}^-)-[1-c_{ij}(\mathbf{x}^+)]\Delta u_j(\mathbf{x})\end{aligned} \tag{7.18}$$

Replace $\mathbf{x}$ in $\mathbf{u}^*(\mathbf{x})|\mathbf{y}^+$ by $\mathbf{x}^+$, and one can have $\mathbf{u}^*(\mathbf{x}^+)|\mathbf{y}^+$.

Then Eq.(7.1) for crack problems can be written as

$$\left.\begin{array}{ll}u_i(\mathbf{x}), & \mathbf{x}\in\Omega\\ c_{ij}(\mathbf{x})u_j(\mathbf{x}), & \mathbf{x}\in\Gamma\\ \sum u_i(\mathbf{x}), & \mathbf{x}\in S^+\end{array}\right\}=\int_\Gamma\left[U_{ij}(\mathbf{x},\mathbf{y})t_j(\mathbf{y})-T_{ij}(\mathbf{x},\mathbf{y})u_j(\mathbf{y})\right]\mathrm{d}\Gamma(\mathbf{y})+u_i^*(\mathbf{x})|\mathbf{y} \tag{7.19}$$

and

$$u_i^*(\mathbf{x})|\mathbf{y}=\int_{S^+}\left[U_{ij}(\mathbf{x},\mathbf{y})\sum t_j(\mathbf{y})-T_{ij}(\mathbf{x},\mathbf{y})\Delta u_j(\mathbf{y})\right]\mathrm{d}\Gamma(\mathbf{y}) \tag{7.20}$$

Similarly, the traction boundary equation for crack problems can be

written as

$$\left.\begin{array}{ll} c_{ij}(\mathbf{x})t_j(\mathbf{x}), & \mathbf{x}\in\Gamma \\ \Delta t_i(\mathbf{x}), & \mathbf{x}\in S^+ \end{array}\right\}=\int_\Gamma\left[K_{ik}(\mathbf{x},\mathbf{y})t_k(\mathbf{y})-H_{ik}(\mathbf{x},\mathbf{y})u_k(\mathbf{y})\right]\mathrm{d}\Gamma(\mathbf{y})+t_i^*(\mathbf{x})\,|\,\mathbf{y} \quad (7.21)$$

where

$$t_i^*(\mathbf{x})\,|\,\mathbf{y}=\int_{S^+}\left[K_{ik}(\mathbf{x},\mathbf{y})\sum t_k(\mathbf{y})-H_{ik}(\mathbf{x},\mathbf{y})\Delta u_k(\mathbf{y})\right]\mathrm{d}\Gamma(\mathbf{y}) \quad (7.22)$$

and

$$\begin{aligned}\Delta t_i(\mathbf{x}) &= c_{ij}(\mathbf{x}^+)t_j(\mathbf{x}^+)-[1-c_{ij}(\mathbf{x}^+)]t_j(\mathbf{x}^-) \\ &= c_{ij}(\mathbf{x}^+)\sum t_j(\mathbf{x})-t_i(\mathbf{x}^-) \\ &= -[1-c_{ij}(\mathbf{x}^+)]\sum t_j(\mathbf{x})+t_i(\mathbf{x}^+)\end{aligned} \quad (7.23)$$

If the load on the crack surface is assumed to be equilibrium, i.e., $\sum t_i(\mathbf{y})=0$, then $u_i^*(\mathbf{x})\,|\,\mathbf{y}$ and $t_i^*(\mathbf{x})\,|\,\mathbf{y}$ can be written as

$$u_i^*(\mathbf{x})\,|\,\mathbf{y}=-\int_{S^+}T_{ij}(\mathbf{x},\mathbf{y})\Delta u_j(\mathbf{y})\mathrm{d}\Gamma(\mathbf{y}) \quad (7.24)$$

$$t_i^*(\mathbf{x})\,|\,\mathbf{y}=-\int_{S^+}H_{ki}(\mathbf{x},\mathbf{y})\Delta u_k(\mathbf{y})\mathrm{d}\Gamma(\mathbf{y}) \quad (7.25)$$

and Eq.(7.23) will be reduced to

$$\Delta t_i(\mathbf{x})=-t_i(\mathbf{x}^-)=t_i(\mathbf{x}^+) \quad (7.26)$$

Apparently, Eqs.(7.19) and (7.21) can be applied for solving crack problems and will be the same for the infinite domain.

As shown in Eqs.(7.19) and (7.21), the boundary integrals on Γ of the finite domain can be computed by CBEM or HBEM, both are direct BEM. This is the reason these two approaches are called CBEM and HBEM, respectively. Now they can be written as

$$\begin{cases}\int_\Gamma\left[U_{ij}(\mathbf{x},\mathbf{y})t_j(\mathbf{y})-T_{ij}(\mathbf{x},\mathbf{y})u_j(\mathbf{y})\right]\mathrm{d}\Gamma(\mathbf{y})+u_i^*(\mathbf{x})\,|\,\mathbf{y}=c_{ij}(\mathbf{x})u_j(\mathbf{x}), & \mathbf{x}\in\Gamma \\ \int_\Gamma\left[U_{ij}(\mathbf{x},\mathbf{y})t_j(\mathbf{y})-T_{ij}(\mathbf{x},\mathbf{y})u_j(\mathbf{y})\right]\mathrm{d}\Gamma(\mathbf{y})+u_i^*(\mathbf{x})\,|\,\mathbf{y}=\sum u_i(\mathbf{x}), & \mathbf{x}\in S^+ \\ \int_\Gamma\left[K_{ik}(\mathbf{x},\mathbf{y})t_k(\mathbf{y})-H_{ik}(\mathbf{x},\mathbf{y})u_k(\mathbf{y})\right]\mathrm{d}\Gamma(\mathbf{y})+t_i^*(\mathbf{x})\,|\,\mathbf{y}=\Delta t_i(\mathbf{x}), & \mathbf{x}\in S^+\end{cases} \quad (7.27)$$

and

$$\begin{cases}\int_\Gamma\left[K_{ik}(\mathbf{x},\mathbf{y})t_k(\mathbf{y})-H_{ik}(\mathbf{x},\mathbf{y})u_k(\mathbf{y})\right]\mathrm{d}\Gamma(\mathbf{y})+t_i^*(\mathbf{x})\,|\,\mathbf{y}=c_{ij}(\mathbf{x})t_j(\mathbf{x}), & \mathbf{x}\in\Gamma \\ \int_\Gamma\left[U_{ij}(\mathbf{x},\mathbf{y})t_j(\mathbf{y})-T_{ij}(\mathbf{x},\mathbf{y})u_j(\mathbf{y})\right]\mathrm{d}\Gamma(\mathbf{y})+u_i^*(\mathbf{x})\,|\,\mathbf{y}=\sum u_i(\mathbf{x}), & \mathbf{x}\in S^+ \\ \int_\Gamma\left[K_{ik}(\mathbf{x},\mathbf{y})t_k(\mathbf{y})-H_{ik}(\mathbf{x},\mathbf{y})u_k(\mathbf{y})\right]\mathrm{d}\Gamma(\mathbf{y})+t_i^*(\mathbf{x})\,|\,\mathbf{y}=\Delta t_i(\mathbf{x}), & \mathbf{x}\in S^+\end{cases} \quad (7.28)$$

The first equation in Eq.(7.27) or Eq.(7.28) can be applied to form the coefficient matrix relative to the values on boundary Γ. The second equation can be used when $u_i(\mathbf{x}^+)$ or $u_i(\mathbf{x}^-)$ are known on S (BCI), while the last

equation is used when $\Delta t_i(\mathbf{y})$ are known on S (BCII).

By discretizing the boundary into elements, one can assemble the Eq.(32) for CBEM into the matrix as

$$\begin{bmatrix} \mathbf{T}^{\Gamma\Gamma} & \mathbf{T}^{\Gamma S} \\ \mathbf{T}^{S\Gamma} & \mathbf{T}^{SS} \end{bmatrix} \begin{bmatrix} \mathbf{u}^{\Gamma} \\ \mathbf{u}^{S} \end{bmatrix} = \begin{bmatrix} \mathbf{U}^{\Gamma\Gamma} & \mathbf{0} \\ \mathbf{U}^{S\Gamma} & \mathbf{0} \end{bmatrix} \begin{bmatrix} \mathbf{t}^{\Gamma} \\ \mathbf{0} \end{bmatrix} + \begin{bmatrix} \mathbf{0} \\ \sum \mathbf{u}^{S} \end{bmatrix} \tag{7.29}$$

or

$$\begin{bmatrix} \mathbf{T}^{\Gamma\Gamma} & \mathbf{T}^{\Gamma S} \\ \mathbf{H}^{S\Gamma} & \mathbf{H}^{SS} \end{bmatrix} \begin{bmatrix} \mathbf{u}^{\Gamma} \\ \mathbf{u}^{S} \end{bmatrix} = \begin{bmatrix} \mathbf{U}^{\Gamma\Gamma} & \mathbf{0} \\ \mathbf{K}^{S\Gamma} & \mathbf{0} \end{bmatrix} \begin{bmatrix} \mathbf{t}^{\Gamma} \\ \mathbf{0} \end{bmatrix} + \begin{bmatrix} \mathbf{0} \\ \Delta \mathbf{t}^{S} \end{bmatrix} \tag{7.30}$$

where the superscript represents the coefficient matrices assembled under the interaction of elements on boundary Γ and crack S respectively. And $\mathbf{T}^{\Gamma\Gamma}$, $\mathbf{T}^{\Gamma S}$, $\mathbf{T}^{S\Gamma}$, $\mathbf{T}^{SS}$, $\mathbf{U}^{\Gamma\Gamma}$, $\mathbf{U}^{S\Gamma}$, $\mathbf{H}^{S\Gamma}$, $\mathbf{H}^{SS}$ and $\mathbf{K}^{S\Gamma}$ are the coefficient matrices related with kernels $T_{ij}(\mathbf{x},\mathbf{y})$, $U_{ij}(\mathbf{x},\mathbf{y})$, $H_{ik}(\mathbf{x},\mathbf{y})$ and $K_{ik}(\mathbf{x},\mathbf{y})$, respectively.

The Eq.(7.29) is assembled for the case BCI, while when BCII is known, then Eq.(7.30) is useful.

Similarly, the equations in HBEM can also be discretised as

$$\begin{bmatrix} \mathbf{H}^{\Gamma\Gamma} & \mathbf{H}^{\Gamma S} \\ \mathbf{T}^{S\Gamma} & \mathbf{T}^{SS} \end{bmatrix} \begin{bmatrix} \mathbf{u}^{\Gamma} \\ \mathbf{u}^{S} \end{bmatrix} = \begin{bmatrix} \mathbf{K}^{\Gamma\Gamma} & \mathbf{0} \\ \mathbf{U}^{S\Gamma} & \mathbf{0} \end{bmatrix} \begin{bmatrix} \mathbf{t}^{\Gamma} \\ \mathbf{0} \end{bmatrix} + \begin{bmatrix} \mathbf{0} \\ \sum \mathbf{u}^{S} \end{bmatrix} \tag{7.31}$$

or

$$\begin{bmatrix} \mathbf{H}^{\Gamma\Gamma} & \mathbf{H}^{\Gamma S} \\ \mathbf{H}^{S\Gamma} & \mathbf{H}^{SS} \end{bmatrix} \begin{bmatrix} \mathbf{u}^{\Gamma} \\ \mathbf{u}^{S} \end{bmatrix} = \begin{bmatrix} \mathbf{K}^{\Gamma\Gamma} & \mathbf{0} \\ \mathbf{K}^{S\Gamma} & \mathbf{0} \end{bmatrix} \begin{bmatrix} \mathbf{t}^{\Gamma} \\ \mathbf{0} \end{bmatrix} + \begin{bmatrix} \mathbf{0} \\ \Delta \mathbf{t}^{S} \end{bmatrix} \tag{7.32}$$

The Eq.(7.31) is assembled for the case BCI, while when BCII is known, then Eq.(7.32) is useful.

7.3.2 The indirect BEM and DDM

7.3.2.1 The DD-IBEM

From Eqs.(7.4) and (7.19), one can have

$$\begin{aligned} &\int_{\Gamma} \left\{ U_{ij}(\mathbf{x},\mathbf{y}) \left[t_j(\mathbf{y}) + t_j^{ex}(\mathbf{y}) \right] - T_{ij}(\mathbf{x},\mathbf{y}) \left[u_j(\mathbf{y}) - u_j^{ex}(\mathbf{y}) \right] \right\} \mathrm{d}\Gamma(\mathbf{y}) + u_i^{*}(\mathbf{x}) \,|\, \mathbf{y} \\ &= \begin{cases} u_i(\mathbf{x}), & \mathbf{x} \in \Omega \\ c_{ij}(\mathbf{x}) \left[u_j(\mathbf{y}) - u_j^{ex}(\mathbf{y}) \right] + u_j^{ex}(\mathbf{y}) - u_{ij}^{\mathrm{ex}}(\infty), & \mathbf{x} \in \Gamma \\ \sum u_i(\mathbf{x}), & \mathbf{x} \in S^{+} \end{cases} \end{aligned} \tag{7.33}$$

From Eqs.(7.5) and(7.21), one can have

$$\int_\Gamma \left\{ K_{ik}(\mathbf{x},\mathbf{y})\left[t_k(\mathbf{y}) + t_k^{ex}(\mathbf{y}) \right] - H_{ik}(\mathbf{x},\mathbf{y})\left[u_k(\mathbf{y}) - u_k^{ex}(\mathbf{y}) \right] \right\} \mathrm{d}\Gamma(\mathbf{y}) + t_i^*(\mathbf{x}) \,|\, \mathbf{y} = \begin{cases} c_{ij}(\mathbf{x})\left[t_j(\mathbf{x}) + t_j^{ex}(\mathbf{x}) \right] - t_j^{ex}(\mathbf{x}), & \mathbf{x} \in \Gamma \\ \Delta t_i(\mathbf{x}), & \mathbf{x} \in S^+ \end{cases} \tag{7.34}$$

If assuming $t_i(\mathbf{y}) + t_i^{ex}(\mathbf{y}) = \mathbf{0}$ on Γ, Eqs.(7.33) and (7.34) can be written as

$$-\int_\Gamma T_{ij}(\mathbf{x},\mathbf{y})\psi_j(\mathbf{y})\mathrm{d}\Gamma(\mathbf{y}) + u_i^*(\mathbf{x}) \,|\, \mathbf{y} = \begin{cases} u_i(\mathbf{x}), & \mathbf{x} \in \Omega \\ u_i(\mathbf{x}) - \left[1 - c_{ij}(\mathbf{x}) \right]\psi_i(\mathbf{y}) - u_{ij}^{\mathrm{ex}}(\infty), & \mathbf{x} \in \Gamma \\ \sum u_i(\mathbf{x}), & \mathbf{x} \in S^+ \end{cases} \tag{7.35}$$

$$-\int_\Gamma H_{ik}(\mathbf{x},\mathbf{y})\psi_j(\mathbf{y})\mathrm{d}\Gamma(\mathbf{y}) + t_i^*(\mathbf{x}) \,|\, \mathbf{y} = \begin{cases} t_i(\mathbf{x}), & \mathbf{x} \in \Gamma \\ \Delta t_i(\mathbf{x}), & \mathbf{x} \in S^+ \end{cases} \tag{7.36}$$

where

$$\psi_i(\mathbf{y}) = u_i(\mathbf{y}) - u_i^{ex}(\mathbf{y}) \tag{7.37}$$

Then the BIEs for DD-IBEM can be written as

$$\begin{cases} -\int_\Gamma T_{ij}(\mathbf{x},\mathbf{y})\psi_j(\mathbf{y})\mathrm{d}\Gamma(\mathbf{y}) + u_i^*(\mathbf{x}) \,|\, \mathbf{y} = u_i(\mathbf{x}) - \left[1 - c_{ij}(\mathbf{x}) \right]\psi_i(\mathbf{y}) - u_{ij}^{\mathrm{ex}}(\infty), & \mathbf{x} \in \Gamma \\ -\int_\Gamma H_{ik}(\mathbf{x},\mathbf{y})\psi_k(\mathbf{y})\mathrm{d}\Gamma(\mathbf{y}) + t_i^*(\mathbf{x}) \,|\, \mathbf{y} = t_i(\mathbf{x}), & \mathbf{x} \in \Gamma \\ -\int_\Gamma T_{ij}(\mathbf{x},\mathbf{y})\psi_j(\mathbf{y})\mathrm{d}\Gamma(\mathbf{y}) + u_i^*(\mathbf{x}) \,|\, \mathbf{y} = \sum u_i(\mathbf{x}), & \mathbf{x} \in S^+ \\ -\int_\Gamma H_{ik}(\mathbf{x},\mathbf{y})\psi_k(\mathbf{y})\mathrm{d}\Gamma(\mathbf{y}) + t_i^*(\mathbf{x}) \,|\, \mathbf{y} = \Delta t_i(\mathbf{x}), & \mathbf{x} \in S^+ \end{cases} \tag{7.38}$$

The first and second equations in Eq.(7.38) are used for the displacement and traction boundary, respectively. And the last two equations are used in the same way as the CBEM or HBEM.

7.3.2.2 The FS-IBEM

If assuming $u_i(\mathbf{y}) - u_i^{ex}(\mathbf{y}) = \mathbf{0}$ on Γ, Eqs.(7.33) and (7.34) can be written as

$$\int_\Gamma U_{ij}(\mathbf{x},\mathbf{y})\rho_j(\mathbf{y})\mathrm{d}\Gamma(\mathbf{y}) + u_i^*(\mathbf{x}) \,|\, \mathbf{y} = \begin{cases} u_i(\mathbf{x}), & \mathbf{x} \in \Omega \\ u_i(\mathbf{x}) - u_{ij}^{\mathrm{ex}}(\infty), & \mathbf{x} \in \Gamma \\ \sum u_i(\mathbf{x}), & \mathbf{x} \in S^+ \end{cases} \tag{7.39}$$

and

$$\int_\Gamma K_{ik}(\mathbf{x},\mathbf{y})\rho_k(\mathbf{y})\mathrm{d}\Gamma(\mathbf{y}) + t_i^*(\mathbf{x}) \,|\, \mathbf{y} = \begin{cases} t_i(\mathbf{x}) - \left[1 - c_{ij}(\mathbf{x}) \right]\rho_j(\mathbf{y}), & \mathbf{x} \in \Gamma \\ \Delta t_i(\mathbf{x}), & \mathbf{x} \in S^+ \end{cases} \tag{7.40}$$

where

$$\rho_i(\mathbf{y}) = t_i(\mathbf{y}) + t_i^{ex}(\mathbf{y}) \tag{7.41}$$

Then the BIEs for FS-IBEM can be written as

$$\begin{cases} \int_\Gamma U_{ij}(\mathbf{x},\mathbf{y})\rho_j(\mathbf{y})\mathrm{d}\Gamma(\mathbf{y}) + u_i^*(\mathbf{x}) \,|\, \mathbf{y} = u_i(\mathbf{x}) - u_{ij}^{\mathrm{ex}}(\infty), & \mathbf{x}\in\Gamma \\ \int_\Gamma K_{ik}(\mathbf{x},\mathbf{y})\rho_k(\mathbf{y})\mathrm{d}\Gamma(\mathbf{y}) + t_i^*(\mathbf{x}) \,|\, \mathbf{y} = t_i(\mathbf{x}) - \left[1 - c_{ij}(\mathbf{x})\right]\rho_i(\mathbf{y}), & \mathbf{x}\in\Gamma \\ \int_\Gamma U_{ij}(\mathbf{x},\mathbf{y})\rho_j(\mathbf{y})\mathrm{d}\Gamma(\mathbf{y}) + u_i^*(\mathbf{x}) \,|\, \mathbf{y} = \sum u_i(\mathbf{x}), & \mathbf{x}\in S^+ \\ \int_\Gamma K_{ik}(\mathbf{x},\mathbf{y})\rho_k(\mathbf{y})\mathrm{d}\Gamma(\mathbf{y}) + t_i^*(\mathbf{x}) \,|\, \mathbf{y} = \Delta t_i(\mathbf{x}), & \mathbf{x}\in S^+ \end{cases} \tag{7.42}$$

Eqs.(7.38) and(7.42) can be called DD-IBEM and FS-IBEM, respectively. The first two equations in Eq.(7.38) or Eq.(7.42) can be applied to form the coefficient matrix relative to the values on boundary Γ. And the last two equations are used in the same way as the CBEM or HBEM.

7.3.3 The modified IBEM

The results of target objects are unacceptable and cannot be ignored instead of the acceptable error caused by element division, and it has been found that the rigid displacements, including rigid movement and rotation, are responsible for the unacceptable error. So one needs to figure out a way to subtract the negative influence of the rigid displacements.

Then for Eq.(7.4), instead of letting $u_{ij}^{\mathrm{ex}}(\infty)=0$, $u_{ij}^{\mathrm{ex}}(\infty)$ can be assumed to be finite constants $\mathbf{C}=\left[C_1, C_2\right]^{\mathrm{T}}$, then the first equations in Eqs.(7.38) and (7.42) can be written as

$$-\int_\Gamma T_{ij}(\mathbf{x},\mathbf{y})\psi_j(\mathbf{y})\mathrm{d}\Gamma(\mathbf{y}) + u_i^*(\mathbf{x}) \,|\, \mathbf{y} = u_i(\mathbf{x}) - \left[1 - c_{ij}(\mathbf{x})\right]\psi_i(\mathbf{y}) - \mathbf{C},\ \mathbf{x}\in\Gamma \tag{7.43}$$

and

$$\int_\Gamma U_{ij}(\mathbf{x},\mathbf{y})\rho_j(\mathbf{y})\mathrm{d}\Gamma(\mathbf{y}) + u_i^*(\mathbf{x}) \,|\, \mathbf{y} = u_i(\mathbf{x}) - \mathbf{C}, \mathbf{x}\in\Gamma \tag{7.44}$$

Since displacements $\mathbf{C}$ are also unknown, additional boundary conditions are needed to ensure the matrix equation is computable, a previous study [215]proposed the following additional equation:

$$\sum_{k=1}^{N}\boldsymbol{\rho}_k = \mathbf{0} \tag{7.45}$$

where N is the number of boundary nodes and $\boldsymbol{\rho}_k$ are values at the kth node.

In this chapter, a new additional equation is provided, as the tractions on the boundary should satisfy the equilibrium equation, we can also use the following equation as the additional equation:

$$\int_\Gamma t_i(\mathbf{y})\mathrm{d}\Gamma(\mathbf{y}) = \mathbf{0} \tag{7.46}$$

where $t_i(\mathbf{y})$ is the i^{th} traction of boundary $\Gamma(\mathbf{y})$.

For the current research, both DD-IBEM and FS-IBEM are added with Eq.(7.46) as the additional equation.

To show how to assemble the coefficient matrix, the following two sections, 7.3.3.1 and 7.3.3.2 are introduced. In addition, to prove the efficiency and accuracy of this modified indirect BEM, the results will be compared in the first example in **Section 7.4**.

7.3.3.1 Discretise and assemble the modified DD-IBEM

By discretizing the boundary into elements, one can have the matrix form as

$$\begin{cases} \begin{bmatrix} -\mathbf{A} & \mathbf{I} \\ \mathbf{N} & \mathbf{0} \end{bmatrix} \begin{bmatrix} \mathbf{Y} \\ \mathbf{C} \end{bmatrix} = \begin{bmatrix} \mathbf{u} \\ \mathbf{0} \end{bmatrix} \\ -\mathbf{E}\mathbf{Y} = \mathbf{t} \end{cases} \tag{7.47}$$

where $\mathbf{A}$ and $\mathbf{E}$ are the coefficient matrices related with kernels $T_{ij}(\mathbf{x},\mathbf{y})$ and $H_{ik}(\mathbf{x},\mathbf{y})$, respectively, $\mathbf{I}$ is the 2×2 identity matrix, and

$$\mathbf{Y} = \begin{bmatrix} \boldsymbol{\varphi}_1 & \cdots & \boldsymbol{\varphi}_N \end{bmatrix}^{\mathrm{T}} \tag{7.48}$$

$$\mathbf{N} = -\boldsymbol{\Phi}\mathbf{E} \tag{7.49}$$

$$\left[\boldsymbol{\Phi}\right]_i = \int_\Gamma \begin{bmatrix} N_i(\mathbf{y}) & \\ & N_i(\mathbf{y}) \end{bmatrix} \mathrm{d}\Gamma(\mathbf{y}) \tag{7.50}$$

where $N_i(\mathbf{y})$ is the ith shape function.

The modified DD-IBEM is marked as M-DD-IBEM.

7.3.3.2 Discretise and assemble the modified FS-IBEM

After discretizing the boundary into elements, the matrix can be assembled as

$$\begin{cases} \begin{bmatrix} \mathbf{B} & \mathbf{I} \\ \mathbf{M} & \mathbf{0} \end{bmatrix} \begin{bmatrix} \mathbf{X} \\ \mathbf{C} \end{bmatrix} = \begin{bmatrix} \mathbf{u} \\ \mathbf{0} \end{bmatrix} \\ \mathbf{D}\mathbf{X} = \mathbf{t} \end{cases} \tag{7.51}$$

where $\mathbf{B}$ and $\mathbf{D}$ are the coefficient matrices related with kernels $U_{ij}(\mathbf{x},\mathbf{y})$ and $K_{ik}(\mathbf{x},\mathbf{y})$, respectively, and

$$\mathbf{X} = \begin{bmatrix} \boldsymbol{\rho}_1 & \cdots & \boldsymbol{\rho}_N \end{bmatrix}^{\mathrm{T}} \tag{7.52}$$

$$\mathbf{M} = \boldsymbol{\Phi}\mathbf{D} \tag{7.53}$$

The modified FS-IBEM is marked as M-FS-IBEM.

7.4 Numerical examples

In this section, three examples will be introduced to prove the correctness of the formulas proposed in this paper. For all these examples, the plane strain assumption is taken, and the liner discontinued element is used to discretise the boundaries and cracks. Besides, the relative error used in this section is defined in Section 3.5.

For the latter three examples, the stress intensity factors (SIFs), K_{I} and K_{II}, and the normalized stress intensity factors (NSIFs), F_{I} and F_{II}, are introduced to testify to the accuracy and make comparisons between the four methods. After getting the displacements, tractions, strains and stress of the boundary, cracks and points in the domain, the crack opening displacements (CODs) on crack surfaces can be calculated. Then the SIFs of crack tips can be figured out easily. And the following two formulas are taken to get K_{I}, K_{II}, F_{I} and F_{II}:

$$K_{\mathrm{I}}=\frac{G}{(\kappa+1)}\sqrt{\frac{2\pi}{r}}\Delta u_n(r) \tag{7.54}$$

$$K_{\mathrm{II}}=\frac{G}{(\kappa+1)}\sqrt{\frac{2\pi}{r}}\Delta u_s(r) \tag{7.55}$$

$$F_{\mathrm{I}}=\frac{K_{\mathrm{I}}}{\sigma\sqrt{\pi a}} \tag{7.56}$$

$$F_{\mathrm{II}}=\frac{K_{\mathrm{II}}}{\sigma\sqrt{\pi a}} \tag{7.57}$$

where K_{I} and K_{II} are SIFs of model I and model II at the tip of a crack, G represents the shear modulus. For plane strain problems, $k=3-4\nu$, for plane stress problems, $k=(3-4\nu)/(1+\nu)$. And ν is Poisson's ratio, r represents the radial distance from the observed point to the crack tip. $\Delta u_n(r)$ and $\Delta u_s(r)$ represent the normal and tangential components of the nodal displacements on crack surfaces. σ represents the known traction on the boundary. a is the half-length of a crack.

Last but not least, different boundary conditions are used to simulate the theoretical condition, before discussing the three examples, for simplicity, some symbols in **Table 7.1** are set to represent different boundary conditions.

Table 7.1 Symbols of different boundary conditions

BC-A	A pair of uniform loads are put at the upper and lower sides, and σ=1 Mpa, no displacement constraint is set on the left or right sides.
BC-B	A pair of uniform loads are put at the upper and lower sides, and σ=1 Mpa, an x-direction displacement constraint is set on the left side as $u_x=0$, the right side is free.
BC-C	A uniform load is put on the upper side, and σ=1 Mpa, and a y-direction displacement constraint is set on the lower side as $u_y=0$, no displacement constraint is set on the left or right sides.
BC-D	A uniform load is put on the upper side, and σ=1 Mpa, and a y-direction displacement constraint is set on the lower side as $u_y=0$, in addition, an x-direction displacement constraint is set on the left side as $u_x=0$, the right side is free.

7.4.1 A finite plate with one crack

As shown in **Fig.7.2**, this model is a rectangular plate containing a centre crack with different lengths, the elastic modulus E=1 Mpa and the Poisson's ratio v=0.3, and the length and width of the finite rectangular plate are $2H$ and $2W$, the length of the crack is $2a$. In this paper, all three parameters are set in the following **Table 7.2**, during the numerical computation, the rectangular boundary and the crack surface are discretised by 400 elements separately.

Table 7.2 parameters of H, W, a

$2H$	20 mm
$2W$	10 mm
a/W	0.2

And for the case a/W=0.2, the analytical formula is written as follows

$$\Delta u(x)=\frac{2(1-\nu)a}{G}\sigma^{\infty}\sqrt{1-\left(\frac{x}{a}\right)^2} \tag{7.58}$$

Firstly, as two more BIEs are proposed based on the modified indirect BEM and DDM, there are six BIEs for crack problems all in all. To prove the six BIEs are efficient and correct, their results are compared with the

theoretical result under the boundary condition set as BC-A, as the result presented in **Figs.7.3** and **7.4**. Sorting the six BIEs by accuracy, CBEM is closest to the theoretical result, and the next five BIEs are HBEM, DD-IBEM, M-DD-IBEM, M-FS-IBEM and FS-IBEM. One can see that the relative error of COD at the middle of crack (RE-CODMC) for CBEM, HBEM, DD-IBEM and M-DD-IBEM are 0.0118, 0.0262, 0.0312 and 0.0312, which are lower than the general requirement that RE-CODMC is less than 0.05 obviously, but FS-IBEM and M-FS-IBEM do not satisfy that and the RE-CODMC are 0.076 and 0.076, furthermore, one can notice that the result of the two pairs, DD-IBEM and M-DD-IBEM, FS-IBEM and M-FS-IBEM are the same, the reason is that, in the current boundary condition, BC-A, there is no displacement known apparently, namely, the first equation in both Eqs.(7.47) and (7.51) are not involved in assembling matrix, so the correction does not work under displacement-free boundary conditions.

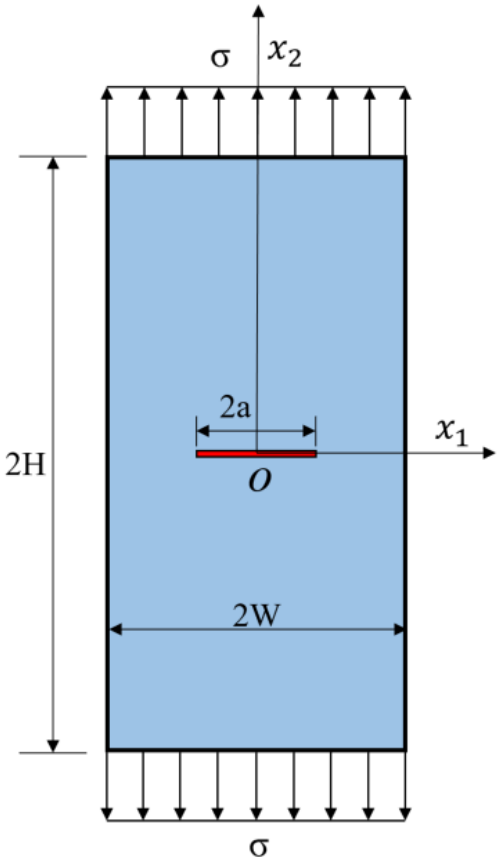

Fig.7.2 A rectangular plate containing a centre crack

Now, whether the modified indirect BEM work or not under the boundary

conditions which contain the known displacements is tested and verified. The four boundary conditions named at the beginning of section four are involved in this discussion. In fact, the latter three cases are very similar to the first one, which is the ideal case and can be seen as approximations, the CBEM and HBEM are used to prove their similarity. As one can see in **Figs.7.5** and **7.6**, under the four boundary conditions, both the two methods are rather exact, and the difference among the four cases can be ignored. However, when it comes to the two indirect BEMs, the result changes a lot. According to **Figs.7.7** and **7.8**, the results of COD vary with the four boundary conditions, and the results of BC-D in **Fig.7.7** and all the four cases in **Fig.7.8** are unacceptable. However, the results of both the two methods, M-DD-IBEM and M-FS-IBEM, improve a lot in the four cases, especially for BC-C and BC-D, which get the worst results by the unmodified DD-IBEM and FS-IBEM. Moreover, in some cases, the modified indirect BEM present a more exact result than the direct BEM, detailed results are shown in **Table 7.3**.

But, the accuracy of both the unmodified and modified indirect BEM is still unstable, and some results of the modified indirect BEM are still not accurate enough, so the CBEM and HBEM are recommended in this research.

Table 7.3 RE-CODMCs under four boundary conditions by four methods

	CBEM	HBEM	M-DD-IBEM	M-FS-IBEM
BC-A	0.01179	0.02619	0.03123	0.07603
BC-B	0.01339	0.02322	0.03084	0.07422
BC-C	0.02074	0.02609	0.01088	0.00377
BC-D	0.01931	0.02304	0.00693	0.00377

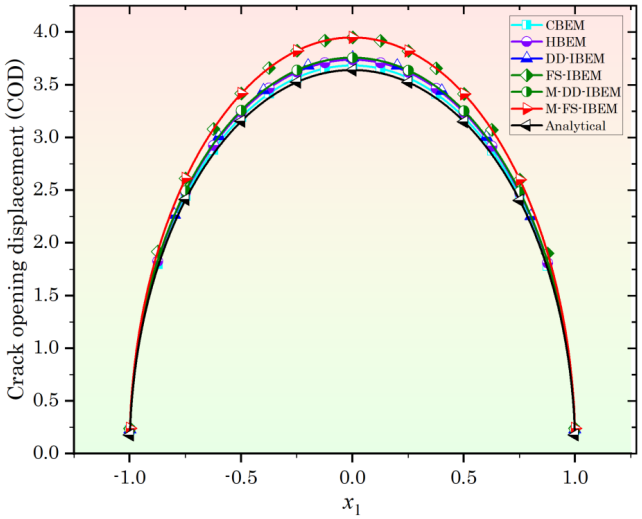

Fig.7.3 Comparison of COD

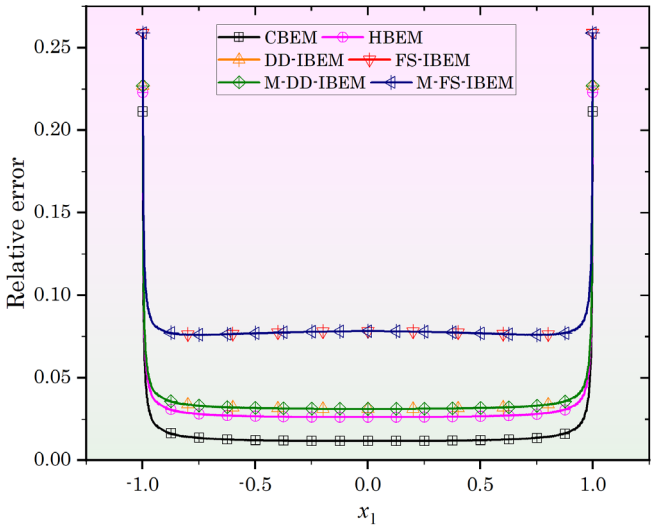

Fig.7.4 Comparison of relative error

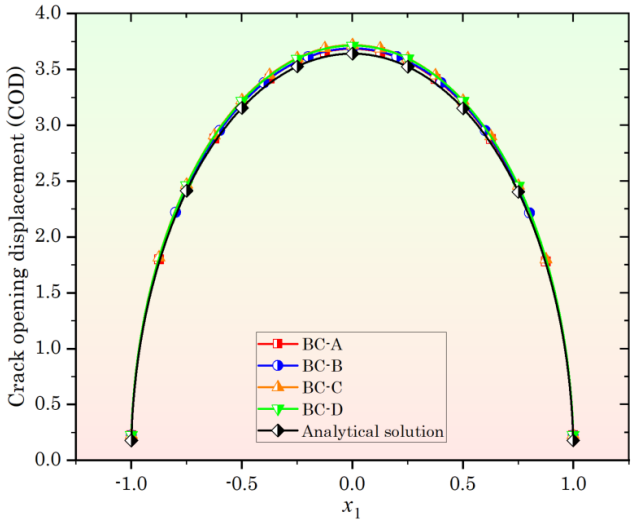

Fig.7.5 Comparisons of four boundary conditions by CBEM

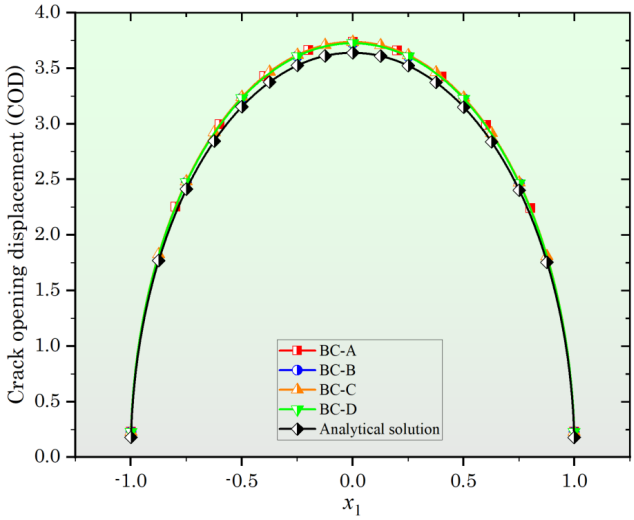

Fig.7.6 Comparisons of four boundary conditions by HBEM

The last problem discussed in this part is the relationship between the relative error of COD and the number of elements on the boundary and crack surface. To test that, models discretised by a series of element numbers, and the information is listed in **Table 7.4**. The boundary condition is set as BC-A.

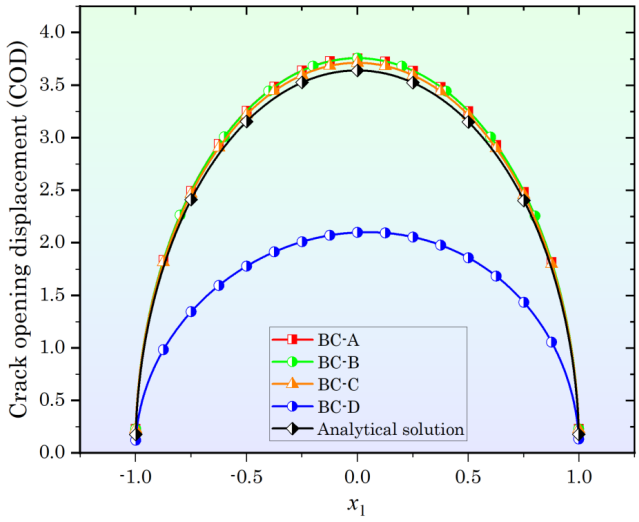

Fig.7.7 Comparisons of four boundary conditions by DD-IBEM

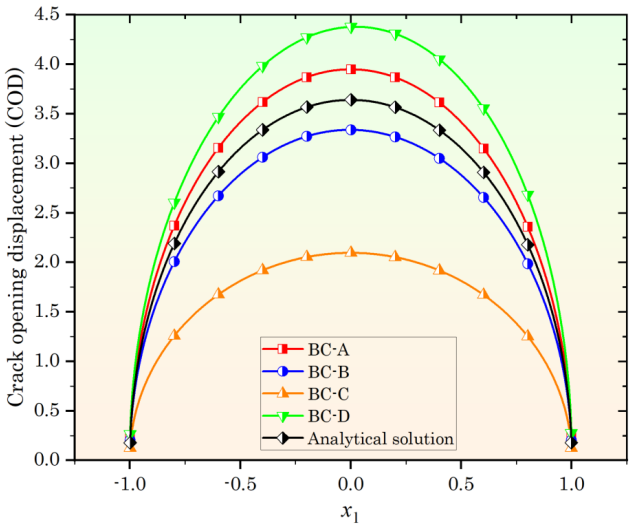

Fig.7.8 Comparisons of four boundary conditions by FS-IBEM

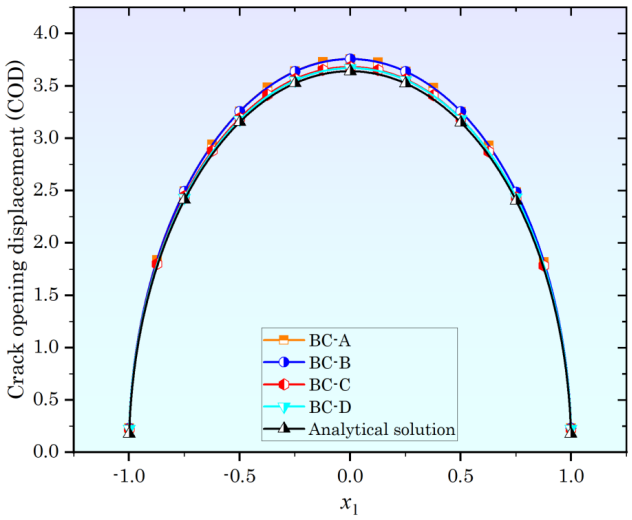

Fig.7.9 Comparisons of four boundary conditions by M-DD-IBEM

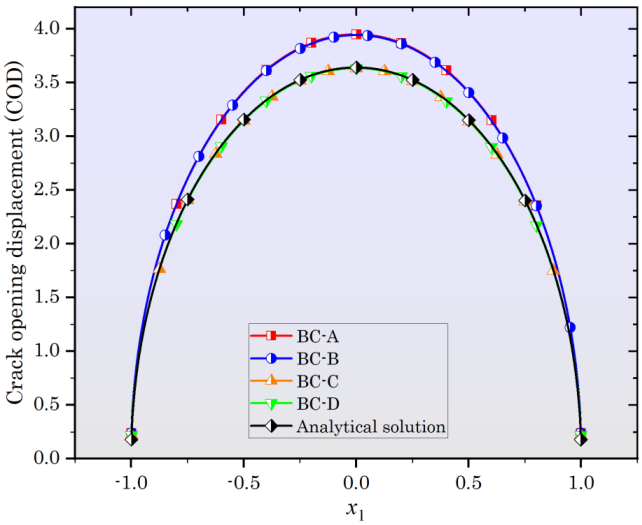

Fig.7.10 Comparisons of four boundary conditions by M-FS-IBEM

Table 7.4 A series of element numbers set for boundary and crack surface

	Element Number								
	Case 1	Case 2	Case 3	Case 4	Case 5	Case 6	Case 7	Case 8	Case 9
Boundary	20	32	40	80	160	320	640	1280	2560
Crack	5	8	10	20	40	80	160	320	640

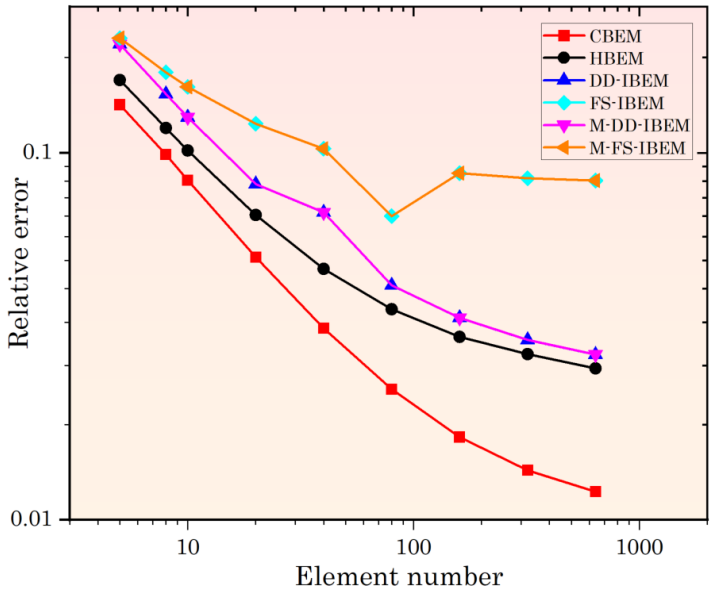

Fig.7.11 The relationship between R-Error and Element number

As can be seen in **Fig.7.11**, the data is put in a logarithmic coordinate system. All six BIEs show a trend that the relative error is decreasing with the increase of element number, which testify to convergence. And the CBEM present the smallest relative error compared to the other five methods, HBEM is slightly inferior to CBEM. Secondly, the method FS-IBEM and M-FS-IBEM show a downward trend overall, but there is a sudden increase in case 4, followed by a slight decrease. That proves the unstable character of indirect BEM. One also can notice that the results of modified indirect BEM are the same as unmodified indirect BEM, due to the boundary condition, BC-A.

It is worth mentioning that, for the following two examples, only the direct and modified indirect BEM, namely, CBEM, HBEM, M-DD-IBEM and M-FS-IBEM, are involved.

7.4.2 A finite plate with four cracks

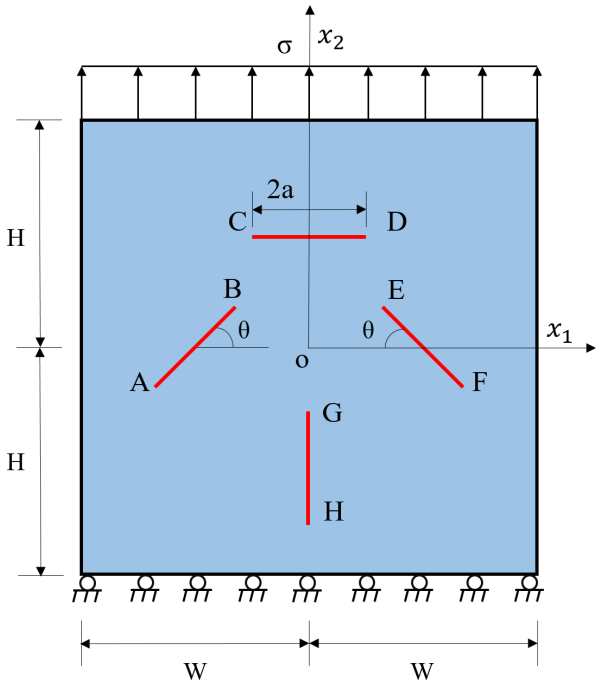

Fig.7.12 A rectangular plate containing four cracks

In order to present the accuracy and efficiency of the four methods, CBEM, HBEM, M-DD-IBEM and M-FS-IBEM when it comes to a random distribution of multi-crack problem, a finite plate with four distributed cracks are taken.

This model was analyzed already in Ref_1 [216] and Ref_2 [224], and the normalized SIFs(F_I and F_{II}) are used to compare the proposed methods with the results in Ref_1 and Ref_2. The shear modulus of material is μ=2019 Mpa, and Poisson's ratio is set as ν=0.3, seeing **Fig.7.12**, the width and height of the rectangular plate are 2W and 2H, and the length of the four cracks are all 2a. The geometry relationship is chosen as W/H=1, and W/a=5. Then the coordinates of the centre of crack AB, CD, EF, and GH are (-W/2, 0), (0, H/2), (W/2, 0) and (0,-H/2). The outer boundary and each crack are discretised by 400 elements. Then, the boundary condition is BC-C. Since the model is geometrically symmetric by the y-axis, then one can observe that the F_{I} of the crack tips, A and F are the same. The conclusions are suitable for the other two pairs of crack tips, B and E, C and D, as well. For generality, the cracks, AB and EF are set by various inclined angles: 0, 30, 45, 60, 90. From Table 7.5, compared with the results in the references, one can notice that, with the

increase of θ, the F_{I} of all the crack tips decrease. And it is easy to conclude that the proposed four methods prove their accuracy when confronted with multi-crack problems.

Table 7.5 F_{I} of the crack tips for the plate containing four cracks

θ (deg.)		0	30	45	60	90
A, **F**	Reference_2	1.10322	0.81924	0.5132	0.25287	0
	Reference_1	1.1051	0.8208	0.5354	0.2533	0
	CBEM	1.1078	0.82063	0.5301	0.2551	0
	HBEM	1.1131	0.8280	0.5329	0.2569	0
	M-DD-IBEM	1.1170	0.8117	0.5381	0.253765	0
	M-FS-IBEM	1.1201	0.8400	0.5495	0.279623	0
B, **E**	Reference_2	1.0825	0.8403	0.5654	0.27289	0.0024
	Reference_1	1.0848	0.8467	0.5703	0.2741	0.0024
	CBEM	1.0877	0.8481	0.5712	0.2784	0.0024
	HBEM	1.0907	0.8564	0.5830	0.2798	0.0010
	M-DD-IBEM	1.0745	0.8316	0.5660	0.2744	0.0021
	M-FS-IBEM	1.1690	0.8507	0.6001	0.3032	0.0031
C, **D**	Reference_2	1.2036	1.2141	1.2019	1.1789	1.13314
	Reference_1	1.2011	1.2119	1.1999	1.1771	1.1329
	CBEM	1.2098	1.2172	1.2076	1.1780	1.1363
	HBEM	1.2102	1.2181	1.2077	1.1775	1.1371
	M-DD-IBEM	1.2047	1.2141	1.2057	1.1687	1.1281
	M-FS-IBEM	1.2144	1.2204	1.2285	1.1906	1.1564

7.4.3 A finite plate with two radial cracks emanating from a hole

To display the applicability of the proposed method for curved boundaries and simulate the hole-edge cracks, this model is involved. This model was analyzed in the book, "The handbook of stress intensity factors", written by G. Sih (Ref_3) [225].

The elastic modulus $E=1$ Mpa and Poisson's ratio ν=0.3. The width and height are 2W and 2H, and the geometry ratio is taken as $H/W=2$, $R/W=0.25$ and a/W changes from 0.3 to 0.9. Each crack is discretised by 400 elements, and the outer boundary and inner circle are meshed by 400 and 100 elements respectively. According to the geometric symmetry, the two cracks show the same result. So only one tip, far away from the circle, is taken.

According to the F_I listed in **Table 7.6**, the correctness of the proposed four methods is testified.

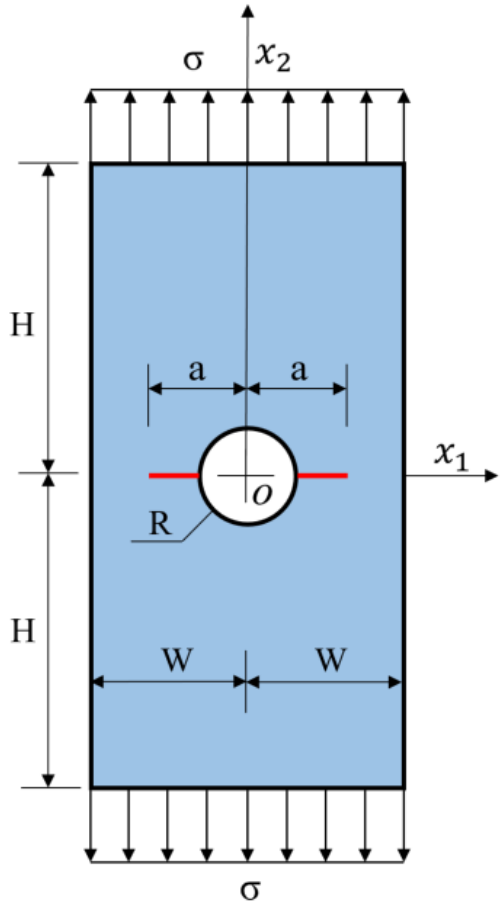

Fig.7.13 A hollow plate with two radial cracks

Table 7.5 F_I of the crack tips for the plate with two radial cracks

a/W	Ref_3	CBEM	DBIE-DDM	M-DD-IBEM	M-FS-IBEM
0.3	0.9605	0.9655	0.9880	0.9696	0.9534
0.4	1.0304	1.0395	1.0907	1.0493	1.0215
0.5	1.0776	1.0718	1.1128	1.0571	1.0760
0.6	1.1783	1.1593	1.1824	1.1654	1.1690
0.7	1.2156	1.1935	1.2270	1.2224	1.2055
0.8	1.2853	1.2936	1.3100	1.2896	1.2629
0.9	1.3965	1.4022	1.4085	1.372	1.3705

Chapter 8

The novel boundary integral equation with AOIMLS enhanced LIBEM for cracked domains under thermal stress

Summary

For finite cracked domains under unknown thermal field distribution, based on the direct BEM and DDM, a set of novel BIEs are derived. The main BIE is derived based on the displacement BIE, followed by two supplementary equations for ensuring enough equations as the unknowns on crack are considered. Besides, the two supplementary BIEs are alternatively used depending on the type of known quantities, traction or displacement. The thermal field is simulated by heat conduction BIEs first, and then thermal stress analysis for cracked domains is performed by the newly derived thermo-elastic BIEs. To treat the domain integrals caused by thermal stress, the AOIMLS enhanced LIBEM is proposed for domain integrals containing unknown functions. With AOIMLS enhanced LIBEM, domain integrals are reduced into boundary integrals with line integrals dimensionally and calculated by adding the line integrals up next. All the necessary temperature values for the line integral points can be interpolated from discretise nodes.

8.1 Introduction

Thermal and mechanical damage is one of the important fracture problems and has drawn much attention. As a vital factor in structural instability, thermal stress is not negligible for damaged structures [11, 226, 227]. Thereby research on cracked domains under thermo-elasticity is rather necessary.

Many methods, like FEM and XFEM, are well-known for dealing with relevant problems. The direct BEM [31, 228, 229], like other boundary collocation methods [230, 231], is widely applied in many fields, such as acoustic problems [232, 233] and heat conduction problems [41, 234, 235], is also popular as a treatment for crack problems [236-238]. However, most works are focused on using the DDM [97, 239], and indirect BEM to deal with the cracks in the infinite domain [121, 240] for simplicity, while the BIEs for crack problems are based on the direct BEM and DDM is also practicable but rare. In addition, thermo-elastic problems have been studied based on BEM as well [241-243]. Gao et al. [244] have developed thermo-elastic BIEs for crack-free domains with known temperature distribution, but it is not capable of treating those problems with unknown temperature distribution. While for most cases, the temperature distribution of structures are unknown, the heat conduction BIEs is needed for obtaining temperature of nodes on boundary or inner field.

As cracked domains under thermal stress are rather common as well [245] and worth paying attention to as mentioned earlier which is the main target of this research. To extend cracked domains to thermo-elasticity, a novel set of BIEs is derived in this paper. The unknown thermal field of cracked domains is simulated first which is introduced in detail in **Section 8.2**. As the heat conduction BIEs can be obtained already, thermo-elastic BIEs for finite cracked domains under thermal stress are needed, which, as one of the key points of this research, is proposed based on the direct BEM and DDM. One can refer to **Section 8.2** and **Appendix A** and **B** for the derivation process. Hence, thermal stresses of cracked domains can be simulated by the newly

derived thermo-elastic BIEs.

However, an unavoidable question occurs. As thermal stress is considered, domain integrals are introduced in the thermo-elastic BIEs. For dealing with them, the AOIMLS-LIM is proposed which avoids losing the advantage, boundary-only discretisation of the BEM. In recent years, Wang et al. proposed LIM [78, 127, 196] which is an efficient dimension reduction method and owns the ability that reduces domain integrals to line integrals. Further, for high accuracy, the initial integral lines are subdivided, adopting adaptive background cells [191], into sub-lines, then the domain integrals are calculated by summing up line integrals.

However, the traditional LIM does not own the ability to deal with the domain integrals as the values for integral points are unknown. As another key in this paper, the AOIMLS-LIM is proposed, which is a method that couples the LIM with AOIMLS [162], the AOIMLS can interpolate the values for integral points. Unlike other moving least-square methods [176, 246, 247], the AOIMLS method possesses the advantage that avoiding ill-condition or singular moment matrix adaptively during interpolation. Besides, the AOIMLS owns the delta function property which allows imposing boundary conditions easily.

This chapter is organized as follows. The thermo-elastic BIEs based on the directed BEM and DDM for cracked domains are derived in **Section 8.2** and **Appendix A**, **B**. Then the AOIMLS enhanced LIBEM is put forward and presented in detail in **Section 8.3** to deal with the domain integrals, which can reduce the domain integrals dimensionally and interpolate values for integral points. In the end, three examples are proposed to testify to the correctness of AOIMLS enhanced LIBEM.

8.2 The BEM for thermo-elastic problems with cracks

In this section, the BIEs for thermo-elasticity with cracks are derived based on the direct BEM and DDM.

Theorem 1 Assuming a Dirichlet domain Ω with a bounded boundary Γ

and a crack which has two surfaces (see **Fig.8.1**), S^+ and S^-, one surface is employed to represent the crack and one can assume the S^- is collapsed onto S^+. Hence, the displacement and traction BIEs for thermo-elastic problems containing cracks are obtained

$$\begin{aligned} c_{ij}(\mathbf{x})u_j(\mathbf{x}) &= \int_\Gamma U_{ij}(\mathbf{x},\mathbf{y})t_j(\mathbf{y})\mathrm{d}\Gamma(\mathbf{y}) - \int_\Gamma T_{ij}(\mathbf{x},\mathbf{y})u_j(\mathbf{y})\mathrm{d}\Gamma(\mathbf{y}) \\ &\quad - \int_\Omega \beta\Phi_i(\mathbf{x},\mathbf{y})\theta(\mathbf{y})\mathrm{d}\Omega(\mathbf{y}) + u_i^*(\mathbf{x})|\mathbf{y}, \quad \mathbf{x}\in\Gamma \end{aligned} \tag{8.1}$$

$$\begin{aligned} \sum u_i(\mathbf{x}) &= \int_\Gamma U_{ij}(\mathbf{x},\mathbf{y})t_j(\mathbf{y})\mathrm{d}\Gamma(\mathbf{y}) - \int_\Gamma T_{ij}(\mathbf{x},\mathbf{y})u_j(\mathbf{y})\mathrm{d}\Gamma(\mathbf{y}) \\ &\quad - \int_\Omega \beta\Phi_i(\mathbf{x},\mathbf{y})\theta(\mathbf{y})\mathrm{d}\Omega(\mathbf{y}) + u_i^*(\mathbf{x})|\mathbf{y}, \quad \mathbf{x}\in S^+ \end{aligned} \tag{8.2}$$

$$\begin{aligned} \Delta t_i(\mathbf{x}) &= \Big\{\int_\Gamma \big[U_{ik,j}(\mathbf{x},\mathbf{y})t_k(\mathbf{y}) - T_{ik,j}(\mathbf{x},\mathbf{y})u_k(\mathbf{y})\big]\mathrm{d}\mathbf{y} \\ &\quad + \int_\Gamma \beta r_{,\mathrm{m}} n_m \ln(r^r)\theta(\mathbf{x})\Psi_{ij}(\mathbf{x},\mathbf{y})\mathrm{d}\Gamma(\mathbf{y}) \\ &\quad + \int_\Omega \beta\big[\theta(\mathbf{y}) - \theta(\mathbf{x})\big]\Psi_{ij}(\mathbf{x},\mathbf{y})\mathrm{d}\Omega(\mathbf{y}) \\ &\quad - b\beta\delta_{ij}\theta(\mathbf{y}) + t_{ij}^*(\mathbf{x})|\mathbf{y}\Big\} n_j(\mathbf{x}), \quad \mathbf{x}\in S^+ \end{aligned} \tag{8.3}$$

where

$$\begin{aligned} \sum u_i(\mathbf{x}) &= c_{ij}(\mathbf{x}^+)u_j(\mathbf{x}^+) + [1 - c_{ij}(\mathbf{x}^+)]u_j(\mathbf{x}^-) \\ &= u_i(\mathbf{x}^-) + c_{ij}(\mathbf{x}^+)\Delta u_j(\mathbf{x}) \\ &= u_i(\mathbf{x}^-) - [1 - c_{ij}(\mathbf{x}^+)]\Delta u_j(\mathbf{x}) \end{aligned} \tag{8.4}$$

$$\begin{aligned} \Delta t_i(\mathbf{x}) &= c_{ij}(\mathbf{x}^+)t_j(\mathbf{x}^+) - [1 - c_{ij}(\mathbf{x}^+)]t_j(\mathbf{x}^-) \\ &= c_{ij}(\mathbf{x}^+)\sum t_j(\mathbf{x}) - t_i(\mathbf{x}^-) \\ &= -[1 - c_{ij}(\mathbf{x}^+)]\sum t_j(\mathbf{x}) + t_i(\mathbf{x}^+) \end{aligned} \tag{8.5}$$

$$u_i^*(\mathbf{x})|\mathbf{y} = -\int_{S^+} T_{ij}(\mathbf{x},\mathbf{y})\Delta u_j(\mathbf{y})\mathrm{d}\Gamma(\mathbf{y}) \tag{8.6}$$

$$t_i^*(\mathbf{x})|\mathbf{y} = -\int_{S^+} T_{ik,j}(\mathbf{x},\mathbf{y})\Delta u_k(\mathbf{y})\mathrm{d}\Gamma(\mathbf{y}) \tag{8.7}$$

$$\Phi_i(\mathbf{x},\mathbf{y}) = \frac{-(1+\nu)r_{,i}}{2\pi(1-\nu)r} \tag{8.8}$$

$$\Psi_{ij}(\mathbf{x},\mathbf{y}) = \frac{-\mu(1+\nu)(\delta_{ij} - 2r_{,i}r_{,j})}{\pi(1-\nu)r^2} \tag{8.9}$$

$$b = \frac{\mu(1+\nu)}{1-\nu} \tag{8.10}$$

and δ_{ij}=1 for the case, $i=j$, else δ_{ij}=0. Δu_i is crack opening displacement. μ and λ are the Lame constants, $i,j=1,2$, ν represents the Poisson ratio, θ symbolize the temperature, β represents the coefficient of thermal expansion.

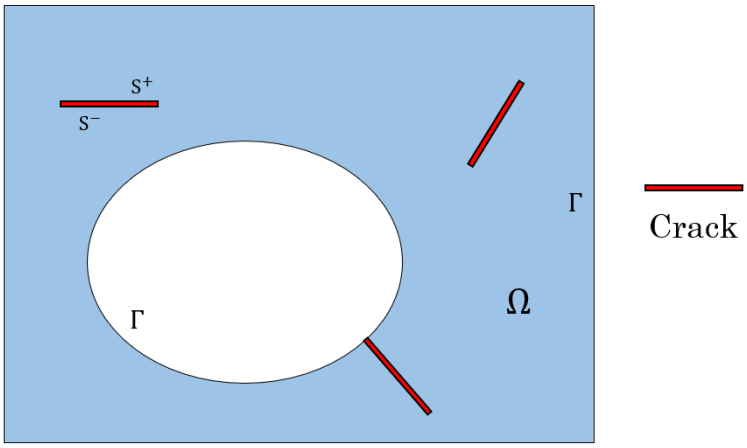

Fig.8.1 Domain with cracks

Proof.1

In this part, Eq.(8.1) is proved first.

The governing equation of thermo-elastic problems is as follows [10]

$$(\lambda+\mu)u_{j,ji}(\mathbf{x},\mathbf{y})+\mu u_{i,jj}(\mathbf{x},\mathbf{y})-\frac{\beta\lambda(1+\nu)}{\nu}\theta_{,i}(\mathbf{y})=0 \qquad i,j=1,\ 2;\ \mathbf{x},\mathbf{y}\in\Omega \tag{8.11}$$

Based on Bett's reciprocal theorem, one can deduce the following regularized displacement BIE

$$\begin{aligned} c_{ij}(\mathbf{x})u_i(\mathbf{x})=&\int_\Gamma U_{ij}(\mathbf{x},\mathbf{y})\mathbf{t}_j(\mathbf{y})d\Gamma(\mathbf{y})-\int_\Gamma T_{ij}(\mathbf{x},\mathbf{y})\mathbf{u}_j(\mathbf{y})\mathrm{d}\Gamma(\mathbf{y})\\ &-\int_\Omega \beta\Phi_i(\mathbf{x},\mathbf{y})\theta(\mathbf{y})\mathrm{d}\Omega(\mathbf{y}) \end{aligned} \tag{8.12}$$

Based on the thermo-elastic BIEs Eq.(8.12), for points $\mathbf{x}\in\Gamma$, the displacement BIEs can be written as

$$\begin{aligned} c_{ij}(\mathbf{x})u_j(\mathbf{x})=&\int_\Gamma U_{ij}(\mathbf{x},\mathbf{y})t_j(\mathbf{y})\mathrm{d}\Gamma(\mathbf{y})-\int_\Gamma T_{ij}(\mathbf{x},\mathbf{y})u_j(\mathbf{y})\mathrm{d}\Gamma(\mathbf{y})\\ &-\int_\Omega \beta\Phi_i(\mathbf{x},\mathbf{y})\theta(\mathbf{y})\mathrm{d}\Omega(\mathbf{y})+u_i(\mathbf{x})|\mathbf{y}^+\\ &+\lim_{S^-\to S^+}u_i(\mathbf{x})|\mathbf{y}^- \end{aligned} \tag{8.13}$$

where $\mathbf{y}^+$ and $\mathbf{y}^-$ are points on S^+ and S^- respectively and

$$u_i(\mathbf{x})|\mathbf{y}^\pm=\int_{S^\pm}U_{ij}(\mathbf{x},\mathbf{y}^\pm)t_j(\mathbf{y}^\pm)\mathrm{d}\Gamma(\mathbf{y}^\pm)-\int_{S^\pm}T_{ij}(\mathbf{x},\mathbf{y}^\pm)u_j(\mathbf{y}^\pm)\mathrm{d}\Gamma(\mathbf{y}^\pm) \tag{8.14}$$

Since one can have $U(\mathbf{x},\mathbf{y}^+)=U(\mathbf{x},\mathbf{y}^-)$ and $T(\mathbf{x},\mathbf{y}^+)=-T(\mathbf{x},\mathbf{y}^-)$, for $\varsigma\in\Gamma$, Eq.(8.13) is rewritten as

$$\begin{aligned} c_{ij}(\mathbf{x})u_j(\mathbf{x})=&\int_\Gamma U_{ij}(\mathbf{x},\mathbf{y})t_j(\mathbf{y})\mathrm{d}\Gamma(\mathbf{y})-\int_\Gamma T_{ij}(\mathbf{x},\mathbf{y})u_j(\mathbf{y})\mathrm{d}\Gamma(\mathbf{y})\\ &-\int_\Omega \beta\Phi_i(\mathbf{x},\mathbf{y})\theta(\mathbf{y})\mathrm{d}\Omega(\mathbf{y})+u_j^*(\mathbf{x})|\mathbf{y}^+ \end{aligned} \tag{8.15}$$

$$u_j^*(\mathbf{x})|\mathbf{y}^+=\int_{S^+}U_{ij}(\mathbf{x},\mathbf{y}^+)\sum t_j(\mathbf{y})\mathrm{d}\Gamma(\mathbf{y}^+)-\int_{S^+}T_{ij}(\mathbf{x},\mathbf{y}^+)\Delta u_j(\mathbf{y})\mathrm{d}\Gamma(\mathbf{y}^+) \tag{8.16}$$

and

$$\sum t_j(\mathbf{y}) = t_j(\mathbf{y}^+) + t_j(\mathbf{y}^-) \tag{8.17}$$

$$\Delta u_j(\mathbf{y}) = u_j(\mathbf{y}^+) - u_j(\mathbf{y}^-) \tag{8.18}$$

Hence, Eq.(8.1) is proved.

Proof.2

Secondly, Eq.(8.2) is proved in this part.

For points $\mathbf{x} \in S^+$ and $\mathbf{x} \in S^-$, the displacement BIEs are expressed below

$$\begin{aligned} c_{ij}(\mathbf{x}^+)u_j(\mathbf{x}^+) = &\int_\Gamma U_{ij}(\mathbf{x}^+,\mathbf{y})t_j(\mathbf{y})\mathrm{d}\Gamma(\mathbf{y}) - \int_\Gamma T_{ij}(\mathbf{x}^+,\mathbf{y})u_j(\mathbf{y})\mathrm{d}\Gamma(\mathbf{y}) \\ &- \int_\Omega \beta\Phi_i(\mathbf{x}^+,\mathbf{y})\theta(\mathbf{y})\mathrm{d}\Omega(\mathbf{y}) + u_i(\mathbf{x}^+)|\,\mathbf{y}^+ \\ &+ \lim_{S^-\to S^+} u_i(\mathbf{x}^+)|\,\mathbf{y}^- \end{aligned} \tag{8.19}$$

$$\begin{aligned} c_{ij}(\mathbf{x}^-)u_j(\mathbf{x}^-) = &\int_\Gamma U_{ij}(\mathbf{x}^-,\mathbf{y})t_j(\mathbf{y})\mathrm{d}\Gamma(\mathbf{y}) - \int_\Gamma T_{ij}(\mathbf{x}^-,\mathbf{y})u_j(\mathbf{y})\mathrm{d}\Gamma(\mathbf{y}) \\ &- \int_\Omega \beta\Phi_i(\mathbf{x}^+,\mathbf{y})\theta(\mathbf{y})\mathrm{d}\Omega(\mathbf{y}) + u_i(\mathbf{x}^-)|\,\mathbf{y}^+ \\ &+ \lim_{S^-\to S^+} u_i(\mathbf{x}^-)|\,\mathbf{y}^- \end{aligned} \tag{8.20}$$

For $\mathbf{x} \in S^+$, Eq.(8.19) and (8.20), can be reduced to one equation [97] as the following equation and the detailed derivation process can be found in **Appendix A**.

$$\begin{aligned} \sum u_i(\mathbf{x}) = &\int_\Gamma U_{ij}(\mathbf{x},\mathbf{y})t_j(\mathbf{y})\mathrm{d}\Gamma(\mathbf{y}) - \int_\Gamma T_{ij}(\mathbf{x},\mathbf{y})u_j(\mathbf{y})\mathrm{d}\Gamma(\mathbf{y}) \\ &- \int_\Omega \beta\Phi_i(\mathbf{x},\mathbf{y})\theta(\mathbf{y})\mathrm{d}\Omega(\mathbf{y}) + u_i^*(\mathbf{x})|\,\mathbf{y} \end{aligned} \tag{8.21}$$

Besides, the load on the crack surface can be assumed to be equal, i.e. $\sum t_i(\mathbf{y}) = 0$, then Eq.(8.16) can be reduced to

$$u_j^*(\mathbf{x})|\,\mathbf{y} = -\int_{S^+} T_{ij}(\mathbf{x},\mathbf{y}^+)\Delta u_j(\mathbf{y})\mathrm{d}\Gamma(\mathbf{y}) \tag{8.22}$$

So one can obtain Eq.(8.2).

Proof.3

The regularized inner stress BIE got based on the governing equation and the strain-displacement relationship is shown as follows [244]

$$\begin{aligned} \sigma_{ij}(\mathbf{x}) = &\int_\Gamma U_{ijk}(\mathbf{x},\mathbf{y})t_k(\mathbf{y})\mathrm{d}\Gamma - \int_\Gamma \mathrm{T}_{ijk}(\mathbf{x},\mathbf{y})u_k(\mathbf{y})\mathrm{d}\Gamma \\ &+ \beta\theta(\mathbf{y})\int_\Gamma r_{,\mathrm{m}} n_m \ln(r^r)\varphi_{ij}(\mathbf{x},\mathbf{y})\mathrm{d}\Gamma(\mathbf{y}) \\ &+ \int_\Omega \beta\Psi_{ij}(\mathbf{x},\mathbf{y})\theta(\mathbf{y})\mathrm{d}\Omega(\mathbf{y}) \\ &- \int_\Omega \beta\Psi_{ij}(\mathbf{x},\mathbf{y})\theta(\mathbf{x})\mathrm{d}\Omega(\mathbf{y}) \\ &- \delta_{ij}\beta b\theta(\mathbf{x}) \end{aligned} \tag{8.23}$$

Combining Eq.(8.23) with

$$t_i = \sigma_{ij} n_j \tag{8.24}$$

one can obtain

$$\begin{aligned} c_{ij}(\mathbf{x}) t_j(\mathbf{x}) = & \int_\Gamma K_{ki}(\mathbf{x},\mathbf{y}) t_k(\mathbf{y}) \mathrm{d}(\mathbf{y}) - \int_\Gamma H_{ki}(\mathbf{x},\mathbf{y}) u_k(\mathbf{y}) \mathrm{d}(\mathbf{y}) \\ & + \int_\Gamma \beta r_{,\mathrm{m}} n_m \ln(r^r) \theta(\mathbf{x}) \Psi_{ij}(\mathbf{x},\mathbf{y}) n_j(\mathbf{x}) \mathrm{d}\Gamma(\mathbf{y}) \\ & + \int_\Omega \beta \left[\theta(\mathbf{y}) - \theta(\mathbf{x}) \right] \Psi_{ij}(\mathbf{x},\mathbf{y}) n_j(\mathbf{x}) \mathrm{d}\Omega(\mathbf{y}) \\ & - b\beta\delta_{ij} \theta(\mathbf{y}) n_j(\mathbf{x}) \end{aligned} \tag{8.25}$$

For points $\mathbf{x} \in S^+$ and $\mathbf{x} \in S^-$, the traction BIEs can be written as

$$\begin{aligned} c_{ij}(\mathbf{x}^+) t_j(\mathbf{x}^+) = & \int_\Gamma K_{ki}(\mathbf{x}^+,\mathbf{y}) t_k(\mathbf{y}) \mathrm{d}\Gamma(\mathbf{y}) - \int_\Gamma H_{ki}(\mathbf{x}^+,\mathbf{y}) u_k(\mathbf{y}) \mathrm{d}\Gamma(\mathbf{y}) \\ & + \int_\Gamma \beta r_{,\mathrm{m}} n_m \ln(r^r) \theta(\mathbf{x}) \Psi_{ij}(\mathbf{x}^+,\mathbf{y}) n_j(\mathbf{x}^+) \mathrm{d}\Gamma(\mathbf{y}) \\ & + \int_\Omega \beta \left[\theta(\mathbf{y}) - \theta(\mathbf{x}^+) \right] \Psi_{ij}(\mathbf{x}^+,\mathbf{y}) n_j(\mathbf{x}^+) \mathrm{d}\Omega(\mathbf{y}) \\ & - b\beta\delta_{ij} \theta(\mathbf{y}) n_j(\mathbf{x}^+) + t_i(\mathbf{x}^+) | \mathbf{y}^+ \\ & + \lim_{S^- \to S^+} t_i(\mathbf{x}^+) | \mathbf{y}^- \end{aligned} \tag{8.26}$$

$$\begin{aligned} c_{ij}(\mathbf{x}^-) t_j(\mathbf{x}^-) = & \int_\Gamma K_{ki}(\mathbf{x}^-,\mathbf{y}) t_k(\mathbf{y}) \mathrm{d}\Gamma(\mathbf{y}) - \int_\Gamma H_{ki}(\mathbf{x}^-,\mathbf{y}) u_k(\mathbf{y}) \mathrm{d}\Gamma(\mathbf{y}) \\ & + \int_\Gamma \beta r_{,\mathrm{m}} n_m \ln(r^r) \theta(\mathbf{x}) \Psi_{ij}(\mathbf{x}^-,\mathbf{y}) n_j(\mathbf{x}^-) \mathrm{d}\Gamma(\mathbf{y}) \\ & + \int_\Omega \beta \left[\theta(\mathbf{y}) - \theta(\mathbf{x}^-) \right] \Psi_{ij}(\mathbf{x}^-,\mathbf{y}) n_j(\mathbf{x}^-) \mathrm{d}\Omega(\mathbf{y}) \\ & - b\beta\delta_{ij} \theta(\mathbf{y}) n_j(\mathbf{x}^-) + t_i(\mathbf{x}^-) | \mathbf{y}^+ \\ & + \lim_{S^- \to S^+} t_i(\mathbf{x}^-) | \mathbf{y}^- \end{aligned} \tag{8.27}$$

and

$$t_i(\mathbf{x}) | \mathbf{y}^\pm = \int_{S^\pm} K_{ki}(\mathbf{x},\mathbf{y}^\pm) t_k(\mathbf{y}^\pm) \mathrm{d}\Gamma(\mathbf{y}) - \int_{S^\pm} H_{ki}(\mathbf{x},\mathbf{y}^\pm) u_k(\mathbf{y}^\pm) \mathrm{d}\Gamma(\mathbf{y}) \tag{8.28}$$

Last, from Eq.(8.26) and (8.27), one can have

$$\begin{aligned} \Delta t_i(\mathbf{x}) = & \int_\Gamma K_{ki}(\mathbf{x},\mathbf{y}) t_k(\mathbf{y}) \mathrm{d}\Gamma(\mathbf{y}) - \int_\Gamma H_{ki}(\mathbf{x},\mathbf{y}) u_k(\mathbf{y}) \mathrm{d}\Gamma(\mathbf{y}) \\ & + \int_\Gamma \beta r_{,\mathrm{m}} n_m \ln(r^r) \theta(\mathbf{x}) \Psi_{ij}(\mathbf{x},\mathbf{y}) n_j(\mathbf{x}) \mathrm{d}\Gamma(\mathbf{y}) \\ & + \int_\Omega \beta \left[\theta(\mathbf{y}) - \theta(\mathbf{x}) \right] \Psi_{ij}(\mathbf{x},\mathbf{y}) n_j(\mathbf{x}) \mathrm{d}\Omega(\mathbf{y}) \\ & - b\beta\delta_{ij} \theta(\mathbf{y}) n_j(\mathbf{x}) + t_i^*(\mathbf{x}) | \mathbf{y}, \quad \mathbf{x} \in S^+ \end{aligned} \tag{8.29}$$

with

$$t_i^*(\mathbf{x}) | \mathbf{y} = \int_{S^+} K_{ki}(\mathbf{x},\mathbf{y}^+) \sum t_j(\mathbf{y}^+) \mathrm{d}\Gamma(\mathbf{y}) - \int_{S^+} H_{ki}(\mathbf{x},\mathbf{y}^+) \Delta u_j(\mathbf{y}^+) \mathrm{d}\Gamma(\mathbf{y}) \tag{8.30}$$

And one can refer to **Appendix B** for the derivation process.

Since $\sum t_i(\mathbf{y}) = 0$, then Eq.(8.30) can be reduced to

$$t_i^*(\mathbf{x})|\mathbf{y}=-\int_{S^+} H_{ki}(\mathbf{x},\mathbf{y}^+)\Delta u_j(\mathbf{y}^+)\mathrm{d}\Gamma(\mathbf{y}) \tag{8.31}$$

Hence, Eq.(8.3) is proved, further, the derivation of **Proof.1** is finished.

During simulation, Eq.(8.1) can be applied to form the coefficient matrix relative to the values on the boundary Γ, the second equation is used when $\Delta t_i(\mathbf{x})$ are known on S, while the last equation can be used when $u_i(\mathbf{x}^+)$ or $u_i(\mathbf{x}^-)$ are known on S.

8.3 AOIMLS enhanced LIBEM

The AOIMLS enhanced LIBEM is put forward in particular as a dimension reduction method. For thermo-elastic problems, LIBEM can be used for dimension reduction directly as the temperature distribution is known. While it is not feasible to compute all the temperature values for the line integral points when it comes to thermo-elastic problems with unknown temperature distribution, so the AOIMLS is applied to couple with the LIBEM for interpolating to get the values of the line integral points.

One can calculate the domain integrals in Eqs.(8.1), (8.2) and (8.3) by the AOIMLS enhanced LIBEM as the following form respectively

$$\begin{aligned} D_1(\mathbf{x}) &= \int_\Omega \beta\theta(\mathbf{y})\Phi_i(\mathbf{x},\mathbf{y})\mathrm{d}\Omega(\mathbf{y}) \\ &= \sum_{k=1}^{N}\sum_{i=1}^{M} n_1^i(\mathbf{y}) w^i \int_{L_i} \beta\Phi_i(\mathbf{x},\mathbf{y})\varphi_k(\mathbf{y})\mathrm{d}y_1\theta_k(\mathbf{y}) \end{aligned} \tag{8.32}$$

$$\begin{aligned} D_2(\mathbf{x}) &= \int_\Omega \beta\left[\theta(\mathbf{y})-\theta(\mathbf{x})\right]\Psi_{ij}(\mathbf{x},\mathbf{y})n_j(\mathbf{x})\mathrm{d}\Omega(\mathbf{y}) \\ &= \sum_{k=1}^{N}\sum_{i=1}^{M} n_1^i(\mathbf{y}) w^i \int_{L_i} \Psi_{ij}(\mathbf{x},\mathbf{y})n_j(\mathbf{x})\varphi_k(\mathbf{y})\mathrm{d}y_1\beta\left[\theta_k(\mathbf{y})-\theta_k(\mathbf{x})\right] \end{aligned} \tag{8.33}$$

8.4 Numerical examples

To prove the correctness of the novel theorem described previously, three numerical instances are introduced. The first case is aimed at proving the theoretical model can be applied to elastic problems with cracks and the thermal field is not considered. While the thermal field is involved in the latter two examples, i.e. the thermal field is simulated by the heat conduction BIEs, then with the help of the AOIMLS enhanced LIBEM, the cracked structure is simulated in the elastic field. And for testifying to the correctness of the

proposed method, the stress intensity factors (SIFs), K_{I} or K_{II} [238], normalized SIFs of crack tips are introduced and compared with the previous research. The normalized SIFs are expressed below

$$F_{\mathrm{I}} = \frac{K_{\mathrm{I}}}{\sigma\sqrt{\pi a}} \tag{8.34}$$

$$F_{\mathrm{II}} = \frac{K_{\mathrm{II}}}{\sigma\sqrt{\pi a}} \tag{8.35}$$

where σ represents the known traction on the boundary. a is the half-length of a crack.

8.4.1 A rectangle contains an angled crack

There is an angled crack preset in the rectangular plate (see **Fig.8.2**). The geometrical parameters, boundary conditions and mechanical parameters are shown in **Table 8.1**. The angle of the crack, θ varies in 15^0, 22.5^0, 30^0, 45^0 and 60^0. To testify to the correctness, the normalized SIFs are presented and compared with the previous research [248-250].

Table 8.1 Parameters of the rectangular plate with angled crack

The length	2L=40mm
The width	2W=40mm
The ratio of a to W	a/W=0.2
Angle of crack	$\theta = 15^0 \sim 60^0$
Poisson's ratio	$\mu = 0.3$
Elastic modulus	$E = 210\mathrm{Gpa}$
Uniform pressure	$\sigma = 1\mathrm{Mpa}$

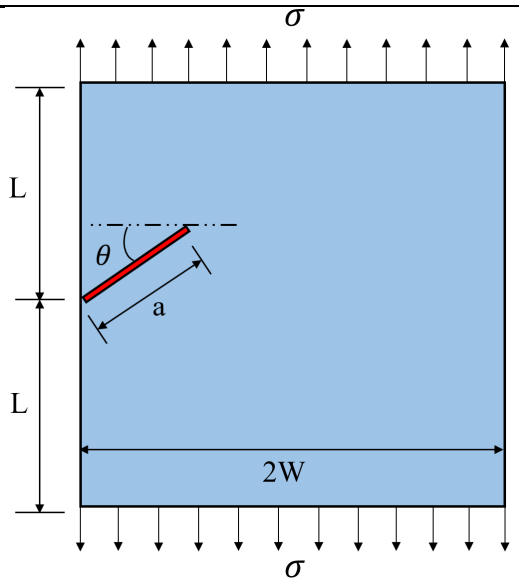

Fig.8.2 A rectangular plate with an angled crack

Table 8.2 The comparison of normalized SIFs

θ	Mode	Normalized SIFs			
		Ref. [250]	Ref. [249]	Ref.[248]	The proposed method
15.0	I		2.548	2.560	2.566
	II		0.370	0.362	0.359
22.5	I	2.280	2.255	2.274	2.275
	II	0.495	0.500	0.488	0.472
30.0	I		1.906	1.936	1.941
	II		0.579	0.561	0.557
45.0	I	1.200	1.231	1.252	1.261
	II	0.570	0.585	0.568	0.565
60.0	I			0.680	0.673
	II			0.449	0.440

In **Table 8.2**, the comparison of previous research with the new approach is listed. See **Fig.8.3**, the solid lines represent the new mathematic theorem, while dash lines and dash-dot lines represent previous research Ref.[249] and Ref. [248]. Obviously, the normalized SIFs for model I descend gradually with the increase of θ, while the normalized SIFs for model I ascend firstly, then decrease slightly. Moreover, the results obtained based on the new method are in high accuracy compared with the results of previous research. Hence, the efficiency and correctness of the proposed method for elastic problems with cracks are proved moreover, this model proves that the proposed theorem can deal with cracks in all kinds of locations.

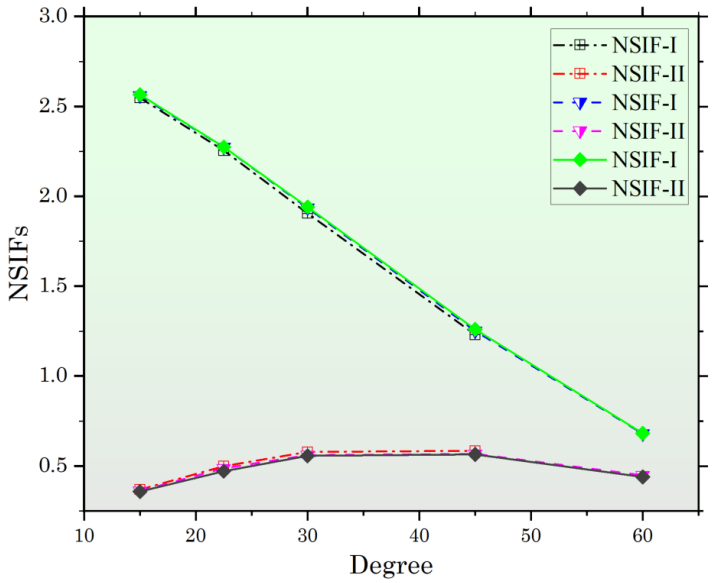

Fig.8.3 The comparison of normalized SIFs

8.4.2 A centre cracked plate

In this numerical model, a centre crack is set in the middle of a rectangular plate, and all the necessary geometrical and mechanical parameters are presented in **Table 8.3**, it is a thermo-elastic problem with unknown temperature distribution.

Table 8.3 Parameters of the rectangular plate contains centre crack

The Length	L=40mm
The Width	W=40mm
The ratio of a to W	a/W=0.1-0.6
The Poisson's ratio	$\mu = 0.3$
The Elastic Modulus	$E = 1\text{Mpa}$
Thermal expansion coefficient	$\alpha = 10^{-4}/^{0}C$
The temperature of the crack surface	$\theta_1 = 0^0 C$
The temperature of the outer boundary	$\theta_2 = 100^0 C$

See **Table 8.4**, the ratio of a to W varies from 0.1 to 0.6, which means the length of cracks changes varies with the ratio, and this is aimed at proving the correctness of the proposed method when dealing with different sizes of cracks, by analyzing **Fig.8.5**, one can obtain that with the increase of the length of the crack, the normalized SIFs rise meanwhile. Besides, the proposed method shows a high coincidence with the previous research, and the relative error in Table 8.4 can testify to that as well.

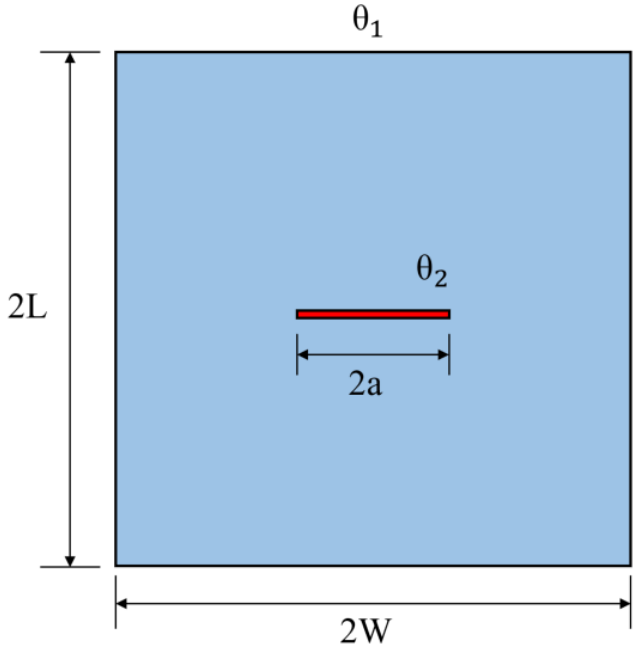

Fig.8.4 A rectangular plate contains a central crack

Table 8.4 The comparison of normalized SIFs

a/W	Normalized SIFs			
	Ref_1.[251]	Ref_2.[248]	The proposed	Error (%)
0.1	0.0174	0.0171	0.0170	2.30
0.2	0.0221	0.0219	0.0216	0.90
0.4	0.0291	0.0284	0.0280	0.68
0.5	0.0310	0.0310	0.0307	0.32
0.6	0.0332	0.0332	0.0330	0.60

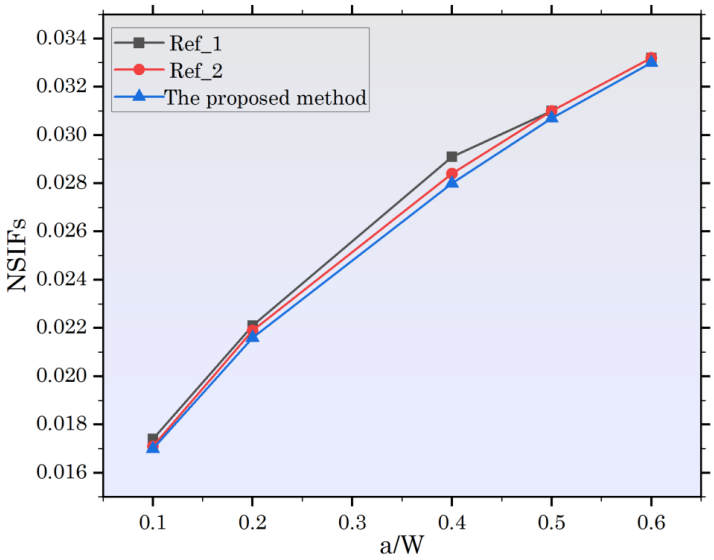

Fig.8.5 Results comparison of normalized SIFs

8.4.3 Pressurized annulus with radial crack

In this section, for further proof, a pressurized annulus with radial crack (see **Fig.8.6**), undertakes the thermal field as well, and is modelled which is more complicated in geometry, one can see that all the necessary geometrical and mechanical parameters and boundary conditions are presented in **Table 8.5**.

Table 8.5 Parameters of the pressurized annulus with radial crack

The radius of the circle inside	R_1=10cm
The radius of the circle outside	R_2=20cm
Variety of the length of crack	$a/(R_2-R_1)$=0.2-0.6
The Poisson's ratio	$\mu = 0.3$
The Elastic Modulus	$E = 2.1\times10^5$ Mpa
The inner pressure	$p = 1$Mpa
Thermal expansion coefficient	$\beta = 1.2\times10^{-5}/^0C$
The temperature of the circle inside	$\theta_1 = 0^0C$
The temperature of the circle outside	$\theta_2 = 300^0C$

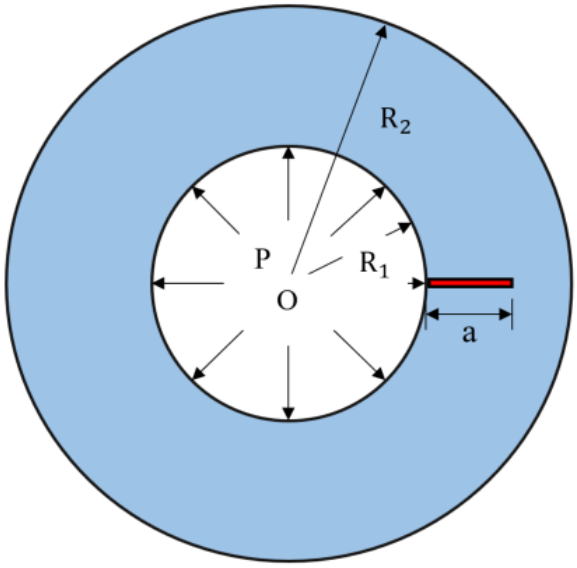

Fig.8.6 Pressured annulus with radial crack

Table 8.6 SIFs for the annulus with radial crack

SIFs	$a/(R_2-R_1)$				
	0.2	0.3	0.4	0.5	0.6
Ref_3.[252]	128.19	136.07	135.68	129.35	117.31
The proposed method	129.80	138.02	137.32	130.55	117.74
Error (%)	1.26	1.43	1.21	0.93	0.37

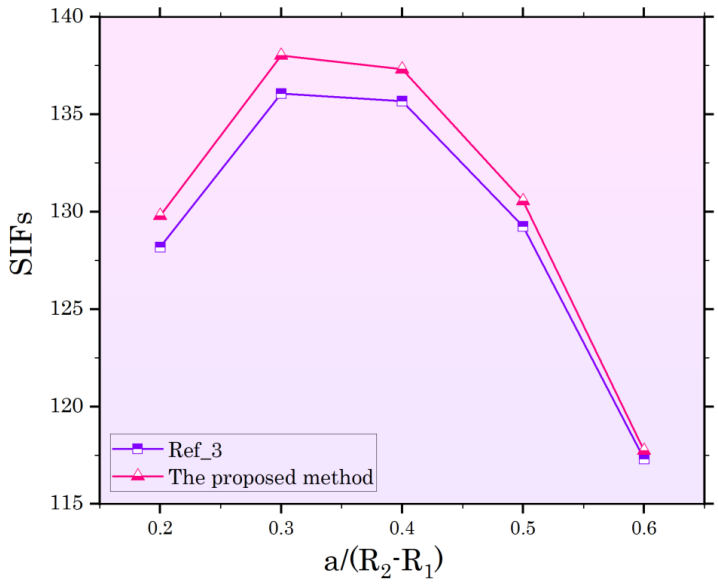

Fig.8.7 SIFs for the annulus with radial crack

As one can see in **Table 8.6**, the SIFs are listed under different conditions. In general, the result got from the proposed method are larger than the result of previous research (Ref_3) [252], additionally, the relative errors are rather low and the largest one is only 1.43%. Then see **Fig.8.7**, one can draw the

conclusion that, with the increase of $a/(R_2-R_1)$, the SIFs show an increasing trend, then decrease gradually. All in all, compared with the results in Ref.[252], the accuracy of the proposed mathematic theorem is proved.

Appendix A.

One can derivate the term $\lim_{S^-\to S^+} u_i(\mathbf{x}^+)|\mathbf{y}^-$ in Eq.(8.19) as follows

$$\begin{aligned}
&\lim_{S^-\to S^+}\int_{S^-} U_{ij}(\mathbf{x}^+,\mathbf{y}^-)t_j(\mathbf{y}^-)\mathrm{d}\Gamma(\mathbf{y})-\int_{S^-} T_{ij}(\mathbf{x}^+,\mathbf{y}^-)u_j(\mathbf{y}^-)\mathrm{d}\Gamma(\mathbf{y})\\
&=\lim_{\mathbf{x}^+\to S^-}\int_{S^-} U_{ij}(\mathbf{x}^+,\mathbf{y}^-)t_j(\mathbf{y}^-)\mathrm{d}\Gamma(\mathbf{y})-\int_{S^-} T_{ij}(\mathbf{x}^+,\mathbf{y}^-)u_j(\mathbf{y}^-)\mathrm{d}\Gamma(\mathbf{y})\\
&=-c_{ij}(\mathbf{x}^-)u_j(\mathbf{x}^-)+\int_{S^-} U_{ij}(\mathbf{x}^+,\mathbf{y}^-)t_j(\mathbf{y}^-)\mathrm{d}\Gamma(\mathbf{y})-\int_{S^-} T_{ij}(\mathbf{x}^+,\mathbf{y}^-)u_j(\mathbf{y}^-)\mathrm{d}\Gamma(\mathbf{y})\\
&=-c_{ij}(\mathbf{x}^-)u_j(\mathbf{x}^-)+\int_{S^+} U_{ij}(\mathbf{x}^+,\mathbf{y}^+)t_j(\mathbf{y}^-)\mathrm{d}\Gamma(\mathbf{y})+\int_{S^+} T_{ij}(\mathbf{x}^+,\mathbf{y}^+)u_j(\mathbf{y}^-)\mathrm{d}\Gamma(\mathbf{y})
\end{aligned}\tag{8.36}$$

In addition, the derivation of $u_i(\mathbf{x}^-)|\mathbf{y}^+$ and $\lim_{S^-\to S^+} u_i(\mathbf{x}^-)|\mathbf{y}^-$ in Eq.(8.20) can be expressed as

$$\begin{aligned}
&\int_{S^-} U_{ij}(\mathbf{x}^-,\mathbf{y}^+)t_j(\mathbf{y}^+)\mathrm{d}\Gamma(\mathbf{y})-\int_{S^-} T_{ij}(\mathbf{x}^-,\mathbf{y}^+)u_j(\mathbf{y}^+)\mathrm{d}\Gamma(\mathbf{y})\\
&=\lim_{\mathbf{x}^-\to S^+}\int_{S^+} U_{ij}(\mathbf{x}^-,\mathbf{y}^+)t_j(\mathbf{y}^+)\mathrm{d}\Gamma(\mathbf{y})-\int_{S^+} T_{ij}(\mathbf{x}^-,\mathbf{y}^+)u_j(\mathbf{y}^+)\mathrm{d}\Gamma(\mathbf{y})\\
&=-c_{ij}(\mathbf{x}^+)u_j(\mathbf{x}^+)+\int_{S^+} U_{ij}(\mathbf{x}^+,\mathbf{y}^+)t_j(\mathbf{y}^+)\mathrm{d}\Gamma(\mathbf{y})-\int_{S^+} T_{ij}(\mathbf{x}^+,\mathbf{y}^+)u_j(\mathbf{y}^+)\mathrm{d}\Gamma(\mathbf{y})
\end{aligned}\tag{8.37}$$

and

$$\begin{aligned}
&\lim_{S^-\to S^+}\int_{S^-} U_{ij}(\mathbf{x}^-,\mathbf{y}^-)t_j(\mathbf{y}^-)\mathrm{d}\Gamma(\mathbf{y})-\int_{S^-} T_{ij}(\mathbf{x}^-,\mathbf{y}^-)u_j(\mathbf{y}^-)\mathrm{d}\Gamma(\mathbf{y})\\
&=\int_{S^-} U_{ij}(\mathbf{x}^+,\mathbf{y}^-)t_j(\mathbf{y}^-)\mathrm{d}\Gamma(\mathbf{y})-\int_{S^-} T_{ij}(\mathbf{x}^+,\mathbf{y}^-)u_j(\mathbf{y}^-)\mathrm{d}\Gamma(\mathbf{y})\\
&=\int_{S^+} U_{ij}\mathbf{x}(\varsigma^+,\mathbf{y}^+)t_j(\mathbf{y}^-)\mathrm{d}\Gamma(\mathbf{y})+\int_{S^+} T_{ij}(\mathbf{x}^+,\mathbf{y}^+)u_j(\mathbf{y}^-)\mathrm{d}\Gamma(\mathbf{y})
\end{aligned}\tag{8.38}$$

Then Eq.(8.19) is rewritten below

$$\begin{aligned}
c_{ij}(\mathbf{x}^+)u_j(\mathbf{x}^+)=&\int_\Gamma U_{ij}(\mathbf{x}^+,\mathbf{y})t_j(\mathbf{y})\mathrm{d}\Gamma(\mathbf{y})-\int_\Gamma T_{ij}(\mathbf{x}^+,\mathbf{y})u_j(\mathbf{y})\mathrm{d}\Gamma(\mathbf{y})\\
&+\int_{S^+} U_{ij}(\mathbf{x}^+,\mathbf{y}^+)t_j(\mathbf{y}^+)\mathrm{d}\Gamma(\mathbf{y})-\int_{S^+} T_{ij}(\mathbf{x}^+,\mathbf{y}^+)u_j(\mathbf{y}^+)\mathrm{d}\Gamma(\mathbf{y})\\
&+\int_{S^+} U_{ij}(\mathbf{x}^+,\mathbf{y}^+)t_j(\mathbf{y}^-)\mathrm{d}\Gamma(\mathbf{y})+\int_{S^+} T_{ij}(\mathbf{x}^+,\mathbf{y}^+)u_j(\mathbf{y}^-)\mathrm{d}\Gamma(\mathbf{y})\\
&-c_{ij}(\mathbf{x}^-)u_j(\mathbf{x}^-)-\int_\Omega \beta\Phi_i(\mathbf{x}^+,\mathbf{y})\theta(\mathbf{y})\mathrm{d}\Omega(\mathbf{y})
\end{aligned}\tag{8.39}$$

Further,

$$\begin{aligned}
c_{ij}(\mathbf{x}^+)u_j(\mathbf{x}^+)=&\int_\Gamma U_{ij}(\mathbf{x}^+,\mathbf{y})t_j(\mathbf{y})\mathrm{d}\Gamma(\mathbf{y})-\int_\Gamma T_{ij}(\mathbf{x}^+,\mathbf{y})u_j(\mathbf{y})\mathrm{d}\Gamma(\mathbf{y})\\
&+\int_{S^+} U_{ij}(\mathbf{x}^+,\mathbf{y}^+)\sum t_j(\mathbf{y})\mathrm{d}\Gamma(\mathbf{y})-\int_{S^+} T_{ij}(\mathbf{x}^+,\mathbf{y}^+)\Delta u_j(\mathbf{y})\mathrm{d}\Gamma(\mathbf{y})\\
&-c_{ij}(\mathbf{x}^-)u_j(\mathbf{x}^-)-\int_\Omega \beta\Phi_i(\mathbf{x}^+,\mathbf{y})\theta(\mathbf{y})\mathrm{d}\Omega(\mathbf{y})
\end{aligned}\tag{8.40}$$

At last, Eq.(8.19) is expressed as follows

$$
\begin{aligned}
&c_{ij}\left(\mathbf{x}^{+}\right)u_j\left(\mathbf{x}^{+}\right)+c_{ij}\left(\mathbf{x}^{-}\right)u_j\left(\mathbf{x}^{-}\right)= \\
&\int_{\Gamma}U_{ij}\left(\mathbf{x}^{+},\mathbf{y}\right)t_j\left(\mathbf{y}\right)\mathrm{d}\Gamma\left(\mathbf{y}\right)-\int_{\Gamma}T_{ij}\left(\mathbf{x}^{+},\mathbf{y}\right)u_j\left(\mathbf{y}\right)\mathrm{d}\Gamma\left(\mathbf{y}\right) \\
&+\int_{S^{+}}U_{ij}\left(\mathbf{x}^{+},\mathbf{y}^{+}\right)\sum t_j\left(\mathbf{y}\right)\mathrm{d}\Gamma\left(\mathbf{y}\right)-\int_{S^{+}}T_{ij}\left(\mathbf{x}^{+},\mathbf{y}^{+}\right)\Delta u_j\left(\mathbf{y}\right)\mathrm{d}\Gamma\left(\mathbf{y}\right) \\
&-\int_{\Omega}\beta\Phi_i\left(\mathbf{x}^{+},\mathbf{y}\right)\theta\left(\mathbf{y}\right)\mathrm{d}\Omega\left(\mathbf{y}\right)
\end{aligned}
\tag{8.41}
$$

In a similar way, Eq.(8.20) is rewritten as

$$
\begin{aligned}
c_{ij}\left(\mathbf{x}^{-}\right)u_j\left(\mathbf{x}^{-}\right)=&\int_{\Gamma}U_{ij}\left(\mathbf{x}^{-},\mathbf{y}\right)t_j\left(\mathbf{y}\right)\mathrm{d}\Gamma\left(\mathbf{y}\right)-\int_{\Gamma}T_{ij}\left(\mathbf{x}^{-},\mathbf{y}\right)u_j\left(\mathbf{y}\right)\mathrm{d}\Gamma\left(\mathbf{y}\right) \\
&+\int_{S^{+}}U_{ij}\left(\mathbf{x}^{+},\mathbf{y}^{+}\right)t_j\left(\mathbf{y}^{+}\right)\mathrm{d}\Gamma\left(\mathbf{y}\right)-\int_{S^{+}}T_{ij}\left(\mathbf{x}^{+},\mathbf{y}^{+}\right)u_j\left(\mathbf{y}^{+}\right)\mathrm{d}\Gamma\left(\mathbf{y}\right) \\
&+\int_{S^{+}}U_{ij}\left(\mathbf{x}^{+},\mathbf{y}^{+}\right)t_j\left(\mathbf{y}^{-}\right)\mathrm{d}\Gamma\left(\mathbf{y}\right)+\int_{S^{+}}T_{ij}\left(\mathbf{x}^{+},\mathbf{y}^{+}\right)u_j\left(\mathbf{y}^{-}\right)\mathrm{d}\Gamma\left(\mathbf{y}\right) \\
&-c_{ij}\left(\mathbf{x}^{+}\right)u_j\left(\mathbf{x}^{+}\right)-\int_{\Omega}\beta\Phi_i\left(\mathbf{x}^{-},\mathbf{y}\right)\theta\left(\mathbf{y}\right)\mathrm{d}\Omega\left(\mathbf{y}\right)
\end{aligned}
\tag{8.42}
$$

Then

$$
\begin{aligned}
&c_{ij}\left(\mathbf{x}^{-}\right)u_j\left(\mathbf{x}^{-}\right)+c_{ij}\left(\mathbf{x}^{+}\right)u_j\left(\mathbf{x}^{+}\right) \\
&=\int_{\Gamma}U_{ij}\left(\mathbf{x}^{-},\mathbf{y}\right)t_j\left(\mathbf{y}\right)\mathrm{d}\Gamma\left(\mathbf{y}\right)-\int_{\Gamma}T_{ij}\left(\mathbf{x}^{-},\mathbf{y}\right)u_j\left(\mathbf{y}\right)\mathrm{d}\Gamma\left(\mathbf{y}\right) \\
&+\int_{S^{+}}U_{ij}\left(\mathbf{x}^{+},\mathbf{y}^{+}\right)\sum t_j\left(\mathbf{y}\right)\mathrm{d}\Gamma\left(\mathbf{y}\right)-\int_{S^{+}}T_{ij}\left(\mathbf{x}^{+},\mathbf{y}^{+}\right)\Delta u_j\left(\mathbf{y}\right)\mathrm{d}\Gamma\left(\mathbf{y}\right) \\
&-\int_{\Omega}\beta\Phi_i\left(\mathbf{x}^{+},\mathbf{y}\right)\theta\left(\mathbf{y}\right)\mathrm{d}\Omega\left(\mathbf{y}\right)
\end{aligned}
\tag{8.43}
$$

Then the same formula as Eq.(8.41) can be obtained.

Since

$$
c_{ij}\left(\mathbf{x}^{+}\right)+c_{ij}\left(\mathbf{x}^{-}\right)=1 \tag{8.44}
$$

Finally, Eq.(8.21) is proved.

Appendix B.

The term $\lim_{S^{-}\to S^{+}} t_i\left(\mathbf{x}^{+}\right)|\,\mathbf{y}^{-}$ in Eq.(8.26) as follows

$$
\begin{aligned}
&\lim_{S^{-}\to S^{+}}\int_{S^{-}}K_{ki}\left(\mathbf{x}^{+},\mathbf{y}^{-}\right)t_k\left(\mathbf{y}^{-}\right)\mathrm{d}\Gamma\left(\mathbf{y}\right)-\int_{S^{-}}H_{ki}\left(\mathbf{x}^{+},\mathbf{y}^{-}\right)u_k\left(\mathbf{y}^{-}\right)\mathrm{d}\Gamma\left(\mathbf{y}\right) \\
&=\lim_{\mathbf{x}^{+}\to S^{-}}\int_{S^{-}}K_{ki}\left(\mathbf{x}^{+},\mathbf{y}^{-}\right)t_k\left(\mathbf{y}^{-}\right)\mathrm{d}\Gamma\left(\mathbf{y}\right)-\int_{S^{-}}H_{ki}\left(\mathbf{x}^{+},\mathbf{y}^{-}\right)u_k\left(\mathbf{y}^{-}\right)\mathrm{d}\Gamma\left(\mathbf{y}\right) \\
&=c\left(\mathbf{x}^{-}\right)\mathbf{t}\left(\mathbf{x}^{-}\right)+\int_{S^{-}}K_{ki}\left(\mathbf{x}^{+},\mathbf{y}^{-}\right)t_k\left(\mathbf{y}^{-}\right)\mathrm{d}\Gamma\left(\mathbf{y}\right)-\int_{S^{-}}H_{ki}\left(\mathbf{x}^{+},\mathbf{y}^{-}\right)u_k\left(\mathbf{y}^{-}\right)\mathrm{d}\Gamma\left(\mathbf{y}\right) \\
&=c\left(\mathbf{x}^{-}\right)\mathbf{t}\left(\mathbf{x}^{-}\right)+\int_{S^{+}}K_{ki}\left(\mathbf{x}^{+},\mathbf{y}^{+}\right)t_k\left(\mathbf{y}^{-}\right)\mathrm{d}\Gamma\left(\mathbf{y}\right)+\int_{S^{+}}H_{ki}\left(\mathbf{x}^{+},\mathbf{y}^{+}\right)u_k\left(\mathbf{y}^{-}\right)\mathrm{d}\Gamma\left(\mathbf{y}\right)
\end{aligned}
\tag{8.45}
$$

The term $t_{ij}\left(\mathbf{x}^{-}\right)|\,\mathbf{y}^{+}$ and $\lim_{S^{-}\to S^{+}} t_i\left(\mathbf{x}^{-}\right)|\,\mathbf{y}^{-}$ in Eq.(8.27) can be deduced as the following equations

$$
\begin{aligned}
&\int_{S^+} K_{ki}\left(\mathbf{x}^-,\mathbf{y}^+\right)t_k\left(\mathbf{y}^+\right)\mathrm{d}\Gamma\left(\mathbf{y}\right)-\int_{S^+} H_{ki}\left(\mathbf{x}^-,\mathbf{y}^+\right)u_k\left(\mathbf{y}^+\right)\mathrm{d}\Gamma\left(\mathbf{y}\right)\\
&=\lim_{\mathbf{x}^-\to S^+}\int_{S^+} K_{ki}\left(\mathbf{x}^-,\mathbf{y}^+\right)t_k\left(\mathbf{y}^+\right)\mathrm{d}\Gamma\left(\mathbf{y}\right)-\int_{S^+} H_{ki}\left(\mathbf{x}^-,\mathbf{y}^+\right)u_k\left(\mathbf{y}^+\right)\mathrm{d}\Gamma\left(\mathbf{y}\right)\\
&=c\left(\mathbf{x}^+\right)\mathbf{t}\left(\mathbf{x}^+\right)+\int_{S^+} K_{ki}\left(\mathbf{x}^-,\mathbf{y}^+\right)t_k\left(\mathbf{y}^+\right)\mathrm{d}\Gamma\left(\mathbf{y}\right)-\int_{S^+} H_{ki}\left(\mathbf{x}^-,\mathbf{y}^+\right)u_k\left(\mathbf{y}^+\right)\mathrm{d}\Gamma\left(\mathbf{y}\right)\\
&=c\left(\mathbf{x}^+\right)\mathbf{t}\left(\mathbf{x}^+\right)-\int_{S^+} K_{ki}\left(\mathbf{x}^+,\mathbf{y}^+\right)t_k\left(\mathbf{y}^+\right)\mathrm{d}\Gamma\left(\mathbf{y}\right)+\int_{S^+} H_{ki}\left(\mathbf{x}^+,\mathbf{y}^+\right)u_k\left(\mathbf{y}^+\right)\mathrm{d}\Gamma\left(\mathbf{y}\right)
\end{aligned}
\tag{8.46}
$$

and

$$
\begin{aligned}
&\lim_{S^-\to S^+}\int_{S^-} K_{ki}\left(\mathbf{x}^-,\mathbf{y}^-\right)t_k\left(\mathbf{y}^-\right)\mathrm{d}\Gamma\left(\mathbf{y}\right)-\int_{S^-} H_{ki}\left(\mathbf{x}^-,\mathbf{y}^-\right)u_k\left(\mathbf{y}^-\right)\mathrm{d}\Gamma\left(\mathbf{y}\right)\\
&=-\int_{S^-} K_{ki}\left(\mathbf{x}^+,\mathbf{y}^-\right)t_k\left(\mathbf{y}^-\right)\mathrm{d}\Gamma\left(\mathbf{y}\right)+\int_{S^-} H_{ki}\left(\mathbf{x}^+,\mathbf{y}^-\right)u_k\left(\mathbf{y}^-\right)\mathrm{d}\Gamma\left(\mathbf{y}\right)\\
&=-\int_{S^+} K_{ki}\left(\mathbf{x}^+,\mathbf{y}^+\right)t_k\left(\mathbf{y}^-\right)\mathrm{d}\Gamma\left(\mathbf{y}\right)-\int_{S^+} H_{ki}\left(\mathbf{x}^+,\mathbf{y}^+\right)u_k\left(\mathbf{y}^-\right)\mathrm{d}\Gamma\left(\mathbf{y}\right)
\end{aligned}
\tag{8.47}
$$

Then Eq.(8.26) can be rewritten as

$$
\begin{aligned}
c_{ij}\left(\mathbf{x}^+\right)t_j\left(\mathbf{x}^+\right)=&\int_\Gamma K_{ki}\left(\mathbf{x}^+,\mathbf{y}\right)t_k\left(\mathbf{y}\right)\mathrm{d}\Gamma\left(\mathbf{y}\right)-\int_\Gamma H_{ki}\left(\mathbf{x}^+,\mathbf{y}\right)u_k\left(\mathbf{y}\right)\mathrm{d}\Gamma\left(\mathbf{y}\right)\\
&+\int_{S^+} K_{ki}\left(\mathbf{x}^+,\mathbf{y}^+\right)t_k\left(\mathbf{y}^+\right)\mathrm{d}\Gamma\left(\mathbf{y}\right)+\int_{S^+} H_{ki}\left(\mathbf{x}^+,\mathbf{y}^+\right)u_k\left(\mathbf{y}^+\right)\mathrm{d}\Gamma\left(\mathbf{y}\right)\\
&+\int_{S^+} K_{ki}\left(\mathbf{x}^+,\mathbf{y}^+\right)t_k\left(\xi^-\right)\mathrm{d}\Gamma\left(\mathbf{y}\right)+\int_{S^+} H_{ki}\left(\mathbf{x}^+,\mathbf{y}^+\right)u_k\left(\mathbf{y}^-\right)\mathrm{d}\Gamma\left(\mathbf{y}\right)\\
&+\int_\Gamma \beta r_{,\mathrm{m}} n_m \ln\left(r^r\right)\theta\left(\mathbf{x}\right)\Psi_{ij}\left(\mathbf{x}^+,\mathbf{y}\right)n_j\left(\mathbf{x}^+\right)\mathrm{d}\Gamma\left(\mathbf{y}\right)\\
&+\int_\Omega \beta\left[\theta\left(\mathbf{y}\right)-\theta\left(\mathbf{x}^+\right)\right]\Psi_{ij}\left(\mathbf{x}^+,\mathbf{y}\right)n_j\left(\mathbf{x}^+\right)\mathrm{d}\Omega\left(\mathbf{y}\right)\\
&-b\beta\delta_{ij}\theta\left(\mathbf{y}\right)n_j\left(\mathbf{x}^+\right)+c\left(\mathbf{x}^-\right)\mathbf{t}\left(\mathbf{x}^-\right)
\end{aligned}
\tag{8.48}
$$

Further

$$
\begin{aligned}
&c_{ij}\left(\mathbf{x}^+\right)t_j\left(\mathbf{x}^+\right)-c\left(\mathbf{x}^-\right)\mathbf{t}\left(\mathbf{x}^-\right)\\
&=\int_\Gamma K_{ki}\left(\mathbf{x}^+,\mathbf{y}\right)t_k\left(\mathbf{y}\right)\mathrm{d}\Gamma\left(\mathbf{y}\right)-\int_\Gamma H_{ki}\left(\mathbf{x}^+,\mathbf{y}\right)u_k\left(\mathbf{y}\right)\mathrm{d}\Gamma\left(\mathbf{y}\right)\\
&+\int_{S^+} K_{ki}\left(\mathbf{x}^+,\mathbf{y}^+\right)\sum t_k\left(\mathbf{y}\right)\mathrm{d}\Gamma\left(\mathbf{y}\right)+\int_{S^+} H_{ki}\left(\mathbf{x}^+,\mathbf{y}^+\right)\Delta u_k\left(\mathbf{y}\right)\mathrm{d}\Gamma\left(\mathbf{y}\right)\\
&+\int_\Gamma \beta r_{,\mathrm{m}} n_m \ln\left(r^r\right)\theta\left(\mathbf{x}\right)\Psi_{ij}\left(\mathbf{x}^+,\mathbf{y}\right)n_j\left(\mathbf{x}^+\right)\mathrm{d}\Gamma\left(\mathbf{y}\right)\\
&+\int_\Omega \beta\left[\theta\left(\mathbf{y}\right)-\theta\left(\mathbf{x}^+\right)\right]\Psi_{ij}\left(\mathbf{x}^+,\mathbf{y}\right)n_j\left(\mathbf{x}^+\right)\mathrm{d}\Omega\left(\mathbf{y}\right)\\
&-b\beta\delta_{ij}\theta\left(\mathbf{y}\right)n_j\left(\mathbf{x}^+\right)
\end{aligned}
\tag{8.49}
$$

In addition, Eq.(8.27) can be rewritten as

$$
\begin{aligned}
c_{ij}\left(\mathbf{x}^{-}\right)t_j\left(\mathbf{x}^{-}\right)=&\int_{\Gamma}K_{ki}\left(\mathbf{x}^{-},\mathbf{y}\right)t_k\left(\mathbf{y}\right)\mathrm{d}\Gamma\left(\mathbf{y}\right)-\int_{\Gamma}H_{ki}\left(\mathbf{x}^{-},\mathbf{y}\right)u_k\left(\mathbf{y}\right)\mathrm{d}\Gamma\left(\mathbf{y}\right)\\
&-\int_{S^{+}}K_{ki}\left(\mathbf{x}^{+},\mathbf{y}^{+}\right)t_k\left(\mathbf{y}^{-}\right)\mathrm{d}\Gamma\left(\mathbf{y}\right)-\int_{S^{+}}H_{ki}\left(\mathbf{x}^{+},\mathbf{y}^{+}\right)u_k\left(\mathbf{y}^{-}\right)\mathrm{d}\Gamma\left(\mathbf{y}\right)\\
&-\int_{S^{+}}K_{ki}\left(\mathbf{x}^{+},\mathbf{y}^{+}\right)t_k\left(\mathbf{y}^{+}\right)\mathrm{d}\Gamma\left(\xi\right)+\int_{S^{+}}H_{ki}\left(\mathbf{x}^{+},\mathbf{y}^{+}\right)u_k\left(\mathbf{y}^{+}\right)\mathrm{d}\Gamma\left(\mathbf{y}\right)\\
&+\int_{\Gamma}\beta r_{,\mathrm{m}}n_m\ln\left(r^{r}\right)\theta\left(\mathbf{x}\right)\Psi_{ij}\left(\mathbf{x}^{+},\mathbf{y}\right)n_j\left(\mathbf{x}^{+}\right)\mathrm{d}\Gamma\left(\mathbf{y}\right)\\
&+\int_{\Omega}\beta\left[\theta\left(\mathbf{y}\right)-\theta\left(\mathbf{x}^{-}\right)\right]\Psi_{ij}\left(\mathbf{x}^{-},\mathbf{y}\right)n_j\left(\mathbf{x}^{-}\right)\mathrm{d}\Omega\left(\mathbf{y}\right)\\
&-b\beta\delta_{ij}\theta\left(\mathbf{y}\right)n_j\left(\mathbf{x}^{-}\right)+t_i\left(\mathbf{x}^{-}\right)|\,\mathbf{y}^{+}\\
&+\lim_{S^{-}\to S^{+}}t_i\left(\mathbf{x}^{-}\right)|\,\mathbf{y}^{-}+c\left(\mathbf{x}^{+}\right)\mathbf{t}\left(\mathbf{x}^{+}\right)
\end{aligned}
\tag{8.50}
$$

Then the same formula as Eq.(8.49) can be obtained.

Part IV

Application of boundary element method in particle breakage

Chapter 9

A combined boundary element method and discrete element method for particle stress field and breakage evaluation of granular systems with similar particle shapes

Summary

In this chapter, a combined BEM and discrete element method (DEM), named B-DEM, is developed to compute particle stress fields and breakage paths of granular brittle materials. The interaction between particles is simulated via DEM, while the stress field of a particle is computed, when needed, by BEM and the non-static or dynamic equilibrium of a particle is considered by treating its acceleration as a constant body force, which leads to a domain integral over the particle. To avoid losing the traditional advantage of BEM, i.e., boundary-only discretisation, the domain integral is transformed into multiple one-dimensional boundary integrals by a line integration method. For the stress field computation of particles with similar geometry, a template particle is used as the representative particle, so that only the related coefficient matrices of one template particle in the local coordinate system are needed to be calculated, while the coefficient matrices of the other particles, can be obtained by mapping between the local and global coordinate systems. Thus, the proposed method is much more time-effective when modelling a large-scale particle system with a small number of distinct possible particle shapes. Furthermore, to obtain possible particle breakage paths, the template particle is discretised into triangular cells by Delaunay triangulation. Then, the Hoek-Brown criterion is employed to evaluate the failure state of each pre-determined cell inside a particle. Hence, the possible cracks or breakage paths of a particle, which are assumed as straight lines, are obtained if all the cells intersected with them are in a failure state.

9.1 Introduction

Understanding the mechanical behaviour of particle systems has been an important research topic for a long time [253] because of not only the importance but also the complexity of the problem where the system behaviour involves microstructural evolution, strain localization, and possible particle breakage. In particular, particle breakage, which describes the fracture of the constituent components of granular materials, is ubiquitous in various soil or rockfill masses. Existing research work has shown that particle breakage changes the size and shape of a particle, and further results in changes both in state variables and the mechanical behaviour of the granular system at the macroscopic level: such as the stress-strain relationship, deformability, and density, etc. [254, 255].

Over the last few decades, DEM has been widely accepted as a powerful modelling tool for granular materials [256, 257]. However, modelling particle breakage in DEM is still in an early stage of development and is still limited in the ability of realistically capturing particle breakage. At present, the determination of the occurrence of breakage in DEM is mainly based on two approaches [258, 259]: (I) set a threshold value for the average pressure on a grain; (II) set a threshold value for the largest compressive force at the contacts of a grain. Upon the threshold is reached, two alternative paradigms can be employed to break particles: the fragment replacement model (FRM) [260-262] and the bonded particle model (BPM) [263-265]. In the FRM approach, when a single particle is identified as broken, it is replaced by a group of new, smaller fragments. An agglomerates-based model for circular particle breakage with the average stress tensor criteria is proposed by Tsoungui et al. [266]. Cantor et al. [267] made a modification of that method for irregular particles. The BPM method, despite being very helpful for the understanding of the micromechanics occurring in a single particle, becomes impractical for

large-scale problems as the number of particles will increase exponentially after particle breakage happens. The fundamental problem of the above particle breakage methods is the lack of accurate computation of particle stress distribution.

On the other hand, the fracture theory is much more mature for continuously based methods, including FEM [268-270], extended finite element method (XFEM) [271, 272], phase-field method [114, 171], and BEM [273, 274], and therefore can be applied to obtain the internal stress distribution within a particle. Several continuous-discontinuous methods have been proposed to fulfil the breakage requirements. The basic idea of these hybrid methods is to combine different types of continuously based techniques with DEM. The interaction among particles is simulated via DEM, while the stress state inside each particle is calculated by continuously based methods using the loading or boundary conditions of the particle obtained from DEM. For example, the combined DEM-FEM for particle breakage of angular particles is presented by Bagherzadeh et al. [253], in which FEM calculates the stress state inside particles by meshing each particle with elements, and the status of elements, plastic or not, is evaluated by the Hoek-Brown criterion. Furthermore, the breakage path is simplified as a straight line and approximated based on the plastic elements. Luo et al. [275] propose a combined scaled boundary finite-discrete element method for grain breakage modelling in which a single particle is modelled by one polygonal element with the scaled boundary finite element method, and a simple fracture criterion and crack path insertion procedure is proposed to break a particle when it is failed. Besides, Raisianzadeh et al. [276] carry out a micromechanical study of particle breakage in 2D angular rockfill materials under biaxial compression loading by a combined DEM and XFEM approach. In this study, the crack propagation is performed inside particles without the limitations of classic FEM, namely, the breakage path does not need to follow the boundaries of discretised elements. In addition, Fan and Zhao

[277] propose a combination of peridynamics and contact dynamics based physics engine for simulation of particle breakage.

The continuous-discontinuous methods mentioned above are capable of dealing with particle breakage to a certain degree, but finding a more appropriate and efficient method for simulating interior stress fields and subsequent breakage paths of particles are rather important because a granular system often involves a large number of particles. BEM [278, 279] is a well-known efficient method and is also widely applied to fracture problems [4, 97, 121, 280] due to its unique advantages: boundary-only discretisation and dimensional reduction [49, 59]. Specifically, only the boundary is required to be discretised [234, 281], i.e., domain meshing is unnecessary when simulating the stress field of a particle. Also, as a semi-analytical numerical method, BEM can provide a more accurate result compared to FEM with the same degrees of freedom.

In this research, a combined boundary element method and discrete element method, named B-DEM, is proposed to address some particle breakage modelling issues, in which contact forces between particles are simulated via DEM, while stress fields of particles are computed, when needed, by BEM from which possible particle failure zones and breakage paths can be evaluated.

In particular, BEM is used to calculate the stress distribution inside each particle for a particle system with similar geometric shape. By exploiting the geometric similarity between particles, only the coefficient matrix construction of one template particle is needed, while the coefficient matrices of the other similar particles can be obtained by mapping between the local and global coordinate systems. Thus the proposed combined method is more time-efficient for problems with a large number of similar particles. Furthermore, the particle is assumed to be linear elastic with a body force to account for the non-zero acceleration. The domain integrals, caused by considering the particle acceleration as a constant body force, will be treated by the LIM [57, 77, 78]. The rigid motion

of the particle is eliminated from the BEM solution by using the pseudo-inverse of a coefficient matrix, which leads to a high solution accuracy.

After the discretised boundary displacement of a particle is obtained from BEM, the stress distribution of the particle can be evaluated at a set of pre-defined points from which a triangular cell can be formed. Then assuming that particles are brittle materials (for instance, rocks), the Hoek-Brown criterion [282-284] is applied to evaluate and determine the brittle failure zone of a particle-based on the mesh, from which possible breakage paths can be identified.

This chapter is organised as follows. The boundary integral equation for a single particle with concentrated contact forces acting on its boundary and a distributed body force is presented in **Section 9.2**. The mapping between the BIE of a template particle and those of geometrically similar particles is provided in **Section 9.3**. In **Section 9.4**, the Hoek-Brown breakage criterion is introduced, followed by the description of the method to obtain failure zones and possible breakage paths inside particles. To demonstrate the accuracy and efficiency of the proposed methodology, numerical examples with circular particles are presented in **Section 9.5**. The well-known Brazil disk test is conducted as the first example to evaluate the accuracy of the proposed method against the analytical solution. The rationality of the proposed method for obtaining breakage paths inside a disc under different cases is also discussed. Another two numerical examples, consisting of a large number of circular particles, are simulated to obtain particle stress distributions and possible cracks or breakage paths by the proposed B-DEM.

9.2 The boundary integral equation for a single particle

In the proposed B-DEM methodology, the contact forces between particles in a particle system are obtained by DEM. Then, the stress field inside a particle is obtained by BEM in order to predict possible breakage

and fracture patterns. In this section, only the necessary formulations of BEM are covered.

Consider an arbitrary particle subject to mechanical contact with its neighbouring particles in a particle assembly at a time instant, as shown in **Fig.9.1**. Also, assume that the particle has an instantaneous translational acceleration (but the angular acceleration will be ignored). Then the dynamic equilibrium equation of the particle can be expressed as

$$\sum_{i=0}^{n} \mathbf{f}^i = \rho S \mathbf{a} \tag{9.1}$$

where $\mathbf{f}^i$ is the i^{th} contact vector, ρ is the density of the particle, S is the area of the particle, and $\mathbf{a}$ is the acceleration vector (including the gravitational acceleration $\mathbf{g}$).

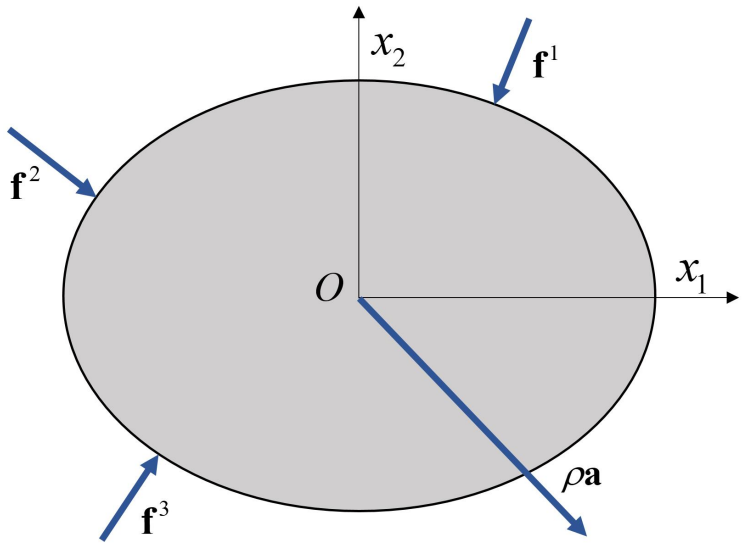

Fig.9.1 The forces acting on a particle

Further, assume that the particle is a linear elastic body with a (constant) body force $\mathbf{b} = \rho\mathbf{a}$, and that the contact forces $\mathbf{f}^i$ are treated as a special traction $\mathbf{t}$ on the boundary. Then the equilibrium equation for this 2D elasticity problem can be written as

$$\mu\nabla_{\mathbf{x}}^2\mathbf{u}(\mathbf{x}) + (\lambda+\mu)\nabla_{\mathbf{x}}\nabla_{\mathbf{x}}\bullet\mathbf{u}(\mathbf{x}) = \mathbf{b} \tag{9.2}$$

where $\mathbf{u}$ is the displacement vector field, μ is the shear modulus, $\lambda = 2\nu\mu/(1-2\nu)$ is the Lamé constant, and ν is the Poisson's ratio of the particle. $\nabla_{\mathbf{x}}(\ )$ and $\nabla_{\mathbf{x}}\bullet(\ )$ are respectively gradient and divergence

operators with respect to coordinates $\mathbf{x}=(x_1,x_2)$.

The strain tensor ε_{ij} can be represented as

$$\varepsilon_{ij}=\frac{1}{2}\left(u_{i,j}+u_{j,i}\right) \tag{9.3}$$

where u_i are the components of the displacement vector $\mathbf{u}$. The Hooke's law relating stress σ_{ij} and strain ε_{ij} can be stated in the following form

$$\sigma_{ij}=C_{ijkl}\varepsilon_{kl} \tag{9.4}$$

with

$$C_{ijkl}=\lambda\delta_{ij}\delta_{kl}+\mu\left(\delta_{ik}\delta_{jl}+\delta_{il}\delta_{jk}\right) \tag{9.5}$$

The well-known integral equation of Eq.(9.2) can be written as

$$\begin{aligned}\tilde{c}(\mathbf{x})\mathbf{u}(\mathbf{x})=&\int_\Gamma \mathbf{U}(\mathbf{x},\mathbf{y})\mathbf{t}(\mathbf{y})\mathrm{d}\Gamma(\mathbf{y})-\int_\Gamma \mathbf{T}(\mathbf{x},\mathbf{y})\mathbf{u}(\mathbf{y})\mathrm{d}\Gamma(\mathbf{y})\\&-\int_\Omega \mathbf{U}(\mathbf{x},\mathbf{y})\mathbf{b}\mathrm{d}\Omega(\mathbf{y})\end{aligned} \tag{9.6}$$

where $\mathbf{x}$ and $\mathbf{y}$ are two points in $\mathbb{R}^2$, $\tilde{c}(\mathbf{x})$ is a coefficient relative to the position of $\mathbf{x}$, and $\mathbf{U}(\mathbf{x},\mathbf{y})$ and $\mathbf{T}(\mathbf{x},\mathbf{y})$ are the Kelvin kernels. For 2D plane strain problems,

$$U_{ki}(\mathbf{x},\mathbf{y})=\frac{-1}{8\pi(1-\nu)\mu}\left\{(3-4\nu)\ln(r)\delta_{ki}-r_{,k}r_{,i}\right\} \tag{9.7}$$

$$T_{ki}(\mathbf{x},\mathbf{y})=\frac{-1}{4\pi(1-\nu)r}\left\{\left[(1-2\nu)\delta_{ki}+2r_{,k}r_{,i}\right]\frac{\partial r}{\partial\mathbf{n}(\mathbf{y})}-(1-2\nu)\left[r_{,k}n_i(\mathbf{y})-r_{,i}n_k(\mathbf{y})\right]\right\} \tag{9.8}$$

where $r=r(\mathbf{x},\mathbf{y})=|\mathbf{x}-\mathbf{y}|$ is the distance between points $\mathbf{x}$ and $\mathbf{y}$, $\mathbf{n}(\mathbf{y})$ is the unit outward normal at the point $\mathbf{y}$ on the boundary. For plane stress problems, ν and E in Eqs.(9.7) and (9.8) are replaced by the following $\bar{\nu}$ and $\bar{E}$

$$\bar{\nu}=\frac{\nu}{1-\nu} \tag{9.9}$$

$$\bar{E}=\frac{E}{1-\nu^2} \tag{9.10}$$

For the current problem where there are m concentrated forces $\mathbf{f}(\mathbf{z}_l)$ acting at boundary points $\mathbf{z}_l$ (l=1 ,..., m) and no tractions imposed on the boundary, the boundary integral equation can be written as [285]

$$\tilde{c}(\mathbf{x})\mathbf{u}(\mathbf{x}) = -\int_{\Gamma}\mathbf{T}(\mathbf{x},\mathbf{y})\mathbf{u}(\mathbf{y})\mathrm{d}\Gamma(\mathbf{y}) - \int_{\Omega}\mathbf{U}(\mathbf{x},\mathbf{y})\mathrm{d}\Omega(\mathbf{y})\mathbf{b} + \sum_{l=1}^{m}\mathbf{U}(\mathbf{x},\mathbf{z}_l)\mathbf{f}(\mathbf{z}_l) \tag{9.11}$$

9.3 Map solutions between local and global coordinate systems

It will be time-consuming if Eq.(9.11) is applied to and solved by BEM for each particle in a large-scale particle system. Thus, an approach for improving computation efficiency is proposed in this section. The granular system concerned is assumed that all particles are geometrically similar to a representative shape, called the template particle below. Thus, any particle will be a scaled version of the template particle described in a local coordinate system. Then the solutions of these particles are first obtained in the template particle in the local coordinate system, and then are transformed back to the physical or global coordinate system by matrix transformation. The proposed approach is efficient since the most two time-consuming parts, i.e., computing the coefficient matrices and solving the linear system of equations, as will be detailed below, are performed only once on the template particle.

9.3.1 The transformation matrix

In this work, only the translation, rotation, and uniform scaling transformations are considered between particles and the template particle. Consider a set of particles that are geometrically similar to the template particle (see **Fig.9.2**). The set of particles are in a global coordinate system $\mathbf{x} = (x_1, x_2)$ while the template particle is in a local coordinate system $\mathbf{s} = (s_1, s_2)$. Then for the K^{th} particle, the transformation between the local coordinate system and the global coordinate system can be written as

$$\begin{cases} x_1 = c^K (s_1 \cos\theta^K - s_2 \sin\theta^K) + d_1^K \\ x_2 = c^K (s_1 \sin\theta^K + s_2 \cos\theta^K) + d_2^K \end{cases} \tag{9.12}$$

where θ^K is the angle from the axis-x_1 to the axis-s_1, c^K is the uniform scaling factor, d_1^K and d_2^K are two constants which denote the global coordinates of the local origin of the template particle. The Jacobi matrix $\mathbf{J}^K$ of the transformation can be identified as

$$\mathbf{J}^K = \begin{bmatrix} \frac{\partial x_1}{\partial s_1} & \frac{\partial x_1}{\partial s_2} \\ \frac{\partial x_2}{\partial s_1} & \frac{\partial x_2}{\partial s_2} \end{bmatrix} = c^K \begin{bmatrix} \cos\theta^K & -\sin\theta^K \\ \sin\theta^K & \cos\theta^K \end{bmatrix} \tag{9.13}$$

and $\left|\mathbf{J}^K\right| = \left(c^K\right)^2$. The transformation between a unit outward normal from the local $\tilde{\mathbf{n}}(\mathbf{s})$ to the global $\mathbf{n}^K(\mathbf{x})$ is

$$\mathbf{n}^K(\mathbf{x}) = \frac{1}{c^K} \mathbf{J}^K \tilde{\mathbf{n}}(\mathbf{s}) \tag{9.14}$$

where $\tilde{\mathbf{n}}(\mathbf{s})$ is the unit outward normal in the local coordinate system.

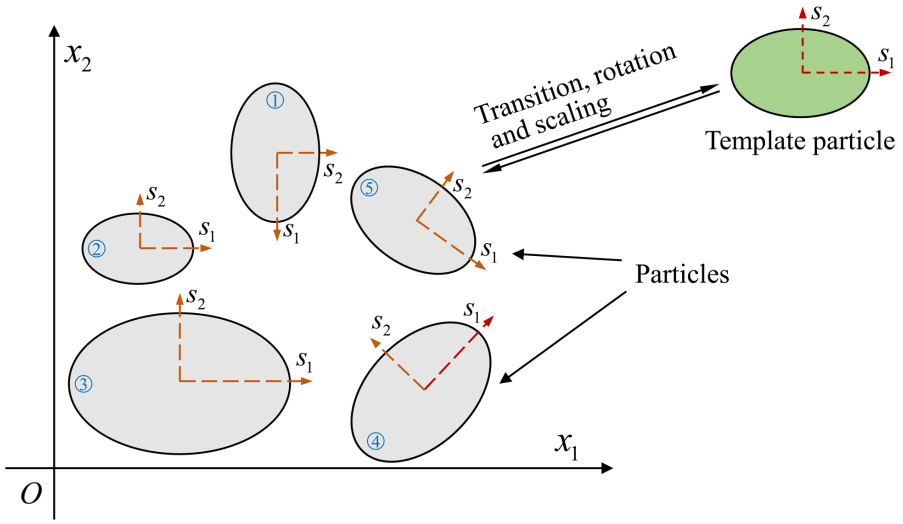

Fig.9.2 Map the solutions between local and global coordinate systems

9.3.2 The boundary integral equation in the local domain

Suppose that the set of particles and the template particle shown in Fig. 9.2 have the same Poisson's ratio v, and the shear modulus of the template particle is set to 1.0. The displacement $\mathbf{u}^K(\mathbf{x})$ of particle K in the global coordinate system and the corresponding displacement $\tilde{\mathbf{u}}^K(\mathbf{s})$ of the template particle in the local coordinate system satisfy

$$\mathbf{u}^K(\mathbf{x}) = \mathbf{J}^K \tilde{\mathbf{u}}^K(\mathbf{s}) \tag{9.15}$$

The strain $\boldsymbol{\varepsilon}^K(\mathbf{x})$ and stress $\boldsymbol{\sigma}^K(\mathbf{x})$ tensors can be computed by

$$\boldsymbol{\varepsilon}^K(\mathbf{x}) = \mathbf{J}^K \tilde{\boldsymbol{\varepsilon}}^K(\mathbf{s})[\mathbf{J}^K]^{-1} \tag{9.16}$$

$$\boldsymbol{\sigma}^K(\mathbf{x}) = \mu^K \mathbf{J}^K \tilde{\boldsymbol{\sigma}}^K(\mathbf{s})[\mathbf{J}^K]^{-1} \tag{9.17}$$

where $\tilde{\boldsymbol{\varepsilon}}^K(\mathbf{s})$ and $\tilde{\boldsymbol{\sigma}}^K(\mathbf{s})$ are respectively the strain and scaled stress tensors of the template particle in the local coordinate system, and

$$\tilde{\sigma}_{ij}^K = \tilde{C}_{ijkl} \tilde{\varepsilon}_{kl}^K \tag{9.18}$$

with

$$\tilde{C}_{ijkl} = \frac{2v}{1-2v} \delta_{ij}\delta_{kl} + \left(\delta_{ik}\delta_{jl} + \delta_{il}\delta_{jk}\right) \tag{9.19}$$

Applying Eq.(9.15), one can rewrite Eq.(9.2) of the K^{th} particle for the template particle as

$$\mu^K \mathbf{J}^K \nabla_{\mathbf{s}}^2 \tilde{\mathbf{u}}^K(\mathbf{s}) + \left(\lambda^K + \mu^K\right) \mathbf{J}^K \nabla_{\mathbf{s}} \nabla_{\mathbf{s}} \bullet \tilde{\mathbf{u}}^K(\mathbf{s}) = \mathbf{b}^K \tag{9.20}$$

or

$$\nabla_{\mathbf{s}}^2 \tilde{\mathbf{u}}^K(\mathbf{s}) + \frac{1}{1-2v} \nabla_{\mathbf{s}} \nabla_{\mathbf{s}} \bullet \tilde{\mathbf{u}}^K(\mathbf{s}) = \frac{1}{\mu^K} [\mathbf{J}^K]^{\mathrm{T}} \mathbf{b}^K \left[\mathbf{x}(\mathbf{s})\right] = \tilde{\mathbf{b}}^K \tag{9.21}$$

where λ^K and $\mathbf{b}^K$ are the Lame constant and body force for the K^{th} particle, and $\tilde{\mathbf{b}}^K$ is the corresponding body force of the template particle in the local coordinate system:

$$\tilde{\mathbf{b}}^K = \frac{1}{\mu^K} [\mathbf{J}^K]^{\mathrm{T}} \mathbf{b}^K \tag{9.22}$$

In addition, the concentrated forces in the local coordinate system can be rewritten in a similar manner. For the I^{th} force

$$\tilde{\mathbf{f}}_I^K = \frac{[\mathbf{J}^K]^{\mathrm{T}} \mathbf{f}_I^K}{\mu^K} \tag{9.23}$$

Finally, the boundary integral equation in the local domain can be written as

$$\tilde{c}(\mathbf{s})\tilde{\mathbf{u}}^K(\mathbf{s}) = -\int_\Gamma \mathbf{T}^0(\mathbf{s},\tilde{\mathbf{s}})\tilde{\mathbf{u}}^K(\tilde{\mathbf{s}})\mathrm{d}\Gamma(\tilde{\mathbf{s}}) - \int_\Omega \mathbf{U}^0(\mathbf{s},\tilde{\mathbf{s}})\mathrm{d}\Omega(\tilde{\mathbf{s}})\tilde{\mathbf{b}}^K + \sum_{l=1}^{m} \mathbf{U}^0(\mathbf{s},\mathbf{q}_l)\tilde{\mathbf{f}}^K(\mathbf{q}_l) \tag{9.24}$$

where $\mathbf{s}$ and $\tilde{\mathbf{s}}$ are two points in the local coordinate system, $U_{kp}^0(\mathbf{s},\tilde{\mathbf{s}})$ and $T_{ki}^0(\mathbf{s},\tilde{\mathbf{s}})$ are expressed as

$$U_{kp}^0(\mathbf{s},\tilde{\mathbf{s}}) = \frac{-1}{8\pi(1-v)}\left\{(3-4v)\ln r\delta_{ki} - r_{,k}r_{,i}\right\} \tag{9.25}$$

$$T_{ki}^0(\mathbf{s},\tilde{\mathbf{s}}) = \frac{-1}{4\pi(1-v)r}\left\{\left[(1-2v)\delta_{ki} + 2r_{,k}r_{,i}\right]\frac{\partial r}{\partial \mathbf{n}(\tilde{\mathbf{s}})} - (1-2v)\left[r_{,k}n_i(\tilde{\mathbf{s}}) - r_{,i}n_k(\tilde{\mathbf{s}})\right]\right\} \tag{9.26}$$

where $r = r(\mathbf{s},\tilde{\mathbf{s}})$.

9.3.3 Discretisation form of the boundary integral equation

Eq.(9.24) can be discretised by boundary elements and the displacement on the boundary can be approximated by

$$\left(\tilde{u}^K\right)_i(\mathbf{s}) = \sum_{I=1}^{N}\phi_I(\mathbf{s})\left(\tilde{u}^K\right)_i^I \tag{9.27}$$

where N is the number of nodes on the boundary, $\phi_I(\mathbf{s})$ are the shape functions and $\phi_I(\mathbf{s}) = 0$ if s and s^I are not in the same boundary element, and the nodal displacement at node $\mathbf{s}^I$ is

$$\left(\tilde{u}^K\right)_i^I = \left(\tilde{u}^K\right)_i(\mathbf{s}^I) \tag{9.28}$$

The displacement singular elements proposed in [285] are adopted in this research since there is singularity caused by concentrated forces.

Substituting Eq.(9.27) into Eq.(9.24) leads to

$$\begin{aligned}&\tilde{c}_i(\tilde{\mathbf{s}})(\tilde{u}^K)_i(\tilde{\mathbf{s}}) + \int_\Gamma T_{ki}^0(\tilde{\mathbf{s}},\mathbf{s})\sum_{I=1}^{N}\phi_I(\mathbf{s})(\tilde{u}^K)_i^I\mathrm{d}\Gamma(\mathbf{s})\\ &= \sum_{l=1}^{m} U_{ki}^0(\tilde{\mathbf{s}},\mathbf{q}_l)(\tilde{f}^K)_i(\mathbf{q}_l) - \int_\Omega U_{ki}^0(\mathbf{s})\mathrm{d}\Omega(\mathbf{s})(\tilde{b}^K)_i\end{aligned} \tag{9.29}$$

Applying Eq.(9.29) to all boundary nodes $\mathbf{s}^J$, the final equations in matrix form can be obtained as

$$\mathbf{H}\tilde{\mathbf{u}}^K = \bar{\mathbf{G}}\tilde{\mathbf{f}}^K - \mathbf{M}\tilde{\mathbf{b}}^K \tag{9.30}$$

where

$$\tilde{\mathbf{u}}^K = \left[(\tilde{u}^K)_1^1 \quad (\tilde{u}^K)_2^1 \quad \cdots \quad (\tilde{u}^K)_1^N \quad (\tilde{u}^K)_2^N\right]^{\mathrm{T}} \tag{9.31}$$

$$\tilde{\mathbf{f}}^K = \left[(\tilde{f}^K)_1^1 \quad (\tilde{f}^K)_1^2 \quad \cdots \quad (\tilde{f}^K)_1^N \quad (\tilde{f}^K)_2^N \right]^{\mathrm{T}} \tag{9.32}$$

$$\tilde{\mathbf{b}}^K = \left[(\tilde{b}^K)_1 \quad (\tilde{b}^K)_2 \right]^{\mathrm{T}} \tag{9.33}$$

while submatrices in $\mathbf{H}$, $\bar{\mathbf{G}}$, $\mathbf{M}$ are

$$H_{JI} = \int_\Gamma \begin{bmatrix} T_{11}^0(\mathbf{s}^J, \mathbf{s}) & T_{12}^0(\mathbf{s}^J, \mathbf{s}) \\ T_{21}^0(\mathbf{s}^J, \mathbf{s}) & T_{22}^0(\mathbf{s}^J, \mathbf{s}) \end{bmatrix} \phi_I(\mathbf{s}) \mathrm{d}\Gamma(\mathbf{s}) \tag{9.34}$$

$$\bar{G}_{JI} = \begin{bmatrix} U_{11}^0(\mathbf{s}^J, \mathbf{q}_I) & U_{12}^0(\mathbf{s}^J, \mathbf{q}_I) \\ U_{21}^0(\mathbf{s}^J, \mathbf{q}_I) & U_{22}^0(\mathbf{s}^J, \mathbf{q}_I) \end{bmatrix} \tag{9.35}$$

$$M_J = \int_\Omega \begin{bmatrix} U_{11}^0(\mathbf{s}^J, \mathbf{s}) & U_{12}^0(\mathbf{s}^J, \mathbf{s}) \\ U_{21}^0(\mathbf{s}^J, \mathbf{s}) & U_{22}^0(\mathbf{s}^J, \mathbf{s}) \end{bmatrix} \mathrm{d}\Omega(\mathbf{s}) \tag{9.36}$$

Note that the matrices $\mathbf{H}$, $\bar{\mathbf{G}}$ and $\mathbf{M}$ are only related to the template particle in the local coordinate system and thus are the same for all particles.

The displacement on the boundary in the local coordinate system cannot be directly computed from

$$\tilde{\mathbf{u}}^K = \mathbf{H}^{-1} \left(\bar{\mathbf{G}} \tilde{\mathbf{f}}^K - \mathbf{M} \tilde{\mathbf{b}}^K \right) \tag{9.37}$$

as $\mathbf{H}$ is singular and thus $\mathbf{H}^{-1}$ does not exist. In this work, however, $\mathbf{H}^{-1}$ is replaced by its pseudo-inverse which can be computed by the singular value decomposition (SVD) as

$$\mathbf{H}^{-1} = \mathbf{V}_2 \Sigma^+ \mathbf{V}_1^{\mathrm{T}} \tag{9.38}$$

where $\mathbf{V}_1$ and $\mathbf{V}_2$ are the left and right singular vectors, and Σ^+ is the pseudo inverse of the singular values Σ of $\mathbf{H}$, which can be written as

$$\Sigma = \begin{bmatrix} \Sigma_0 & & & \\ & a_1 & & \\ & & a_2 & \\ & & & a_3 \end{bmatrix} \tag{9.39}$$

where Σ_0 are N-3 non-zero singular values (from large to small), and the three smallest singular values in 2D case, i.e., a_1, a_2, and a_3, should be zero

without considering computer round-off error. The corresponding left and right singular vectors of a_1, a_2, and a_3 are three rigid motions of the particle. Then, their inverses of a_1, a_2, and a_3 in $\sum^+$ are set to zero. This is essentially equivalent to eliminating any rigid motion of the particle from the solution, since such motion will not induce any strain/stress in the particle. This treatment seems to be the best way, in terms of solution accuracy, to impose (boundary) conditions to make Eq.(9.29) solvable.

After obtaining the displacements on the boundary, the displacement in the domain $\left(\tilde{u}^K\right)_i(\mathbf{s})$ can be computed by Eq.(9.29) with $\tilde{c}_i(\mathbf{s})=1$, and the strain $\tilde{\boldsymbol{\varepsilon}}(\mathbf{s})$ can be computed by

$$\begin{aligned}\left(\tilde{\varepsilon}^K\right)_{ij}(\tilde{\mathbf{s}}) = \frac{1}{2}\Bigg[& -\int_\Gamma \frac{\partial T^0_{ik}(\tilde{\mathbf{s}},\mathbf{s})}{\partial x_j}\left(\tilde{u}^K\right)_k(\mathbf{s})\,\mathrm{d}\Gamma(\mathbf{s}) - \int_\Gamma \frac{\partial T^0_{jk}(\tilde{\mathbf{s}},\mathbf{s})}{\partial x_i}\left(\tilde{u}^K\right)_k(\mathbf{s})\,\mathrm{d}\Gamma(\mathbf{s}) \\ & + \sum_{l=0}^{m} \frac{\partial U^0_{ik}(\tilde{\mathbf{s}},\mathbf{q}_l)}{\partial x_j}\left(\tilde{f}^K\right)_k(\mathbf{q}_l) + \sum_{l=0}^{m} \frac{\partial U^0_{jk}(\tilde{\mathbf{s}},\mathbf{q}_l)}{\partial x_i}\left(\tilde{f}^K\right)_k(\mathbf{q}_l) \\ & - \int_\Omega \frac{\partial U^0_{ik}(\tilde{\mathbf{s}},\mathbf{s})}{\partial x_j}\left(\tilde{b}^K\right)_k(\mathbf{s})\,\mathrm{d}\Omega(\mathbf{s}) - \int_\Omega \frac{\partial U^0_{jk}(\tilde{\mathbf{s}},\mathbf{s})}{\partial x_i}\left(\tilde{b}^K\right)_k(\mathbf{s})\,\mathrm{d}\Omega(\mathbf{s})\Bigg]\end{aligned} \tag{9.40}$$

Suppose that there are $\tilde{m}$ pre-defined points $\mathbf{s}^J$ inside the particle where strains (and stresses) needed to be computed, Eq.(9.40) can be written in matrix form as

$$\bar{\tilde{\boldsymbol{\varepsilon}}}^K = -\mathbf{H}'\tilde{\mathbf{u}}^K + \bar{\mathbf{G}}'\tilde{\mathbf{f}}^K - \mathbf{M}'\tilde{\mathbf{b}}^K \tag{9.41}$$

where

$$\bar{\tilde{\boldsymbol{\varepsilon}}}^K = \left[\left(\tilde{\varepsilon}^K\right)^1_1 \quad \left(\tilde{\varepsilon}^K\right)^1_2 \quad \cdots \quad \left(\tilde{\varepsilon}^K\right)^M_1 \quad \left(\tilde{\varepsilon}^K\right)^{\tilde{m}}_2\right]^{\mathrm{T}} \tag{9.42}$$

$$H'_{JI} = \int_\Gamma \begin{bmatrix} \dfrac{\partial T^0_{11}(\mathbf{s}^J,\mathbf{s})}{\partial s_1} & \dfrac{1}{2}\left[\dfrac{\partial T^0_{12}(\mathbf{s}^J,\mathbf{s})}{\partial s_2} + \dfrac{\partial T^0_{21}(\mathbf{s}^J,\mathbf{s})}{\partial s_1}\right] \\ \dfrac{1}{2}\left[\dfrac{\partial T^0_{21}(\mathbf{s}^J,\mathbf{s})}{\partial s_1} + \dfrac{\partial U^0_{12}(\mathbf{s}^J,\mathbf{s})}{\partial s_2}\right] & \dfrac{\partial T^0_{22}(\mathbf{s}^J,\mathbf{s})}{\partial s_2} \end{bmatrix} \phi_I(\mathbf{s})\,\mathrm{d}\Gamma(\mathbf{s}) \tag{9.43}$$

$$\bar{G}'_{JI} = \begin{bmatrix} \dfrac{\partial U^0_{11}(\mathbf{s}^J,\mathbf{q}_l)}{\partial s_1} & \dfrac{1}{2}\left[\dfrac{\partial U^0_{12}(\mathbf{s}^J,\mathbf{q}_l)}{\partial s_2} + \dfrac{\partial U^0_{21}(\mathbf{s}^J,\mathbf{q}_l)}{\partial s_1}\right] \\ \dfrac{1}{2}\left[\dfrac{\partial U^0_{21}(\mathbf{s}^J,\mathbf{q}_l)}{\partial s_1} + \dfrac{\partial U^0_{12}(\mathbf{s}^J,\mathbf{q}_l)}{\partial s_2}\right] & \dfrac{\partial U^0_{22}(\mathbf{s}^J,\mathbf{q}_l)}{\partial s_2} \end{bmatrix} \tag{9.44}$$

$$M'_J = \int_\Omega \begin{bmatrix} \dfrac{\partial U^0_{11}\left(\mathbf{s}^J,\mathbf{s}\right)}{\partial s_1} & \dfrac{1}{2}\left[\dfrac{\partial U^0_{12}\left(\mathbf{s}^J,\mathbf{s}\right)}{\partial s_2}+\dfrac{\partial U^0_{21}\left(\mathbf{s}^J,\mathbf{s}\right)}{\partial s_1}\right] \\ \dfrac{1}{2}\left[\dfrac{\partial U^0_{21}\left(\mathbf{s}^J,\mathbf{s}\right)}{\partial s_1}+\dfrac{\partial U^0_{12}\left(\mathbf{s}^J,\mathbf{s}\right)}{\partial s_2}\right] & \dfrac{\partial U^0_{22}\left(\mathbf{s}^J,\mathbf{s}\right)}{\partial s_2} \end{bmatrix} \mathrm{d}\Omega\left(\mathbf{s}\right) \tag{9.45}$$

Similar to $\mathbf{H}$, $\bar{\mathbf{G}}$ and $\mathbf{M}$, the matrices $\bar{\mathbf{G}}'$, $\mathbf{H}'$ and $\mathbf{M}'$ also only need to be evaluated once for particles with the geometrically similar shape and the same Poisson's ratio.

The stress in the local coordinate system can be obtained by Eq.(9.18) once the strain is obtained, and the displacement, the strain, and the stress in the global coordinate system can be computed from the values in the local coordinate system by Eqs.(9.15), (9.16) and (9.17), respectively.

9.3.4 Treatment of the domain integral

The integrals in Eqs.(9.36) and (9.45) are domain integrals, which will lead to domain discretisation if computed directly. In this paper, a dimension reduction method, called the line integral method (LIM) [77, 78], is employed to reduce the domain integral to boundary integrals. A brief description of the LIM is presented below. More details can be found in [77, 78]. Taking the domain integral in Eq.(9.36) as an example, the integral can be rewritten by LIM as

$$M_J = \int_\Omega \mathbf{U}^0\left(\mathbf{s}^J,\mathbf{s}\right)\mathrm{d}\Omega\left(\mathbf{s}\right) = \sum_{j=1}^{\tilde{n}} n_1^j\left(\mathbf{s}\right)\omega^j \int_{L_j} \mathbf{U}^0\left(\mathbf{s}^J,\mathbf{s}\right)\mathrm{d}L_j\left(\mathbf{s}\right) \tag{9.46}$$

where L_j is the j^{th} sub-integral line for the one-dimensional line integrals created by the background cells and associated with Gaussian quadrature points of the boundary elements; $\tilde{n}$ represents the number of sub-integral lines; n_1^j and ω^j denote the unit outward normal in the s_1-axial and the Gaussian integration weight of L_j. The other domain integrals can be computed by LIM similar to Eq.(9.46) where only the boundary is needed to be discretised.

Note again that by utilising the fact that only constant body forces are considered, the main operations involved in these domain integrals

only need to be done once in the template particle. For each particle, only insignificant extra computations need to be performed to obtain the boundary displacements, strain and stress distribution.

9.4 Particle breakage evaluation from the stress field

After the stress field of a particle is computed via BEM, the breakage state of any selected point inside the particle will be evaluated using the Hoek-Brown criterion, as it can consider both tension and shear failure which is common for brittle materials, such as rock.

To obtain a continuous failure zone insides a particle, the particle is discretised into triangular cells. In this research, the cells are created by Delaunay triangulation of the pre-selected sample points [286, 287]. The state of each cell is evaluated by the Hoek-Brown criterion, and a cell is defined as in a "failure" state if one or more vertexes of this cell are in such a state. Possible breakage paths can be approximated when the breakage states of all cells inside the particle are obtained. The related methods and computational procedures are introduced below. Furthermore, the tensile and compressive stresses are defined as negative and positive, respectively.

9.4.1 The Hoek-Brown breakage criterion

The Hoek-Brown criterion can be written as [288]

$$\sigma_1 > \begin{cases} \sigma_3 + \sigma_c \left(m_b \dfrac{\sigma_3}{\sigma_c} + \xi \right)^{\alpha}, & \sigma_3 \geq -\dfrac{\xi \sigma_c}{m_b} \\ \sigma_3, & \sigma_3 < -\dfrac{\xi \sigma_c}{m_b} \end{cases} \tag{9.47}$$

where σ_1 and σ_3 are the major and minor principal stresses, respectively; σ_c is the uniaxial compressive strength of the material, which can be measured by uniaxial pressure and point load tests; ξ, m_b and α are constants concerning the characteristics of the rock. Specifically, ξ reflects the degree of rock fragmentation, and its value ranges from 0 to 1: for

broken rock mass, ξ=0; for intact rock mass, ξ=1. m_b reflects the hardness degree of the rock and its value ranges from 10^{-7} to 25: m_b=10^{-7} for seriously disturbed rock mass; for intact hard rock mass, m_b=25. For rock mass in good quality, α=0.5.

According to this criterion, shear failure occurs when the major principal stress σ_1 meets the condition in Eq.(9.47), while when the tensile stress is greater than $-\xi\sigma_c/m_b$, tensile failure occurs. Thus, the state of each point can be established by the Hoek-Brown criterion: if either shear or tensile failure occurs at the point, its state is set to be "failure". Furthermore, as the (template) particle has been discretised into triangular cells (see **Fig.9.3** (a)), the state of each cell can be determined: if one of the three nodal points of a triangular cell fails, the state of the cell is marked as "failure".

9.4.2 Approximation of particle breakage paths

For a potentially broken particle, the approximation to breakage paths is needed. According to both previous experimental and numerical investigations [289-292], breakage paths initiate from and also most likely end at the positions of contact forces, because stress concentration always occurs near the area the contact forces are applied and the stresses there are often much larger than the rest of the particle. Thus, it is reasonable to assume that the endpoints of breakage paths for a particle are at the positions of contact forces. As the approximation nature of DEM, the breakage paths are simplified as straight lines in this work. As a result, all possible lines that connect the positions of contact forces can be treated as potential breakage paths, shown in **Fig.9.3** (b).

Next, these potential breakage paths are further analysed to determine those real paths that will occur. It is easy to understand that a real crack or breakage path must be across a continuous failure region formed by "failure" cells. Then, a numerical approach to determine such a real breakage path is needed. In this work, for a given potential breakage

path (a straight line), the cells that the line intersects with are identified as the associated cells (see **Fig.9.3** (b)). If all of them are "failure", then the potential breakage path becomes a real crack (see **Fig.9.3** (c)).

In the next section, the performance of the approximation and determination of particle breakage paths outlined above will be fully discussed and illustrated with numerical examples.

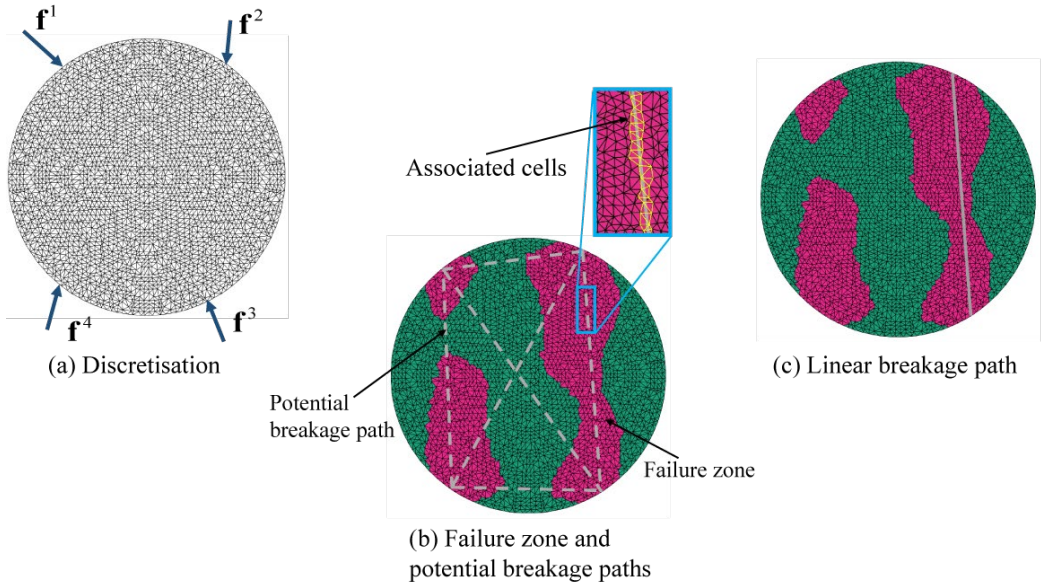

Fig.9.3 The determination process of a particle

9.5 Results and discussions

In this section, three examples are conducted to validate the proposed B-DEM in simulating the stress field and possible breakage paths of particles.

9.5.1 Validation and discussion via a single particle

9.5.1.1 Validation by the Brazilian disc test

This example consists of a single circular particle under the action of an equal pair of radial concentrated forces, also known as the Brazilian disc test. The disc is centred at (0, 0). The mechanical properties and diameter D of the disc, and parameters of the Hoek-Brown criterion used are listed in **Table 9.1**. As displayed in **Fig.9.4**, the two opposite radial

concentrated forces act at (0, 0.03) and (0, -0.03) respectively.

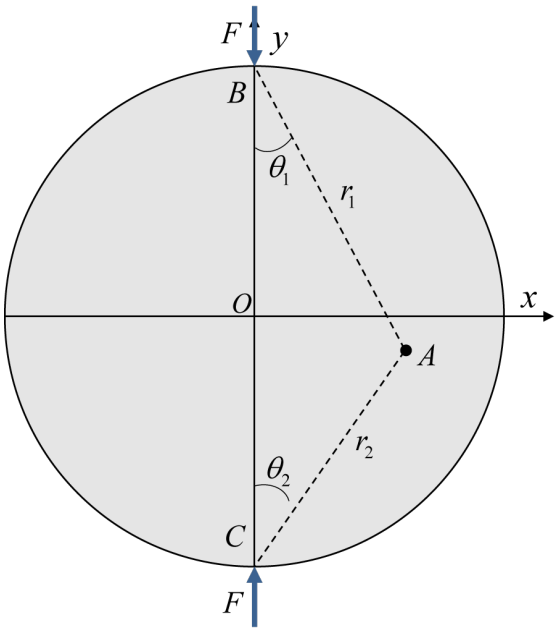

Fig.9.4 Brazil disc under the concentrated force

Table 9.1 Parameters of the disc[275]

Simulation parameters		Value
Geometric information	Diameter (m)	0.03
Mechanical parameters	Poisson's ratio	0.15
	Young's Modulus (GPa)	80
	Density (kg/m3)	2380
Parameters of Hoek-Brown criterion	s	1.0
	a	0.5
	mb	25
	σ_c (MPa)	80

Refer to **Fig.9.3**, the analytical solution of the stress distribution inside the particle can be expressed as [293]

$$\sigma_{xx} = \frac{2F}{\pi}\left(\frac{\sin^2\theta_1\cos\theta_1}{r_1} + \frac{\sin^2\theta_2\cos\theta_2}{r_2}\right) - \frac{2F}{\pi D} \tag{9.48}$$

$$\sigma_{xy} = \frac{2F}{\pi}\left(\frac{\sin\theta_1\cos^2\theta_1}{r_1} - \frac{\sin\theta_2\cos^2\theta_2}{r_2}\right) \tag{9.49}$$

$$\sigma_{yy} = \frac{2F}{\pi}\left(\frac{\cos^3\theta_1}{r_1} + \frac{\cos^3\theta_2}{r_2}\right) - \frac{2F}{\pi D} \tag{9.50}$$

where the sign convention of θ_1 and θ_2 is: θ_1 and θ_2 are positive if point A

locates on the right side of the loading line (as shown in **Fig.9.4**), but are negative otherwise.

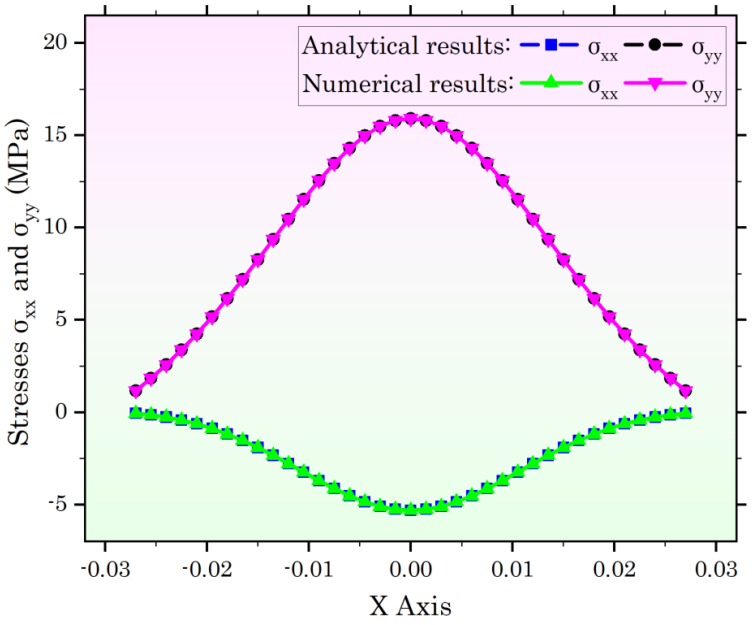

Fig.9.5 Comparison of the stresses on y=0 with analytical results

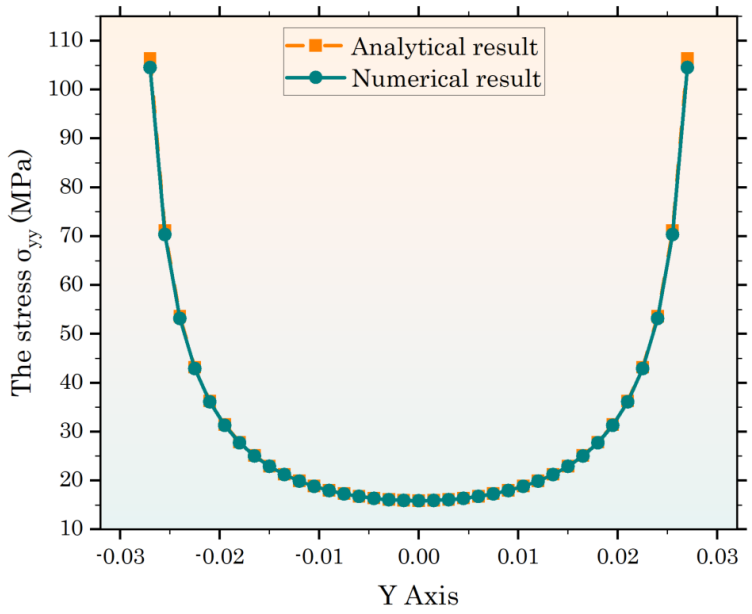

Fig.9.6 Comparison of σ_{yy} on x=0 with analytical results

The concentrated force is set to be F=0.5 MPa and the disc boundary is discretised into 100 elements. To access the accuracy of BEM computed stresses, evenly distributed 37 points are selected on the lines y=0 and x=0 respectively. **Fig.9.5** shows that the numerical results of σ_{xx} and σ_{yy} at the selected points on the line y=0 are in very good agreement with the

analytical solutions. The relative errors of σ_{xx} and σ_{yy} are 0.0396% and 0.0324% respectively.

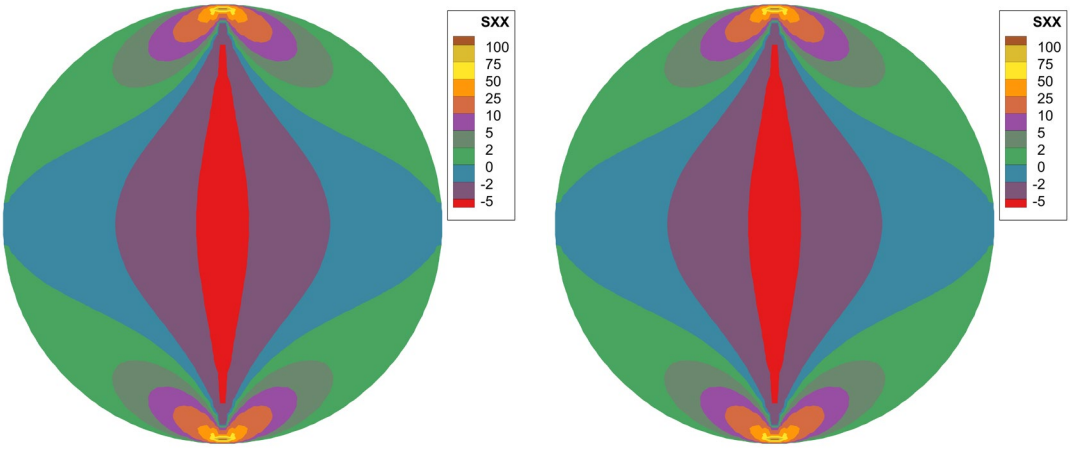

(a) The proposed method (b) The analytical solution

Fig.9.7 Comparison of the stress σ_{xx} with the analytical solution

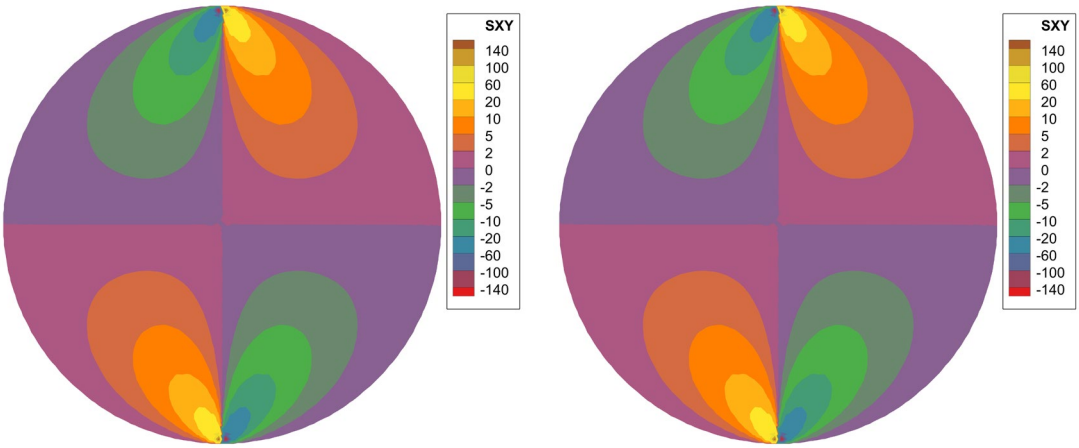

(a) The proposed method (b) The analytical solution

Fig.9.8 Comparison of the stress σ_{xy} with the analytical solution

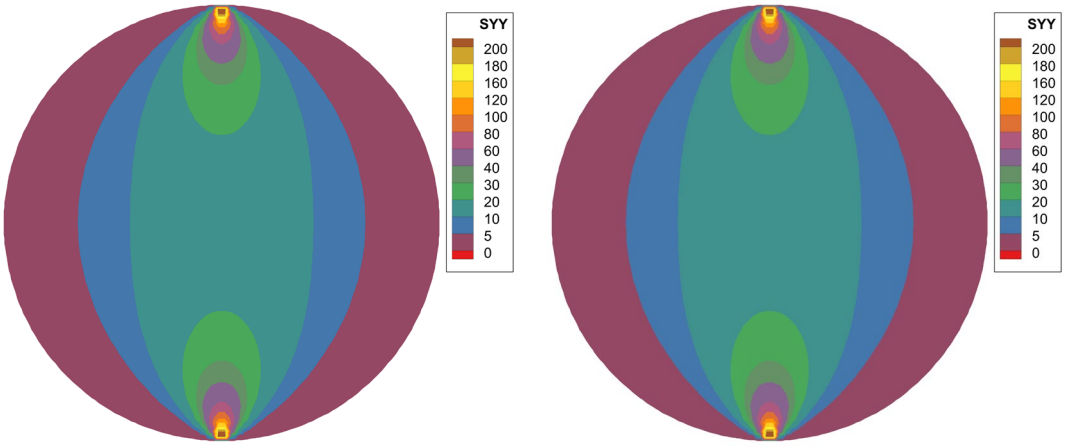

(a) The proposed method (b) The analytical solution

Fig.9.9 Comparison of the stress σ_{yy} with the analytical solution

Moreover, as shown in **Fig.9.6**, the computed values of σ_{yy} at the selected points on the line x=0 also coincide well with the analytical solutions with a relative error of 0.431%.

Furthermore, **Figs.7-9** compare the stresses distributions over the entire disc between the numerical and analytical solutions.

Moreover, to test and validate the convergence of the proposed method in terms of boundary discretisation, the boundary of the Brazilian disc is discretised into different numbers of elements, i.e., 50, 100, 200, 400, 800, 1600 and 3200. The relative errors of the previously selected 37 points on the lines x=0 and y=0 respectively are computed and shown in **Fig.9.10**. It seems that using 100 boundary elements is sufficient to obtain reasonably accurate stress distributions in circular particles.

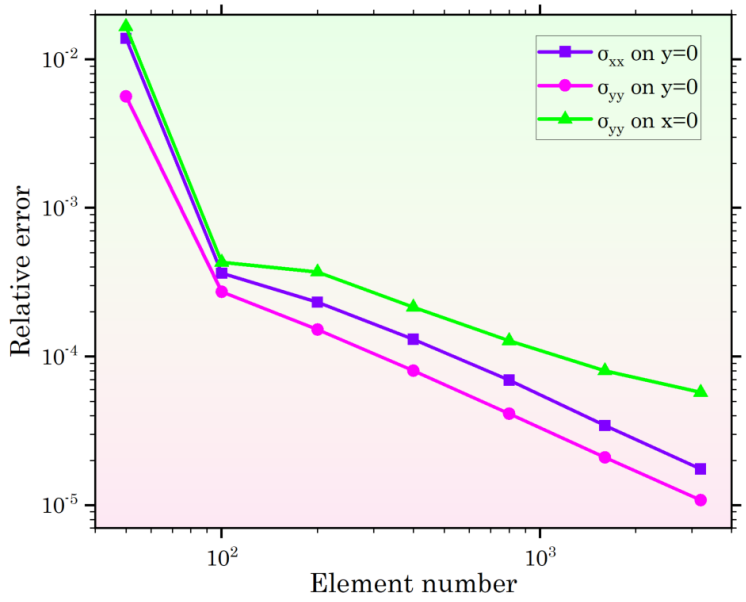

Fig.9.10 Relative error varies with the number of elements

9.5.1.2 The failure zone and breakage paths

After the correctness and convergence of the proposed method for calculating the particle stress field are verified, the performance of the assumption and determination of breakage paths proposed in **Section 9.4.2** is discussed for the cases where three different concentrated boundary forces are considered, as shown in **Table 9.2** and **Fig.9.11**. Note that the

disc boundary is discretised into 80 elements.

Table 9.2 Parameters of the disc

Cases		The concentrated forces
(a)		F1=F2=0.5 MPa
(b)	(b-1)	F1=F2=F3=2 MPa
	(b-2)	F1=3 MPa; F2=2 MPa; F3=1 MPa
(c)	(c-1)	F1=F2=F3=F4=4 MPa
	(c-2)	F1=F2=F3=F4=2 MPa
	(c-3)	F1=F3=1 MPa; F2=F4=4 MPa

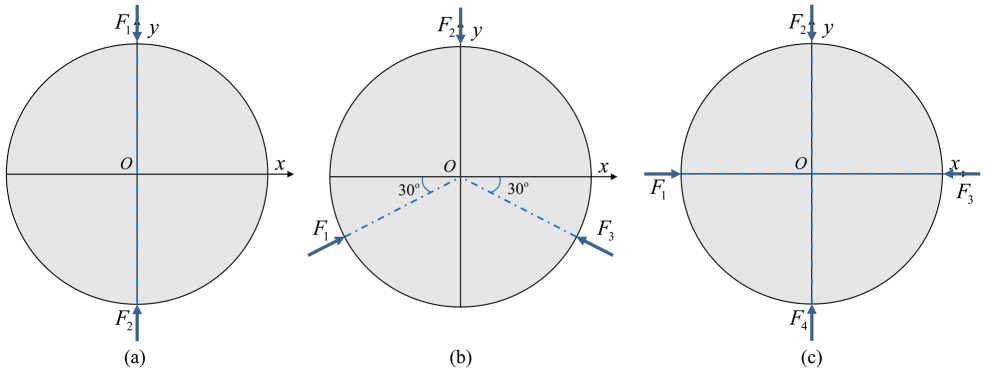

Fig.9.11 Three cases of a disc under concentrated forces

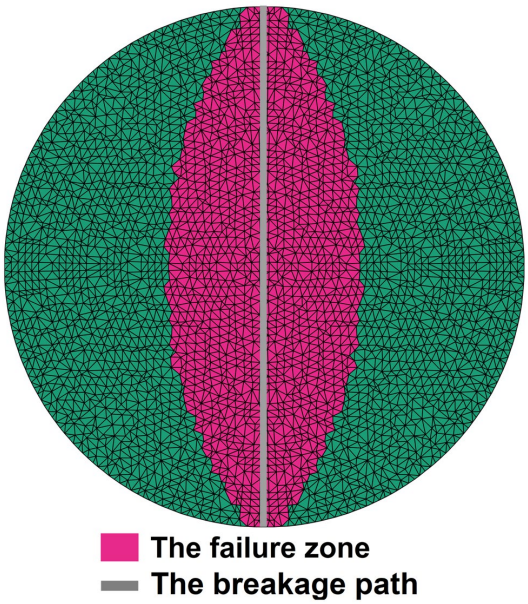

Fig.9.12 The failure zone and breakage path (F_1=F_2=0.5 MPa)

For case (a) where the disc is under one equal pair of contact forces, F_1=F_2=0.5 MPa, the stress field is already obtained in **Section 9.5.1** from which the failure zone is identified as the pink zone in **Fig.9.12**. As the

failure zone has penetrated across the disc already, there is a large possibility that the disc has split into two parts along the diameter connecting the two concentrated forces, which is the breakage path (the grey line) numerically identified.

In case (b), the disc is subjected to three concentrated forces (see **Fig.9.11** (b)). As shown in **Table 9.2**, two different sets of force magnitudes are tested. The distributions of σ_{xx}, σ_{xy} and σ_{yy} for cases (b-1) and (b-2) are depicted in **Fig.9.13** (a) and **Fig.9.14** (a) respectively. The failure (pink) area in case (b-1), as shown in **Fig.9.13** (b), penetrates the disc along the three sides of a triangular region. While the failure zone in case (b-2) is an *L*-shaped region and only two breakage paths are obtained.

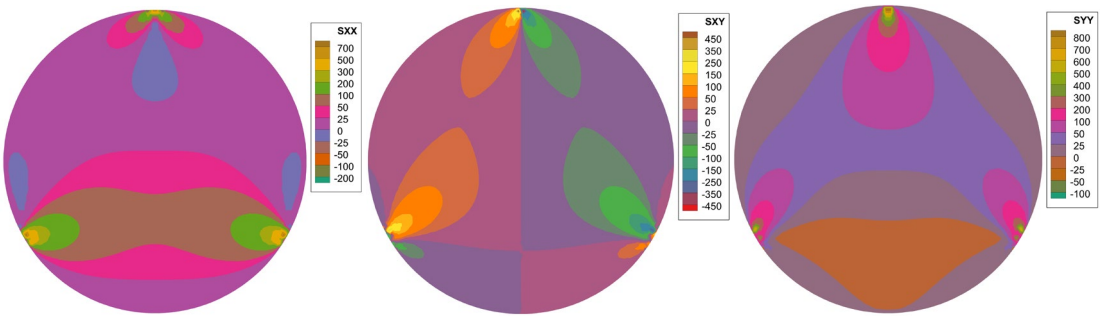

(a) Contour plot of stress σ_{xx}, σ_{xy} and σ_{yy}

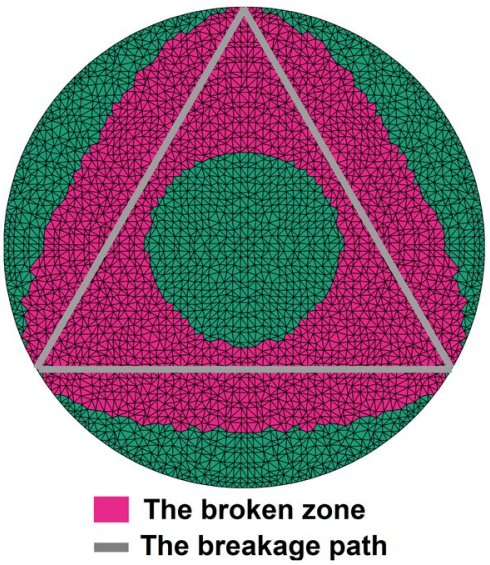

(b) The failure zone and breakage path

Fig.9.13 Stress distributions and state of case (b-1)

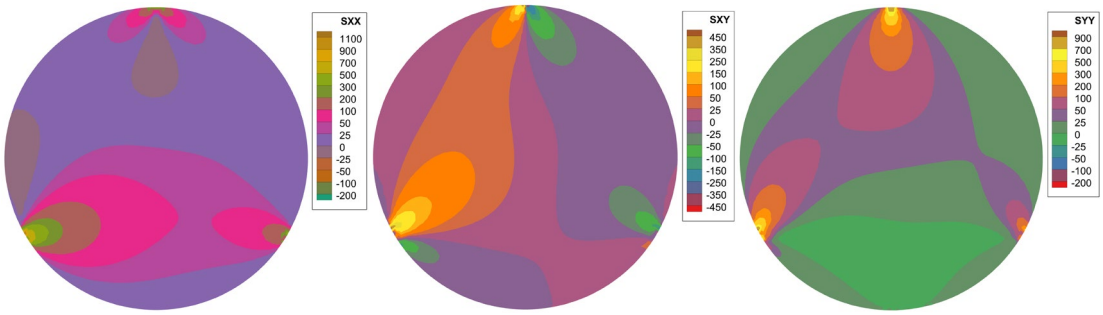

(a) Contour plot of stress σ_{xx}, σ_{xy} and σ_{yy}

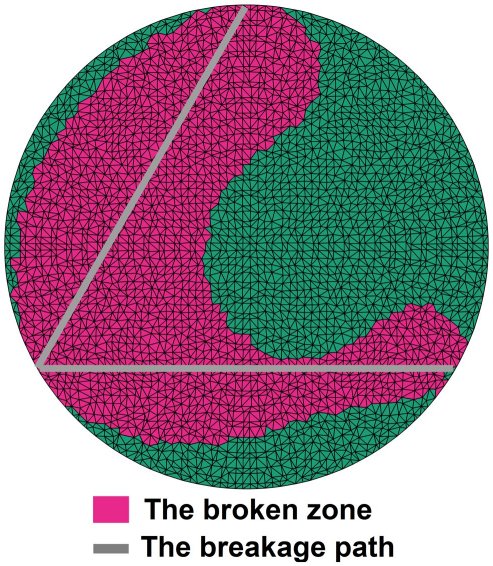

(b) The failure zone and breakage path

Fig.9.14 Stress distributions and status of case (b-2)

For case (c), two pairs of concentrated forces, one in the horizontal direction and the other in the vertical direction, act on the disc. (see **Fig.9.11** (c)). Furthermore, three different sets of the magnitudes of the forces are considered, as are listed in **Table 9.2**. The distributions of σ_{xx}, σ_{xy} and σ_{yy} for cases (c-1), (c-2), and (c-3) are depicted in **Figs.9.15-17** (a). Shown in **Fig.9.13** (b) for case (c-1), the failure area penetrates the disc along the four sides of a diamond-shaped zone. While the four failure zones in case (c-2) are not connected to each other because the magnitude of the concentrated forces is not sufficiently large to produce any breakage path. In addition, case (c-3) presents a totally different failure mode compared to case (c-1): the failure zone associated with the vertical pair that have a greater magnitude is formed across the disc and one breakage

path is identified.

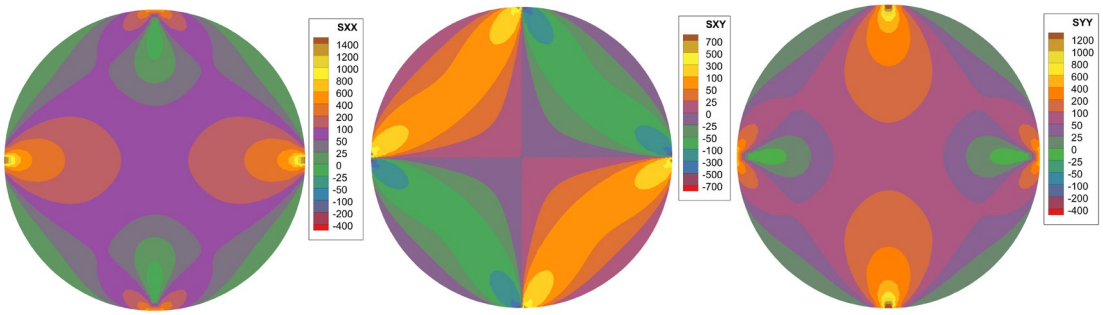

(a) Contour plot of stress σ_{xx}, σ_{xy} and σ_{yy}

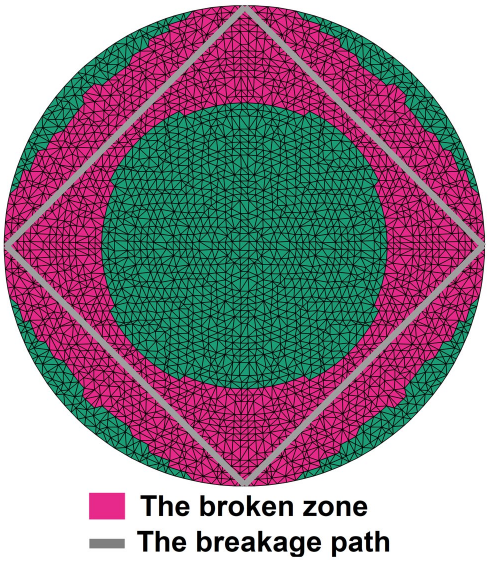

(b) The failure zone and breakage path

Fig.9.15 Stress distributions and status of case (c-1)

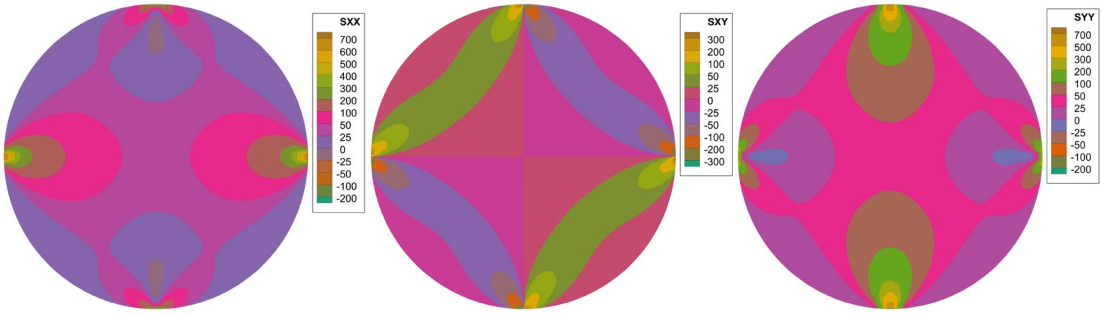

(a) Contour plot of stress σ_{xx}, σ_{xy} and σ_{yy}

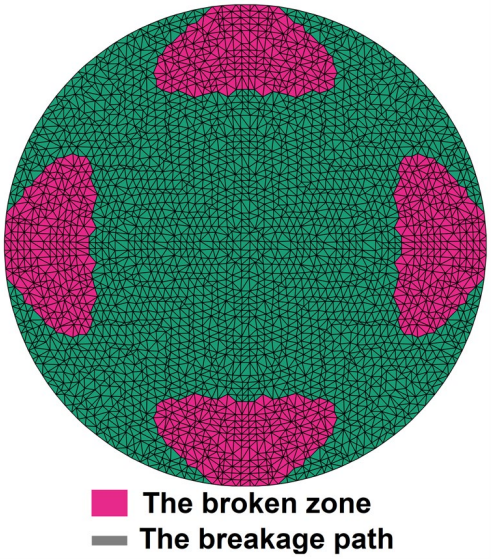

(b) The failure zone and breakage path

Fig.9.16 Stress distributions and status of case (c-2)

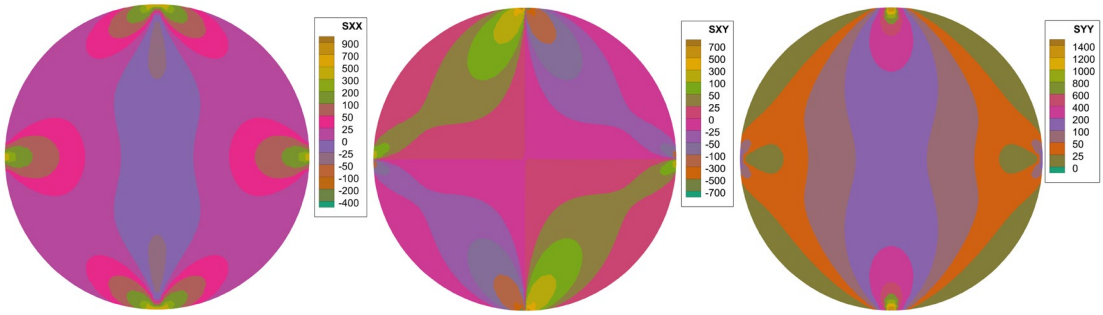

(a) Contour plot of stress σ_{xx}, σ_{xy} and σ_{yy}

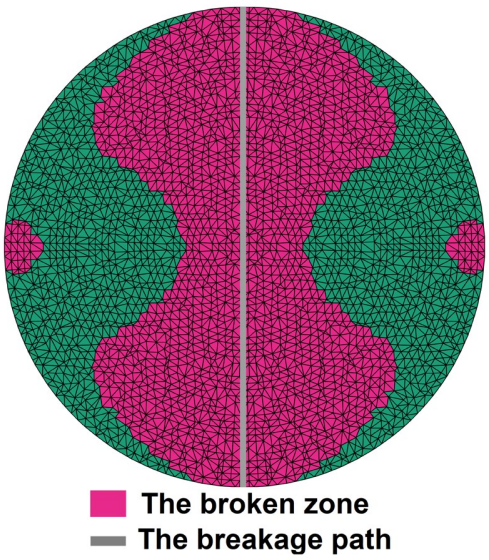

(b) The failure zone and breakage path

Fig.9.17 Stress distributions and status of case (c-3)

The cases above show several different failure modes, and all actual breakage paths have been identified correctly by the proposed approach. However, these cases only cover a very small number of loading cases, and in particular not sufficiently complex: most of the concentrated forces that act on the disc are symmetric and equal in magnitude. The study of Tsoungui et al. [294, 295] shows that it is much more difficult for particles to break under isotropic action and easier to break under inhomogeneous contact forces. It is thus expected that the particle subjected to contact forces of different magnitudes and loading locations is easier to break, and the failure zone may be more irregular, winding, and complex. Consequently, to further illustrate the performance of the proposed methodology, cases with far more complex combinations of force number, magnitudes and locations should be considered.

9.5.2 Simulation of circular particle assemblies

In this section, two uniaxial compression tests of granular materials are performed via 2D DEM simulations to investigate the particle breakage behaviour. There are respectively 314 and 614 particles uniformly distributed in the two specimens. The Hertz-Mindilin model is used to model the interaction of particles [296]. The detailed numerical parameters are shown in **Table 9.3**.

Table 9.3 DEM parameters for uniaxial compression models

Simulation parameters		Values
Geometric information	Radius (m)	0.022-0.035
Mechanical parameters	Density (kg/m3)	2380
	Friction	0.0
	Shear modulus	43.5
	Poisson's ratio	0.15
	Local damping	0.7
Parameters of Hoek-Brown criterion	s	0.015
	a	0.5
	m_b	6.18
	σ_c (MPa)	80

The initial specimens are generated using the following procedures [297]. First, an assembly of particles with the specified number is created

inside a sufficiently large square region with frictionless walls. Then the walls are controlled to move towards the centre by a servo algorithm to achieve a confining stress of 2 MPa with an initial porosity of 0.18.

Then the uniaxial loading process is followed by moving the upper and bottom walls inwards with the same speed while keeping the lateral walls fixed. To make sure a quasi-static loading process, a loading rate of 10^{-4} m/s is used. The loading stops when the axial strain reaches 12%. The corresponding stress states of the two specimens are analysed and discussed below.

Figs.9.18 and **9.19** are the contour plots of the stress distributions with logarithmic data, failure zone, and breakage paths of the two specimens respectively. **Figs.9.18** (a)-(d) demonstrate that the particle-scale stress contour can be a useful indicator to describe the internal force distribution within the granular system undergoing deformation. The numerical results reproduce the fact that the external loads are transferred in granular materials by significant force chains, which is a unique signature in contrast to continuum media. These force chains constitute a highly inhomogeneous contact force network. In addition, the failure area and identified breakage paths, shown in **Figs.9.19** (e)-(f), are also heterogeneous.

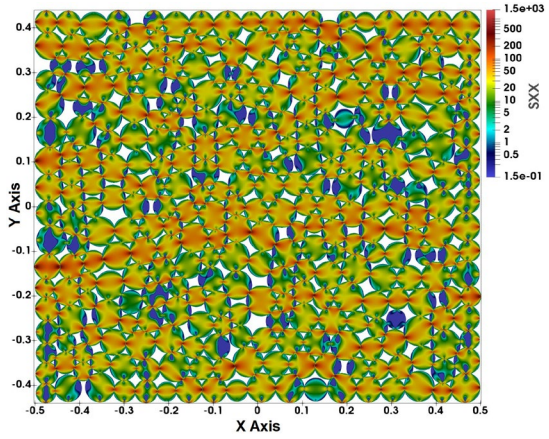

(a) Contour plot of σ_{xx}

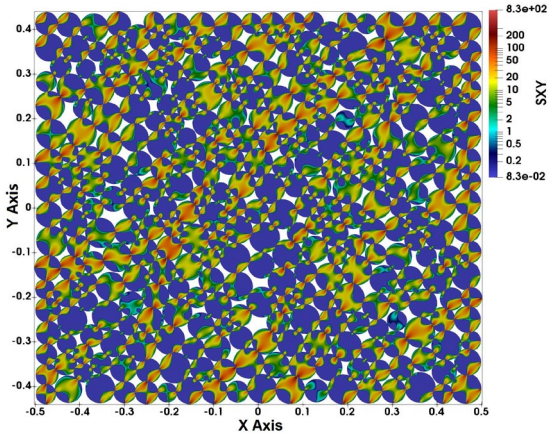

(b) Contour plot of σ_{xy}

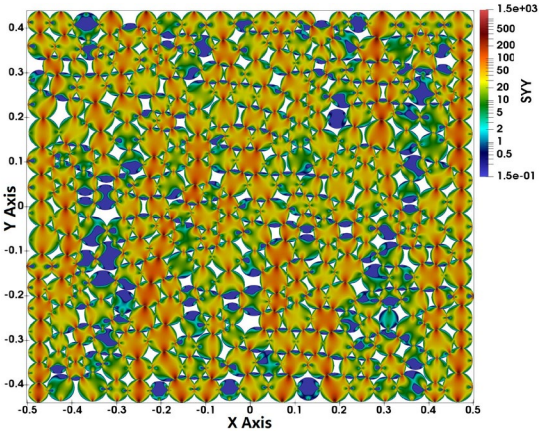

(c) Contour plot of σ_{yy}

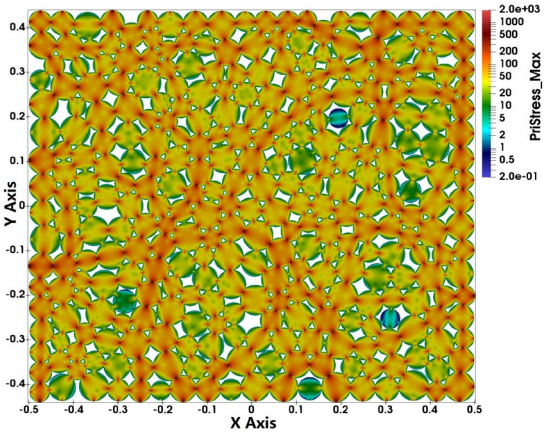

(d) Contour plot of major principal stress

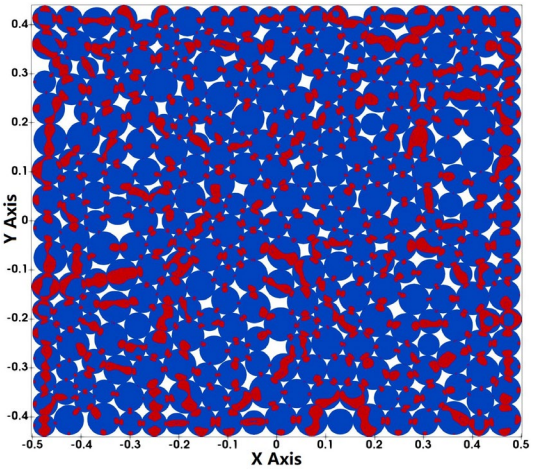

(e) The failure zone

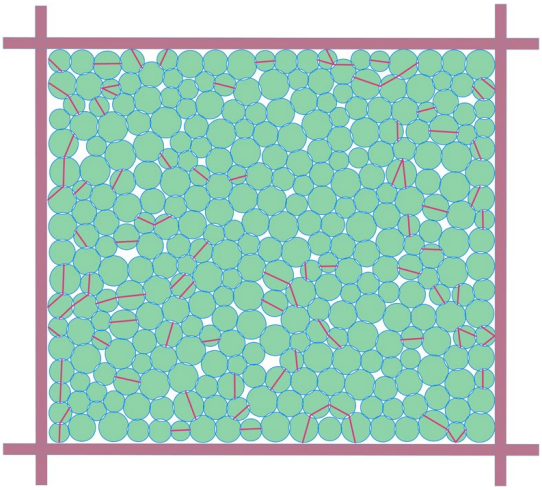

(f) The breakage paths

Fig.9.18 Inner stresses and breakage paths of the 314-particle specimen

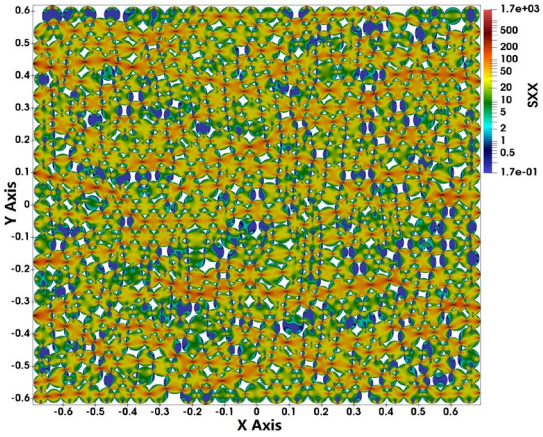

(a) Contour plot of σ_{xx}

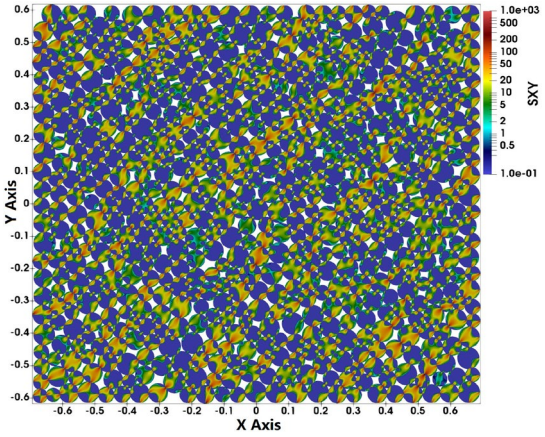

(b) Contour plot of σ_{xy}

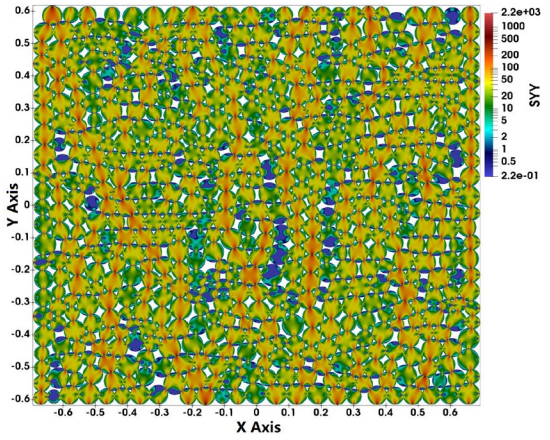

(c) Contour plot of σ_{yy}

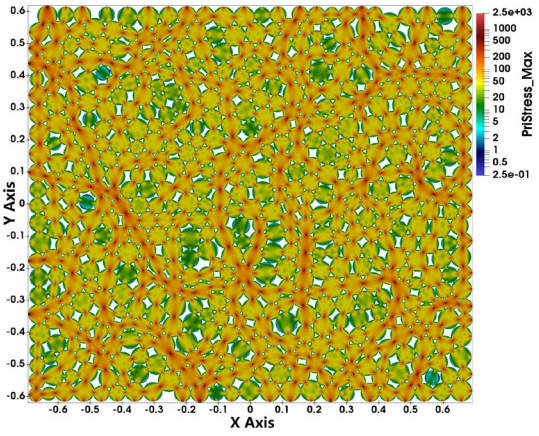

(d) Contour plot of major principal stress

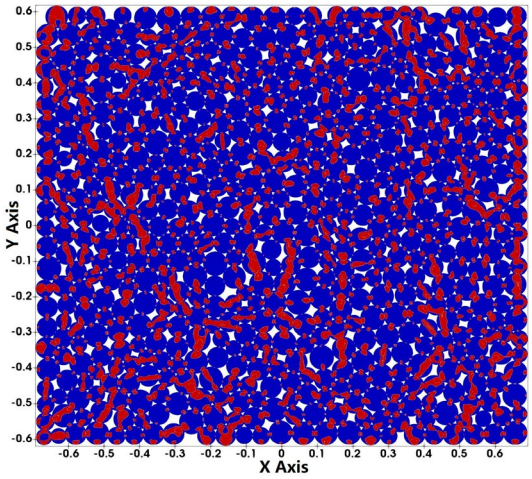

(e) The failure zone

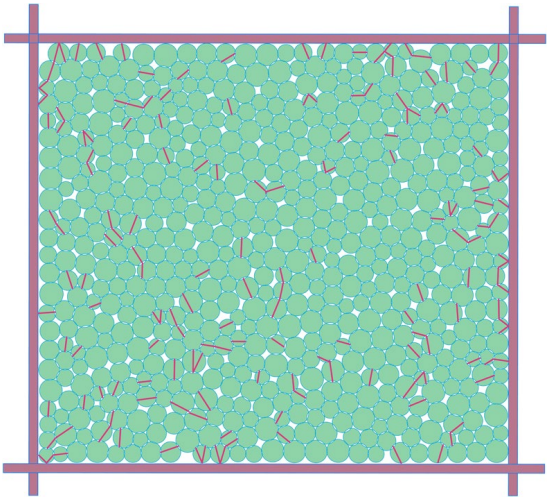

(f) The breakage paths

Fig.9.19 Inner stresses and breakage paths of the 614-particle specimen

As can be seen in **Fig.9.18** (e)-(f) and **Fig.9.19** (e)-(f), most failure zones that penetrate through a particle have been identified, simplified and represented by straight-line breakage paths.

9.6 Concluding remarks

In a standard DEM simulation concerning particle breakage, only the average stress of a particle can be obtained based on its contacting forces. The combined boundary-discrete element method proposed in this research provides a much more accurate stress distribution within a particle by taking advantage of the boundary discretisation feature of

BEM. The solution accuracy is further enhanced by taking account of the particle acceleration and using the pseudo-inverse to eliminate the rigid motion of a particle. Furthermore, based on the Hoek-Brown criterion for brittle materials, a new and simple approach is proposed to obtain the fracture failure state map and also to determine possible breakage paths inside a particle.

The current work fully exploits the particle system where all particles are geometrically similar so that the matrices and their constructions in the BEM formulation only need to be conducted once for the template particle. Thus, the computations involved in the subsequent evaluations of the boundary displacement and stress distribution of each particle become negligible. The proposed methodology should also be very effective where particles are similar to a small number of distinct template particles.

It should be highlighted that within the proposed method, after each DEM simulation step, BEM serves as an *optional* post-processing step to obtain the stress distribution within a particle and further determine breakage paths. In other words, such a post-processing step may only need to be invoked for those particles in the system that may be deemed to be fractured and may not be necessary after each DEM step. The development of a comprehensive mechanism to determine which particles to be post-processed for possible breakage evaluation is currently undertaken.

The performance of the proposed BEM part for the evaluation of stress distribution and possible breakage paths of particles has been assessed by several examples. Particles involved in these examples are circular for simplicity. Nevertheless, arbitrarily shaped particles can be equally handled in the proposed methodology in principle.

However, in this research, potential breakage paths for a particle subject to contact forces have been assumed as straight lines connecting these contact forces. This is a profound assumption that leads to the proposed numerical procedure to predict the breakage paths, and is

validated by the examples, to a certain extent. However, true cracks can be far from straight lines. A new development is currently in progress which will address these issues, and a more generic approach will be reported shortly.

Finally, although the main ideas behind the current development seem also applicable to 3D cases, there are some practical issues needed to be resolved before 3D particle breakage can be modelled within the proposed framework.

Part V

Conclusion

Chapter 10

Conclusions and Outlook

10.1 Major contributions

This thesis is mainly devoted to developing a high-performance BEM, to overcome the obstacles that the traditional BEM is confronted with, i.e., domain integrals and non-symmetrical and dense matrix systems. Specifically speaking, three main contributions of this thesis can be concluded and summarized below:

(1) To compute domain integrals with known or unknown integrand functions, a novel BEM, AOIMLS enhanced LIBEM, which inherits the well-known advantage of traditional BEM, namely, boundary-only discretisation, is proposed.

The LIBEM is an accurate and stable method for computing domain integrals in boundary integral equations and keeps the merit of traditional BEM, i.e., boundary-only discretisation, and it is applied to the computation of 3D heat conduction with heat sources (**Chapter 3**), 2D thermoelastic problems (**Chapter 5**) and 3D thermoelastic problems (**Chapter 6**) and performs its accuracy and convergence. However, LIBEM only works when the integral function in domain integrals is known, specifically, the mathematical expression of heat sources is given, and the mathematical expression of temperature distribution is given for thermoelastic problems.

To extend the application scope of LIBEM, the AOIMLS enhanced LIBEM is proposed for computing domain integrals with known or unknown integral functions, which ensures all the nonlinear and nonhomogeneous problems can be solved without domain discretisation. In addition, AOIMLS can adaptively avoid singular or ill-conditioned moment matrices, thus ensuring the stability of the calculation results, and it owns the advantage that the delta property of its shape function ensures it is easier to impose boundary conditions. To test the correctness of AOIMLS enhanced LIBEM, it is applied to the analysis of 3D non-homogeneous heat conduction problems with heat sources (**Chapter 4**), 3D thermoelastic problems (**Chapter 6**), and thermoelastic fracture problems (**Chapter 8**) thereby.

(2) To deal with the non-symmetrical and dense matrix system, the fast multipole method is introduced to couple with LIBEM, thereby ensuring BEM performs better in efficiency. In addition, a high-efficiency combined BEM and DEM is addressed to compute the inner stress distribution and particle breakage of particle assemblies based on the solution mapping scheme.

The coefficient matrix of equations formed by BEM in solving problems is fully-populated, so it will occupy large computer memory and cannot be applied to compute large-scale engineering problems. For a large-scale continuous media object, the fast multipole method is introduced to enhance the efficiency of LIBEM, and it is applied to the analysis of heat conduction with heat sources (**Chapter 3**).

For massive discontinuous materials in geometric similar shapes, a novel scheme, the combined BEM and DEM, is proposed, which can provide much more accurate stress distribution within a particle by taking advantage of the boundary discretisation feature of BEM. For the stress field computation of particles with similar geometry, a template particle is used as the representative particle, so that only the related coefficient matrices of one template particle in the local coordinate system are needed to be calculated, while the coefficient matrices of the other particles, can be obtained by mapping between the local and global coordinate systems. Thus, the proposed method is much more time-effective when modelling a large-scale particle system with a small number of distinct possible particle shapes. Furthermore, with the help of the Hoek-Brown criterion, the possible cracks or breakage paths of a particle can be obtained (**Chapter 9**).

(3) A series of novel unified boundary integral equations based on BEM and DDM are derived for solving fracture problems and thermoelastic fracture problems in finite and infinite domains.

Two sets of unified BIEs are derived for fracture problems in finite and infinite domains based on the direct BEM and DDM respectively, which can provide accurate and stable results. Another two sets of BIEs are addressed by employing indirect BEM and DDM, which can not ensure a stable result,

thereby a modified indirect BEM is proposed which performs much more stable (**Chapter 7**).

Moreover, a set of novel BIEs based on the direct BEM and DDM for cracked domains under thermal stress is proposed. The main BIE is derived based on the displacement BIE, followed by two supplementary equations for ensuring enough equations as the unknowns on crack are considered. Besides, the two supplementary BIEs are alternatively used depending on the type of known quantities, traction or displacement. In addition, the BIEs are numerically computed by the AOIMLS enhanced LIBEM (**Chapter 8**).

10.2 Future work

Although significant improvements have been made in enhancing the performance of BEM, some work is still preliminary and more can be further extended within the scope of the thesis. The potential future work is suggested below.

(1) In Part III, the BIEs are proposed for cracked domains with preset cracks, but crack propagation is not considered, which can be complete in the future.

(2) In my opinion, the research in Part IV is very interesting and meaningful, but I only present a scheme, i.e., the combined BEM and DEM due to the graduation timing, a lot of details need to be done and perfected.

The main limitation of the current work in conjunction with using circular particles is that no actual particle breakage is introduced and subsequently simulated, though it is possible in principle. In addition, potential breakage paths for a particle subject to contact forces have been assumed as straight lines connecting these contact forces. A new development is currently in progress which will address these issues, and a more generic approach will be reported shortly. Finally, although the main ideas behind the current development seem also applicable to 3D cases, there are some practical issues needed to be resolved before 3D particle breakage can be modelled within the proposed framework.

(3) BEM can be an important supplement method for FEM and give full play in many engineering fields, but there is few commercial software developed based on BEM which limits its promotion and development, if parallel algorithms can be applied to further enhance the efficiency of BEM, a better future may be curved.

References

[1] Fu Z, Xi Q, Chen W, Cheng A. A boundary-type meshless solver for transient heat conduction analysis of slender functionally graded materials with exponential variations [J]. Computers & Mathematics with Applications, 2018, 76: 760-773.

[2] Rana SK, Jena A. A BEM formulation of two dimensional steady state heat conduction in exchanger tubes of arbitrary cross sections [J]. International Journal of Heat and Mass Transfer, 2017, 106: 195-211.

[3] Xu M. A novel numerical method for solving heat conduction problems [J]. International Journal of Heat and Mass Transfer, 2016, 103: 285-290.

[4] Liu B, Zhou W, Wang Q. The novel boundary integral equation with adaptive orthogonal IMLS based line integration method for cracked domains under thermal stress [J]. Engineering Fracture Mechanics, 2020, 239: 107325.

[5] Zhang X, Li X. Transient thermal stress intensity factors for a circumferential crack in a hollow cylinder based on generalized fractional heat conduction [J]. International Journal of Thermal Sciences, 2017, 121: 336-347.

[6] Burczyński T, Długosz A. Evolutionary optimization in thermoelastic problems using the boundary element method [J]. Computational Mechanics, 2002, 28: 317-324.

[7] Dobroskok AA, Linkov AM. CV BEM for 2D transient thermo-(poro-) elastic problems concerning with blocky systems with singular points and lines of discontinuities [J]. International Journal of Engineering Science, 2010, 48: 658-669.

[8] Chen F, Liu H, Zhang S. Coupled heat transfer and thermo-mechanical behavior of hypersonic cylindrical leading edges [J]. International Journal of Heat and Mass Transfer, 2018, 122: 846-862.

[9] Liu Q, Zhang P, Cheng S, Niu J, Liu D. Heat transfer and thermo-elastic analysis of

copper steel composite stave [J]. International Journal of Heat and Mass Transfer, 2016, 103: 341-348.

[10] Qu W, Zhang Y, Gu Y, Wang F. Three-dimensional thermal stress analysis using the indirect BEM in conjunction with the radial integration method [J]. Advances in Engineering Software, 2017, 112: 147-153.

[11] Zhang S, Huang Z, Li G, Wu X, Peng C, Zhang W. Numerical analysis of transient conjugate heat transfer and thermal stress distribution in geothermal drilling with high-pressure liquid nitrogen jet [J]. Applied Thermal Engineering, 2018, 129: 1348-1357.

[12] Gu Y, He X, Chen W, Zhang C. Analysis of three-dimensional anisotropic heat conduction problems on thin domains using an advanced boundary element method [J]. Computers & Mathematics with Applications, 2018, 75: 33-44.

[13] Bayati SA, Wrobel LC. Radial integration boundary element method for two-dimensional non-homogeneous convection–diffusion–reaction problems with variable source term [J]. Engineering Analysis with Boundary Elements, 2019, 101: 89-101.

[14] Feng S, Han X. A novel multi-grid based reanalysis approach for efficient prediction of fatigue crack propagation [J]. Computer Methods in Applied Mechanics and Engineering, 2019, 353: 107-122.

[15] Muñoz R, Buroni F, Sáez A, García S, F 3D explicit-BEM fracture analysis for materials with anisotropic multifield coupling [J]. Applied Mathematical Modelling, 2016, 40: 2897-2912.

[16] Zheng B, Yang Y, Gao X, Zhang C. Dynamic fracture analysis of functionally graded materials under thermal shock loading by using the radial integration boundary element method [J]. Composite Structures, 2018, 201: 468-476.

[17] Griffith A. The phenomena of rupture and flow in solids [J]. Philosophical Transactions of the Royal Society, 1920, 221: 163-198.

[18] Orowan E. Fracture and strength of solids [J]. Reports on Progress in Physics, 1949, 12: 185-232.

[19] Chahine E, Laborde P, Renard Y. A reduced basis enrichment for the extended finite element method [J]. Mathematical Modelling of Natural Phenomena, 2009, 4: 88-105.

[20] Menouillard T, Réthoré J, Combescure A, Bung H. Efficient explicit time stepping for

the extended finite element method (X-FEM) [J]. International Journal for Numerical Methods in Engineering, 2010, 68: 911-939.

[21] Sukumar N, Chopp D, Moes N, Belytschko T. Modeling holes and inclusions by level sets in the extended finite-element method [J]. Computer Methods in Applied Mechanics and Engineering, 2001, 190: 6183-6200.

[22] Zhou F, Xie G, Zhang J, Zheng X. Transient heat conduction analysis of solids with small open-ended tubular cavities by boundary face method [J]. Engineering Analysis with Boundary Elements, 2013, 37: 542–550.

[23] Melenk J, Babuka I. The partition of unity finite element method: Basic theory and applications [J]. Computer Methods in Applied Mechanics and Engineering, 1996, 139: 289-314.

[24] Hughes, Thomasj. R. The finite element method : linear static and dynamic finite element analysis [M]. Prentice-Hall, 2000.

[25] Ciarlet P, Oden J. The Finite Element Method for Elliptic Problems [J]. Journal of Applied Mechanics, 1978, 45: 968-969.

[26] Zienkiewicz O, Taylor R, Fox D. The Finite Element Method for Solid and Structural Mechanics: Seventh Edition, 2013.

[27] Yagawa G, Yamada T. Free mesh method : A new meshless method [J]. Computational Mechanics, 1996, 18: 383-386.

[28] Zhang X, Song K, Lu M. Research progress and application of meshless method [J]. Chinese Journal of Computational Mechanics, 2003, 20: 730-742.

[29] Gu Y, Gao H, Chen W, Zhang C. A general algorithm for evaluating nearly singular integrals in anisotropic three-dimensional boundary element analysis [J]. Computer Methods in Applied Mechanics and Engineering, 2016, 308: 483-498.

[30] Gu Y, Zhang C. Novel special crack-tip elements for interface crack analysis by an efficient boundary element method [J]. Engineering Fracture Mechanics, 2020, 239: 107302.

[31] Yao Z. A new type of high-accuracy BEM and local stress analysis of real beam, plate and shell structures [J]. Engineering Analysis with Boundary Elements, 2016, 65: 1-17.

[32] Zhang J, Chauhan S. Fast explicit dynamics finite element algorithm for transient

heat transfer [J]. International Journal of Thermal Sciences, 2019, 139: 160-175.

[33] Zhou H, Li Y, Yu B, Chen H. Shape identification for inverse geometry heat conduction problems by FEM without iteration [J]. Numerical Heat Transfer, Part A: Applications, 2017, 72: 628-641.

[34] Li P, Liu J, Lin G, Zhang P, Yang G. A NURBS-based scaled boundary finite element method for the analysis of heat conduction problems with heat fluxes and temperatures on side-faces [J]. International Journal of Heat and Mass Transfer, 2017, 113: 764-779.

[35] Lu S, Liu J, Lin G, Zhang P. Modified scaled boundary finite element analysis of 3D steady-state heat conduction in anisotropic layered media [J]. International Journal of Heat and Mass Transfer, 2017, 108: 2462-2471.

[36] Chen L, Li X. A complex variable boundary element-free method for the Helmholtz equation using regularized combined field integral equations [J]. Applied Mathematics Letters, 2020, 101: 106067.

[37] Li X. An interpolating boundary element-free method for three-dimensional potential problems [J]. Applied Mathematical Modelling, 2015, 39: 3116-3134.

[38] Wang Q, Zhou W, Feng Y, Ma G, Cheng Y, Chang X. An adaptive orthogonal improved interpolating moving least-square method and a new boundary element-free method [J]. Applied Mathematics Computation, 2019, 353: 347-370.

[39] Wang Q, Zhou W, Cheng Y, Ma G, Chang X, Miao Y, Chen E. Regularized moving least-square method and regularized improved interpolating moving least-square method with nonsingular moment matrices [J]. Applied Mathematics and Computation, 2018, 325: 120-145.

[40] Chati M, Mukherjee S, Mukherjee Y. The boundary node method for three-dimensional linear elasticity [J]. International Journal for Numerical Methods in Engineering, 1999, 46.

[41] Gu Y, Chen W, Zhang C, He X. A meshless singular boundary method for three-dimensional inverse heat conduction problems in general anisotropic media [J]. International Journal of Heat and Mass Transfer, 2015, 84: 91-102.

[42] Li X. Meshless analysis of two-dimensional Stokes flows with the Galerkin boundary node method [J]. Engineering Analysis with Boundary Elements, 2010, 34: 79-91.

[43] Li X, Zhang S. Meshless analysis and applications of a symmetric improved Galerkin boundary node method using the improved moving least-square approximation [J]. Applied Mathematical Modelling, 2016, 40: 2875-2896.

[44] Reutskiy S. A meshless radial basis function method for 2D steady-state heat conduction problems in anisotropic and inhomogeneous media [J]. Engineering Analysis with Boundary Elements, 2016, 66: 1-11.

[45] Brebbia C. The boundary element method for engineers [M]. Pentech Press, 1978.

[46] Liao S. Boundary element method for general nonlinear differential operators [J]. Engineering Analysis with Boundary Elements, 1997, 20: 91-99.

[47] Marin L, Elliott L, Ingham DB, Lesnic D. Boundary element method for the Cauchy problem in linear elasticity [J]. Engineering Analysis with Boundary Elements, 2005, 25: 783-793.

[48] Zhou W, Liu B, Wang Q, Chang X, Chen X. Formulations of displacement discontinuity method for crack problems based on boundary element method [J]. Engineering analysis with boundary elements, 2020, 115: 86-95.

[49] Zhou W, Liu B, Wang Q, Cheng Y, Ma G, Chang X, Chen X. NURBS-enhanced boundary element method based on independent geometry and field approximation for 2D potential problems [J]. Engineering Analysis with Boundary Elements, 2017, 83: 158-166.

[50] Fu Z, Xi Q, Chen W, Cheng AH. A boundary-type meshless solver for transient heat conduction analysis of slender functionally graded materials with exponential variations [J]. Computers & Mathematics with Applications, 2018, 76: 760-773.

[51] Liu B, Zhou W, Wang Q, Chang X. An AOIMLS enhanced LIBEM and for solving 3D thermo-elastic problems and non-homogeneous heat conduction problems with heat generation [J]. International Journal of Thermal Sciences, 2021, 163: 106864.

[52] Cheng A, Cheng D. Heritage and early history of the boundary element method [J]. Engineering Analysis with Boundary Elements, 2005, 29: 268-302.

[53] Martin P. Maurice Jaswon and boundary element methods [J]. Engineering Analysis with Boundary Elements, 2012, 36: 1699-1704.

[54] Schafbuch P, Rizzo F, Thompson R. Boundary element method solutions for elastic wave scattering in 3D [J]. International Journal for Numerical Methods in

Engineering, 1993, 36: 437-455.

[55] Cruse T. Recent advances in boundary element analysis methods [J]. Computer Methods in Applied Mechanics and Engineering 1987, 62: 227-244.

[56] Cruse T. Boundary element analysis in computational fracture mechanics [M]. Springer Science & Business Media, 2012.

[57] Zhou W, Wang Q, Cheng Y, Ma G. A fast multipole method accelerated adaptive background cell-based domain integration method for evaluation of domain integrals in 3D boundary element method [J]. Engineering Analysis with Boundary Elements, 2016, 67: 1-12.

[58] Zheng B, Gao X, Zhang C. Radial integration BEM for vibration analysis of two-and three-dimensional elasticity structures [J]. Applied Mathematics and Computational 2016, 277: 111-126.

[59] Wang Q, Zhou W, Cheng Y, Ma G, Chang X. NURBS-enhanced line integration boundary element method for 2D elasticity problems with body forces [J]. Computers & Mathematics with Applications, 2019, 77: 2006-2028.

[60] Ingber M, Mammoli A, Brown M. A comparison of domain integral evaluation techniques for boundary element methods [J]. International Journal for Numerical Methods in Engineering, 2001, 52: 417-432.

[61] Nardini D, Brebbia C. A new approach to free vibration analysis using boundary elements [J]. Applied Mathematical Modelling, 1983, 7: 157-162.

[62] Zhou F, Zhang J, Sheng X, Li G. Shape variable radial basis function and its application in dual reciprocity boundary face method [J]. Engineering Analysis with Boundary Elements, 2011, 35: 244-252.

[63] Zhou F, Zhang J, Sheng X, Li G. A dual reciprocity boundary face method for 3D non-homogeneous elasticity problems [J]. Engineering Analysis with Boundary Elements, 2012, 36: 1301-1310.

[64] Schaback R. Error estimates and condition numbers for radial basis function interpolation [J]. Advances in Computational Mathematics, 1995, 3: 251-264.

[65] Bustamante C, Power H, Sua Y, Florez W. A global meshless collocation particular solution method (Integrated Radial Basis Function) for two-dimensional Stokes flow problems [J]. Applied Mathematical Modelling, 2013, 37: 4538-4547.

[66] Neves A, Brebbia C. The multiple Reciprocity boundary element method in elasticity: A new approach for transforming domain integrals to the boundary [J]. International Journal for Numerical Methods in Engineering, 2010, 31: 709-727.

[67] Nowak A, Brebbia C. The multiple-reciprocity method. A new approach for transforming BEM domain integrals to the boundary [J]. Engineering Analysis with Boundary Elements, 1989, 6: 164-167.

[68] Sladek V, Sladek J, Tanaka M. Boundary-element solution of some structural-acoustic coupling problems using the multiple reciprocity method [J]. Communications in Numerical Methods in Engineering, 2005, 10: 237-248.

[69] Safari F, Chen W. Coupling of the improved singular boundary method and dual reciprocity method for multi-term time-fractional mixed diffusion-wave equations [J]. Computers & Mathematics with Applications, 2019, 78: 1594-1607.

[70] Yan F, Jiang Q, Bai G, Li S, Li Y, Qiao Z. Dual reciprocity hybrid boundary node method for nonlinear problems [J]. Engineering Analysis with Boundary Elements, 2019, 108: 385-392.

[71] Ochiai Y. Three-dimensional steady thermal stress analysis by triple-reciprocity boundary element method [J]. International Journal for Numerical Methods in Engineering, 2005, 63: 1741-1756.

[72] Ochiai Y. Meshless thermo - elastoplastic analysis by triple - reciprocity boundary element method [J]. International Journal for Numerical Methods in Engineering, 2010, 81: 1609-1634.

[73] Gao X. Boundary element analysis in thermoelasticity with and without internal cells [J]. International Journal for Numerical Methods in Engineering, 2010, 57: 975-990.

[74] Gao X. The radial integration method for evaluation of domain integrals with boundary-only discretisation [J]. Engineering Analysis with Boundary Elements, 2002, 26: 905-916.

[75] Gao X, Zheng B, Yang K, Zhang C. Radial integration BEM for dynamic coupled thermoelastic analysis under thermal shock loading [J]. Computers and Structures, 2015, 158: 140-147.

[76] Cui M, Xu B, Feng W, Zhang Y, Gao X, Peng H. A radial integration boundary element method for solving transient heat conduction problems with heat sources and variable

thermal conductivity [J]. Numerical Heat Transfer, Part B: Fundamentals, 2018, 73: 1-18.

[77] Wang Q, Zhou W, Cheng Y, Ma G, Chang X. A line integration method for the treatment of 3D domain integrals and accelerated by the fast multipole method in the BEM [J]. Computational Mechanics, 2016, 59: 611-624.

[78] Wang Q, Zhou W, Cheng Y, Ma G, Chang X. Line integration method for treatment of domain integrals in 3D boundary element method for potential and elasticity problems [J]. Engineering Analysis with Boundary Elements, 2017, 75: 1-11.

[79] Elliotis M, Georgiou G, Xenophontos C. Solving Laplacian problems with boundary singularities: A comparison of a singular function boundary integral method with the p/hp version of the finite element method [J]. Applied Mathematics Computation, 2005, 169: 485-499.

[80] Ervin V, Stephan E. A boundary element Galerkin method for a hypersingular integral equation on open surfaces [J]. Mathematical Methods in the Applied Sciences, 2010, 13: 281-289.

[81] Kalaichelvan S, Lavers J. A sub-triangulation method to improve the accuracy of singular integral evaluation in 3-D boundary element methods [J]. IEEE Transactions on Magnetics, 2002, 24: 2515-2517.

[82] Liao H, Xu Z. A method for direct evaluation of singular integral in direct boundary element method [J]. International Journal for Numerical Methods in Engineering, 2010, 35: 1473-1485.

[83] Makarov SN, Noetscher GM, Raij T, Nummenmaa A. A quasi-static boundary element approach with fast multipole acceleration for high-resolution bioelectromagnetic models [J]. IEEE Transactions on Biomedical Engineering, 2018, 65: 2675-2683.

[84] Qu W, Chen W, Fu Z, Gu Y. Fast multipole singular boundary method for Stokes flow problems [J]. Mathematics and Computers in Simulation, 2018, 146: 57-69.

[85] Qu W, Chen W, Zheng C. Diagonal form fast multipole singular boundary method applied to the solution of high - frequency acoustic radiation and scattering [J]. International Journal for Numerical Methods in Engineering, 2017, 111: 803-815.

[86] Takahashi T, Coulier P, Darve E. Application of the inverse fast multipole method as a preconditioner in a 3D Helmholtz boundary element method [J]. Journal of

Computational Physics, 2017, 341: 406-428.

[87] Lacerda L, Wrobel L. Dual boundary element method for axisymmetric crack analysis [J]. International Journal of Fracture, 2002, 113: 267-284.

[88] ÈllerP P, Haas M, Kuhn G. Comparison of the basic and the discontinuity formulation of the 3D-dual boundary element meth [J]. International Journal for Numerical Methods in Engineering, 2000, 24: 777-788.

[89] Portela A, Aliabadi M. The dual boundary element method Effective implementation for crack problems [J]. International Journal for numerical methods in engineering, 1992, 33: 1269-1287.

[90] Blandford G, Ingraffea A, Liggett J. Two-dimensional stress intensity factor computations using the boundary element method [J]. International Journal for Numerical Methods in Engineering, 2010, 17: 387-404.

[91] Fontes E, Santiago J, Telles J. On a regularized method of fundamental solutions coupled with the numerical Green's function procedure to solve embedded crack problems [J]. Engineering Analysis with Boundary Elements, 2013, 37: 1-7.

[92] Vera T, Telles J. A numerical Green's function and dual reciprocity BEM method to solve elastodynamic crack problems [J]. Engineering Analysis with Boundary Elements, 2005, 29: 204-209.

[93] Takumi S, Katsuhiko K, Yuzo O, Katsuhiko S. Applicability of displacement discontinuity method to crack problems [J]. Shigen-to-Sozai, 1989, 105: 981-986.

[94] Chen W, Chen T. An efficient dual boundary element technique for a two-dimensional fracture problem with multiple cracks [J]. International Journal for Numerical Methods in Engineering, 1995, 38: 1739-1756.

[95] Romlay F, Ouyang H, Ariffin A, Mohamed N. Modeling of fatigue crack propagation using dual boundary element method and Gaussian Monte Carlo method [J]. Engineering Analysis with Boundary Elements, 2010, 34: 297-305.

[96] Crouch S. Solution of plane elasticity problems by the displacement discontinuity method. I. Infinite body solution [J]. International Journal for Numerical Methods in Engineering, 1976, 10: 301-343.

[97] Liu Y, Li Y. Revisit of the equivalence of the displacement discontinuity method and boundary element method for solving crack problems [J]. Engineering Analysis with

Boundary Elements, 2014, 47: 64-67.

[98] Junping P, Yao Z. Study for 2D moving contact elastic body with closed crack using BEM [J]. Acta Mechanica Sinica, 2003, 19: 340-346.

[99] Erba D, Aliabadi M. BEM analysis of fracture problems in three-dimensional thermoelasticity using J -integral [J]. International Journal of Solids and Structures, 2001, 38: 4609-4630.

[100] Ekhlakov A, Khay O, Zhang C, Sladek J, Sladek V, Gao X. Thermoelastic crack analysis in functionally graded materials and structures by a BEM [J]. Fatigue Fracture of Engineering Materials Structures, 2012, 35: 742-766.

[101] Denda M, Kosaka I. Dislocation and point - force - based approach to the special Green's Function BEM for elliptic hole and crack problems in two dimensions [J]. International Journal for Numerical Methods in Engineering, 2015, 40: 2857-2889.

[102] Triantafyllidis T. 3-D time domain BEM using half-space Green's functions [J]. Engineering Analysis with Boundary Elements, 1991, 8: 115-124.

[103] Gómez J, Powert H. A multipole direct and indirect BEM for 2D cavity flow at low Reynolds number [J]. Engineering Analysis with Boundary Elements, 1997, 19: 17-31.

[104] Karabalis D, Rizosd D. An advanced direct time domain BEM formulation for general 3-D elastodynamic problems [J]. Computational Mechanics, 1994, 15: 249-269.

[105] Ahmed M, Lavers J. Constrained indirect BEM for eddy current calculations in multiple conductor TM induction problems [J]. IEEE Transactions on Magnetics 1989, 25: 3946-3948.

[106] Bonnet M. Exploiting partial or complete geometrical symmetry in 3D symmetric Galerkin indirect BEM formulations [J]. International Journal for Numerical Methods in Engineering, 2010, 57: 1053-1083.

[107] Ghassemi A, Cheng H, Diek A, JC R. Complete plane strain fictitious stress boundary element method for poroelastic media [J]. Engineering Analysis with Boundary Elements, 2001, 25: 41-48.

[108] Ghassemi A, Zhang Q. A transient fictitious stress boundary element method for porothermoelastic media [J]. Engineering Analysis with Boundary Elements, 2004, 28: 1363-1373.

[109] Liu C, Mizuta Y, Kuriyama K. Analytical Integrations for Three-dimensional

Fictitious Stress Method Based on Kelvin Solution [J]. Shigen-to-Sozai, 1999, 115: 719-724.

[110] Phan A, Napier J, Gray L, Kaplan T. Symmetric-Galerkin BEM simulation of fracture with frictional contact [J]. International Journal for Numerical Methods in Engineering, 2008, 57: 835-851.

[111] Budiansky B, Rice J. An integral equation for dynamic elastic response of an isolated 3-D crack [J]. Wave Motion, 1979, 1: 187-191.

[112] Guiggiani M, Krishnasamy G, Rudolphi T, Rizzo F. A general algorithm for the numerical solution of hypersingular boundary integral equations [J]. Journal of Applied Mechanics, 1992, 59: 604-614.

[113] Lachat J, Watson J. Effective numerical treatment of boundary integral equations: A formulation for three - dimensional elastostatics [J]. International Journal for Numerical Methods in Engineering, 2010, 10: 991-1005.

[114] Wang Q, Zhou W, Feng Y. The phase-field model with an auto-calibrated degradation function based on general softening laws for cohesive fracture [J]. Applied Mathematical Modelling, 2020, 86: 185-206.

[115] Wang Q, Feng Y, Zhou W, Cheng Y, Ma G. A phase-field model for mixed-mode fracture based on a unified tensile fracture criterion [J]. Computer Methods in Applied Mechanics and Engineering, 2020, 370: 113270.

[116] De Belie N, Gruyaert E, Al - Tabbaa A, Antonaci P, Baera C, Bajare D, Darquennes A, Davies R, Ferrara L, Jefferson T. A review of self - healing concrete for damage management of structures [J]. Advanced Materials Interfaces, 2018, 5: 1800074.

[117] Shi J, Liu B, Zhou F, Shen S, Dai J, Ji R, Tan J. Heat damage of concrete surfaces under steam curing and improvement measures [J]. Construction and Building Materials, 2020, 252: 119104.

[118] Sekiya OT. Steady heat conduction analysis by improved multiple-reciprocity boundary element method [J]. Engineering Analysis with Boundary Elements, 1996, 18: 111-117.

[119] Cui M, Peng H, Xu B, Gao X, Zhang Y. A new radial integration polygonal boundary element method for solving heat conduction problems [J]. International Journal of Heat and Mass Transfer, 2018, 123: 251-260.

[120] Barbarino M, Bianco D. A BEM–FMM approach applied to the combined convected Helmholtz integral formulation for the solution of aeroacoustic problems [J]. Computer Methods in Applied Mechanics and Engineering, 2018, 342: 585-603.

[121] Liu Y, Li Y, Xie W. Modeling of multiple crack propagation in 2-D elastic solids by the fast multipole boundary element method [J]. Engineering Fracture Mechanics, 2017, 172: 1-16.

[122] Wang Q, Zhou W, Cheng Y, Ma G, Chang X, Liu B. A NURBS-enhanced improved interpolating boundary element-free method for 2D potential problems and accelerated by fast multipole method [J]. Engineering Analysis with Boundary Elements, 2019, 98: 126-136.

[123] Chen L, Marburg S, Zhao W, Liu C, Chen H. Implementation of isogeometric fast multipole boundary element methods for 2D half-space acoustic scattering problems with absorbing boundary condition [J]. Journal of Theoretical and Computational Acoustics, 2019, 27: 1850024.

[124] Chen L, Zhao W, Liu C, Chen H, Marburg S. Isogeometric fast multipole boundary element method based on burton-miller formulation for 3D acoustic problems [J]. Archives of Acoustics, 2019, 44.

[125] Liu Z, Sun S, Cheng AH, Wang Y. A fast multipole accelerated indirect boundary element method for broadband scattering of elastic waves in a fluid - saturated poroelastic domain [J]. International Journal for Numerical and Analytical Methods in Geomechanics, 2018, 42: 2133-2160.

[126] Rezaei A, Siddiqui F, Bornia G, Soliman M. Applications of the fast multipole fully coupled poroelastic displacement discontinuity method to hydraulic fracturing problems [J]. Journal of Computational Physics, 2019, 399: 108955.

[127] Wang Q, Zhou W, Cheng Y, Ma G, Chang X. A line integration method for the treatment of 3D domain integrals and accelerated by the fast multipole method in the BEM [J]. Computational Mechanics, 2017, 59: 611-624.

[128] Ahmad MH, Kasilingam DP. Spectral domain fast multipole method for solving integral equations of electromagnetic wave scattering [J]. Progress In Electromagnetics Research, 2019, 80: 121-131.

[129] Ren Z, Tang J, Kalscheuer T, Maurer H. Fast 3 - D large - scale gravity and

magnetic modeling using unstructured grids and an adaptive multilevel fast multipole method [J]. Journal of Geophysical Research: Solid Earth, 2017, 122: 79-109.

[130] Feng W, Gao L, Du J, Qian W, Gao X. A meshless interface integral BEM for solving heat conduction in multi-non-homogeneous media with multiple heat sources [J]. International Communications in Heat and Mass Transfer, 2019, 104: 70-82.

[131] Dölz J, Harbrecht H, Kurz S, Schöps S, Wolf F. A fast isogeometric BEM for the three dimensional Laplace-and Helmholtz problems [J]. Computer Methods in Applied Mechanics and Engineering, 2018, 330: 83-101.

[132] Kpadonou F, Chaillat S, Ciarlet Jr P. On the efficiency of nested GMRES preconditioners for 3D acoustic and elastodynamic H-matrix accelerated Boundary Element Methods [J]. Computers & Mathematics with Applications, 2020, 80: 471-489.

[133] Liegeois K, Boman R, Phipps ET, Wiesner TA, Arnst M. GMRES with embedded ensemble propagation for the efficient solution of parametric linear systems in uncertainty quantification of computational models [J]. Computer Methods in Applied Mechanics and Engineering, 2020, 369: 113188.

[134] Gao X, Huang S, Cui M, Ruan B, Zhu Q, Yang K, Lv J, Peng H. Element differential method for solving general heat conduction problems [J]. International Journal of Heat and Mass Transfer, 2017, 115: 882-894.

[135] Tong Y. High precision solution for thermo-elastic equations using stable node-based smoothed finite element method [J]. Applied Mathematics Computation, 2018, 336: 272-287.

[136] Zhou L, Li M, Ma Z, Ren S, Li X, Tang J, Ma Z. Steady-state characteristics of the coupled magneto-electro-thermo-elastic multi-physical system based on cell-based smoothed finite element method [J]. Composite Structures, 2019, 219: 111-128.

[137] Jaśkowiec J, Milewski S. Coupling finite element method with meshless finite difference method in thermomechanical problems [J]. Computers & Mathematics with Applications, 2016, 72: 2259-2279.

[138] Sun Y, He S. A meshless method based on the method of fundamental solution for three-dimensional inverse heat conduction problems [J]. International Journal of Heat and Mass Transfer, 2017, 108: 945-960.

[139] Zheng B, Lin J, Chen W. Simulation of heat conduction problems in layered materials using the meshless singular boundary method [J]. Engineering Analysis with Boundary Elements, 2019, 100: 88-94.

[140] Gu Y, Gao H, Chen W, Zhang C. A general algorithm for evaluating nearly singular integrals in anisotropic three-dimensional boundary element analysis [J]. Computer Methods in Applied Mechanics Engineering, 2016, 308: 483-498.

[141] Gao X. A meshless BEM for isotropic heat conduction problems with heat generation and spatially varying conductivity [J]. International journal for numerical methods in engineering, 2006, 66: 1411-1431.

[142] Yang K, Peng H, Cui M, Gao X. New analytical expressions in radial integration BEM for solving heat conduction problems with variable coefficients [J]. Engineering Analysis with Boundary Elements, 2015, 50: 224-230.

[143] Peng H, Cui M, Yang K, Gao X. Radial integration BEM for steady convection-conduction problem with spatially variable velocity and thermal conductivity [J]. International Journal of Heat and Mass Transfer, 2018, 126: 1150-1161.

[144] Yang K, Wang J, Du J, Peng H, Gao X. Radial integration boundary element method for nonlinear heat conduction problems with temperature-dependent conductivity [J]. International Journal of Heat and Mass Transfer, 2017, 104: 1145-1151.

[145] Dehghan M, Safarpoor M. Application of the dual reciprocity boundary integral equation approach to solve fourth-order time-fractional partial differential equations [J]. International Journal of Computer Mathematics, 2018, 95: 2066-2081.

[146] Soares Jr R, Palermo Jr L, Wrobel L. Application of the dual reciprocity method for the buckling analysis of plates with shear deformation [J]. Engineering Analysis with Boundary Elements, 2019, 106: 427-439.

[147] Zhou F, You Y, Li G, Xie G. The precise integration method for semi-discretised equation in the dual reciprocity method to solve three-dimensional transient heat conduction problems [J]. Engineering Analysis with Boundary Elements, 2018, 95: 160-166.

[148] Fu ZJ, Yang LW, Xi Q, Liu CS. A boundary collocation method for anomalous heat conduction analysis in functionally graded materials [J]. Computers Mathematics with Applications, 2020.

[149] Xi Q, Fu Z, Alves C, Ji H. A semi-analytical boundary collocation solver for the inverse Cauchy problems in heat conduction under 3D FGMs with heat source [J]. Numerical Heat Transfer, Part B: Fundamentals, 2019, 76: 1-17.

[150] Xi Q, Fu ZJ, Rabczuk T. An efficient boundary collocation scheme for transient thermal analysis in large-size-ratio functionally graded materials under heat source load [J]. Computational Mechanics, 2019, 64: 1221-1235.

[151] Huang C, Chin S. A two-dimensional inverse problem in imaging the thermal conductivity of a non-homogeneous medium [J]. International Journal of Heat and Mass Transfer, 2000, 43: 4061-4071.

[152] Li X, Li S. On the augmented moving least squares approximation and the localized method of fundamental solutions for anisotropic heat conduction problems [J]. Engineering Analysis with Boundary Elements, 2020, 119: 74-82.

[153] Wang J, Wang J, Sun F, Cheng Y. An Interpolating Boundary Element-Free Method with Nonsingular Weight Function for Two-Dimensional Potential Problems [J]. International Journal of Computational Methods, 2013, 10.

[154] Wang JF, Sun FX. A Meshless Method Based on the Improved Interpolating Moving Least-Squares Method for the Regularized Long Wave Equation [J]. Applied Mechanics and Materials, 2011, 101-102: 467-470.

[155] Fasshauer G. Dual bases and discrete reproducing kernels: a unified framework for RBF and MLS approximation [J]. Engineering Analysis with Boundary Elements, 2005, 29: 313-325.

[156] Xie H, Li D. A meshless method for Burgers' equation using MQ-RBF and high-order temporal approximation [J]. Applied Mathematical Modelling, 2013, 37: 9215-9222.

[157] Feng W, Yang K, Cui M, Gao X. Analytically-integrated radial integration BEM for solving three-dimensional transient heat conduction problems [J]. International Communications in Heat and Mass Transfer, 2016.

[158] Hu H, Ding F. An iterative least squares estimation algorithm for controlled moving average systems based on matrix decomposition [J]. Applied Mathematics Letters, 2012, 25: 2332-2338.

[159] Li X. Error estimates for the moving least-square approximation and the element-free Galerkin method in n-dimensional spaces [J]. Applied Numerical Mathematics,

2016, 99: 77-97.

[160] Li X, Li S. On the stability of the moving least squares approximation and the element-free Galerkin method [J]. Computers & Mathematics with Applications, 2016, 72: 1515-1531.

[161] Lancaster P, Salkauskas K. Surfaces generated by moving least squares methods [J]. Mathematics of Computation, 1981, 37: 141-158.

[162] Wang Q, Zhou W, Feng Y, Ma G, Cheng Y, Chang X. An adaptive orthogonal improved interpolating moving least-square method and a new boundary element-free method [J]. Applied Mathematics and Computation, 2019, 353: 347-370.

[163] Chowdhury H, Wittek A, Miller K, Joldes G. An element free Galerkin method based on the modified moving least squares approximation [J]. Journal of Scientific Computing, 2017, 71: 1197-1211.

[164] Joldes GR, Chowdhury H, Wittek A, Doyle B, Miller K. Modified moving least squares with polynomial bases for scattered data approximation [J]. Applied mathematics and Computation, 2015, 266: 893-902.

[165] Mirzaei D. Analysis of moving least squares approximation revisited [J]. Journal of Computational and Applied Mathematics, 2015, 282: 237-250.

[166] Adineh M, Kadkhodayan M. Three-dimensional thermo-elastic analysis and dynamic response of a multi-directional functionally graded skew plate on elastic foundation [J]. Composites Part B: Engineering, 2017, 125: 227-240.

[167] Benner P, Herzog R, Lang N, Riedel I, Saak J. Comparison of model order reduction methods for optimal sensor placement for thermo-elastic models [J]. Engineering Optimization, 2019, 51: 465-483.

[168] Deng S, Suresh K. Topology optimization under thermo-elastic buckling [J]. Structural Multidisciplinary Optimization, 2017, 55: 1759-1772.

[169] Yan F, Pan PZ, Feng XT, Li SJ, Jiang Q. A novel fast overrelaxation updating method for continuous-discontinuous cellular automaton [J]. Applied Mathematical Modelling, 2019, 66: 156-174.

[170] Yan F, Feng XT, Lv JH, Pan PZ, Li SJ. Continuous-discontinuous cellular automaton method for cohesive crack growth in rock [J]. Engineering Fracture Mechanics, 2018, 188: 361-380.

[171] Wang Q, Feng Y, Zhou W, Cheng Y, Ma G. A phase-field model for mixed-mode fracture based on a unified tensile fracture criterion [J]. Computer Methods in Applied Mechanics and Engineering, 2020, 370.

[172] Miao Y, He T, Luo H, Zhu H. Dual hybrid boundary node method for solving transient dynamic fracture problems [J]. Computer Modeling in Engineering & Sciences, 2012, 85: 481-498.

[173] Miao Y, He T, Yang Q, Zheng J. Multi-domain hybrid boundary node method for evaluating top-down crack in Asphalt pavements [J]. Engineering Analysis with Boundary Elements, 2010, 34: 755-760.

[174] Wang Q, Miao Y, Zheng J. The hybrid boundary node method accelerated by fast multipole expansion technique for 3D elasticity [J]. Computer Modeling in Engineering and Sciences, 2010, 70: 123.

[175] Zhou F, Xie G, Zhang J, Zheng X. Transient heat conduction analysis of solids with small open-ended tubular cavities by boundary face method [J]. Engineering Analysis with Boundary Elements, 2013, 37: 542-550.

[176] Chen L, Li X. A complex variable boundary element-free method for the Helmholtz equation using regularized combined field integral equations [J]. Applied Mathematics Letters, 2020, 101.

[177] Wang Q, Zhou W, Feng YT, Ma G, Cheng Y, Chang X. An adaptive orthogonal improved interpolating moving least-square method and a new boundary element-free method [J]. Applied Mathematics and Computation, 2019, 353: 347-370.

[178] Liu Z, Liang J, Huang Y, Liu L. IBIEM modelling of the amplification of seismic waves by a three-dimensional layered alluvial basin [J]. Geophysical Journal International, 2015, 204: 999-1023.

[179] Liu Z, Liu L, Liang J, Zhou Y. An indirect boundary element method to model the 3-D scattering of elastic waves in a fluid-saturated poroelastic half-space [J]. Engineering Analysis with Boundary Elements, 2016, 66: 91-108.

[180] Anflor C. Optimization applied to dynamic poroelasticity using boundary element method (BEM) and genetic algorithm (GA) [J]. Research on Engineering Structures and Materials, 2018, 4.

[181] Chen B, Chen W, Cheng AH, Wei X. The singular boundary method for two-

dimensional static thermoelasticity analysis [J]. Computers Mathematics with Applications, 2016, 72: 2716-2730.

[182] Dobroskok AA, Linkov AM. CV BEM for 2D transient thermo-(poro-) elastic problems concerning with blocky systems with singular points and lines of discontinuities [J]. International Journal of Engineering Science, 2010, 48: 658-669.

[183] Zhang YM, Qu WZ, Chen JT. BEM analysis of thin structures for thermoelastic problems [J]. Engineering Analysis with Boundary Elements, 2013, 37: 441-452.

[184] Gao X. Boundary element analysis in thermoelasticity with and without internal cells [J]. International Journal for Numerical Methods in Engineering, 2003, 57: 975-990.

[185] Nowak A, Brebbia C. The multiple-reciprocity method. A new approach for transforming BEM domain integrals to the boundary [J]. Engineering Analysis with Boundary Elements, 1989, 6: 164-167.

[186] Wen P, Aliabadi M, Young A. Transformation of domain integrals to boundary integrals in BEM analysis of shear deformable plate bending problems [J]. Computational Mechanics, 1999, 24: 304-309.

[187] Yang L, Albregtsen F, Taxt T. Fast computation of three-dimensional geometric moments using a discrete divergence theorem and a generalization to higher dimensions [J]. Graphical Models Image Processing, 1997, 59: 97-108.

[188] Melo Í, Pujals E. A divergence theorem for non-compact Riemannian manifolds: a dynamical approach [J]. Nonlinearity, 2019, 32: 1125-1145.

[189] Wang Q, Zhou W, Cheng Y, Ma G, Chang X, Huang Q. The boundary element method with a fast multipole accelerated integration technique for 3D elastostatic problems with arbitrary body forces [J]. Journal of Scientific Computing, 2017, 71: 1238-1264.

[190] Wang Q, Zhou W, Cheng Y, Ma G, Chang X. NURBS-enhanced line integration boundary element method for 2D elasticity problems with body forces [J]. Computers Mathematics with Applications, 2019, 77: 2006-2028.

[191] Wang Q, Zhou W, Cheng Y, Ma G, Chang X, Huang Q. An adaptive cell-based domain integration method for treatment of domain integrals in 3D boundary element method for potential and elasticity problems [J]. Acta Mechanica Solida Sinica, 2017,

30: 99-111.

[192] Ying L, Biros G, Zorin D. A kernel-independent adaptive fast multipole algorithm in two and three dimensions [J]. Journal of Computational Physics, 2004, 196: 591-626.

[193] Wang Q, Zhou W, Cheng Y, Ma G, Chang X, Chen E. A fast boundary integral equation method for point location problem [J]. Engineering Analysis with Boundary Elements, 2018, 87: 9-18.

[194] Li S, Trevelyan J, Zhang W, Wang D. Accelerating isogeometric boundary element analysis for 3 - dimensional elastostatics problems through black - box fast multipole method with proper generalized decomposition [J]. International Journal for Numerical Methods in Engineering, 2018, 114: 975-998.

[195] Simpson RN, Bordas SP, Trevelyan J, Rabczuk T. A two-dimensional isogeometric boundary element method for elastostatic analysis [J]. Computer Methods in Applied Mechanics and Engineering, 2012, 209: 87-100.

[196] Wang Q, Zhou W, Cheng Y, Ma G, Chang X, Chen E. NE-IIBEFM for problems with body forces: A seamless integration of the boundary type meshfree method and the NURBS boundary in CAD [J]. Adv Eng Softw, 2018, 118: 1-17.

[197] Gu J, Zhang J, Li G. Isogeometric analysis in BIE for 3-D potential problem [J]. Engineering Analysis with Boundary Elements, 2012, 36: 858-865.

[198] Keuchel S, Hagelstein NC, Zaleski O. Evaluation of hypersingular and nearly singular integrals in the Isogeometric Boundary Element Method for acoustics [J]. Computer Methods in Applied Mechanics and Engineering, 2017, 325: 488-504.

[199] Peake MJ, Trevelyan J, Coates G. Extended isogeometric boundary element method (XIBEM) for two-dimensional Helmholtz problems [J]. Computer Methods in Applied Mechanics and Engineering, 2013, 259: 93-102.

[200] Powell MJ. Algorithms for nonlinear constraints that use Lagrangian functions [J]. Mathematical Programming, 1978, 14: 224-248.

[201] Simpson RN, Scott MA, Taus M, Thomas DC, Lian H. Acoustic isogeometric boundary element analysis [J]. Computer Methods in Applied Mechanics and Engineering, 2014, 269: 265-290.

[202] Liu Y, Li Y, Huang S. A fast multipole boundary element method for solving two-dimensional thermoelasticity problems [J]. Computational Mechanics, 2014, 54: 821-

831.

[203] Gao X. Boundary element analysis in thermoelasticity with and without internal cells [J]. International Journal for Numerical Methods in Engineering, 2003, 57: 975-990.

[204] Zhang Y, Qu W, Chen J. BEM analysis of thin structures for thermoelastic problems [J]. Engineering Analysis with Boundary Elements, 2013, 37: 441-452.

[205] Chen J, Liu Z, Zou Z. The central crack problem for a functionally graded piezoelectric strip [J]. International Journal of Fracture, 2003, 121: 81-94.

[206] Xie G, Zhou F, Zhang D, Wen X, Li H. A novel triangular boundary crack front element for 3D crack problems based on 8-node serendipity element [J]. Engineering Analysis with Boundary Elements, 2019, 105: 296-302.

[207] Xie G, Zhou F, Zhang D, Zhai H, Cui G. Construction of special shape functions for triangular elements with one edge lying in the crack front [J]. Engineering Analysis with Boundary Elements, 2018, 91: 14-23.

[208] Liu Y. Analysis of shell - like structures by the boundary element method based on 3 - D elasticity: formulation and verification [J]. International Journal for Numerical Methods in Engineering, 1998, 41: 541-558.

[209] Xie G, Zhang D, Meng F, Du W, Zhang J. Calculation of stress intensity factor along the 3D crack front by dual BIE with new crack front elements [J]. Acta Mechanica, 2017, 228: 3135-3153.

[210] Feng S, Han XJCMiAM, Engineering. A novel multi-grid based reanalysis approach for efficient prediction of fatigue crack propagation [J]. 2019, 353: 107-122.

[211] Miao Y, He T, Yang Q, Zheng JJEAwBE. Multi-domain hybrid boundary node method for evaluating top-down crack in asphalt pavements [J]. 2010, 34: 755-760.

[212] Yu M, He T, Hui L, Zhu HJCMiE, Sciences. Dual Hybrid Boundary Node Method for Solving Transient Dynamic Fracture Problems [J]. 2012, 85: 481-498.

[213] Yan F, Pan P, Feng X, Li S. The continuous-discontinuous cellular automaton method for elastodynamic crack problems [J]. Engineering Fracture Mechanics, 2018, 204: 482-496.

[214] Yan F, Pan P, Feng X, Li S, Jiang Q. A novel fast overrelaxation updating method for continuous-discontinuous cellular automaton [J]. Applied Mathematical Modelling,

2019, 66: 156-174.

[215] Youtian Z, Lei W, Ping C. The correction for indirect boundary element method in elastostatics [J]. Engineering Mechanics, 1987, 4: 1-6.

[216] Lacerda L, Wrobel L. Dual boundary element method for axisymmetric crack analysis [J]. International Journal of Fracture, 2002, 113: 267-284.

[217] Partheymüller P, Haas M, Kuhn G. Comparison of the basic and the discontinuity formulation of the 3D-dual boundary element method [J]. Engineering Analysis with Boundary Elements, 2000, 24: 777-788.

[218] Portela A, Aliabadi M, Rooke D. The dual boundary element method: effective implementation for crack problems [J]. International Journal for Numerical Methods in Engineering, 1992, 33: 1269-1287.

[219] Chen W, Chen T. An efficient dual boundary element technique for a two - dimensional fracture problem with multiple cracks [J]. International Journal for Numerical Methods in Engineering, 1995, 38: 1739-1756.

[220] Romlay F, Ouyang H, Ariffin A, Mohamed N. Modeling of fatigue crack propagation using dual boundary element method and Gaussian Monte Carlo method [J]. Engineering Analysis with Boundary Elements, 2010, 34: 297-305.

[221] Li R, Chudnovsky A. The stress intensity factor Green's function for a crack interacting with a circular inclusion [J]. International Journal of Fracture, 1994, 67: 169-177.

[222] Zhuang X, Cai Y, Augarde C. A meshless sub-region radial point interpolation method for accurate calculation of crack tip fields [J]. Theoretical and Applied Fracture Mechanics, 2014, 69: 118-125.

[223] Crouch S. Solution of plane elasticity problems by the displacement discontinuity method. I. Infinite body solution [J]. International Journal for Numerical Methods in Engineering, 1976, 10: 301-343.

[224] Guiggiani M, Krishnasamy G, Rudolphi T, Rizzo F. A general algorithm for the numerical solution of hypersingular boundary integral equations [J]. Journal of Applied Mechanics, 1992, .59(3): 604-614.

[225] GC S. Handbook of stress-intensity factors. Handbook of stress-intensity factors [M]. Science Press, 1973.

[226] Liu Q, Zhang P, Cheng S, Niu J, Liu D. Heat transfer and thermo-elastic analysis of copper steel composite stave [J]. International Journal of Heat and Mass Transfer, 2016, 103: 341-348.

[227] Yang W, Chen Z. Investigation of the thermal-elastic problem in cracked semi-infinite FGM under thermal shock using hyperbolic heat conduction theory [J]. Journal of Thermal Stresses, 2019, 42: 993-1010.

[228] Gu Y, Chen W, Zhang C. Singular boundary method for solving plane strain elastostatic problems [J]. International Journal of Solids and Structures, 2011, 48: 2549-2556.

[229] Ibanez M, Power H. An efficient direct BEM numerical scheme for phase change problems using Fourier series [J]. Computer Methods in Applied Mechanics and Engineering, 2002, 191: 2371-2402.

[230] Yan F, Feng X, Zhou H. Dual reciprocity hybrid radial boundary node method for the analysis of Kirchhoff plates [J]. Applied mathematical modelling, 2011, 35: 5691-5706.

[231] Yan F, Lv J, Feng X, Pan P. A new hybrid boundary node method based on Taylor expansion and the Shepard interpolation method [J]. International Journal for Numerical Methods in Engineering, 2015, 102: 1488-1506.

[232] Chen L, Liu X, Li X. The boundary element-free method for 2D interior and exterior Helmholtz problems [J]. Computers & Mathematics with Applications, 2019, 77: 846-864.

[233] Qu W. A high accuracy method for long-time evolution of acoustic wave equation [J]. Applied Mathematics Letters, 2019, 98: 135-141.

[234] Gu Y, Chen W, He X. Singular boundary method for steady-state heat conduction in three dimensional general anisotropic media [J]. International Journal of Heat and Mass Transfer, 2012, 55: 4837-4848.

[235] Wang F, Hua Q, Liu C. Boundary function method for inverse geometry problem in two-dimensional anisotropic heat conduction equation [J]. Applied Mathematics Letters, 2018, 84: 130-136.

[236] Chen J, Liu Z, Zou Z. The central crack problem for a functionally graded piezoelectric strip [J]. International Journal of Fracture, 2003, 121: 81-94.

[237] Liu Y. Analysis of shell-like structures by the Boundary Element Method based on 3-

D elasticity: formulation and verification [J]. International Journal for Numerical Methods in Engineering, 41: 541-558.

[238] Xie G, Zhang D, Meng F, Du W, Zhang J. Calculation of stress intensity factor along the 3D crack front by dual BIE with new crack front elements [J]. Acta Mechanica Solida Sinica, 2017, 228: 3135-3153.

[239] Liu Y. On the displacement discontinuity method and the boundary element method for solving 3-D crack problems [J]. Engineering Fracture Mechanics, 2016, 164: 35-45.

[240] Garcia S, Zhang C, Sladek J, Sladek V. 2D transient dynamic crack analysis in piezoelectric solids by BEM [J]. Computational Materials Science, 2007, 39: 179-186.

[241] Wang T, Ye X, Liu Z, Liu X, Chu D, Zhuang Z. A phase-field model of thermo-elastic coupled brittle fracture with explicit time integration [J]. Computational Mechanics, 2020, : 1-17.

[242] Najibi A, Talebitooti R. Nonlinear transient thermo-elastic analysis of a 2D-FGM thick hollow finite length cylinder [J]. Composites Part B: Engineering, 2017, 111: 211-227.

[243] Ghosh D, Lahiri A, Abbas IA. 32. Two-dimensional generalized thermo-elastic problem for anisotropic half-space [J]. Journal of Mathematical Models in Engineering, 2017, 3: 27-41.

[244] Gao X. Boundary element analysis in thermoelasticity with and without internal cells [J]. International Journal for Numerical Methods in Engineering, 57: 975-990.

[245] Demirbas MD. Thermal stress analysis of functionally graded plates with temperature-dependent material properties using theory of elasticity [J]. Composites Part B: Engineering, 2017, 131: 100-124.

[246] Chowdhury HA, Joldes GR, Wittek A, Doyle B, Pasternak E, Miller K. Implementation of a modified moving least squares approximation for predicting soft tissue deformation using a meshless method. Computational Biomechanics for Medicine. 59-71 2015.

[247] Wang C, Tang T. Recursive least squares estimation algorithm applied to a class of linear-in-parameters output error moving average systems [J]. Applied Mathematics Letters, 2014, 29: 36-41.

[248] Mukhopadhyay N, Maiti S, Kakodkar A. Effect of modelling of traction and thermal

singularities on accuracy of SIFs computation through modifed crack closure integral in BEM [J]. Engineering Fracture Mechanics, 1999, 64: 141-159.

[249] Sethuraman R. Analytical and fnite element studies on two dimensional panels with doubly bonded rectangular finite crack stiffeners [J]. PhD thesis, Department of Mechanical Engineering, IIT, Bombay, India, 1989.

[250] Rooke D, Cartwright D. Compendium of stress intensity factors [J]. London: HMSO, 1976.

[251] Sumi N, Katayama T. Thermal stress singularities at tips of a Griffith crack in a fnite rectangular plate [J]. Nuclear Engineering and Design, 1980, 60: 389-394.

[252] Mukhopadhyay N, Maiti S, Kakodkar A. Modified crack closure integral based computation of stress intensity factors for 2-D thermoelastic problems through boundary element method [J]. Nuclear engineering and design, 1999, 187 (3): 277-290.

[253] Bagherzadeh K, Mirghasemi A, Mohammadi S. Numerical simulation of particle breakage of angular particles using combined DEM and FEM [J]. Powder Technology, 2011, 205: 15-29.

[254] Lade P, Yamamuro J. Undrained sand behavior in axisymmetric tests at high pressures [J]. Journal of Geotechnical Engineering, 1997, 122: 120-129.

[255] Sulem J, Ouffroukh H. Shear-banding in drained and undrained triaxial tests on a saturated sandstone; porosity and permeability evolution [J]. International Journal of Rock Mechanics Mining Sciences, 2007, 43: 292-310.

[256] Hosseininia E, Mirghasemi A. Numerical simulation of breakage of two-dimensional polygon-shaped particles using discrete element method [J]. Powder Technology, 2006, 166: 100-112.

[257] Luís M, Chagas A. A stochastic particle replacement strategy for simulating breakage in DEM [J]. Powder Technology, 2021, 377: 222-232.

[258] Xu K, Zhou W, Ma G, Chang X, Yang L. Review of particle breakage simulation based on DEM [J]. Chinese Journal of Geotechnical Engineering, 2018, 40: 880-889.

[259] Zhou W, Yang L, Ma G, Xu K, Lai Z, Chang X. DEM modeling of shear bands in crushable and irregularly shaped granular materials [J]. Granular Matter, 2017, 19: 25.

[260] Bruchmüller J, Wachem B, Gu S, Luo K. Modelling discrete fragmentation of brittle

particles [J]. Powder Technology, 2011, 208: 731-739.

[261] Marketos G, Bolton M. Compaction bands simulated in Discrete Element Models [J]. Journal of Structural Geology, 2009, 31: 479-490.

[262] McDowell G, BonoJP D. On the micro mechanics of one-dimensional normal compression [J]. Geotechnique, 2013, 63: 895-908.

[263] Asadi M, Rasouli V, Barla G. A bonded particle model simulation of shear strength and asperity degradation for rough rock fractures [J]. Rock Mechanics and Rock Engineering, 2012, 45: 649–675.

[264] Marji M. A bonded particle model for analysis of the flaw orientation effect on crack propagation mechanism in brittle materials under compression [J]. Archives of Civil and Mechanical Engineering, 2014, 14: 40-52.

[265] Potyondy D. Simulating stress corrosion with a bonded-particle model for rock [J]. International Journal of Rock Mechanics and Mining Sciences, 2007, 44: 677-691.

[266] Tsoungui O, Vallet D, Charmet J. Numerical model of crushing of grains inside two-dimensional granular materials [J]. Powder Technology, 1999, 105: 190-198.

[267] Cantor D, Estrada N, Azema E. Split-Cell Method for grain fragmentation [J]. Computers Geotechnics, 2015, 67: 150-156.

[268] Latham J, Xiang J, Farsi A, Joulin C, Karantzoulis N. A class of particulate problems suited to FDEM requiring accurate simulation of shape effects in packed granular structures [J]. Computational Particle Mechanics, 2020, 7: 975-986.

[269] Wei D, Zhao B, Daniel D, Gan Y. An FDEM study of particle breakage under rotational point loading [J]. Engineering Fracture Mechanics, 2019, 212: 221-237.

[270] Zeng W, Liu G, Kitamura Y, XuanH N. A three-dimensional ES-FEM for fracture mechanics problems in elastic solids [J]. Engineering Fracture Mechanics, 2013, 114: 127-150.

[271] Feng S, Han X. A novel multi-grid based reanalysis approach for efficient prediction of fatigue crack propagation [J]. Computer Methods in Applied Mechanics and Engineering, 2019, 353: 107-122.

[272] Lv J, Jiao Y, Wriggers P, Rabczuk T, Feng X, Tan F. Efficient integration of crack singularities in the extended finite element method: Duffy-distance transformation and conformal preconditioning strategy [J]. Computer Methods in Applied Mechanics

and Engineering, 2018, 340: 559-576.

[273] Xie G, Zhou F, Zhang D, Wen X, Li H. A novel triangular boundary crack front element for 3D crack problems based on 8-node serendipity element [J]. Engineering Analysis with Boundary Elements, 2019, 105: 296-302.

[274] Zhou W, Liu B, Wang Q, Chang X, Chen X. Formulations of displacement discontinuity method for crack problems based on boundary element method [J]. Engineering Analysis with Boundary Elements, 2020, 115: 86-95.

[275] Luo T, Ooi E, Chan A, Fu S. The combined scaled boundary finite-discrete element method: Grain breakage modelling in cohesion-less granular media [J]. Computers and Geotechnics, 2017, 88: 199-221.

[276] Raisianzadeh J, Mohammadi S, Mirghasemi A. Micromechanical study of particle breakage in 2D angular rockfill media using combined DEM and XFEM [J]. Granular Matter, 2019, 21: 48.

[277] Zhu F, Zhao J. Modeling continuous grain crushing in granular media: A hybrid peridynamics and physics engine approach [J]. Computer Methods in Applied Mechanics and Engineering, 2019, 348: 334-355.

[278] Liu B, Wang Q, Zhou W, Chang X. NURBS-enhanced line integration BEM for thermo-elastic problems considering the gravity load [J]. Engineering Analysis with Boundary Elements, 2021, 126: 118-127.

[279] Liu B, Zhou W, Wang Q, Chang X. An AOIMLS enhanced LIBEM and for solving 3D thermo-elastic problems and non-homogeneous heat conduction problems with heat generation [J]. International Journal of Thermal Sciences, 2021, 163.

[280] Zhong S, Jiang Q, Liu C, Li S, Qin W, Zhou J, Sun W. In-site core disking phenomenon and break mechanism of hard marble: Investigation in 2400 m deep-buried underground laboratory [J]. Journal of Central South University, 2020, 27: 2959-2970.

[281] Xie G, Zhou F, Zhang D, Zhai H, Cui G. Construction of special shape functions for triangular elements with one edge lying in the crack front [J]. Engineering Analysis with Boundary Elements, 2018, 91: 14-23.

[282] Clausen J, Damkilde L. An exact implementation of the Hoek–Brown criterion for elasto-plastic finite element calculations [J]. International Journal of Rock Mechanics

and Mining Sciences, 2008, 45: 831-847.

[283] Priest S. Determination of shear strength and three-dimensional yield strength for the Hoek-Brown criterion [J]. Rock Mechanics and Rock Engineering, 2005, 38: 299-327.

[284] Merifield R, Lyamin A, Sloan S. Limit analysis solutions for the bearing capacity of rock masses using the generalised Hoek–Brown criterion [J]. International Journal of Rock Mechanics and Mining Sciences, 2006, 43: 920-937.

[285] Zhou W, Yue Q, Wang Q, Feng Y, Chang X. The boundary element method for elasticity problems with concentrated loads based on displacement singular elements [J]. Engineering Analysis with Boundary Elements, 2019, 99: 195-205.

[286] Liu J, Yan J, Lo S. A new insertion sequence for incremental Delaunay triangulation [J]. Acta Mechanica Sinica, 2013, 29: 99-109.

[287] Zhan J, Chen J, Xu P, Han X, Chen Y, Ruan Y, Zhou X. Computational framework for obtaining volumetric fracture intensity from 3D fracture network models using Delaunay triangulations [J]. Computers and Geotechnics, 2017, 89: 179-194.

[288] Jianbo S. Empirical strength criterion of rock mass and its application in geological engineering [M]. Geological Press, 18-22, 2002.

[289] Tang C, Xu X, Kou S, Lindqvist P, Liu H. Numerical investigation of particle breakage as applied to mechanical crushing-Part I: Single-particle breakage [J]. International Journal of Rock Mechanics and Mining Sciences, 2001, 38: 1147-1162.

[290] Huang Q, Zhou W, Ma G, Ng T, Xu K. Experimental and numerical investigation of Weibullian behavior of grain crushing strength [J]. Geoscience Frontiers, 2020, 11: 401-411.

[291] Tang C, Liu H, Zhu W, Yang T, Li W, Song L, Lin P. Numerical approach to particle breakage under different loading conditions [J]. Powder Technology, 2004, 143-144: 130-143.

[292] Zhou B, Wei D, Ku Q, Wang J, Zhang A. Study on the effect of particle morphology on single particle breakage using a combined finite-discrete element method [J]. Computers and Geotechnics, 2020, 122.

[293] Erarslan N, Williams D. Experimental, numerical and analytical studies on tensile strength of rocks [J]. International Journal of Rock Mechanics Mining Sciences, 2012,

49: 21-30.

[294] Tsoungui O, Vallet D, Charmet J. Use of contact area trace to study the force distributions inside 2D granular systems [J]. Granular Matter, 1998, 1: 65-69.

[295] Tsoungui O, Vallet D, Charmet J, Roux S. Size effects in single grain fragmentation [J]. Granular Matter, 1999, 2: 19-27.

[296] Qu T, Feng Y, Zhao T, Wang M. A hybrid calibration approach to Hertz - type contact parameters for discrete element models [J]. International Journal for Numerical Analytical Methods in Geomechanics, 2020, 44: 1281-1300.

[297] Qu T, Feng Y, Wang Y, Wang M. Discrete element modelling of flexible membrane boundaries for triaxial tests [J]. Computers & Geotechnics, 2019, 115: 103154.